UNIVERSIDAD DE CANTABRIA

Escuela de Doctorado

Programa de Doctorado en Ingeniería Industrial:
Tecnologías de Diseño y Producción Industrial

DYNAMICAL BEHAVIOUR OF MULTISTAGE GEAR TRANSMISSIONS: ANALYSIS OF THE MESH PHASING

COMPORTAMIENTO DINAMICO DE TRANSMISIONES DE ENGRANAJES MULTIETAPA. ANALISIS DEL DESFASE EN EL ENGRANE

Tesis Doctoral

Autor: **D. Javier Sánchez Espiga**

Directores: **Prof. Dr. D. Fernando Viadero Rueda**

Dr. D. Alfonso Fernandez del Rincón

Santander, mayo 2021

"Los hombres geniales empiezan grandes obras,
los hombres trabajadores las terminan".
Leonardo da Vinci

A Belén, Ramón y Guillermo

Contents

Contents ..... **i**

List of Figures ..... **v**

List of Tables ..... **xi**

Agradecimientos ..... **xv**

Abstract ..... **xvii**

Resumen ..... **xxi**

Part I **1**

CHAPTER 1: INTRODUCTION **3**

1.1. Background & motivation 3

1.2. Objectives 4

1.3. Memory structure 5

Part II **7**

CHAPTER 2: STATE OF THE ART **9**

2.1. Introduction 9

2.2. Simple gear transmissions 10

2.2.1 Geometrical definition: profile cutting, contact point and contact areas 11

2.2.2 Contact forces 14

2.3. Planetary transmissions modelling 19
2.3.1 Lumped parameter and analytical modelling 20
2.3.2 FE and hybrid models 28
2.4. Industrial applications of planetary transmissions 34
2.5. Influence of errors in gear transmissions 39
2.6. Impact of mesh phasing in planetary transmissions 44
2.7. Experimental studies 47
2.8. Critical analysis 50

Part III 53

CHAPTER 3: VIRTUAL MODEL 55

3.1. Introduction 55
3.2. Model inputs 57
3.2.1 Wheel cutting 57
3.2.2 Transmission mounting 60
3.2.3 Definition of errors 63
3.2.4 Load transmission 64
3.3. Model formulation 65
3.3.1 Contact problem 66
3.3.2 Overlap calculation 72
3.3.3 Load balance in the transmission 73
3.4. Results obtaining 76

CHAPTER 4: STUDY OF THE TRANSMISSION GEOMETRY 79

4.1. Introduction 79
4.2. Transmission preliminary verifications 80
4.3. Transmission classification 81
4.4. Planet spacing 82
4.4.1 Equally spacing 82
4.4.2 Non-equal spacing 83
4.4.3 Floatability 84
4.5. Mesh phasing 85

4.5.1 In-phase phasing 86
4.5.2 Sequential phasing 87
4.5.3 Arbitrary phasing 87
4.6. Configurations of interest 88
4.7. Results 91
4.7.1 3-planet configurations 91
4.7.2 5-planet configurations 104
4.8. Main effects recap 114
CHAPTER 5: ERROR PRESENCE IN PLANETARY TRANSMISSIONS 115
5.1. Introduction 115
5.2. Geometrical definition of the studied errors 116
5.2.1 Pinhole position errors 116
5.2.2 Tooth thickness errors 118
5.3. Effect of the errors in the load sharing 120
5.3.1 Tangential position error 120
5.3.2 Radial error 122
5.3.3 Tooth thickness errors 125
5.4. Considered configurations 125
5.5. Results 127
5.5.1 Crucial values of the LSR: Configurations 1 & 2 127
5.5.2 Imbalance created in the LSR: Configuration 1 151
CHAPTER 6:. LOAD SHARING CALCULATION BY MEASURING ROOT STRAINS 157
6.1. Introduction 157
6.2. Methods 158
6.2.1 Finite-element models 158
6.2.2 Definition of the virtual strain gauges 161
6.2.3 Contact sequence 164
6.3. Load sharing calculation 167
6.4. Cases of study 170
6.5. Results 171

Part IV..... 195

CHAPTER 7: CONTRIBUTIONS, CONCLUSIONS AND FUTURE WORK.... 197

7.1. Contributions 197
7.2. Conclusions 198
7.3. Future works 201

References 203

ANNEX: NUMERICAL RESULTS 218

A.I. GEOMETRY 221
A.I.1. 3-planet transmissions 221
A.I.2. 5-planet transmissions 222
A.II. Errors 223
A.II.1 Configuration 1: 223
A.II.2 Configuration 2: 227
A.III. Deltas 231

List of Figures

Figure 1. Layout of a planetary transmission. 10

Figure 2. Gear system lumped-parameter model in (P. Velex & Maatar, 1996) 13

Figure 3. FE models influenced by the helix and cone angles (Jesper Brauer, 2004) 15

Figure 4. Development of the number of publications (1965-2015) (Cooley & Parker, 2014) 20

Figure 5. Lumped-parameter approach for the contact between sun and planet, proposed by Kasuba (August & Kasuba, 1986b) 22

Figure 6. 3D lumped-parameter approach presented by Kahraman in (A Kahraman, 1994b)..... 24

Figure 7. Detail of the dof considered: a) sun-pinion, b) pinion-ring and c) pinion-carrier (A Kahraman, 1994b) 25

Figure 8. Lumped-parameter model with the definition of the position error in any planet (Gu & Velex, 2012) 28

Figure 9. Details of the FE model for the ring gear in (Abousleiman & Velex, 2006): a) elements in the model, b) interface between body and teeth in the gear. 31

Figure 10. GSAM model of the 5-planet transmission studied in (Singh et al., 2008) 32

Figure 11. Models employed in (J. Liu et al., 2020): a) multibody model, b) FE model of the ring gear. 34

Figure 12. Historic development of total wind energy producing installations in GW (GWEC, 2019)..... 35

Figure 13. Growth of the offshore installations in GW (GWEC, 2019) 36

Figure 14. Singh's sketch to analyse the behaviour of a 7-planet transmission with a position error in planet 1 (Singh, 2011) 42

Figure 15. Double phasing gears shown in (Gill-Jeong, 2010) 45

Figure 16. Variation of the meshing stiffness in the contacts of a 3-planet planetary transmission analysed in (R. G. Parker & Lin, 2004) 46

Figure 17. Sketch of the algorithm followed in the employed virtual model. 56

Figure 18. Result of the profile cutting for a) sun gear, b) planet gear 58

Figure 19. Result of the profile cutting in the ring gear 59

Figure 20. 5-planet planetary transmission mounted. 60

Figure 21. Contact forces and its imbalance due to the mounting distance. 62

Figure 22. Construction of the ball bearing*. 63

Figure 23. Scheme of the iterative solution to the contact problem. 66

Figure 24. Global FE model of the sun gear in configuration 1. 67

Figure 25. Compilation of load cases in the global FE model with no load (blue) and under load (red)..... 68

Figure 26. Local FE model for the sun gear. 69

Figure 27. Compilation of load cases in the local FE model with no load (blue) and under load (red)..... 70

Figure 28. Application of the superposition principle to the contact problem steps 70

Figure 29. Balance in the sun gear due to the contacts: a) perfectly balanced, b) With support force..... 75

Figure 30. Influence of the spacing in the sun-planet contact forces and the balance in the sun gear 83

Figure 31. Lumped-parameter approach to the floatability in the sun gear support. 84

Figure 32. Snapshots of the meshing stiffness in an in-phase transmission 86

Figure 33. Snapshots of the meshing stiffness in a sequentially phased transmission 86

Figure 34. LSR in a 3-planet ESIP transmission. 92

Figure 35. Detail of the LSR in a 3-planet ESIP transmission. 92
Figure 36. LSR in a 3-planet NESIP transmission. 93
Figure 37. Detail of the LSR in a 3-planet NESIP transmission. 94
Figure 38. Load sharing in 3-planet ESSP transmission. 95
Figure 39. 3-planet NESSP transmission. 96
Figure 40. Detail of the LSR in a 3-planet ESIP transmission with floating sun. 97
Figure 41. 3-planet ESIP transmission with floating sun: Detail of the sun orbit. 98
Figure 42. Load sharing in 3-planet NESIP transmission with floating sun. 99
Figure 43. 3-planet NESIP transmission with floating sun: Sun orbit. 100
Figure 44. 3-planet ESSP transmission with floating sun: Sun orbit. 101
Figure 45. 3-planet ESSP transmission with floating sun: Sun orbit. 102
Figure 46. 3-planet ESIP transmission with floating sun: Sun orbit. 103
Figure 47. 3-planet ESIP transmission with floating sun: Sun orbit. 104
Figure 48. Load sharing in 5-planet ESIP transmission. 105
Figure 49. Load sharing in 5-planet NESIP transmission. 105
Figure 50. Load sharing in 5-planet ESSP transmission. 106
Figure 51. Load sharing in 5-planet NESSP transmission. 107
Figure 52. Load sharing in 5-planet ESIP transmission with floating sun. 108
Figure 53. 5-planet ESIP transmission with floating sun: Sun orbit. 108
Figure 54. Load sharing in 5-planet NESIP transmission. 109
Figure 55. 5-planet NESIP transmission with floating sun: Sun orbit. 110
Figure 56. Load sharing in 5-planet ESSP transmission with floating sun. 111

Figure 57. 5-planet ESSP transmission with floating sun: Sun orbit. 112

Figure 58. Load sharing in 5-planet NESSP transmission. 113

Figure 59. 5-planet NESSP transmission with floating sun: Sun orbit. 113

Figure 60. Geometrical definition of the pinhole position error 118

Figure 61. Measurement of the wk 119

Figure 62. Influence of the tangential error a) detail of the external contact b) both contacts..... 121

Figure 63. Influence of the radial error a) detail of the external contact b) both contacts..... 123

Figure 64. Contact forces and its imbalance due to the mounting distance. 124

Figure 65. Max. and min. in the LSR for three-planet ESIP a) 1200 Nm CCW b) 1200 Nm CW (Conf. 1)..... 130

Figure 66. Max. and min. in the LSR for three-planet ESIP a) 1200 Nm CCW b) 1200 Nm CW (Conf. 2)..... 131

Figure 67. Max. and min. in the LSR for three-planet ESIP a) 1200 Nm CCW b) 1200 Nm CW (Conf. 1)..... 133

Figure 68. Max. and min. in the LSR for three-planet ESIP a) 3600 Nm CCW b) 3600 Nm CW (Conf. 2)..... 134

Figure 69. Max. and min. in the LSR for three-planet ESSP a) 1200 Nm CCW b) 1200 Nm CW (Conf. 1)..... 136

Figure 70. Max. and min. in the LSR for three-planet ESSP a) 1200 Nm CCW b) 1200 Nm CW (Conf. 2)..... 137

Figure 71. Max. and min. in the LSR for five-planet ESIP a) 3600Nm CCW b) 3600Nm CW (Conf. 1)..... 138

Figure 72. Max. and min. in the LSR for three-planet ESIP a) 3600Nm CCW b) 3600Nm CW (Conf. 2)..... 139

Figure 73. Max. and min. in the LSR for five-planet ESIP a) 1200Nm CCW b) 1200Nm CW (Conf. 1)..... 141

Figure 74. Max. and min. in the LSR for five-planet ESIP a) 1200Nm CCW b) 1200Nm CW (Conf. 2)..... 142

Figure 75. Max. and min. in the LSR for five-planet ESIP a) 3600Nm CCW b) 3600Nm CW (Conf. 1)..... 144

Figure 76. Max. and min. in the LSR for five-planet ESIP a) 3600Nm CCW b) 3600Nm CW (Conf. 2) 145

Figure 77. Max. and min. in the LSR for five-planet ESSP a) 1200Nm CCW b) 1200Nm CW (Conf. 1) 147

Figure 78. Max. and min. in the LSR for five-planet ESSP a) 1200Nm CCW b) 1200Nm CW (Conf. 2) 148

Figure 79. Max. and min. in the LSR for five-planet ESSP a) 3600Nm CCW b) 3600Nm CW (Conf. 1) 149

Figure 80. Max. and min. in the LSR for five-planet ESSP a) 3600Nm CCW b) 3600Nm CW (Conf. 2) 150

Figure 81. ΔLSR ESIP configurations: a) 1200Nm CCW b) 1200Nm CW c) 1200Nm CCW d) 1200Nm CW 153

Figure 82. ΔLSR ESSP configurations: a) 1200Nm CCW b) 1200Nm CW c) 1200Nm CCW d) 1200Nm CW 155

Figure 83. Global FE models for the configuration 2: a) Sun, b) planet, and c) ring..... 160

Figure 84. 3-planet transmission after mounting..... 161

Figure 85. Detail of the possible contacts in the marked section in Figure 84..... 161

Figure 86. Detail of the noded sections in the global FE model. 162

Figure 87. Snapshots of the contact sequence 165

Figure 88. Detail of the global FE model a) under no load b) under one of the load cases. 166

Figure 89. Comparison of the LSR and the strain measurements in the ESIP transmissions..... 168

Figure 90. Comparison of the LSR and the strain measurements in the ESSP transmissions..... 169

Figure 91. Detail of the contacts between sun and planets for 3-planet ESIP transmission. 171

Figure 92. Detail of the contacts between sun and planets for 3-planet ESSP transmission. 172

Figure 93. Mechanical analogy for the load sharing calculation discrepancies..... 174

Figure 94. LSR and strains in the gauge in ESIP with 1.25 μm error (Conf. 2). 176

Figure 95. Strains in the gauge in ESIP with various errors for configuration 1. 178

Figure 96. LSR in ESIP with various errors in configuration 1. 179

Figure 97. Strains in the gauge in ESIP with various errors for configuration 2. 180

Figure 98. LSR in ESIP with various errors for configuration 2. 181

Figure 99. LSR and strains in the gauge in ESSP with 1.25 μm error (Conf. 2). 184

Figure 100. Strains in the gauge in ESSP with various errors for configuration 1. 187

Figure 101. LSR in ESSP with various errors for configuration 1. . 188

Figure 102. Strains in the gauge in ESSP with various errors for configuration 2. 189

Figure 103. LSR in ESSP with various errors for configuration 2. . 190

Figure 104. Discrepancies between the maximum LSR and SGLR results for configuration 1(Graph). 192

Figure 105. Discrepancies between the maximum LSR and SGLR results for configuration 2(Graph). 192

List of Tables

Table 1. Types of planetary transmission regarding their geometry. 81

Table 2. Detailed number of teeth in the proposed transmissions ... 88

Table 3. Classification of the possible transmissions with 3 planets 89

Table 4. Classification of the possible transmissions with 5 planets 90

Table 5. Lumped rigidity in the sun support. 96

Table 6. Considerations for studied cases. 126

Table 7. Dimensions of the shaft mountings in the considered configurations 127

Table 8. Theoretical contact ratios in the studied configurations .. 160

Table 9. Pinhole position errors considered to study for both configurations. 170

Table 10. Numerical results for the ESIP configuration 1 in every case of study for configuration 1. 182

Table 11. Numerical results for the ESIP configuration 2 in every case of study for configuration 2. 183

Table 12. Numerical results for the ESSP configuration 1 in every case of study for configuration 1. 185

Table 13. Numerical results for the ESSP configuration 2 in every case of study. 186

Table 14. Discrepancies between the maximum LSR and SGLR results for configuration 2 (numerical results). 193

Table 15. Discrepancies between the maximum LSR and SGLR results for configuration 2 (numerical results). 194

Table 16. Numerical verification of the angular spacing (3-planet transmission). 221

Table 17. Numerical results to the mesh phasing (3-planet transmission). 221
Table 18. Numerical verification of the angular spacing (5-planet transmission). 222
Table 19. Numerical results to the mesh phasing (5-planet transmission). 222
Table 20. LSR in 3-planet ESIP 1200 Nm CCW (Conf. 1). 223
Table 21. LSR in 3-planet ESIP 1200 Nm CW (Conf. 1). 223
Table 22. LSR in 3-planet ESIP 3600 Nm CCW (Conf. 1). 223
Table 23. LSR in 3-planet ESIP 3600 Nm CW (Conf. 1). 223
Table 24. LSR in 3-planet ESSP 1200 Nm CCW (Conf. 1). 224
Table 25. LSR in 3-planet ESSP 1200 Nm CW (Conf. 1). 224
Table 26. LSR in 3-planet ESSP 3600 Nm CCW (Conf. 1). 224
Table 27. LSR in 3-planet ESSP 3600 Nm CW (Conf. 1). 224
Table 28. LSR in 5-planet ESIP 1200 Nm CCW (Conf. 1). 225
Table 29. LSR in 5-planet ESIP 1200 Nm CW (Conf. 1). 225
Table 30. LSR in 5-planet ESIP 3600 Nm CCW (Conf. 1). 225
Table 31. LSR in 5-planet ESIP 3600 Nm CW (Conf. 1). 225
Table 32. LSR in 5-planet ESSP 1200 Nm CCW (Conf. 1). 226
Table 33. LSR in 5-planet ESSP 1200 Nm CW (Conf. 1). 226
Table 34. LSR in 5-planet ESSP 3600 Nm CCW (Conf. 1). 226
Table 35. LSR in 5-planet ESSP 3600 Nm CW (Conf. 1). 226
Table 36. LSR in 3-planet ESIP 1200 Nm CCW (Conf. 2). 227
Table 37. LSR in 3-planet ESIP 1200 Nm CW (Conf. 2). 227
Table 38. LSR in 3-planet ESIP 3600 Nm CCW (Conf. 2). 227
Table 39. LSR in 3-planet ESIP 3600 Nm CW (Conf. 2). 227
Table 40. LSR in 3-planet ESSP 1200 Nm CCW (Conf. 2). 228
Table 41. LSR in 3-planet ESSP 1200 Nm CW (Conf. 2). 228
Table 42. LSR in 3-planet ESSP 3600 Nm CCW (Conf. 2). 228
Table 43. LSR in 3-planet ESSP 3600 Nm CW (Conf. 2). 228
Table 44. LSR in 5-planet ESIP 1200 Nm CCW (Conf. 2). 229
Table 45. LSR in 5-planet ESIP 1200 Nm CW (Conf. 2). 229

Table 46. LSR in 5-planet ESIP 3600 Nm CCW (Conf. 2). 229
Table 47. LSR in 5-planet ESIP 3600 Nm CCW (Conf. 2). 229
Table 48. LSR in 5-planet ESSP 1200 Nm CCW (Conf. 2). 230
Table 49. LSR in 5-planet ESSP 1200 Nm CW (Conf. 2). 230
Table 50. LSR in 5-planet ESSP 3600 Nm CW (Conf. 2). 230
Table 51. LSR in 5-planet ESSP 3600 Nm CW (Conf. 2). 230
Table 52. ΔLSR in 3 & 5-planet ESIP 1200 Nm (Conf. 1). 231
Table 53. ΔLSR in 3 & 5-planet ESIP 3600 Nm (Conf. 1). 232
Table 54. ΔLSR in 3 & 5-planet ESSP 1200 Nm (Conf. 1). 233
Table 55. ΔLSR in 3 & 5-planet ESSP 3600 Nm (Conf. 1). 234

Agradecimientos

En primer lugar, me gustaría expresar mi agradecimiento a Fernando y Alfonso, mis directores, por aceptar el reto que ha supuesto esta Tesis y haberme guiado de la mejor manera, tratándome como un hijo. Fernando, sin tus conocimientos e innumerables consejos desde que empezamos a trabajar juntos en un TFG dando vida a una máquina propia de ciencia ficción, no habría sido lo mismo y no sería el profesional que he llegado a ser en la actualidad. Alfonso, tus interminables ideas y retos suponen un aliciente diario, que combina perfectamente con la paciencia infinita que has tenido en el desarrollo de esta tesis para transmitirme tus conocimientos. Sin embargo, lo más importante, muchas gracias a los dos por ser como sois personalmente.

Igualmente, mencionar especialmente a los compañeros de despacho, los que fueron, como Alberto, quien por fin se libró de mis pesadas preguntas, pero se fue dejando buena parte de sus conocimientos. Y a Kiko quien actualmente tiene que aguantarme, pero lo hace con tranquilidad y siempre está dispuesto a prestar su ayuda o sus consejos.

Por supuesto, agradezco a Miguel el trabajo de dirección en la sombra, aportando luz cuando la mente se nublaba puntualmente. A Ana por sus detalladas explicaciones y sabios consejos. Y finalmente, pero no por eso menos importante, a Pablo por su ayuda en cualquier momento, ya sea para cacharrear en el laboratorio o para divagar sobre pasarelas flotantes. A todos vosotros os agradezco todos estos años y el hacerme sentir un miembro más del equipo desde el primer momento.

Por otra parte, a mis familiares y amigos por saber estar en los malos momentos y también saber disfrutar de los buenos momentos. Mis padres que siempre han estado ahí, mi hermano siempre tan cerca aun en la de distancia, incluso en estos tiempos de distanciamiento obligado. Por supuesto, a Kasia

por su apoyo continuo, su comprensión y por tener las palabras adecuadas en los malos momentos.

En otro ámbito, me gustaría hacer extensible mi agradecimiento a los compañeros de la empresa Gamesa Gearbox por su colaboración a lo largo de este trabajo, en especial a José Calvo Irisarri por sus ideas y conocimientos. Igualmente, agradecer a Alfredo Fernández Sisón, Harri Aurrekoetxea e Iñaki Ruiz de Ocenda por su colaboración.

Por fim, gostaria de expressar o meu agradecimento aos meus colegas e amigos da Universidade do Minho, em especial ao Prof. Flores, Filipe Marques e Nuno Dourado pela excelente experiência na minha estadia tanto profissional como pessoalmente.

Javier

Abstract

Gear transmissions are complex systems composed of numerous elements with a sophisticated geometry. In order to operate correctly, a gear transmission, and more importantly an epicyclic transmission, requires the synergy of multiple factors. Besides, its proper functioning is affected by numerous issues, which hinder the identification of problems in its performance.

Despite its complexity or maybe because of it, planetary transmissions have vastly grown in popularity in the last few decades. In the industry, new applications and classical applications have emerged or developed to a point where planetary transmissions play a crucial role in its correct performance. This development has led to the creation of new hypothesis along with the appearance of new problems also.

In relation to these new problems and applications, this Thesis aims to deepen the knowledge in some of them, as well as studying other possible scenarios in search for answers to some of the unknowns that both manufacturers and researchers have in relation to this topic. Mainly, this Thesis focuses on the role played by the geometry in the behaviour of a planetary transmission. As far as this work is concerned, the geometry refers to the planet spacing and mesh phasing, which are direct consequences of the transmission's design criteria. Thus, this Thesis analyses in depth the impact of these effects in the behaviour of a planetary transmission. More precisely, the load sharing of the transmission is the magnitude chosen to analyse the state of the planetary transmission throughout the performed simulations.

Once the impact of these effects is established, another point of crucial importance in the gear transmissions involves the inevitable manufacturing errors and their incidence. These will affect the performance, reliability, durability and quality of the planetary transmission. All the previously

mentioned illustrate the importance of this point. In this Thesis, the study has been limited to the tooth thickness error and the pinhole position error. The scope of possible errors is vastly wide, and these errors are considered some of the most important in terms of their influence in the load sharing. In addition, given their geometry the impact of these errors depends on the working conditions, thus, different load levels and directions are studied.

After this, the focus is set on the experimental measuring procedures and the validity of the results obtained by them. This section combines the effects previously studied, geometry and errors, together with the measurements of strain in the root of the sun gear. Thus, a numerical approach is developed to mimic the experimental strain measurements. These are compared to the real load sharing in the transmission in order to analyse the accuracy of this measurement procedure in comparison to the real behaviour of the simulated transmission.

The results obtained prove that for in-phase transmissions the impact of the angular spacing is only visible if there is floatability in the gear supports. In addition, the influence of the floatability is shown to change with the number of planets, which is prove in the impact of the floatability for 5-planet transmissions in comparison to the 3-planet ones. Besides, the behaviour of a sequentially phased transmission is worse, in terms of the amount of load borne by each planet, than the analogous in-phase transmission.

This becomes more notable whenever there exists errors in the transmission. The imbalance created by the error is higher and the impact in the maximum and minimum load values is different from in in-phase transmissions due to the delay in the phasing.

In terms of the measurements, the results prove a lack of accuracy in the experimental procedure results in comparison to the real load sharing. The inclusion of sequential mesh phasing and errors in the simulations dramatically affects the accuracy of the strains measurements as a tool to calculate the load sharing in a planetary transmission.

Finally, as part of the conclusions extracted from this work, it is visible how sequential mesh phasing affects the balance in the load sharing and leads to imbalances in the transmission, due to the delay in the contacts. This phasing also increases the impact of the manufacturing errors in the load sharing. This impact increases with the number of planets because of the raise in the rigidity

in the system. The impact of the stiffness becomes clear with different changes as the various number of planets and the changes in the geometry in the shaft mounting.

On the other hand, the experimental measurements prove to be inaccurate for any configuration different from an equally spaced in-phase transmission without error. This inaccuracy increases with the size of the error and is bigger for sequentially phased transmissions.

Given the conclusions extracted, in a near future this work can be extended in different lines. Firstly, the number of dimensions in the model influences some of the effects studied, thus, the model should be extended to 3D to consider helical gears. At the same time, increase the number of planets in the transmission to more than 5, therefore, more combinations of possibilities will appear for an even number of planets. However, in the planar model without changing the number of planets, it is also possible to extend the measuring approaches to some other procedures than are commonly employed.

Resumen

Las transmisiones de engranajes son sistemas complejos compuestos por numerosos elementos de geometría complicada. El correcto funcionamiento de una transmisión de engranajes, y más concretamente una transmisión planetaria, necesita de la sinergia de muchos factores y se ve afectado por muchos condicionantes que dificultan la identificación de los problemas.

A pesar de su complejidad o quizá consecuencia de ella, las transmisiones de engranajes planetarios han adquirido un papel muy relevante en la industria en las últimas décadas. Nuevas aplicaciones y aplicaciones clásicas han surgido o evolucionado hasta el punto en que las transmisiones de engranajes epicicloidales tienen un papel determinante en su buen funcionamiento. Este desarrollo también ha llevado al planteamiento de nuevas hipótesis y a la aparición de nuevos problemas.

En relación con la aparición de nuevos problemas y aplicaciones, esta Tesis trata de analizar en profundidad algunos de ellos, así como, estudiar otros posibles escenarios en busca de dar respuesta a algunos de los interrogantes que surgen tanto a fabricantes como a investigadores sobre el correcto funcionamiento de dichas transmisiones. Principalmente, esta Tesis se centra en el papel que juega la geometría en el comportamiento de las transmisiones planetarias. En lo que se refiere a la geometría, en esta Tesis el interés se centra en el impacto del espaciado angular y la fase de engrane, que son consecuencia directa de los criterios de diseño de la transmisión. En más detalle, esta Tesis analiza el impacto que tienen esos criterios en el reparto de carga en transmisiones planetarias. El reparto de carga se escoge como la magnitud que permite analizar el estado de la transmisión a lo largo de las simulaciones.

Una vez que se ha establecido el impacto del espaciado y la fase en el comportamiento de la transmisión, se incluyen nuevos efectos. En este caso, se considera la importancia que tienen los inevitables errores de fabricación en las transmisiones planetarias. Estos errores afectan a la calidad, durabilidad y el comportamiento de las transmisiones planetarias, lo cual da una idea de la importancia que los errores tienen en este campo. En esta Tesis, los errores escogidos se limitan a errores en el espesor de los dientes, así como, errores de montaje de los planetas en el portaplanetas. Además, dadas las características de estos errores, su influencia varía dependiendo de las condiciones de trabajo, por esto, se amplía el estudio a diferentes niveles de carga y sentidos de aplicación de la carga.

Después de esto, el interés se centra en el análisis de los procedimientos experimentales de medida y su validez. En esta parte de la Tesis se combinan los estudios anteriores con el uso de la medida de deformaciones en la raíz de los dientes del sol para el cálculo de reparto de carga en transmisiones planetarias.

Los resultados demuestran que en configuraciones en fase solo se hace visible la influencia del espaciado de los planetas cuando los apoyos de las ruedas cuentan con flotabilidad. Además, la influencia de la flotabilidad en los apoyos demuestra tener un efecto diferente para transmisiones de 5 planetas que para transmisiones de 3 planetas. Además, el comportamiento de las transmisiones con fase secuencial prueba ser peor, en su reparto de carga, que el de la configuración en fase análoga.

Esto, se hace más visible cuando se incluyen errores en las transmisiones simuladas. El desequilibrio creado por un error es mayor y el impacto que tiene en los valores máximos y mínimos de carga es mayor debido a la fase en el engrane.

En cuanto a las medidas experimentales, los resultados prueban ser imprecisos en comparación con el reparto de carga real en la transmisión. Además, la inclusión de secuencia en la fase de engrane y errores afecta notablemente la precisión de las medidas de deformaciones como una herramienta de cálculo del reparto de carga en transmisiones planetarias.

Finalmente, como conclusiones extraídas de los resultados comentados anteriormente, se demuestra como la secuencia en el engrane afecta notablemente al equilibrio en el reparto de carga en las transmisiones y genera

desequilibrios debidos al desfase en el engrane. Esta fase de engrane también incrementa el impacto de los errores en el reparto de carga de la transmisión. Por otra parte, otro factor que incrementa el impacto de los errores es el aumento del número de planetas. El impacto de la rigidez se hace patente con otros cambios como la modificación del número de planetas en la transmisión y el tamaño de los ejes sobre los que se montan las ruedas.

En cuanto a las medidas experimentales, prueban ser imprecisas en cualquier configuración diferente de una transmisión equiespaciada y en fase sin errores. Además, esta falta de precisión crece con el tamaño del error y se hace mayor para configuraciones secuenciales.

Vistas las conclusiones que se extraen es posible plantear nuevas líneas para continuar con este trabajo. En primer lugar, el modelo se puede extender a un planteamiento tridimensional para tener en cuenta la influencia de esta tercera dimensión en los fenómenos estudiados mediante el análisis de transmisiones planetarias helicoidales. Al mismo tiempo, el número de planetas se puede incrementar por encima de 5, así, nuevos escenarios de estudio aparecen, principalmente en configuraciones con un número par de planetas superior a 5. No obstante, en el modelo plano con el número de planetas ya estudiado, las técnicas de medida experimental estudiadas se pueden extender a otros procedimientos que también se utilizan habitualmente.

Part I

Chapter 1: Introduction

1.1. Background & motivation

This work is an extension of the works on gear transmissions developed by members of the Mechanical Engineering research group from the University of Cantabria throughout the last decades. At first, a model for simple gear transmissions was presented in (Fernández del Rincón, 2010). This model is appropriate for the simulation of external gears from points of view both quasi-static and dynamic. After this, the logical step to take was to extend this approach to numerous simultaneous meshings in both external and internal gears, making possible the simulation of planetary gears (Iglesias Santamaría, 2013). From the development of those models, numerous contributions have been made to the state of the art in mechanical transmission of power by using gear transmissions, and in the field of efficiency in gear transmissions (Diez-Ibarbia, 2016). The development of the technology in planetary transmissions has led to new scenarios of study in search of the necessary enhancement of the classical approaches in search for higher power, better performances, and a higher reliability. The interest in this branch of study leads to extend the activity performed by this research group with the following Ph. D. Thesis, which extends the study of planetary gears to different scenarios of simulation.

Thus, this work responds to the ongoing growth in the interest of planetary transmissions as a means to transmit torque in various applications. In the current society, these transmissions are used for various applications such as

wind turbines, vehicle transmissions both electric and internal combustion vehicles, rotorcrafts and agricultural machinery among others. In search of fulfilling the emission reduction objective, in order to increase the efficiency of this equipment, its durability and their overall performance, the understanding of these infrastructures has to be enhanced and updated to new approaches. Thus, this work focuses on the importance of the planet spacing and mesh phasing, geometrical characteristics of any planetary transmission, in its performance. To this end, several studies are performed combining those factors, in order to analyse different configurations that correspond to industrial applications. Thus, this work looks at enhancing the understanding of the influence of these changes in the geometry on the transmission performance. The points that are the focus of this work regard the mesh phasing, the planet spacing, and the number of planets. In addition, this work includes the impact of the unavoidable errors in the manufacturing of the transmissions, together with the effects previously mentioned. Besides, the validity of the measuring techniques to address the load sharing in the transmissions. To that aim, a new numerical approach for this procedure is performed and the results are compared to the real load sharing.

1.2. OBJECTIVES

The main objective consists in the expansion and enhancement of the knowledge in the behaviour of the load sharing in planetary transmissions in new scenarios of analysis influenced by changes in its geometry. At the same time, this work aims to deepen the knowledge of these new scenarios as part of the preliminary studies necessary to propose the modelling of these cases of study. Besides, this work presents a series of partial objectives as tasks to complete in order to achieve the previously mentioned global objectives. Thus, these partial objectives are gathered below:

- Determining the impact of design parameters such as the number of teeth and the planet spacing in the performance of any planetary transmission.

- Enhance the knowledge on the behaviour of planetary transmissions with an odd number of planets.
- Establish the impact that the mesh phasing has in the behaviour of any planetary transmission both with and without any error.
- Establishing the impact of various errors in the behaviour of planetary transmissions.
- Numerically address the problem of the measurements in planetary transmission and the calculation of the load sharing from those measurements. Likewise, quantify the error made by the measurements in comparison to the real load sharing in an epicyclic transmission.

1.3. Memory structure

This memory is divided in four parts clearly differentiated in order to organise neatly the contents and to show the development of all the work performed in the context of this Ph. D. thesis.

In more detail, the first part belongs to the introduction to this work. Thus, the origin and motivation to this work are presented together with the objectives that were proposed at the beginning of this multiyear work. All these previous points set the grounds on where the following parts will be developed. Then, the second part of the memory is a mix of a look to the past, present and future due to the combination of the study of the state of the art, highlighting the most important contributions to the topic that have been made in recent times. Besides, apart from revising the previous contributions, new ideas are proposed as the object of the studies that are shown further in this Thesis. The third part gathers every aspect of the definition of the studies performed in regards to the ideas proposed previously. Later, the results of these studies are presented in sequence where different effects are analysed separately and combined in further simulations.

Finally, the last part brings the conclusions extracted from this work and the future scenarios of work that surge after all the ideas commented throughout the memory.

Part II

Chapter 2: State of the art

2.1. Introduction

Mechanical transmissions are broadly employed in the industry, gear transmissions are one of the most common mechanical transmissions. Numerous different solutions exist in terms of gear transmissions depending on its construction, material, and gear teeth to name a few possible aspects. Amongst those possible solutions, planetary transmissions are of great interest given their advantages and numerous applications. These transmissions are composed by three kinds of wheels. The first kind is a central wheel called sun, the second kind are the planets and the last one is an internal gear, the ring. These wheels are disposed as follows, the sun is at the centre of the transmission, the N number of planets are disposed in a structural element called carrier, surrounding the sun. Between the sun and each planet there will be external contact. The carrier is coaxial with the sun. Finally, the ring is in the periphery of the transmission, its centre coincides with the sun and carrier centre and has inner contact with each planet. Given their construction, these transmissions allow handling higher torque levels than a simple gear transmission of equal size. Furthermore, they provide different speed ratios between inlet and outlet members just by changing the reaction (fixed) member. Additionally, there exists a coaxiality between the inlet and the outlet in these transmissions, whereas this is not as common in multi-stage simple transmissions.

Figure 1. Layout of a planetary transmission.

Thus, given all the previous, in the following chapter a review of the state of the art in the topic of gear transmissions is presented.

2.2. Simple gear transmissions

Virtual modelling in gear transmissions is a technique that started to be used in the midst of the 20th century. It has experienced a still ongoing raise in popularity throughout the last decades. This technique is vastly used nowadays, due to the reduction in the cost that it provides. This reduction is comparing it to an analogous experimental work. Not only is it due to the cost, but also it is popular given the high degree of realism that is possible to reach with the latest models. This realism came along with the development of new hardware and software to reduce computational time and allow notably complex simulations in short computational times.

Given all the previous, it is important to understand and study the development of this new branch of study. Furthermore, this understanding is of crucial importance to make a choice for modelling transmissions and to recreate real problems in gear transmissions in a virtual environment.

As a first approach to the topic, before getting into modelling in planetary transmissions, the logical previous step is the study of the modelling in simple gear transmissions. Obviously, the modelling of these simpler transmissions are the grounds on where the planetary transmission models stand.

In the modelling of simple and planetary transmissions, there are different aspects to solve. Then, for planetary gears, these have to be solved for multiple contacts and consider the interactions amongst them. In the following, the main aspects of gear transmission modelling will be studied. Afterwards, the study will be more focused on the modelling of planetary transmissions.

2.2.1 Geometrical definition: profile cutting, contact point and contact areas

For starters, in order to model a gear transmission the geometry of the whole problem must be defined. Not only does it include the tooth profiles, but also it includes the geometry of the entire transmission. This geometrical definition affects crucially the stiffnesses in the elements and consequently, will have a relevant impact on the performance in any model.

The geometrical description of the wheels, together with the location of the contact points and areas, comes from the meshing theory (Faydor L. Litvin & Fuentes, 2004). This is related to the manufacturing, design and metrology in gears.

Therefore, this branch of the science is focused on the definition of the teeth profiles, as well as the tools and verification procedures in order to define not only the teeth, but also the geometry of the wheels and the transmission. Nowadays, the strategy presented by Litvin & Fuentes in (Faydor L. Litvin & Fuentes, 2004) is the most commonly used by researchers in order to define

the geometry of the wheels in their virtual models. This approach is based on the definition of the cutting tool and the simulation of the wheel cutting procedure. One of the strengths of this definition, in comparison to others, relies on the possibility to define the trochoid directly, which is not possible in many other approaches. Besides, this procedure provides the possibility to include slight changes in the profiles such as, profile shifting, tip relief and tip rounding arc. The two latter are highly useful to avoid contacts on the edge of the flank.

Previously, the same author solved the problem of the determination of the contact points and areas in (F.L. Litvin, Tsung, Coy, Handschuh, & Tsay, 1986). This problem is solved by employing a geometrical approach, under the condition of tangentiality between the profiles of opposed teeth. After this, the Hertzian theory allows to obtain the contact ellipses. This methodology allows determining the trajectory of the contact. Likewise, it has been used to improve the efficiency in transmissions by adjusting some details in the manufacturing process, looking for lowering the noise and vibration levels, which is also known as tooth contact analysis.

The calculation of the contact areas is a problem that has been faced from numerous points of view throughout the years. At first, the determination of the contact areas was based on formulations that omitted the deflections due to the effect of the loads. These just focused on the kinematical design of the transmission and the decrease of the noise and vibration. On this line, the approaches focused on the definition of design and synthesis tools to determine the adjustments in the manufacturing process to obtain a precise sequence in each contact. This was solved for spiral conical gears in (Argyris, Fuentes, & Litvin, 2002), hypoidal gears in (J. Zhang, Fang, Cao, & Deng, 2007), and worm gears in (Seol & Litvin, 1996). These look for punctual contacts among the profiles avoiding the contact on the edges. This formulation obtains the parametric coordinates of the contact point and the angular rotation of the wheel to find that contact. This solution is obtained from numerically solving

a system of non-linear equations; however, this is not the only solution to this problem. Other authors such as Sheveleva et al. (Sheveleva, Volkov, & Medvedev, 2007) calculate the minimum distance among profiles, defining a mesh of points in each of them. Thus, it is possible to consider the influence of some flaws along the profile in the contact, as presented by Wink & Sherpa in (Wink & Serpa, 2005, 2008). In a similar approach rather than any flaw, the wear in the profiles due to the operation in the transmission can be considered also. This was performed for spur cylindrical gears by Wojnarowski & Oshnichenko in (Wojnarowski & Onishchenko, 2003).

Despite the wide range of approaches, some of them are not affordable in dynamic models. The complexity of the approaches make impossible its calculation for every contact in a dynamic model, in a reasonable computational time. This makes necessary a simplification in the approaches, thus, Velex & Maatar in (P. Velex & Maatar, 1996) (Figure 2), as well as, Blankenship & Singh in (Wesley Blankenship & Singh, 1995b, 1995a) limit the search for contact to the meshing line or plane. Another possibility consists in the discretization of the profiles and looks for the minimum distance between them, this was presented by Kasuba & Evans (Kasuba & Evans, 1981) and Vijayakar (Vijayakar, 1991).

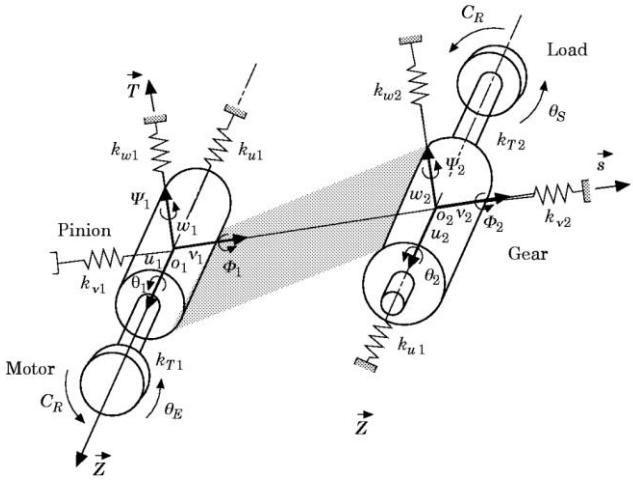

Figure 2. Gear system lumped-parameter model in (P. Velex & Maatar, 1996)

2.2.2 Contact forces

The solution of the contact problem represents one of the most complex aspects in any model for gear transmissions. The complexity of this problem varies depending on the approach taken. However, it is also possible to apply simplifications, which are appropriate in some of the cases to study. Taking into account these notable differences in the approaches, a division in quasi-static and dynamic modelling has been established, looking for organizing the information and trying to avoid any misunderstanding in the simplifications employed in every approach and, more importantly, its applicability.

2.2.2.1 Quasi-static models

Normally, quasi-static approaches to solve the contact between teeth employ the finite-element (FE) method. This approach allows the study of the small changes due to local phenomena and the load distribution along the teeth. However, a previous analysis is necessary to establish the refining of the meshes and the nodes of interest, dependent on the contact point.

In this line, Argyris et al. (Argyris et al., 2002) proposed to model only a portion of the geometry of the gear and the pinion. Besides, the contour of the gear model is embedded and the profiles of every teeth are considered non-deformable. This approach was at the beginning particularized for spiral conical gears and later on, extended to helical cylindrical gears in (F.L. Litvin et al., 2003) and worm gears in (F.L. Litvin, Gonzalez-Perez, Yukishima, Fuentes, & Hayasaka, 2007).

Another point of view taken by other authors consists of focusing on the construction of these models, emphasizing the need for denser meshes along the contact areas and their surroundings. In this area, Sirichai in (Sirichai, 1999) employs a commercial solution for proposing a 2D model. This is later extended by Wang (Jainde Wang, n.d.) reaching 2D and 3D approaches. These models are based on the Simplex method to solve the contact problem and include denser meshes in the areas close to the contact points. Similarly, Li in

(Li, 2007) presents a new model, but this time this model is entirely developed by the author, avoiding the use of commercial solutions. This model also covers up to 3D approaches and employs a similar strategy to solve the contact problem as the one taken by both Sirichai and Wang previously.

At the same time, Brauer presents a series of works about the procedure to follow in the construction of a FE model in conical gears (J. Brauer, 2002; Jesper Brauer, 2004). These models, similarly to the ones presented above, include a more refined mesh in the contact areas, avoiding contacts in just one element. Besides, these models, presented in Figure 3, are extended for their use in applications where both flanks of the teeth are active. Finally, the same author in (J. Brauer, 2005) extends this approach to 3D problems.

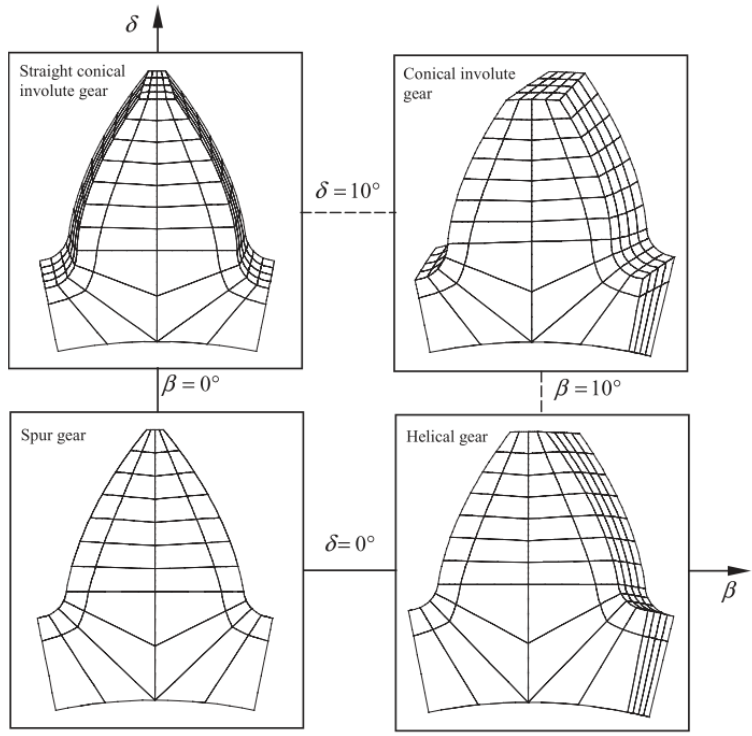

Figure 3. FE models influenced by the helix and cone angles (Jesper Brauer, 2004)

Despite the existence of these solutions, they are not useful for some applications. These require for an immense number of calculations to solve the systems of non-linear equations that describe the models, which translates in long computational times for each iteration. This makes these solutions unaffordable for some approaches. That is the reason why for dynamic models the approach has to be based on other ideas.

2.2.2.2 Dynamic models

The additional complexity of the integration of the dynamic equations makes necessary a simplification in the contact models. It is not possible to face the dynamic problem together with the solution of the systems of non-linear equations in the FE models.

The search for simplifications in the approach to solve the contact problem has led to the development of multibody and lumped-parameter approaches, where the number of degrees of freedom is limited. These approaches focus the contact solving on the overlap between flanks and the calculation of the meshing stiffness. For this meshing stiffness, the deflections in the teeth are calculated under a known applied load. Then, this deflection relates with the meshing stiffness and the contact forces are proportional to that meshing stiffness. However, in dynamic approaches the meshing stiffnesses are calculated beforehand and normally are invariable in time due to the difficulty of repeating its calculation for every contact position, as commented before.

Following this approach in (A. Kahraman, 1993) Kahraman presents the simplest possible solution, where the meshing stiffness is considered constant and its value corresponds to the average value of the meshing stiffness in the meshing cycle. This simplification is useful in dynamic models where the objective is the analysis of the vibrational behaviour in the transmission. However, in search for a more realistic behaviour, some authors like Kasuba (Kasuba & Evans, 1981) or Theodossiades (Theodossiades & Natsiavas, 2001) model the meshing stiffness as the summation of successive harmonics in order

to recreate the sinusoidal meshing stiffness in helical gears. Likewise, the approach to a squared meshing stiffness for spur gears has been employed by Lin & Parker in (J. Lin & Parker, 2002) among others.

Nonetheless, for studies more focused in other aspects of the dynamic behaviour of a gear transmission rather than the vibrational behaviour, the approaches mentioned before are not accurate enough. Consequently, other approaches were proposed along the years. Starting by Weber & Banaschek's proposal in (Weber, C. Banaschek, 1951) where the deformation energy is used to calculate the deformation in any point of the tooth, considering the effects of bending and shear forces. This was a first step, which was taken further by Attia in (Attia, 1959). This work joins the effect of the body of the gear and the adjacent teeth to the above mentioned.

Later in time, Umezawa et al. (Umezawa, Sato, & Ishikawa, 1984) focused in a special aspect in the gears modelling, which refers to the transition in the number of pairs of teeth in contact. These models divide the axial sections of the helical gear in fillets. In any of these fillets, the effects of the bending, shear, and axial stresses are considered. Then, the calculation of the deformations corresponds to the addition of those effects plus the deformations in the body of the gear and the ones due to the contact. On the other hand, Sainsot et al. in (Sainsot, Velex, & Duverger, 2004) present a new analytical approach to include the effect of the gear body in the deformation calculation problem. This approach shows results similar to the ones obtained by using an analogous FE model.

These previous works prove the difficulty in finding the ideal analytical procedure to establish the relation between the deformation and the contact forces between gears. Thus, this led to determining as the most appropriate solution the use of a previous FE analysis. The majority of this approaches are based on the modelling of the contact between a pair of teeth, of which (Chung & Shaw, 2007; Howard, Jia, & Wang, 2001) are proposals applied to spur gears and worm gears respectively.

Once this solution started to be a standard, the next challenge appeared in the ponderation of two different effects. The deformations due to the contact in the teeth and the influence of other components present in the transmission. The hardest part in the contact solving side is related to the local deformations in the contact area. Meanwhile, a highly accurate model has to be able to include the effect of components such as the shafts or the deformations in other components or in the surrounding teeth, which affects the meshing stiffness. All these lead to the situation where a balance has to be found between the accuracy in the local deformations and the computational effort. Considering all those global effects too. In this line, Blankenship & Singh in (Wesley Blankenship & Singh, 1995a) presents the first model where it is possible to apply torque in the transversal direction to the transmission's plane. Furthermore, the model includes a time-dependent meshing stiffness that also varies with the position along the meshing line, which makes it also dependent on the number of pairs of teeth in contact. Likewise, Velex & Maatar in (P. Velex & Maatar, 1996) develop a 6 degree of freedom (dof) model composed by rigid cylinders where the meshing line is discretized. Along this meshing line, the contact points are connected by a series of springs, which represent the meshing stiffness, variable along the contact. In each of the sections along the meshing line, differences in the contact due to variations in the teeth profiles can be included. Once the displacements are obtained, the contact forces will be the result of the product of those displacements and the meshing stiffness for each specific section of the meshing line. The trickiest part of this model, as in previous approaches, rests on the determination of the stiffness value for each section. In this case, the authors highlight that the values employed refer only to the stiffness of the tooth in contact and none other effect. Finally, this model is valid for both spur and helical cylindrical gears. In this same approach, Erltenel & Parker and Ajmi & Velex presented in (Ajmi & Velex, 2005; Erltenel & Parker, 2005) respectively, both proposals based on the previous (P. Velex & Maatar, 1996). The former based on an approach where the effects are splitted between the influence of the bending

and shear stresses in the gear, and the contact effects, whereas the latter establishes a division of the considered effects in three groups. This consists of separating the deformation in the body of the gear, the deformation in the tooth and the deformation due to the contact. A cantilever model emulates the deformations in the gear body, while the deformation in the tooth is based on Pasternak's theory.

This division of the effects in a gear transmission due to the contact between gears led to the development of hybrid solutions, which were proposed firstly by Vijayakar in (Vijayakar, 1991) combining a finite-element model with the Bousinesq solution in a semi-infinite space.

The above mentioned is considered one of the first proposals for a hybrid formulation to the contact problem in gears. Some years after this proposal, these solutions started to spread and become more sophisticated and accurate. Nowadays, these hybrid solutions are common in the modelling of planetary transmissions, which leads us to the next section of this document where the focus is on the modelling of planetary transmissions.

2.3. Planetary transmissions modelling

The research in planetary/epicyclic transmissions has experimented a still ongoing growth in popularity and lately sky-rocketing interest as presented in (Cooley & Parker, 2014) and shown in Figure 4. This development led to the appearance of various valid approaches. These can be classified in lumped-parameter and analytical, finite-element, and hybrid models. As mentioned, all of these approaches are valid, the choice depends on different factors such as the accuracy in the results, the computational effort, the complexity of the formulations, and the problem faced among others. As a result, and seeing the existent kinds of models, from this point on, a detailed compilation of the already present studies in the literature is presented focusing on the modelling in planetary transmissions.

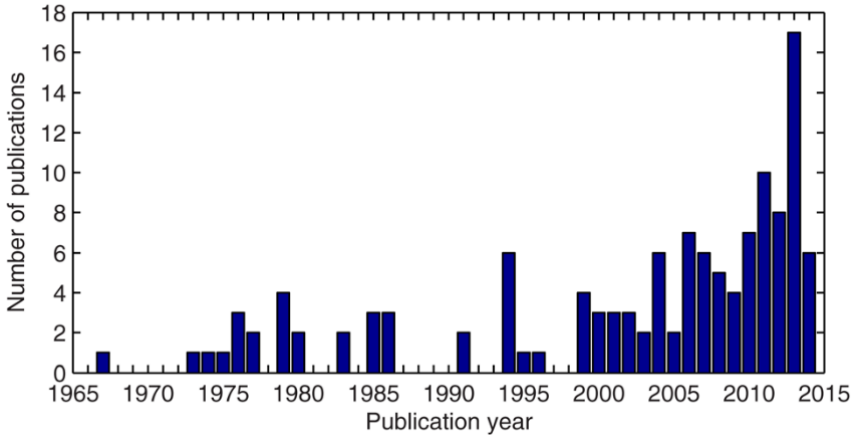

Figure 4. Development of the number of publications (1965-2015) (Cooley & Parker, 2014)

2.3.1 Lumped parameter and analytical modelling

Classical models for the virtual recreation of planetary transmissions normally are based on an analytical approach or a lumped-parameter modelling. Thus, whenever gear transmissions and especially planetary transmissions became more important, this kind of models started to appear. The popularity of these models in the past comes from the existent hardware limitations at that time. At the beginning, the models could just be as complex as proposing a rotational model with meshing elements with a linear constant stiffness or a stiffness variable in time. Thus, allowing non-linearities in the model and obtaining its time response (Cunliffe, Smith, & Welbourn, 1974). This was proposed by Cunliffe et al. as a method to identify the natural frequencies and vibrational modes of a planetary transmission. As a result, that still stands; a classification for the vibrational modes was proposed. The categories for the modes are based on the shape of the mode and the elements affected by the vibrations. Finally, this work highlights the importance of the flexibility in the body of the ring gear for the existence of some vibrational modes. This last detail would have a crucial impact in the models developed in the future. In this same line of study, Botman in (Botman, 1976) presented one of the first lumped-parameter models for a single-stage planetary transmission. This model studied the

vibrational modes of the transmission from a dynamic point of view, by solving the eigenvalue problem. In this model, the gear meshing stiffness is modelled as linear springs and it is invariant in time, therefore, not allowing to obtain the time response. For this model, only the vibrations in the plane are studied, considering the rest negligible due to working with spur gears. The tooth load is considered linear and the tooth stiffness constant. In addition, in this model, the gear supports have a finite stiffness, which means they can float along the plane. Besides, some torsional stiffness is considered in all the gears but the planets. Moreover, the relative movement of the carrier is included and so are their effects in the vibrations. Thus, the author determines that along with the carrier movement the lateral modes disappear and only the axisymmetric stay. This leads to the conclusion that measuring vibrations in the radial direction in the ring gear would lead to no dominant peaks due to resonance. Likewise, McFadden in (McFadden & Smith, 1985) proposes a model to study the asymmetry of the sidebands in the vibrational spectra of epicyclic gears. Furthermore, these results are validated with the data obtained in the experiments carried out in a series of transmissions, finding numerous similarities.

Then, August & Kasuba (August & Kasuba, 1986b) presented a lumped-parameter model, partially shown in Figure 5. The model consists of a lumped-parameter approach for solving the dynamic problem in a planetary transmission under different loads, also modifying the floatability in the sun gear, limiting the degrees of freedom in the rest of the elements to purely rotational ones. Thus, after varying the meshing stiffness, they observed how the orbits described by the sun gear vary with the angular speed. These are mainly translational for low speeds, becoming notably circular whenever the speed is incremented. From these orbits, they induced that the stiffness in the sun gear support plays a crucial role in the loads in the sun, except for a narrow window of angular speeds. Hence, they determined that a fixed sun is better than a floating one from the vibrational point of view.

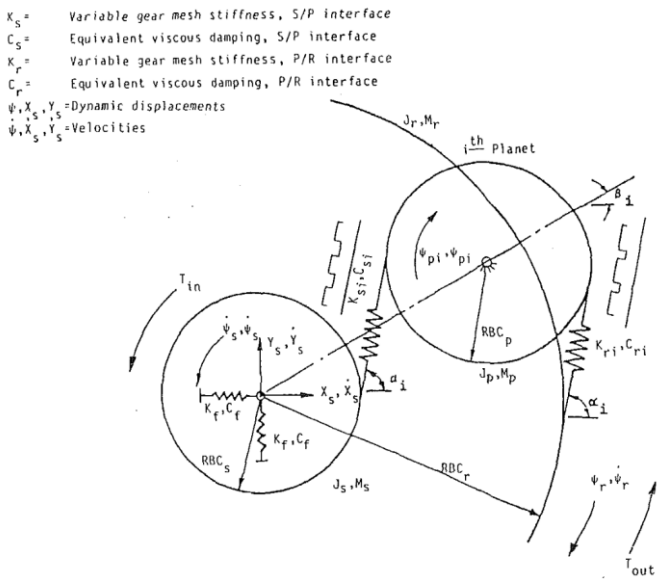

Figure 5. Lumped-parameter approach for the contact between sun and planet, proposed by Kasuba (August & Kasuba, 1986b)

At the same time, the complexity of the dynamic models increased including effects not seen before in models such as non-linear tooth stiffnesses, flexibility in the ring and errors both in the gears and in the alignment of the shafts. Ma & Botman presented this model in (Ma & Botman, 1985) aimed to study the load sharing in transmissions for turboprop engines.

In the early 90s, these gear modelling technique reaches a breakthrough moment with the publication of a series of papers by Kahraman (A. Kahraman, 1994; A Kahraman, 1994a, 1994b; Ahmet Kahraman, 1994) that have had a big impact in this topic throughout the last decades. In (A Kahraman, 1994a) the author presents a spatial lumped-parameter dynamic model of a three-planet planetary gear set with helical gears. Thus, in this model the dof related to the transverse, torsional, axial, and rotational movements are included. This work presents a new technique for analysing the multi-meshing between the middle gear and the other two that mesh with it, proposing two possible configurations, being the middle gear either the driver

or the driven wheel by any of the others. In (A. Kahraman, 1994) the same author presents the comparison between lumped-parameter planar models, including torsional and transversal dof in one and just torsional in the other, to analyse the vibrational behaviour in the transmission and the modes associated to the lower frequencies. Closed form expressions for natural frequencies in a planetary transmission are derived by using the torsional model and contrasting it with the transversal-torsional model. As a conclusion, the author determines that a proposal limited to the torsional dof is accurate enough to determine the natural frequencies in a transmission, which represents a notably simpler approach than the more complex and accurate transversal-torsional model. A more complex planar model is presented in (Ahmet Kahraman, 1994), where the model corresponds to a two-dimensional n-planet planetary transmission where several errors related to manufacturing and mounting of the transmission could be included. At the same time, the meshing stiffness is variable in time and any possible number of pinions and pinion spacing can be included, as well as tooth separations. Finally, this model provides results of the load sharing for a four-planet transmission. From those, guidelines are extracted to improve its performance under the influence of the factors mentioned above. The last contribution of this series (A Kahraman, 1994b) extends the previously mentioned model to a three-dimensional dynamic model, as seen in Figure 6 & Figure 7, but considering some limitations. Amongst the most important ones, the main components of the transmission are considered infinitely rigid; therefore, the deformations of the gears and carrier are negligible. Likewise, the gear tooth flexibilities are considered linear and modelled as springs. Gear backlash and radial bearing clearances are included, but tooth separation is assumed not to exist. Furthermore, the frictional forces derived from the sliding between surfaces are considered negligible. Finally, the errors in the tooth spacing and misalignment, that were possible previously (Ahmet Kahraman, 1994), are not included in order to limit the model and reduce the number of modelling parameters. Overall, this model with its limitations performs an accurate

dynamic study of the resonances in the transmission and the vibrational modes under different considerations of spacing and phasing.

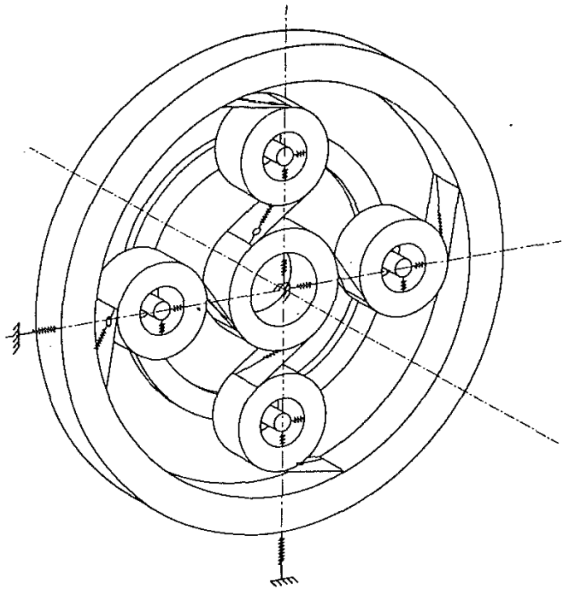

Figure 6. 3D lumped-parameter approach presented by Kahraman in (A Kahraman, 1994b)

Later on, Kahraman (Ahmet Kahraman, 1999) developed a new model with a different approach based on an analytical formulation, including different design parameters to consider various errors. Therefore, this model takes into account the influence of those errors in the transmission geometry and its performance. The model considers not only the backlash in the teeth, but also the floatability in the sun gear, as it is common in planetary gearboxes for automotive industry. This model is oriented to calculate the gear meshing forces and derive the load sharing in the transmission under the influence of different pinhole position errors.

Also in the line of the lumped-parameter models, in (Jian Lin & Parker, 1999) Lin & Parker presented a model for N-planet planetary gear sets that includes three dof in each gear and the carrier, two translational and one rotational, therefore, a planar model. This model is employed to solve the dynamic

problem in planetary gears. In this approach, the meshing stiffness is considered constant. In addition, it includes as a novelty from other similar approaches, matrixes for the gyroscopic and centripetal stiffnesses derived from the carrier movement. This gyroscopic term becomes important for high angular speeds due to its mathematical formulation. In the same year, this model is employed to study the sensitivity of the planetary transmissions vibrational behaviour to the variation of some working parameters in (J Lin & Parker, 1999).

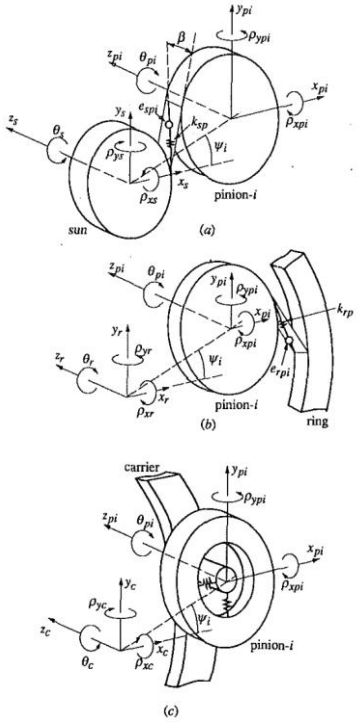

Figure 7. Detail of the dof considered: a) sun-pinion, b) pinion-ring and c) pinion-carrier (A Kahraman, 1994b)

With the beginning of the new century, the popularity of these models dropped dramatically due to the introduction of the new hybrid solutions thanks to the advance in the hardware, which allowed more complexity in the models.

However, these models are still in use for some specific problems where they have proven to be accurate and more efficient than other possible solutions.

Continuing with this line of models, Chaari et al. in (Chaari, Fakhfakh, Hbaieb, Louati, & Haddar, 2006) propose a lumped-parameter model including three dof in every element, two translational and one rotational. This model represents the gear mesh with a linear spring and does not include damping. The input in the model is a torque in either the sun, carrier or ring. This model is employed for solving the dynamic problem and to include some errors and observe its impact in the dynamic behaviour of the transmission.

In this same line, Ligata et al. in (Ligata, Kahraman, & Singh, 2009) present a new approach for a lumped-parameter model to predict the load sharing in planetary transmissions with N planets, in presence of pinhole position errors. This model presents a translational approach as an analogy to previous classical rotational models. This translational approach models the stiffnesses in every contact as a compilation of linear springs, with any number of planets and any possible spacing. Then, the pinhole position errors affect the length of the springs; therefore, considering the load to be applied uniformly on a plane that rests on the springs, the longer ones bear more load than the rest. Finally, the results obtained by this approach, in terms of load sharing, are validated with the results from a FE model and experimental results. This validation shows a notable accuracy in the results considering the simplicity of the approach compared to a FE model.

Continuing with this work, Singh presented the first (Singh, 2005) of two works, where the author works on the influence of pinhole position errors in the load sharing in a planetary transmission. This work employs a system level model to analyse the impact of tangential position errors in transmission with a number of planets from 3 to 6. Also in this topic, the same author in (Singh, 2011) derives a series of analytical expressions to determine the influence of those same errors. This contribution provides a physical explanation to the imbalances produced by the mentioned errors and gives expressions to obtain

the amount of load in each planet parameterized for any error and any load. These are performed both for floating and non-floating systems. However, this approach leads to stating that the influence of radial errors is null, which will be proved to be wrong later on in (M. Iglesias et al., 2017; Sanchez-Espiga, Fernandez-del-Rincon, Iglesias, & Viadero, 2020). Finally, the response of the transmission to the change on different working parameters such as the floatability is observed, and in conclusion, the load sharing improves with higher loads, less tolerance to the errors and less stiffness in the system. These conclusions restate some of the conclusions extracted in previous works, but with a completely different approach. Finally, the results of this new approach are validated by comparison with the results obtained from the models employed in (Singh, 2005), which are more complex.

Likewise, Gu & Velex in (Gu & Velex, 2011, 2012) present a new lumped-parameter model to interpret the influence of planet position errors in the dynamic behaviour of planetary transmissions. This model, in contrast with more conventional approaches mentioned before, includes time-varying meshing stiffness with non-linearities. In addition, this model accounts for the deflections of the components and its immediate influence in the contacts. The results obtained present several similarities with experimental results.

Lately, Hu et al. (Hu, Talbot, & Kahraman, 2018) presented a load distribution model capable of simulating planetary transmissions. This model has a 3D-analytical formulation with different considerations in terms of construction, errors and design variables. This model allows calculating the amount of load in each planet under different conditions such as spacing, phasing, errors etc.

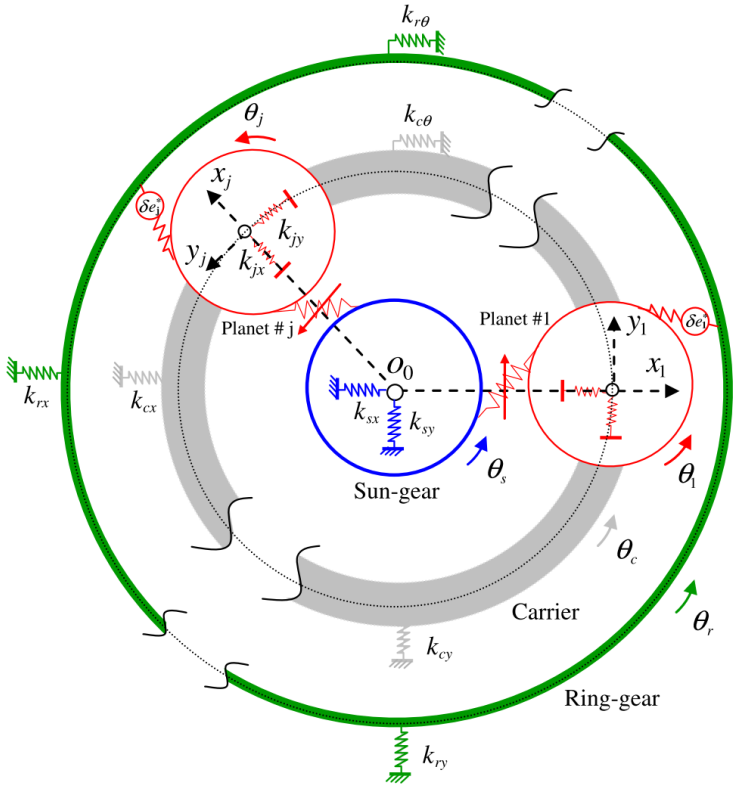

Figure 8. Lumped-parameter model with the definition of the position error in any planet (Gu & Velex, 2012)

2.3.2 FE and hybrid models

In contrast with the lumped-parameter models, FE and hybrid approaches are more recent, even though the beginning of the FE analysis dates back to the 1960s. However, FE analysis requires from either sophisticated hardware or lots of computational time.

Thus, at the beginning of the modelling times in gears, the models were mainly faced from analytical or lumped-parameters approaches. Nonetheless, Hidaka et al. in (Teruaki Hidaka, Terauchi, Nohara, & Oshita, 1977) employ FE models for the calculation of deflections in the ring gear. Firstly, the model consists of a superposition of two, the first for the body of the gear and the

second for the tooth. These models are employed to calculate the strains in the ring gear tooth and compare them with the deflections calculated analytically. Later in this work, the model is extended to the whole ring gear and a higher number of teeth.

Nonetheless, FE models include a high grade of difficulty in their definition. Besides, the search for accuracy in the results requires from refined meshes in the contact area. Apart from that, there exist inherent problems related to the FE modelling such as the stress concentration due to punctual forces. Moreover, meshes should be redefined and refined for every contact position.

These difficulties make necessary the combination of FE approaches and others, in order to develop sophisticated models for the simulation of planetary transmissions. In this line, Vijayakar in (Vijayakar, 1991) at the beginning of the 90s presented a proposal in relation to a hybrid combination of finite-element models and integral surfaces to solve the contact stresses and deformations between three-dimensional surfaces, presenting examples for hypoid surfaces. However, this proposal will not be implemented in a model until some years after.

Following Vijayakar's proposal, Parker et al. in (Robert G. Parker, Agashe, & Vijayakar, 2000) implement a hybrid solution for the modelling of planetary transmissions. This hybrid approach employs the technique suggested by Vijayakar in (Vijayakar, 1991). In this model, given the complexity and the necessary refinement of the meshes, a combination of an analytical solution to the contact and finite-element models is employed. This model studies the dynamic response of a gearbox, under different rotating speeds and torques. This study, firstly, validates the model and then concludes that some vibrational modes appearance depends directly on the mesh phasing.

This previous model presented by Parker et al. (Robert G. Parker et al., 2000) employed a hybrid approach for a dynamic model; on the other hand, Kahraman & Vijayakar (A Kahraman & Vijayakar, 2001) also combined a finite-element and a semi-analytical approach for a quasi-static model. This

proposal models the complicated shapes of the tooth flanks by using FE and a semi-analytical deformation models to avoid problems of bad conditioning in the problem resolution. Furthermore, this approach avoids the need for extremely refined meshes due to the small contact areas, and the remeshing for every contact position. Therefore, two regions are defined, the contact area and its surroundings, where the semi-analytical procedure is employed to solve the contact problem and obtain strains and deflections. The second region corresponds to the rest of the gear, in this part a conventional FE model is accurate and therefore, appropriate. Finally, this model is employed to study the impact of a flexible ring in the transmission performance, considering different width in the ring and some supports along its periphery, avoiding embedding the whole periphery.

In this new trend, Kahraman et al. in (A Kahraman, Kharazi, & Umrani, 2003) presented their contribution for a dynamic model, also pointing out the limitations of a pure finite-element approach. In such a model, the mesh would have to be extremely refined in the contact area given its tiny size, and it would have to be remeshed for every contact position. Therefore, their hybrid approach consists of the combination of finite-element and a surface integral method, described previously by Vijayakar in (Vijayakar, 1991). The FE model solves the contact problem for the area far from the contact, and the surface integral method is employed for the contact area and its surroundings given the lack of accuracy of a conventional FE model in this area.

In this new line of models, which employ hybrid approaches, Abousleiman & Velex (Abousleiman & Velex, 2006) present a new combination for a model, lumped parameter/3D-FE model. This proposal combines the model proposed by Velex & Flamand in (Ph. Velex & Flamand, 1996) for external contact between gears, which was a lumped parameter model, extending this idea for internal gears and including a FE model for the body of the ring gear. In the ring gear, two possibilities are presented, 2D and 3D, as seen in Figure 9. With this approach, it is possible to consider the deflection of the ring gear, which

plays a crucial role, as commented in (Cunliffe et al., 1974; Ahmet Kahraman & Vijayakar, 2001) among others.

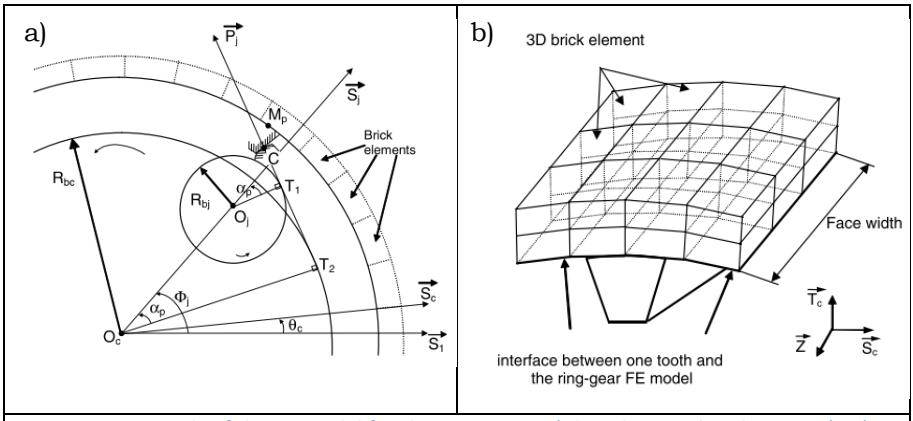

Figure 9. Details of the FE model for the ring gear in (Abousleiman & Velex, 2006)*: a) elements in the model, b) interface between body and teeth in the gear.*

Another combination of approaches, but not considered a hybrid model, is the one proposed by Yuksel & Kahraman (Yuksel & Kahraman, 2004), where a model previously presented in (A Kahraman et al., 2003) that account for flexible planetary transmissions is combined with a wear model presented by Bajpai in (Bajpai, Kahraman, & Anderson, 2004). This way, in the model for the epicyclic transmission the effect of the wear in the gears and the subsequent modifications in its geometry are incorporated to the pre-existent model. Later, this model is employed for the dynamic problem in planetary transmissions observing the highest concentrations of wear in the dedendum of the sun gear.

Later, Ambarisha and Parker in (Ambarisha & Parker, 2007) combine an analytical procedure with a finite-element model to solve the dynamic problem in planetary gears. For the analytical procedure the lumped parameter model corresponds to the one presented in (J. Lin & Parker, 2007) modelling the gear mesh as a nonlinear spring where the meshing stiffness varies periodically due to the number of pairs in contact in each moment. For the friction forces and other similar effects modal damping is employed. Then, for the definition of

the geometry in a 2D finite-element model, the software Calyx is employed. This software implements the hybrid approach proposed by Vijayakar in (Vijayakar, 1991).

In (Singh, Kahraman, & Ligata, 2008) Singh et al. employ a Gear System Analysis Modules (GSAM), "a multi body contact analysis model" that creates 3D multimesh models. These models combine a FE approach with a three-dimensional multibody contact solver (Calyx). This software solves the contact problem beyond the meshing stiffness calculation and then, the stiffness is obtained by combining finite elements and surface integrals. This model is based on the same ideas as previous contributions (A Kahraman & Vijayakar, 2001; Robert G. Parker et al., 2000), but in this case, it is used to make predictions on the strains in the planets and compare them to the experimental results measured by using hoop and root strain gauges.

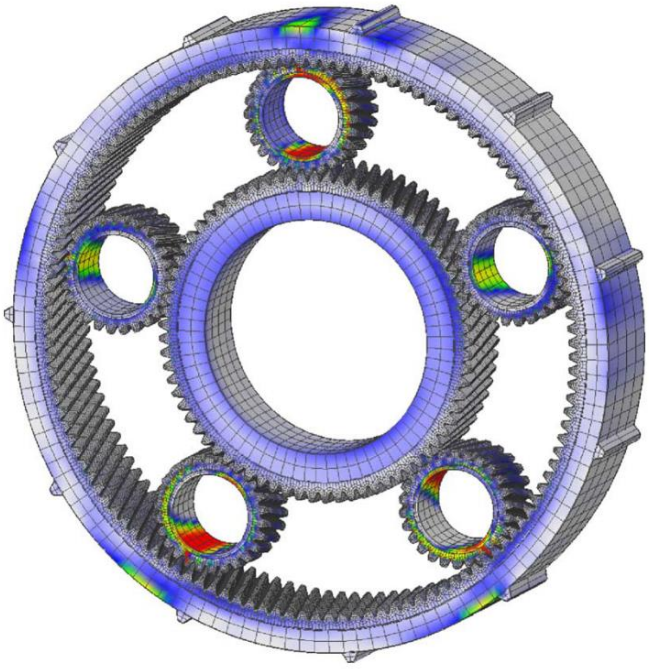

Figure 10. GSAM model of the 5-planet transmission studied in (Singh et al., 2008)

Another proposal was performed by Helsen et al. in (Helsen, Vanhollebeke, Marrant, Vandepitte, & Desmet, 2011) that presents a new approach for modelling in the "booming market of wind turbines" employing three different techniques for modelling of a multi-stage gearbox. This model is oriented to the study of the modal behaviour of the test rig by using three different approaches: a sheer torsional multibody model, a six dof multibody model with discrete flexibility and, finally, a fully flexible multibody model. For the utilization of a model such as the last one, fully flexible, the challenge of condensing dof in a finite element model has to be overcome, and in this work it is done successfully. Also, as a conclusion of this work, new kinds of modes are observed and categorised as planet carrier modes and planetary ring modes. The limitations of the pure torsional model and the eigen frequencies, which are identified in the fully flexible model, are experimentally validated in a back-to-back test rig.

Later, Shweiki et al. in (Shweiki, Mundo, Korta, Oranges, & Palermo, 2016) propose a combination of the ideas presented by Helsen and Kahraman. Firstly, combining finite-element models with multibody models, as seen in (Helsen et al., 2011), and then use a static transmission error as the inlet in the simulations, as Kahraman and other authors do in their models.

In 2020, Liu et al. in (J. Liu, Pang, Ding, & Li, 2020), continuing with works such as the one presented by Helsen (Helsen et al., 2011), presented the combination of a flexible multibody dynamic (FMBD) model and a FE model for the ring gear. The multibody model developed in ADAMS and the FE model in ANSYS. This approach includes bearings in the planets. Besides, the modelling of the ring makes it flexible and therefore reactive to the loads. Apart from this new model, another novelty corresponds to the inclusion of a fault in the races of one of the planets is included. All this is set to analyse the vibrational behaviour in planetary transmissions.

Finally, in this current year, Kahnamouei & Yang in (Kahnamouei & Yang, 2021) present a hybrid approach for a dynamic model. This model consists of

a lumped-parameter approach for the transmission, as well as includes elasticity in the ring gear by employing a FE model to reproduce this gear; these models are shown in Figure 11. In more depth, the FE model includes a number of finite elements with a finite stiffness that represent the elastic supports in the periphery of the ring gear. Then, moving loads are included to model the planet-ring contacts.

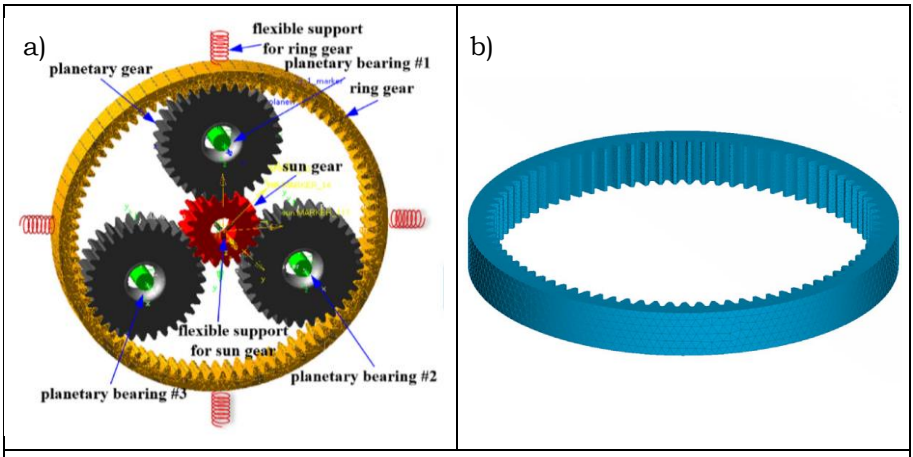

Figure 11. Models employed in (J. Liu et al., 2020)*: a) multibody model, b) FE model of the ring gear.*

All these models are aimed to analyse real problems derived from the use of planetary transmissions, however, those problems vary significantly with depending on its industrial application. Thus, the industrial applications for planetary transmissions are the focus of the next section.

2.4. Industrial applications of planetary transmissions

As mentioned previously, planetary gear transmissions are vastly employed in the industry. This kind of transmission plays a crucial role in some sectors of the industry. Given their notable advantages in comparison to other gear transmissions, planetary transmissions can be found in industries such as automotive, renewable energies, rotorcraft, agricultural machinery and many more.

Planetary transmissions in wind generators include a number from 3 to 5 planets, however, it is expected to be increased. These transmissions are prepared to deal with huge amounts of input torque and are composed by a succession of, either epicyclic or simple gear transmissions (Helsen et al., 2011; Xinghui Qiu, Han, & Chu, 2015; Jungang Wang, Yang, Liu, & Mo, 2019) that convert the rotating speed to the nominal speed of the generator. However, the popularity of the wind energy (GWEC, 2019), with up to 51.3 GW of new installation in 2018, as seen in Figure 12, and the booming spread of this technology leads to the presence of numerous problems related to their presence, performance, and productivity.

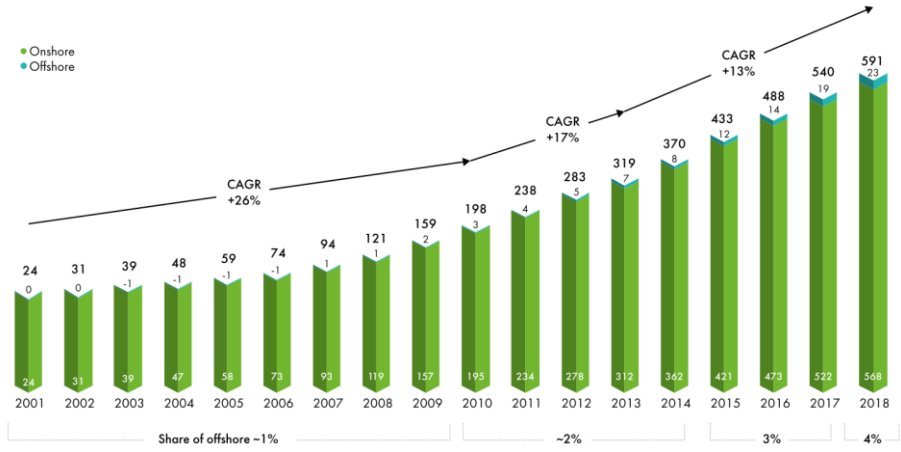

Figure 12. Historic development of total wind energy producing installations in GW (GWEC, 2019).

Firstly, wind generators are a source of controversy due to the noise and vibrations (Gioia, Peeters, Guillaume, & Helsen, 2019; X. Liu, Yang, & Zhang, 2018; Zhu, Xu, Liu, Luo, & Zhai, 2014) that they produce. The dynamic performance of a planetary transmission is not exempt of vibrations and due to it, noise. This problem is even more relevant in the wind generators located close to inhabited areas. Apart from this noise problem, it is another source of debate the location of the generators due to their visual impact and the interaction with living creature habitats. Not only is it because of these

problems, but also it is due to the increment on their productivity (Colmenar-Santos, Perera-Perez, Borge-Diez, & Depalacio-Rodríguez, 2016; Kalogeri et al., 2017; Zountouridou, Kiokes, Chakalis, Georgilakis, & Hatziargyriou, 2015) that wind generators have become an offshore industry also, whose growth is illustrated in Figure 13. This new placement of the generators increases the amount of energy produced by each generator (Global Wind Energy Council, 2020; Karki, 2017), but such increment comes together with a raise in the operation problems. One of such problems was illustrated by Viadero et al. in (Viadero et al., 2014), where the dynamics of the wind generator were modelled considering the effects of the wind, like in onshore facilities, together with the floating platform dynamics and the stiffnesses of the anchoring chains that connect the platform to the rock bottom.

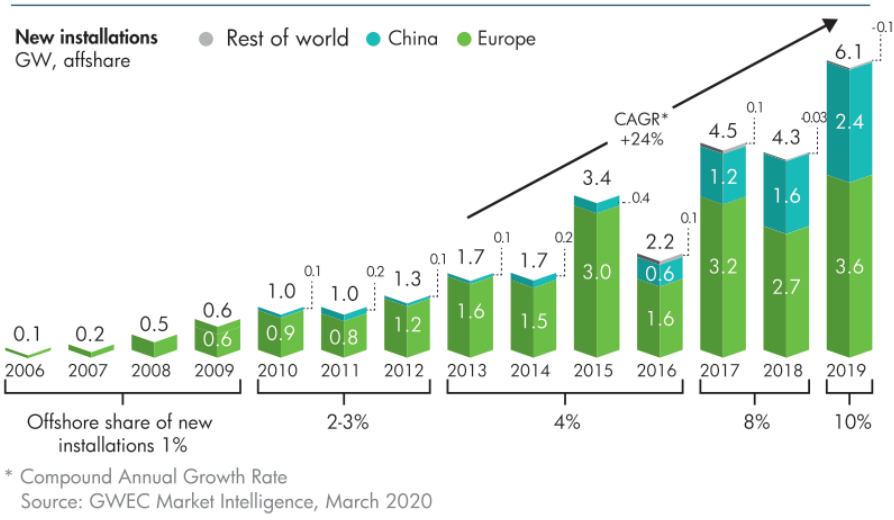

Figure 13. Growth of the offshore installations in GW (GWEC, 2019)

Apart from the floatability and the difficulties that it involves, the productivity of wind generators and the ratio between investment and production depends crucially on the amount of hours the generator is producing, both onshore and offshore. This problem is even more important in offshore wind generators that need from new technologies to access the

founded or floating platforms, in Garcia et al. (García et al., 2019) the authors gather the existent approaches to solve this problem. The need for these systems comes from the impact of the downtime in the economic viability (Faulstich, Hahn, & Tavner, 2011) of the offshore wind industry together with the hard accessibility for its maintenance. Given that, the avoidance of failures in the gearbox and its condition monitoring play a crucial part in its economic viability.

In relation to the avoidance of failures, there are different factors to study in planetary transmissions for wind generators. Firstly, the distribution of the load amongst the planets (X. Qiu, Han, & Chu, 2015; Jungang Wang et al., 2019) will influence dramatically the life expectancy of the components. The overloading of a component could overwork it and lead to the appearance of a crack (Joshi & Darpe, 2019) or the failure of any component (Gallego-Calderon & Natarajan, 2015; Teng et al., 2019) and, therefore, an increment in the noise generated by the gearbox (X. Liu et al., 2018).

Nonetheless, planetary gears are not exclusive to the wind energy industry. They are equally common in an even more popular industry such as automotive. In 2019 alone, more than 80 million cars were sold around the world ("GLOBAL EV OUTLOOK 2020," n.d.). Amongst the different constructive options in internal combustion cars, the ones with an automatic transmission incorporate planetary gears in their powertrain. In this kind of application the analysis and reduction of the vibrational response (A Kahraman, 1994a; Robert G. Parker et al., 2000; Robert G. Parker & Wu, 2010) of the transmission, and the noise they produce, is even more important due to its relation with the comfort in the car and somehow with the market price of the vehicle.

In addition, analogous to what happens in the wind generators, failures in the vehicle transmission are something to avoid, which is the reason why the load sharing in these transmissions is measured experimentally (Boguski, Kahraman, & Nishino, 2012; Ligata, Kahraman, & Singh, 2008) and these

transmissions modelled in presence of errors (Bodas & Kahraman, 2004; Ahmet Kahraman, 1999; Singh, 2005).

Apart from the conventional internal combustion engine cars, the market for electric vehicles (EV) is experimenting an ongoing spread, reaching a maximum of 2.1 million electric cars sold in 2019 ("GLOBAL EV OUTLOOK 2020," n.d.). This is a relatively new application for planetary gear transmission where the problem focuses on the powertrain.

Given the youth of this constructive solution for cars, there is not a standard in its fundamental construction yet (Shimizu, Harada, Bland, Kawakami, & Chan, 1997). At this stage of the development of this technology, one of the faced bottlenecks is the autonomy of these cars. To this point, there are two possible solutions, an improvement in the capacity of the batteries or an improvement in the usage of that energy (C. Zhang, Zhang, Han, & Liu, 2017). To the latter, considering their powertrains, electric vehicles can be classified in distributed and centralized-driven systems (Du, Zhao, Jin, Gao, & Zheng, 2021). The former refers to a configuration where motors are included in each wheel; therefore, there is no need for a powertrain. However, the latter implicates a motor and a reducer. Thus, in (Du et al., 2021) Du et al. analyse the performance of these variety of powertrain solutions in electric vehicles. In addition, the authors model these solutions and analyse its dynamics in search for optimizing each design.

Nonetheless, this area is still experimenting dramatic changes in its technology, consequently, there are new approaches to the transmission system, such as the ones presented by Fang et al. (Fang et al., 2016) and Tian et al. in (Tian, Zhang, Zhou, & Walker, 2020). In both contributions, the authors present proposals for two-speed transmissions to connect the electric motor of the vehicle with its wheels. These configurations improve the comfort in the vehicle in comparison with a distributed approach. This is due to the increment of the unsprung mass of the vehicle in the distributed-driven system (Du et al., 2021). On the contrary, the centralized solutions such as the ones presented before

(Fang et al., 2016; Tian et al., 2020), normally have a low efficiency, however, these approaches opt for a two-speed system and thus increase the efficiency and reduce the energy consumption of the powertrain. In both proposals, an epicyclic transmission provides the opportunity of the two-speed functioning by changing the fix element and input in the transmission. Despite the presented solutions, the efficiency and construction of the powertrains in electric vehicles is still in ongoing development, thus, Peng et al. in (H. Peng, Qin, Hu, & Fu, 2020) present a new tool for the synthesis and analysis of new powertrain solutions in centralized constructions.

Apart from the automotive industry, epicyclic transmissions are also necessary and play a crucial role in the rotorcraft industry. Consequently, these transmissions are the focus of numerous studies, where the number of planets (Singh, 2005, 2011) is incremented and the ring gear thickness is reduced (Ahmet Kahraman & Vijayakar, 2001). Additionally, these models study the influence of the deformations of the ring gear, which is a crucial factor in the rotorcraft transmission given the high working speed (Robert G. Parker & Wu, 2010; Wu & Parker, 2008) . Apart from those studies the dramatic importance of the proper functioning of the rotorcraft transmissions was proved by Fox in (Fox, 2005) where the data prove that a failure in the powertrains is responsible for 15% of the helicopter crashes.

This last point leads us to the importance of the study of the impact that errors have in the performance of a transmission and the possible consequences of their presence.

2.5. Influence of errors in gear transmissions

The complexity of the planetary gearboxes and the imperfection of the manufacturing and mounting processes make the existence of errors inevitable. The impossibility of avoiding the presence of errors in any planetary transmission makes them a popular topic in the field of planetary gear transmissions. However, the importance of them is not in their existence rather

than in the impact that they have in the transmission performance. Therefore, many contributions can be found in the literature related to this topic. This kind of studies offers countless possibilities in terms of points of views and errors to consider. Nonetheless, this section is focused in the works where the target is on the presence of errors, beyond the numerous works presented before, where the possibility of the error existence is considered, but is not developed.

Following this line, there have been numerous different approaches to model and understand the influence of errors in gear transmissions. This coincides with the variety of useful approaches for the modelling of these transmissions. Firstly, Velex and Maatar (P. Velex & Maatar, 1996) presented a dynamic model, previously mentioned, and focused their study in the influence of errors in the shape of the teeth as well as the mounting errors. This model is limited to a pair of gears, avoiding the complication of the epicyclic transmissions. However, in this model, the focus is on the deviations in shape in the teeth profiles and in errors such as pitch and eccentricity errors. To include these errors, the meshing line is discretized and in each of these sections, the meshing stiffness is represented with a spring. Thus, the meshing stiffness consists of a series of springs whose stiffnesses vary depending on the mentioned errors.

At the same time, Kahraman (Ahmet Kahraman, 1999) modelled and experimentally validated the influence of pinhole position errors in the planetary transmissions load sharing. This study is limited to tangential errors, excluding radial pinhole position errors. The radial errors at that time were consider to have a negligible effect. Then, Bodas & Kahraman (Bodas & Kahraman, 2004) widened the scope and considered more kinds of errors for planetary transmissions with 3-6 planets. In this work, the authors observe the impact of pinhole position errors, average tooth thickness errors, and run-out errors. Those errors are implemented in a FE model of a three, four, and five-planet planetary transmission. This work proves the higher sensitivity of a transmission to errors whenever the number of planets is higher. However, in

the pinhole position errors, the radial error is still not considered a case of study. From a completely different point of view, Singh studied the effect of the pinhole position errors in a pair of publications (Singh, 2010, 2011) with a purely analytical approach. Firstly, presented a model where in the the error is included as a parameter in the formulation, the graphical definition of this approach is presented in Figure 14. These works derive the expressions to obtain the load sharing in the transmission and the imbalance generated by the errors, in transmissions from three to seven planets. In (Singh, 2010) the author, due to the employed formulation, reaches the conclusion of the null effect of the radial error. On the other hand, Iglesias et al. firstly in (Miguel Iglesias, Fernández, De-Juan, Sancibrián, & García, 2013), and later in more depth in (M. Iglesias et al., 2017) study from a quasi-static approach the incidence of the pinhole position error in a three-planet planetary transmission. In both works, but more evidently in the latter, it is proved that the incidence of the radial position error is neither null nor negligible, in contrast with what was stated in previous studies (Singh, 2010) or not even considered (Bodas & Kahraman, 2004). More recently, this topic continues to be of interest and in (Hu et al., 2018) Hu et al. present a new approach to model planetary transmissions and study the influence of the pinhole position errors in transmissions with different number of planets, under various load levels and mesh phasing.

However, not everything has been modelling in this topic. Proper experimental results still beat the accuracy of the modelling results. Therefore, experimental works such as the one presented by Singh et al. in (Singh et al., 2008) or the one presented by Ligata et al. (Ligata et al., 2008) are performed. These relate to the works previously presented by Singh. In this case, they present a method to measure the strains in the periphery of the transmission. Strain gauges are placed in the ring, both in the root and in the hoop of the ring. These measurement data are used to observe the load sharing in the transmission with position errors in the planet carriers. Besides, these works test different placements for the gauges and their influence in the measurements. Later on,

Boguski et al. in (Boguski et al., 2012) perform new techniques to monitor the load sharing in epicyclic transmissions. These load sharing is influenced by tangential pinhole position errors of different sizes.

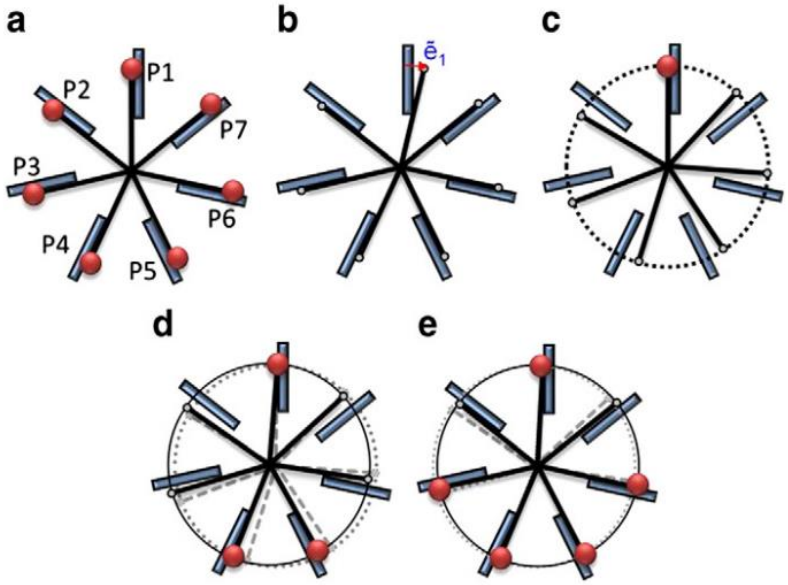

Figure 14. Singh's sketch to analyse the behaviour of a 7-planet transmission with a position error in planet 1 (Singh, 2011)

Despite its importance, the influence of the errors in the load sharing of the transmission is not the only effect of the errors in the performance of the transmission. Errors also affect the vibrational behaviour of the transmission. Thus, Inalpolat & Kahraman (M. Inalpolat & Kahraman, 2009) worked in an analytical model to predict the sidebands in the transmission harmonic spectra. The model consists in a formulation where the modulation of the data acquired by an accelerometer located in the periphery of the ring is considered. To this formulation, a term that accounts for the imbalance in the load sharing due to the manufacturing error in the carrier or gear is included. Consequently, sidebands appear in the theoretical spectra calculated by this analytical approach. Likewise, the authors established a relation between the planet spacing and mesh phasing in the transmission and the sidebands.

The next step taken by these authors is presented in (Murat Inalpolat & Kahraman, 2010), where they employ a dynamic model for a planetary transmission in order to observe the above mentioned sidebands. By means of using a dynamic model, the spectra are predicted under different run-out and eccentricity errors. After this, an experimental validation of the model is performed and presented, proving the appearance of sidebands due to the existence of the mentioned errors.

On the other hand, in (Gu & Velex, 2012) Gu & Velex combine the study of the influence of pinhole position errors with the dynamics of the transmission. However, in this case the focus is not on the vibrational behaviour of the transmission, it is in the impact of the errors in the meshing stiffness instead. This study gets in more depth by changing the rotational speed in the sun gear, proving the influence of the errors under different circumstances. It proves how a higher rotational speed leads to a higher influence of the errors in the maximum values of the load sharing. A similar approach is taken by Saxena et al. (Saxena, Chouksey, & Parey, 2017), however, the authors in this case employ a lumped-parameter approach and include the effect of a crack in a tooth of the sun gear. This work presents a simple gear transmission and the change in the meshing stiffness in consecutive teeth, the first healthy and in the second includes cracks with various sizes. Furthermore, the natural frequencies are determined in every case and a reduction on the value of these frequencies is noted in some of the modes.

As seen in (Hu et al., 2018; Sanchez-Espiga, Fernandez-del-Rincon, Iglesias, & Viadero, 2019; Sanchez-Espiga et al., 2020) a crucial point to understand the impact of the errors relies on its interaction with the mesh phasing, otherwise the results could lead to conclusions that minimize the impact of the errors, specially the pinhole position errors. Thus, in the next section the focus is placed on the relevance of the mesh phasing in planetary gears.

2.6. Impact of mesh phasing in planetary transmissions

The influence of the mesh phasing in the behaviour of planetary transmissions is still subject of study given the fact that there are numerous aspects to analyse. Throughout the last decades, some authors have set their focus on this topic. Thus, mesh phasing has been a technique employed, and proved effective, in order to improve some aspects of the transmission performance.

Despite the fact that it is currently a popular topic in gears and in ongoing study, the mesh phasing in gears was in the spotlight many years ago in works such as the one presented by Hidaka et al. (Teruaki Hidaka, Terauchi, & Nagamura, 1979a). This work presents a comparison of the influence of errors in the dynamic behaviour of a planetary transmission under two different mesh phasings. Thus, it was determined that the imbalance generated by such errors is smaller in the transmissions where the phasing is the same in each planet than whenever they are different. This was one of the first steps to prove the importance of the mesh phasing in gear transmissions. From this point on, mesh phasing was included as a design factor in virtual models such as the ones presented in (Abousleiman & Velex, 2006; August & Kasuba, 1986a; Gu & Velex, 2012; Kahnamouei & Yang, 2021; A Kahraman, 1994b; R G Parker, Agashe, & Vijayakar, 2000; Shweiki et al., 2016) to name a few.

The implications of the mesh phasing are numerous. In simple transmissions, Gill-Jeong in (Gill-Jeong, 2010) proposes the division of the tooth width in two sections shown in Figure 15, thus, providing a second string of teeth with a half-pitch phasing. This aims to reduce the variation of the meshing stiffness, therefore, uniform the load in the teeth. Because of applying this technique, the peak-to-peak value of the meshing stiffness is reduced in half, but the number of variations per meshing cycle is raised. However, the values within the ones the meshing stiffness fluctuates depend on the contact ratio. On the other hand, the efficacy of the mesh phasing in planetary transmissions was analytically analysed by Parker & Lin in (Robert G. Parker, 2000). Nonetheless, the effect of the double line of teeth in a simple gear or the mesh

phasing in the mounting of a planetary transmission is similar. In this case, Parker & Lin focus in the possibility of supress some vibrational modes by choosing the appropriate mesh phasing amongst planets, and prove that mesh phasing is a cost effectively technique to suppress some of those modes just by rearranging the planets.

These same authors continue to study the mesh phasing in (R. G. Parker & Lin, 2004), but this time they observe its impact in the meshing stiffness. This work presents similarities with (Gill-Jeong, 2010) but for planetary transmissions, knowing that (R. G. Parker & Lin, 2004) is a prior work. In this work, Parker & Lin analyse every possible combination in terms of inlet and outlet in the transmission, also determine analytical expressions for the mesh phasing, whose variability appears in Figure 16.

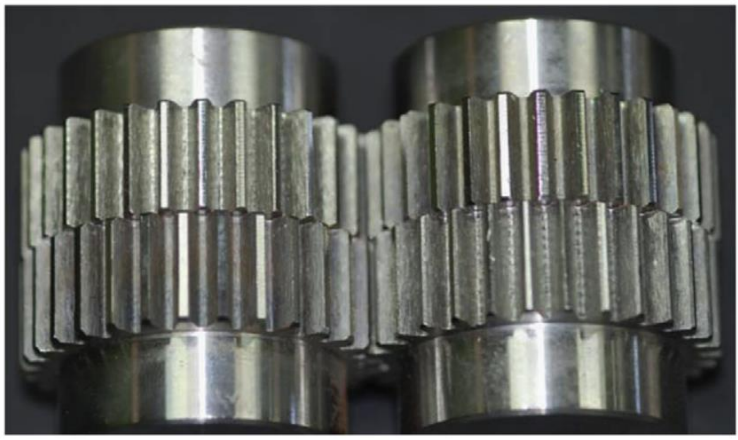

Figure 15. Double phasing gears shown in (Gill-Jeong, 2010)

From an experimental point of view, Boguski et al. in (Boguski et al., 2012) combine the previously mentioned errors in the pinhole position and the effect of the mesh phasing to observe the influence they both have on the load sharing in a 4-planet planetary transmission. This work compares in-phase, sequentially phased, and counter-phased transmissions. This work reaches the conclusion that the imbalances in the load sharing are just a function of the effective errors, while the mesh phasing has a negligible effect. However, in a

recent publication the author of this document et al. (Sanchez-Espiga et al., 2020) prove the relevance of the mesh phasing in the impact errors have in the load sharing in a planetary transmission. This work reaches different number of planets, various load levels, and in phase and sequential phasing amongst the planets.

But mesh phasing affects also the dynamic behaviour of the transmission, such is the effect that Inalpolat & Kahraman (M. Inalpolat & Kahraman, 2009; Murat Inalpolat & Kahraman, 2010) studied the effect of planet spacing and mesh phasing in the harmonic spectra of various planetary transmissions. A technique is derived to obtain these spectra from an analytical approach. Then, this approach is validated experimentally, reaching conclusions that show the use of sequential mesh phasing as a beneficial technique for vibration improvement. Besides, it is possible to relate the spacing and mesh phasing with the sidebands that appear in the harmonic spectrum of a transmission.

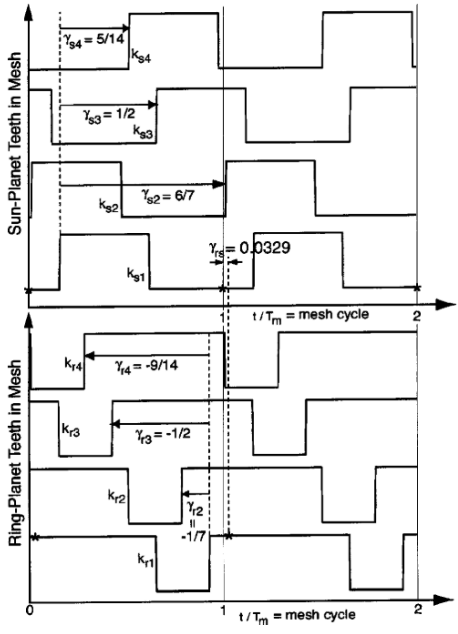

Figure 16. Variation of the meshing stiffness in the contacts of a 3-planet planetary transmission analysed in (R. G. Parker & Lin, 2004)

Lately, phasing has been used to locate faults in any wheel in a planetary transmission by using accelerometers. Peng et al. (D. Peng, Smith, Randall, & Peng, 2019) identify and develop a method to use mesh phasing as a key factor to identify faults in any planet gear inside a planetary transmission. This technique employs the mesh phasing in the vibration monitoring finding a relationship between the position of the fault, which planet presents the fault, and the timing of the fault-related impulse, due to the sequential phasing. Thus, the delay on the impulse related to the relative position of each planet to the accelerometer provides the position of the fault. A phase indicator is developed to be able, with the help of a tachometer, to identify the positioning of the faulty gear.

Experimental studies represent a major quantity of the research related to gears. Although virtual tools become more popular by years, they are not capable to equalize the realism obtained in experimental studies. Thus, new techniques for measuring and monitoring are developed and presented, as well as, are new applications to implement these solutions. In the next section, all these aspects are considered.

2.7. Experimental studies

Despite the popularity of modelling in gear transmissions, the realism of the results is obviously higher in the experimental results. An appropriate experimental work has the capacity for showing the influence of all the effects involved in the performance of the gear transmission. Given this, experimental studies have been and are still performed to characterize the behaviour of gear transmissions, and more precisely, planetary transmissions.

At the beginning of the research in planetary gear transmissions the models were quite limited due to the employed approaches and the limitations in the hardware. Thus, in the studies performed by Hidaka et al. experimental and analytical approaches were combined. These studies focused in the effect of different circumstances in the behaviour of the planetary transmissions from a

dynamic point of view. As a result, a number of reports were published at the end of the 1970s such as (Teruaki Hidaka & Terauchi, 1976; Teruaki Hidaka, Terauchi, & Ishioka, 1976; Teruaki Hidaka et al., 1979a; Teruaki Hidaka, Terauchi, & Nagamura, 1979b; Teruaki Hidaka et al., 1977). These focused on various topics such as the load sharing in the transmission, the influence of errors, its dynamic behaviour or the influence of the mesh phasing. This research led to conclusions such as the importance of measuring the strains in the root of the sun teeth instead of the ring. Thus, for a flexible ring the distortion in the results created by the deformation of the ring invalidates the monitoring in this gear. As a result, the location of the strain gauges in the sun seems to be much more effective in such a situation as described above. Furthermore, Hidaka in (T. Hidaka, 1979) defines the dependency between the modes in the ring and the mesh phasing in the transmission. Not only the modes, but also the load sharing is proved to be drastically influenced by the mesh phasing in the transmission.

However, in (Boguski et al., 2012) Boguski et al. place the strain gauges inside the planet pins in the tangential direction to the planet carrier. This way they measure the load sharing in planetary transmissions under in-phase, sequential and counter-phase mesh phasing. The authors reach the conclusion that the variation of the mesh phasing plays a negligible role in the load sharing of planetary transmissions with presence of tangential pinhole position errors.

Also in relation with the conclusion extracted by Hidaka in (T. Hidaka, 1979), in (Ligata et al., 2008; Singh et al., 2008) the authors place strain gauges in the body and the root of the teeth in the ring gear. With this procedure, they are able to measure the deflection in the ring and calculate the load sharing. Therefore, they proceed oppositely to what was stated in Hidaka's research.

On the contrary, following Hidaka's recommendation Dai et al. in (Dai, Cooley, & Parker, 2016) place the strain gauges in the trochoid of the sun gear tooth. The study focuses on the strains due to the contact and the contact forces calculations. The experimental results are compared to the ones

obtained with a FE model. In this case, the experimental data is employed to validate the results obtained from the model. A similar experimental technique is employed by Aurrekoetxea & Ruiz de Ocenda in (Aurrekoetxea et al., n.d.), in this case, the strain gauges are located along the flank root of the tooth in the sun gear. The strains measured by this procedure are employed to indirectly calculate the load sharing in planetary transmissions.

Nonetheless, experiments are not exclusive for the load sharing in the transmissions. Meltzer & Ivanov present in (Meltzer & Ivanov, 2003) a series of experimental works in the condition monitoring of planetary transmissions employed in the vehicle industry. In this work, the focus is on the run-up run-down of the gears, therefore, under non-stationary rotational speed, and employing time-frequency techniques for the analysis of the data.

The condition monitoring has proven to be crucial in applications like rotorcrafts, given the data presented by Fox in (Fox, 2005), where around 15% of the rotorcraft accidents are due to failures in the powertrains. This kind of statistics led to perform studies like the ones presented by Antolick et al. (Antolick, Branning, Wade, & Dempsey, 2010) and Delgado et al. in (Delgado, Dempsey, Antolick, & Wade, 2013), where they employ condition monitoring and set condition indicators (CI) to address and detect failures in the nose gearbox of a U.S. Army helicopter.

More recently in the condition-monitoring spectrum, a new technology emerged. This technology denominated Acoustic Emission (AE) improves the sensitivity of the measurements compared to accelerometry. This new technology has been employed to monitor rotating machinery (Caso, Fernandez-del-Rincon, Garcia, Iglesias, & Viadero, 2020; Ferrando-Chacon, 2015; Fischer & Coronado, 2015) by using CI in order to predict failures in gears. However, this technology needs from a complex processing of the data given the immense amount of data gathered for each second of monitoring, in the order of MHz for the acquisition frequency.

2.8. Critical analysis

Hereinafter the analysis of all the presented previously is gathered. The study of the behaviour in gear transmissions and, more precisely, in planetary transmissions is a still rather unknown area. The development of different techniques for modelling or experimenting has helped to understand part of the phenomena that occur in the transmission during its operation. However, the modelling techniques prove to be limited and to idealize the results, which compared to the experimental ones, sometimes, makes difficult to find similarities and validation.

The importance of the transmissions in the industrial environment and on everybody's lives is a proven fact. Apparently, this importance is going to stay or even grow in the following decades, thus, the importance to improve the knowledge of these transmissions is proportional to their impact.

In terms of modelling, the hybrid approaches proved to be the best solution in terms of accuracy-computational effort ratio. On the other hand, if there were no limitations in terms of hardware and computational times, then FE approaches would provide the most accurate results, but at a cost. However, lumped-parameter models are the simple quick solution, good enough for many cases and even the best approach in some cases. These prove the difficulty in choosing the most suitable approach for modelling a gear transmission.

Then, in order to study the influence that the errors have in the behaviour of a planetary transmission, there is still a lot of scope to cover. More importantly, in this document contradictions are presented. This proves the difficulty in the choice of the appropriate approach to perform an analysis and how the results to similar ideas can be opposed just by that. Therefore, not only are there many other effects pending of study, but also there are still to unveil these unknowns. In the 0 of this Ph. D. thesis, the study of the impact that errors have in the functioning of planetary transmissions is extended, covering the necessary study of the interaction of these errors with the different

mesh phasing in any planetary transmission, which is something that lacks study in the previous references.

Finally, in terms of experiments and techniques to implement the same experiment, there exists a wide scope of solutions: accelerometry, extensometry, acoustic emission, acoustic intensity, etc. All of them are aimed to understand better what happens in a real transmission. However, the employment of a concrete technique leads to different results than the others. In the load sharing study, it seems obvious that employing extensometers is the right path to take, however, the appropriate location of the strain gauges is still to determine. On the other hand, in condition monitoring seemed that the appropriate technology was accelerometers, but lately acoustic emission appears to be a way more sensitive technology and potentially provide better results or at least notify any kind of problem earlier due to its higher sensitivity.

In regards to the measurements, this Ph. D. Thesis addresses, from a numerical approach, the accuracy of the measuring of strains in the sun tooth root for calculating the load sharing in the transmission. This measuring technique is employed in planetary gearboxes as presented previously, however, its accuracy has not been analysed, and the results obtained are quite relevant given the need of these measurements to certify gearboxes, at least for wind generators (Aurrekoetxea et al., n.d.; "IEC61400 – 4: Design Requirements for wind turbine gearboxes," n.d.).

All in all, the research in gears has suffered numerous changes throughout years, these have transformed the field and have led to more sophisticated techniques, which give better results and provide the opportunity to improve the knowledge of such complex mechanism.

Part III

Chapter 3: Virtual model

3.1. Introduction

Numerous approaches exist nowadays for the formulation of a virtual model that analyses the behaviour of gear transmissions and, more precisely, epicyclic transmissions. However, out of those various possibilities, in this work a hybrid model is employed (M. Iglesias et al., 2015). The employed formulation allows to reduce computational times and maintain a high degree of accuracy in the results.

The computational time is reduced compared to other approaches given the less refined meshes in the finite-element models. These are not necessary due to the hybrid approach, which combines the FE model with an analytical formulation. Apart from this point, there are numerous steps to follow in the model, as seen in Figure 17, in order to simulate the behaviour of an analogous planetary transmission. These are divided in three stages, the definition of the inputs, the formulations in the model and problem solving, and the results obtaining. In the following, all the details of this approach and the foundations of this effective formulation are explained.

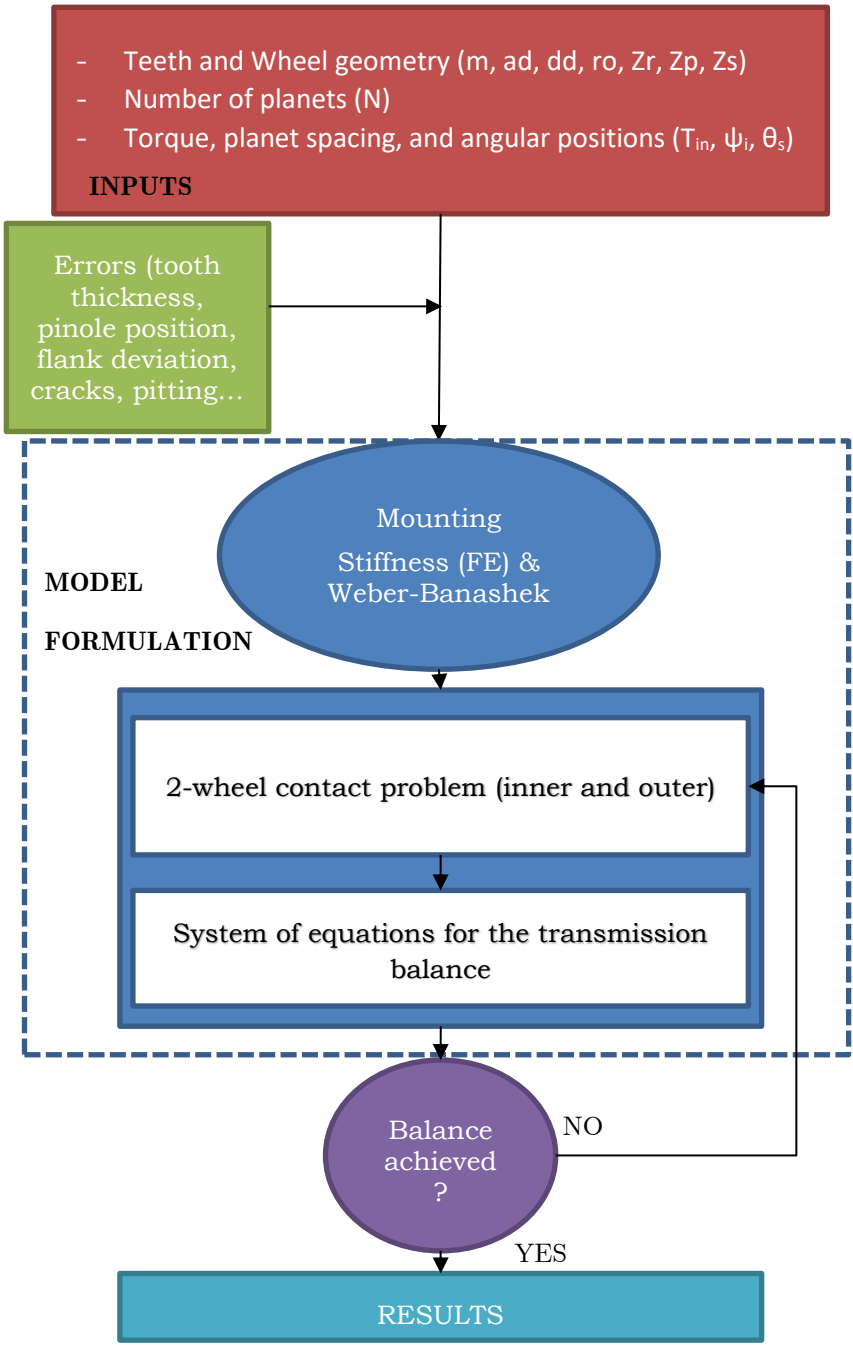

Figure 17. Sketch of the algorithm followed in the employed virtual model.

The model presented in this part of the document, was developed previously by other members of this research team, and their contributions gathered in (Fernández del Rincón, 2010; Fernandez del Rincon, Viadero, Iglesias, García, & Sancibrian, 2013; M. Iglesias et al., 2015; Iglesias Santamaría, 2013). Thus, in this part the aspects of this model that are relevant for this work are compiled and treated. For further explanation, the author refers the reader to the previous references.

3.2. Model inputs

The first step to take in order to set a transmission, both in the physical and virtual world, consist of the definition of an appropriate geometry for its working conditions. This geometry englobes from the tiniest detail, such as the profile shifting or the tip relief, to the number of teeth in each wheel and the mounting distance between wheel's centres. Below, these points are defined together with how they are modelled in the virtual environment. Likewise, the input parameters that define the working conditions are concerned.

3.2.1 Wheel cutting

Firstly, the profiles of the teeth have to be defined. The definition of the profiles, in this model, depends on the gear. In a planetary transmission, the sun and the planets interact as pairs of external gears. For these, the profiles are defined by the vectorial definition proposed by Litvin (Faydor L. Litvin & Fuentes, 2004). This procedure defines analytical expressions for each of the sections along the tooth profile. This procedure mimics the industrial gear cutting process.

In the model, firstly, the geometry of the tool has to be defined. For the external gear, the chosen tool is a rack. This rack is defined by the following parameters: module (m), pressure angle (φ) addendum (ad), dedendum (dd), and tip rounding arc radius (ro). These define the geometry of the tool's flank. By the commented procedure, the teeth in the wheel will be cut. To this end,

it is also important to set the number of teeth for each wheel. This defines the angular length devoted to each teeth and to each section within an individual flank. The analytical expressions that define this cutting process are gathered in (M. Iglesias et al., 2015; Iglesias Santamaría, 2013).

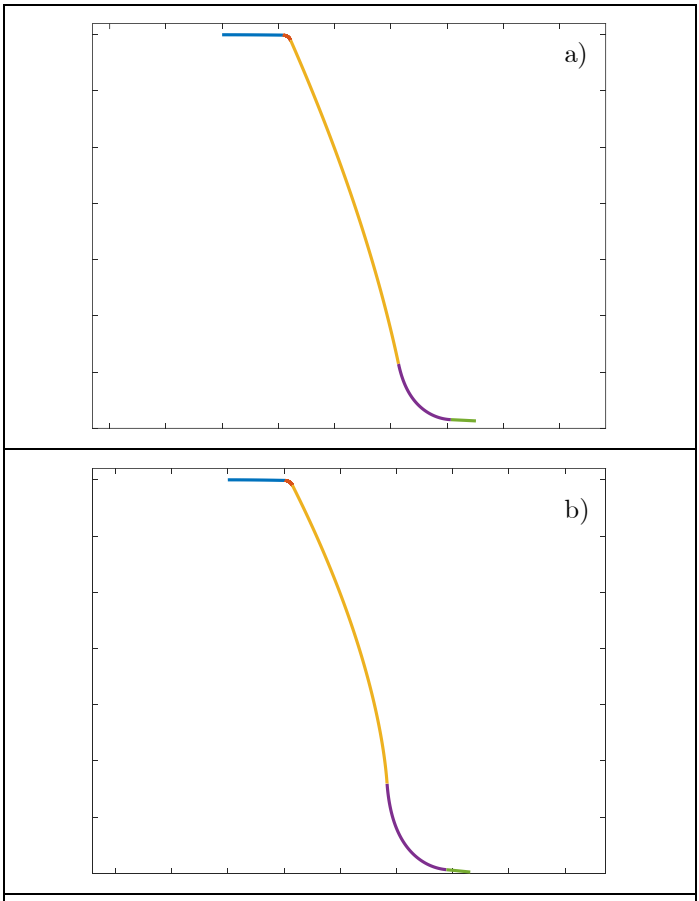

Figure 18. Result of the profile cutting for a) sun gear, b) planet gear

As illustrated in Figure 18, the result of the cutting process, following the commented procedure, leads to a succession of external arc, tip rounding arc (optional), involute, trochoid and internal arc. These sections together compose the geometry of the external gear's flanks. It is important to point

out the fact that the tip-rounding arc is included to avoid contact on the edges of the flank, which would lead to undesired stress concentrations and wear or fault problems.

In contrast to the external gears, the definition of the internal gear (ring gear) is faced by a similar procedure as the previous, but employing a different tool, the pinion cutter. This procedure also responds to the vectorial definition by Litvin (Faydor L. Litvin & Fuentes, 2004) and can be found described in more depth in (M. Iglesias et al., 2015).

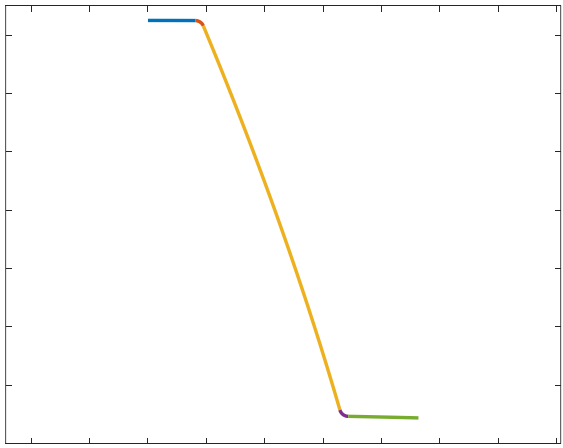

Figure 19. Result of the profile cutting in the ring gear

In the case of the ring gear, the flank concatenates an internal arc, a hypotrochoid, an involute, a tip-rounding arc, and an external arc (Figure 19). Similarly, to the flanks in the external gears, the tip-rounding arc is optional and it was included to avoid the edge effects.

Once the profile of the flanks is defined, this procedure has to be repeated for up to Z_w times, where Z refers to the number of teeth and the subindex w to the wheel, which could be S (sun), P (planet) or R (ring).

3.2.2 Transmission mounting

Once the geometry of the wheels and the teeth profiles are defined, the next step consists in the mounting of the wheels in its location in the transmission. In order to define its mounting, the planet spacing (ψ_i), and mounting distance (d_t) have to be established. This point is of crucial importance in the performance of the transmission given the fact that the mesh phasing is a direct consequence of the planet spacing and the number of teeth in the ring, as explained in more depth in 4.2 in this document. Another relevant detail consists in the definition of the number of planets. The number of planets plays a crucial role in the performance of the transmission and in the influence of various effects, such as errors, non-equal spacing and floatability in the supports.

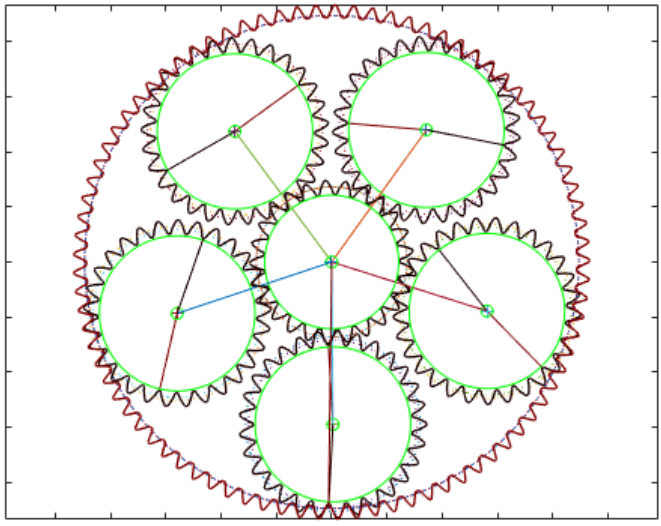

Figure 20. 5-planet planetary transmission mounted.

Nevertheless, it is important not to forget the influence of the mounting distance in the behaviour of the planets and the planet-carrier. A mounting distance that corresponds to its ideal value, calculated following (3), leads to a balance in the radial components of the contact forces in the planets.

Previously to (3), (1) & (2) provide the ideal mounting distance in both contacts, the external and internal.

$$d_{t_{S-P}} = \frac{Z_S \cdot m}{2} + \frac{Z_P \cdot m}{2} \quad (1)$$

$$d_{t_{R-P}} = \frac{Z_R \cdot m}{2} - \frac{Z_P \cdot m}{2} \quad (2)$$

$$d_{t_{ideal}} = \frac{d_{t_{S-P}} + d_{t_{P-R}}}{2} \quad (3)$$

However, modifying the mounting distance is a criteria used by designers to transform the performance of the transmission in their favour. Nonetheless, it is important to take into account the implications of this modification. A change in the mounting distance that affects the effective pressure angle in each of the contacts in each planet will create an imbalance in the contact forces, as seen in Figure 21. Thus, the balance in torque in the planet is reached, however, the different pressure angle leads to a different radial component of the contact forces. Therefore, there will be a net force acting on its support. This force, depending on the mounting distance, will act inwards or outwards with respect to the carrier. Thus, in each meshing cycle the carrier will suffer tractions or compressions due to this imbalance in the contact forces in each planet. Besides, in each planet this imbalance will be the same, so the deflections in the carrier will spread to its entirety. It is important to point out the similarities in some of the effects that the radial pinhole position errors have on the transmission, which will be treated in more depth in section 5.3.2.

Another relevant aspect in the mounting of the transmission refers to the shaft, which is considered by defining its external radius. In this model, the detail in the mounting of the shafts is an approximation given the boundary conditions used later in the FE models. Thus, these shafts are supposed to be cylindrical and the wheel to be embedded in it, along the mounting circle. This will be shown in more detail in section 4.6. The radius of the shaft is important in the definition of the stiffness in the wheels and supports.

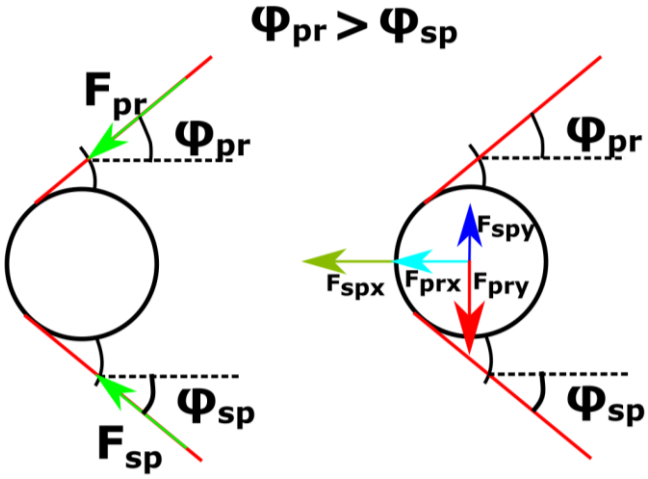

Figure 21. Contact forces and its imbalance due to the mounting distance.

Whenever the inclusion of floatability in the supports is referred, the model employed provides different opportunities for its modelling. The first and simplest consists of a lumped-parameter approach, where the stiffness of the support is defined by a couple of springs in the principal directions in the plane. This approach will be described in more depth in section 4.4.3.

On the contrary, if the focus of the study is on the forces on the supports and their distribution, there exists the possibility of facing the problem by using a ball-bearing model. This component is built by the rolling elements (balls), the cage that keeps them in position, and the inner and outer races (Figure 22).

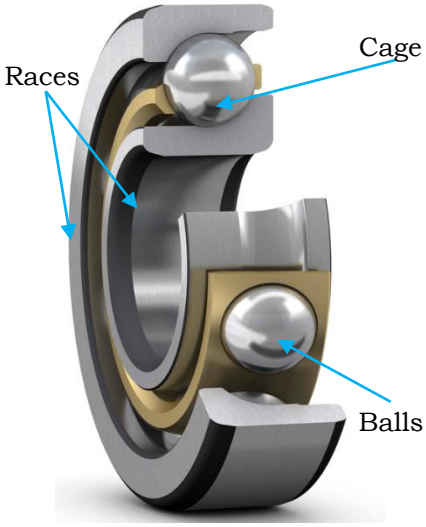

Figure 22. Construction of the ball bearing.*

This model is based on the Hertzian theory for the contact of the balls and the races. The application of this theory leads to obtaining the stiffness of each rolling element. Besides, the number of rolling elements has to be defined. Then, by the calculation of the positions of the balls, and the Hertzian theory the loads on each of them are calculated. By this, the orbit of the gear can be obtained, taking into account the mounting of the bearing. For more details about this point (Iglesias Santamaría, 2013).

3.2.3 Definition of errors

The last step in the definition of the whole geometry of the transmission is the optional inclusion of errors. These errors could respond to various approaches such as mounting, manufacturing and run-out errors. All of them were considered as possibilities in the conception of this model.

In the manufacturing errors every flaw related to the carving of the wheels are included. Thus, the tooth thickness errors, which affect the overlap between wheels, are included in this category (This error is explained in more detail in section 5.2.2). Then, the deviations in the shape of the teeth profile also

*https://www.skf.com/es/products/rolling-bearings/ball-bearings/angular-contact-ball-bearings/single-row-angular-contact-ball-bearings (11/02/2021 19:40)

correspond to this category. The superficial roughness and the deviations of the theoretical shape in the profile influence the contact between active flanks and consequently the performance of the transmission. Likewise, the index error could be included modifying the angular distribution of the teeth and affecting the backlash also. This error is defined as a summation of harmonics, defined by the measurements of the wheels.

The mounting errors considered include the pinhole position errors. This error refers to the existing difference between the ideal positioning of the pinhole and the position of the manufactured pinhole. In this model, these errors are divided in two categories, radial and tangential errors, in relation to the two principal axis in the plane. Also, making a difference between the errors considering its effect in the transmission performance. The virtual definition of this exact error will be explained in more detail in section 5.2.1.

Finally, the run-out errors correspond to the presence of eccentricities in any of the wheels or carrier, thus, modifying the geometry on any consecutive contacts. This problem modifies the distances between the pivoting point and the contact point and has a crucial impact in the search of the balance in the transmission, which will be explained in more detail in section 3.3.3.

3.2.4 Load transmission

In terms of the torque transmission, in every simulation performed for this work the input is set in the sun gear, and the output in the planet carrier. This configuration also conserves the ring gear fixed; therefore, it is the reaction member. Given this configuration, the following kinematics will have to be solved in order to define the movement of the transmission. The kinematics are completely affected by the setup of the configuration, any change in the fixed member and the behaviour of the transmission changes dramatically. Besides, this kinematics relate directly with the load transmission.

The equation (4) shows the transmission ratio in an epicyclic transmission such as the one described above.

$$\dot{\theta_{s/o}} = \dot{\theta_{c/o}} \cdot \left(1 + \frac{Z_R}{Z_S}\right) \quad (4)$$

In the following, the kinematics of the rest of elements is solved, as seen in equations (5) & (6).

$$\dot{\theta}_{P/C} = \dot{\theta}_{S/O} \cdot \frac{Z_S}{Z_P} \quad (5)$$

$$\dot{\theta}_{P/O} = \dot{\theta}_{P/C} + \dot{\theta}_{C/O} \quad (6)$$

These equations also solve the load transmission, given the fact that no losses due to friction or damping will be considered. Besides, throughout the entirety of the simulations the speed will be considered constant, then avoiding dynamic effects. Therefore, the load in the outlet will be transmission ratio times the load in the inlet, as expressed in equation (7).

$$T_o = T_i \cdot \left(1 + \frac{Z_R}{Z_S}\right) \quad (7)$$

Where T_o and T_i refer to the torque in the outlet and the inlet respectively. Thus, the speed in the carrier will be, always, lower than in the sun and its load will be higher.

Once all these preliminary aspects are solved and set, the model can start working and solving the interactions between the elements and the contacts amongst teeth. The approaches taken to solve all these are gathered in the following section.

3.3. Model formulation

The modelling of the analysis of a planetary transmission needs from the solving of various problems. Thus, this section compiles every aspect of the

formulations selected to face the problems found in the simulation of planetary transmissions.

Firstly, in order to solve the simultaneous contacts in the transmission, there are two parallel lines at the same time, the obtaining of the stiffnesses in the problem and the solving of the overlaps among active flanks in the external and internal gears. The junction of both lines provide the contact forces amongst contacting wheels, as seen in Figure 23.

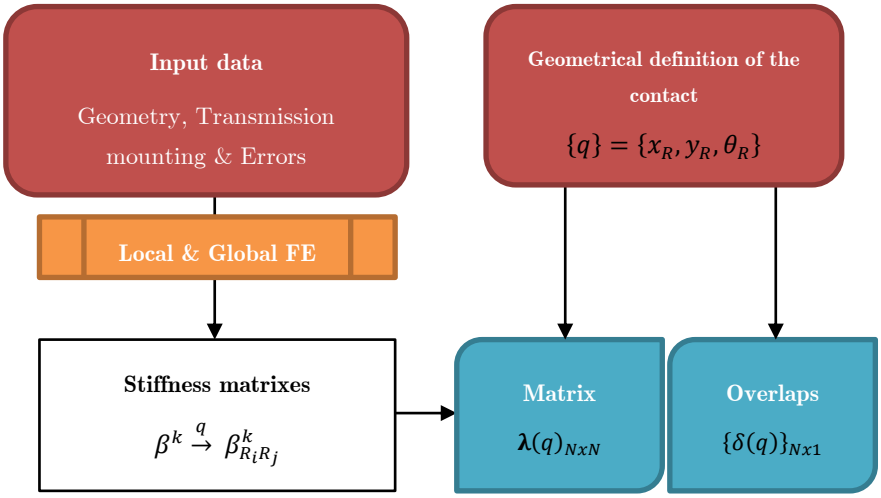

Figure 23. Scheme of the iterative solution to the contact problem.

3.3.1 Contact problem

As seen in Chapter 2:, virtually solving the contact problem in gear transmissions could be faced from various points of view. In this case, after setting the geometrical characteristics of the wheels, cutting each of them and defining its mounting, the next step consist in solving the load transmission in the gearbox. Thus, a succession of steps is employed. At first, the meshing stiffness has to be calculated. To this end, a combination of an analytical and a FE approach is employed. After this, a geometrical approach is employed to locate any contact between wheels and to finish calculating the contact forces.

Firstly, the semi-analytical approach is going to be explained in detail in the following two sections. Later, the geometrical location of the contacts will be explained. Finally, the balance in the transmission will be searched and, thus, the contact problem and the load transmission in the gearbox will be solved.

3.3.1.1 Finite-element models

These models are defined following the proposal in (Jesper Brauer, 2004) by Brauer. A pair of FE models for each gear is employed in order to study the flexibility of the gears in the contact.

The first model consists of a global representation of the body of the gear, the mounting on the shaft, and a Z number of teeth. The model is created in MATLAB environment by using the Partial Differential Equations Toolbox. The geometry mentioned serves to create a mesh of triangular planar elements with nodes in each vertex. Then, in terms of boundary conditions, the nodes along the inner circle, representing the mounting on the shaft, are embedded. The rest of the nodes are free to move in the plane. A global model is defined for each gear. The model for the sun gear is presented in Figure 24.

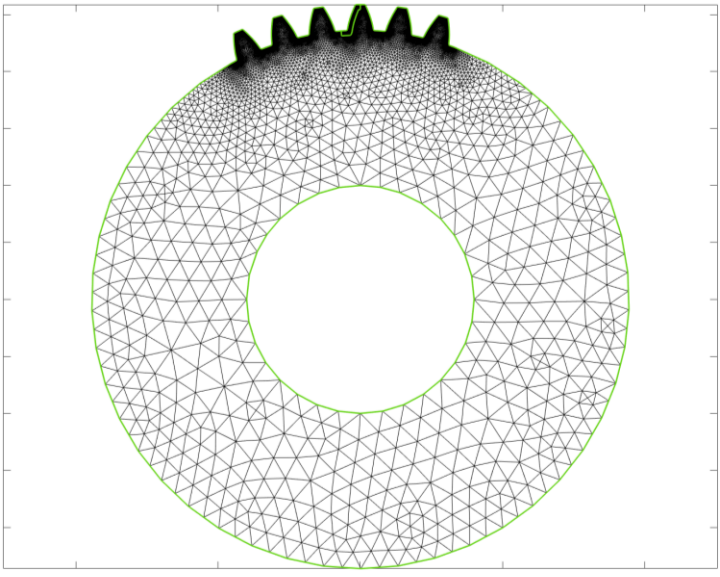

Figure 24. Global FE model of the sun gear in configuration 1.

In this model, a number of load cases are applied in successive points along the active flank in the (Z/2)+1 tooth, where the active flank is the left flank. These loads are unitary and are used to obtain the displacements in the nodes between the initial position of the nodes and their position after applying the load.

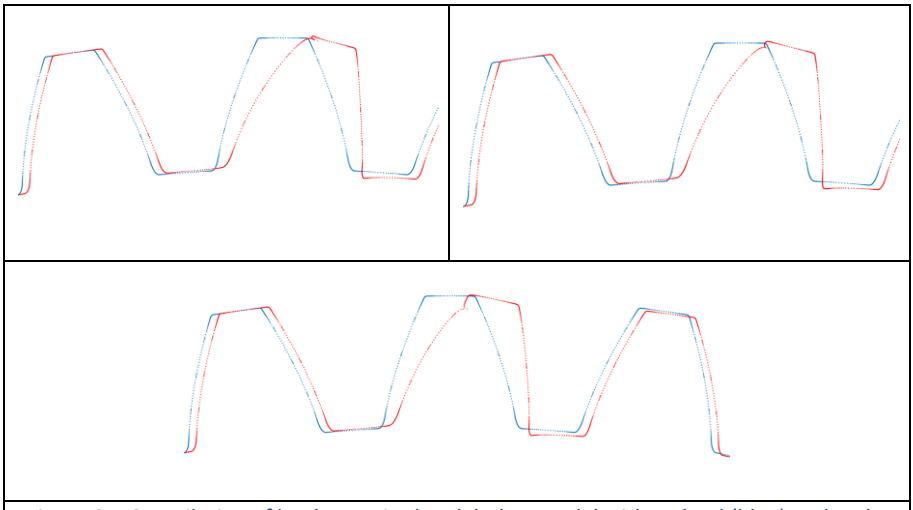

Figure 25. Compilation of load cases in the global FE model with no load (blue) and under load (red)

Then, as it can be seen in Figure 25, the punctual load generates a distortion in the deflections where the load is applied. That is an inherent problem derived from using a FE approach. Thus, a local model is necessary to avoid that distortion.

This model is limited to the geometry of the flank of the middle tooth and an h depth inside the tooth, this geometry is shown in Figure 26. The depth was obtained empirically in (Iglesias Santamaría, 2013). The definition of this model is analogous to the previous, in terms of elements and tools. As far as boundary conditions are concerned, all nodes along the interface between this model and the rest of the tooth are embedded. In this model, a load equal to the one applied in the first model, but with opposite direction is applied in the same position and with the same magnitude. Thus, the distortion in the tooth

flank due to the punctual force is erased by applying the superposition principle to their results.

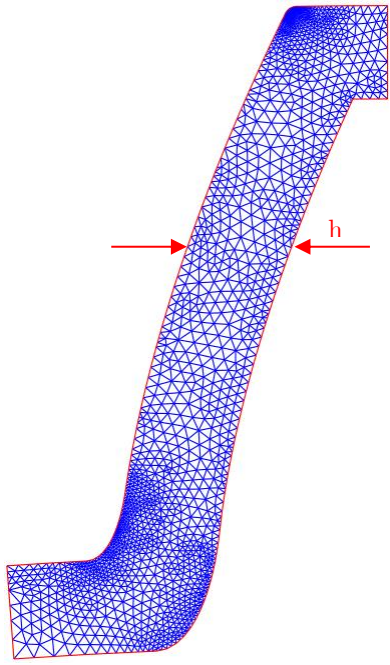

Figure 26. Local FE model for the sun gear.

In Figure 27 a series of results for the deflections of the local model are shown. These results correspond to the same load cases as the ones gathered in Figure 25. The result of the superposition of these, as seen in Figure 28, provides the deflection in the active tooth, the surrounding tooth and the body of the gear. Thus, by knowing the deflections produced by a unitary load applied on the active tooth, the calculation of the meshing stiffness is derived.

Nonetheless, this step represents a crucial part of the contact problem solution, but it is not the only one. The FE models apart from the problem with the punctual force need extremely refined meshes to solve the local contact problem accurately. Thus, in search for reducing the computational cost of each simulation, keeping the level of accuracy, an analytical approach is

combined with the FE models. This approach is presented in detail in the next section.

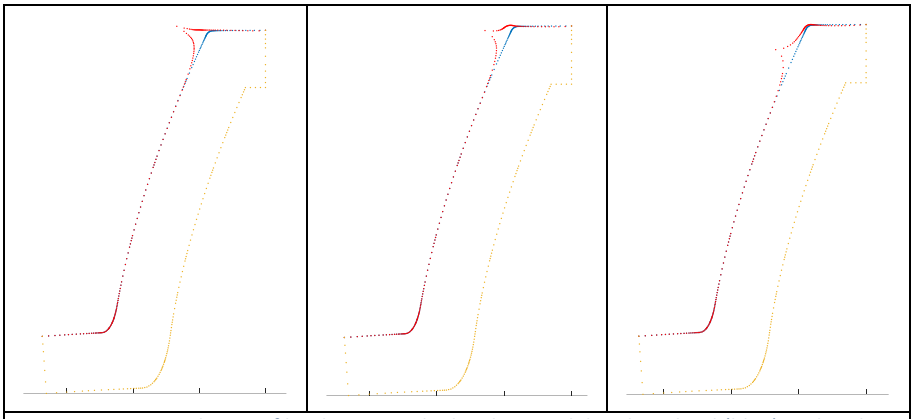

Figure 27. Compilation of load cases in the local FE model with no load (blue) and under load (red)

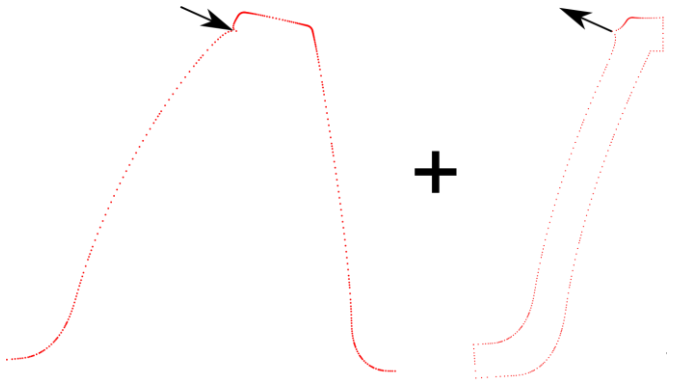

Figure 28. Application of the superposition principle to the contact problem steps

3.3.1.2 Analytical approach

The analytical formulation employed for the solving of the local contact problem is based on the approach presented by Weber & Banaschek in (Weber, C. Banaschek, 1951). This formulation comes to solve the problem of the contact in the local area for external gears. The analytical formulation

employed is presented in equations (8)-(11). The equations (8) & (9) allow calculating the deformations due to contacts in the profile and up to an h depth, both for planar deformation (8) and planar tension (9) scenarios.

$$u_{local}(q) = \frac{2(1-v^2)}{\pi E} q \left[ln\left(\frac{h}{L} + \sqrt{1+\left(\frac{h}{L}\right)^2} \right) - \frac{v}{1-v}\left(\frac{h}{L}\right)^2 \left(\sqrt{1+\left(\frac{L}{h}\right)^2} - 1 \right) \right] \quad (8)$$

$$u_{local}(q) = \frac{2}{\pi E} q \left[ln\left(\frac{h}{L} + \sqrt{1+\left(\frac{h}{L}\right)^2} \right) - v\left(\frac{h}{L}\right)^2 \left(\sqrt{1+\left(\frac{L}{h}\right)^2} - 1 \right) \right] \quad (9)$$

In these expressions, q refers to the intensity of the load (in terms of force by length unit), then the L refers to half the length of the distributed load applied along the profile. In order to calculate this semi-length the equation (10) has to be employed.

$$L = \sqrt{\frac{4}{\pi}\left(\frac{1-v_1^2}{E_1} + \frac{1-v_2^2}{E_2}\right)\frac{\chi_1 \chi_2}{\chi_1 + \chi_2} q} \quad (10)$$

Where E_i, v_i and χ_i refer to the Young's Modulus, Poisson's coefficient and the curvature radius in the body i respectively.

As part of the development of this model, Iglesias derived the formulation for an analogous procedure applicable for the internal contact in gears (M. Iglesias et al., 2015; Iglesias Santamaría, 2013). The calculation of the deflections by using (8) & (9) is accurate for any of the contacts, however, the use of (10) to obtain the length of the flank affected by the contact is only accurate for convex-convex contacts. On the contrary, for contacts between concave and convex flanks the formulation shown in (11) was proposed by Iglesias, and is used in the internal contacts in this model, remembering that the internal contact between the tip rounding arc in the ring gear and the involute in the planet gear does not correspond to a concave-convex contact.

$$L = \sqrt{\frac{4}{\pi}\left(\frac{1-\upsilon_1^2}{E_1}+\frac{1-\upsilon_2^2}{E_2}\right)\frac{\chi_1\chi_2}{abs(\chi_1+\chi_2)}q} \qquad (11)$$

3.3.1.3 Composition of deflections and contact forces

In the previous steps, the relation between the deflections and the loads has been stablished. As a result, the deflections due to a contact can be formulated as the summation of the deflections both local and global in both of the wheels in contact.

The superposition of the results in both FE models brings the deformations both in the body of the gear and in the tooth due to the contact, eliminating the distortion due to the point force in the FE models. Despite representing just one tooth in the Figure 28, the summation of the first two steps considers the whole body of the gear. After this, the analytical approach allows the calculation of the local deflections in the contact area and its surroundings. By adding all these together, the obtained results correspond to the deflection suffered by both the teeth and the body of the gear under a unitary load.

With these data, it is possible to obtain the stiffness for the contacts in the wheels, in any load case along the teeth flank. The next step consist in identifying the contacts and determining the magnitude of the contact forces, which are proportional to the stiffness already obtained. To this end, a geometrical approach is taken in order to calculate the overlaps between flanks.

3.3.2 Overlap calculation

Every one of the previous points will affect in some way the solving of the overlap problem between teeth flanks. Firstly, for this point, this model supposes that the teeth in the wheels are infinitely rigid and can overlap each other. By this, the possible contacts in a Z number of teeth is studied, setting the contact detection as those pairs of teeth where the result of the geometrical

overlap between profiles is positive. Thus, this would mean a contact between them exists, given the fact that the overlap is not possible in reality.

In order to define analytically this problem, it is important to define the sections in the profiles that could get in touch. The expressions employed to solve the overlap problem in each of the possible external contacts are derived in (M. Iglesias et al., 2015; Iglesias Santamaría, 2013).

Once solved this overlap, the magnitude of the overlap combined with the calculated stiffnesses provide the solution for the contact forces. In order to get in more depth in this topic, the author refers the reader to (Fernandez del Rincon et al., 2013; M. Iglesias et al., 2015; Iglesias Santamaría, 2013).

Besides, later in this Thesis the overlap calculation expressions are gathered in section 5.3 in order to analyse the influence of the errors in the overlap calculation problem.

3.3.3 Load balance in the transmission

Once the contact problem is solved, the balance in the numerical problem is searched. By this, a system of linear equations is proposed. This system combines the balance in each of the planets with the balance in the transmission between the inlet and the outlet.

Thus, the balance in the transmission is searched by adding up the entire load transmitted to the outlet, plus, the losses due to the friction and damping. However, in the simulations performed in this work the latter effects are not considered whatsoever. Therefore, there is a balance between the torque in the input and in the output. However, these torques are affected by the transmission ratio, for a lower speed in the carrier, always, there will be a higher torque than in the sun. In this case, this balance has been formulated as seen in (12), observing the balance between the inlet torque and the torque transmitted to the planets by each sun-planet contact. This equation is appropriate given the fact that only the tangential component of the contact force produces torque in the planet, and in the planet carrier.

$$\sum_{i=1}^{N} \vec{F}_{is-p} \times \vec{r}_{is} = \vec{T}_{in} \qquad (12)$$

Each $\vec{F}_{is-p}$ refers to any contact force in the sun due to its contact with any of the planets. Then, $\vec{r}_{is}$ expresses the distance between the centre of the sun and each contact point.

At the same time, the iterative procedure employed to solve the system of equations looks for a balance, in torque, in each of the planets. Thus, the torque in the planet due to its contact with the sun must be equal and in opposite direction to the one due to its contact with the ring. Thus, this balance is searched by employing (13), as many times as the N number of planets.

$$\vec{F}_{ip-s} \times \vec{r}_{ip} = \vec{F}_{ip-r} \times \vec{r}_{ip} \qquad (13)$$

The $\vec{F}_{ip-s}$ refers to any contact force in the planet due to its contact with the sun gear. Likewise, $\vec{F}_{ip-r}$ refers to any contact force between the planet and the ring. Then, $\vec{r}_{ip}$ expresses the distance between the centre of the planet and the contact point.

With these two steps commented above, the basic load balance would be solve after a number of iterations. However, this system considers only the rotational dof. In search for a more complex approach, a number of translational dof can be added to the plan. Thus, in order to include some floatability in the support of any of the wheels a new equation is added. This equation expresses the balance that should exist between the contact forces on the wheel. If this balance does not exist, a force in the support is necessary.

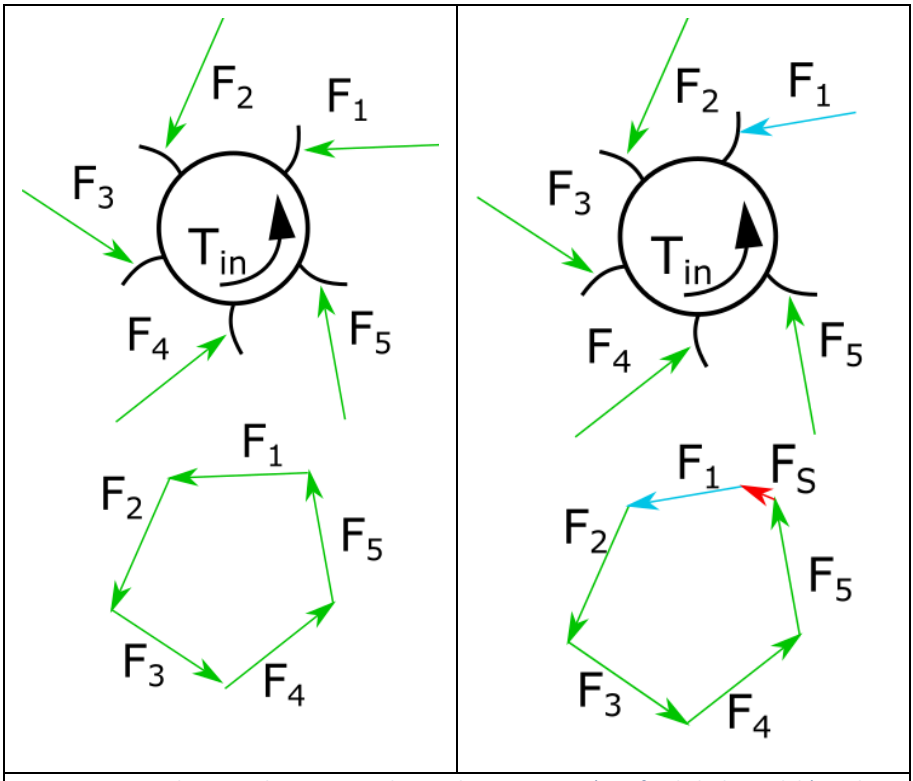

Figure 29. Balance in the sun gear due to the contacts: a) perfectly balanced, b) With support force.

$$\sum_{i=1}^{N} \vec{F}_{ip-s} = K_s \cdot \vec{C}_{cs} \qquad (14)$$

Finally, in the expression (14) the summation of any contact force in the sun with any planet $\vec{F}_{ip-s}$ and its equalize to the stiffness in the support (K_s) multiplied by the local coordinates of the sun centre position.

In terms of the stiffness in the supports, as seen in section 3.2.2, the calculation takes different approaches, however, any of them leads to the determination of the position of the centre of the wheel and a rigidity.

Finally, the solution to the system of equations presented in (12)-(14) leads to finding the balance in each of the angular positions studied. After finding this balance, a number of different results can be obtained. These results are presented in the following section.

3.4. RESULTS OBTAINING

After all the steps detailed above, this model provides the opportunity of determining a wide scope of results that characterize the behaviour of the modelled transmission. These magnitudes can be classified in two groups, the first related to the loads, and the second to the displacements.

In the first group, all the magnitudes related with the contact forces and the loads in the transmission are compiled, such as Load Sharing Ratio (LSR), contact forces, and forces in the supports and the contact force in each tooth.

The LSR refers to the relative magnitude of the contact force in one of the planets compared to the total load in the system. Thus, the LSR analytical expression is gathered in (15).

$$LSR_i = \frac{F_i}{\sum_{j=1}^{N} F_j} \qquad (15)$$

Thus, the F_i refers to the contact force in the planet i and F_j is the contact force in each planet for the summation of all the contact forces. Thus, the LSR_i corresponds to the load sharing ratio in the planet i. This magnitude provides the actual load sharing in a planetary transmission.

As far as contact forces are concerned, they are calculated by following the algorithm to solve the contact problem and the iteration process to solve the balance in the transmission. In order to solve the balance, the resultant forces in each of the wheels are calculated. However, the contact problem algorithm provides the detail of the overlaps for each of the teeth and then the contact forces in each is derived by knowing the meshing stiffness. In conclusion, the contact forces both in every tooth and in every wheel are known.

Apart from the contact force, also the effective pressure angle can be obtained and by using it the components of the forces. Thus, the balance in the planets, as seen in Figure 21, can be analysed.

The magnitudes gathered in the second group refer to the displacements of the elements, as well as the deflections due to the contact loads. Thus, the transmission error (TE), the orbits on the elements, and the deflections in the elements are part of this group.

Whenever the balance is found for each of the angular positions, the locations of the centres of each of the gears are known. Thus, it is possible to draw the orbits of the elements whose support stiffness is not infinite. However, to be able to study better the orbits, the influence of the angular speed and its effect in the vibrational behaviour of the transmission, a dynamic study is more suitable.

Regarding the TE, the definition followed to calculate it refers to its most classical approach, where the TE expresses the difference between the theoretical angular position of the element (Θ_k) and the actual angular position of the element (Θ_a), analytically expressed in (16). Thus, this responds to the difference between the solution of the kinematic problem and the actual position due to the deflections and the contacts.

$$TE = \Theta_k - \Theta_a \qquad (16)$$

Chapter 4: Study of the transmission geometry

4.1. Introduction

Gears are elements of an immense complexity in terms of its geometry. Each teeth flank is composed by 4-5 sections, without considering any correction in the profiles, such as a tip relief. However, in planetary transmissions the geometry is even more complicated due to its configuration. A planetary transmission is composed by three kinds of wheels: sun, planets, and ring. Apart from the wheels, it incorporates a structural element that plays two roles. Firstly, it supports the planets in position surrounding the sun. Secondly, depending on the transmission it can be the inlet or outlet to the transmission. Due to this complexity, it is interesting to study and control the implications of the geometrical characteristics in each transmission. In this section, a study of the influence of macrogeometrical characteristics is performed in order to observe the influence of the planet spacing and mesh phasing in planetary transmissions. Whenever macrogeometrical characteristics are mentioned, it refers to the geometry related to the mounting of the transmission beyond the geometry of the flanks or the wheels.

4.2. TRANSMISSION PRELIMINARY VERIFICATIONS

The design of a planetary transmission depends on a series of factors that have to be taken into account in macrogeometrical terms. All these will be related to the possibility of mounting the transmission. At first, the least mesh angle (LMA) has to be defined.

$$LMA = \frac{2\pi}{Z_r + Z_s} \tag{17}$$

$$\psi_i = k \cdot LMA \tag{18}$$

The LMA (17) is a magnitude necessary to calculate any possible angular positioning of the planets surrounding the sun. Every possible result obtained for the LMA represents every possible relative positioning of a planet, in relation to the sun, by rotating a planetary transmission with just one planet. All these possible solutions are analytically expressed in (18).

Other necessary verification, exclusively for equally spaced planetary transmissions, is the following equation (19).

$$\frac{Z_r + Z_s}{N} = integer \tag{19}$$

This refers to the fact that for every planet to be equally spaced and the transmission to be mounted, there has to exist a proportion between the summation of the sun and ring teeth number with the number of planets. Unless this verification is cleared, the transmission will not be mounted as an equally spaced gearbox.

Finally, the last verification is referred to the space occupied by each wheel. Given the fact that every wheel has the same module, this verification refers to the primitive radius of each wheel. Therefore, equation (20) analyses the existence of the necessary space to mount the transmission, but also there exists the possibility of different combinations depending on the design requirements.

$$Z_r \geq 2 \cdot Z_p + Z_s \qquad (20)$$

4.3. TRANSMISSION CLASSIFICATION

In this section, planetary transmissions are classified taking into consideration two factors, planet spacing and mesh phasing. These factors are a consequence of the wheel geometry amongst other factors. As seen in Table 1, not only the number of teeth in some of the wheels, but also the number of planets affect crucially the transmission.

Table 1. Types of planetary transmission regarding their geometry

Assembly configuration	Mathematical conditions
ESIP	$\psi_i = \frac{2\pi \cdot (i-1)}{N};\ \frac{Z_r \cdot \psi_i}{2\pi} = n$
ESSP	$\psi_i = \frac{2\pi \cdot (i-1)}{N};\ \frac{Z_r \cdot \psi_i}{2\pi} \neq n$
NESIP	$\psi_i \neq \frac{2\pi \cdot (i-1)}{N};\ \frac{Z_r \cdot \psi_i}{2\pi} = n$
NESSP	$\psi_i \neq \frac{2\pi \cdot (i-1)}{N};\ \frac{Z_r \cdot \psi_i}{2\pi} \neq n;\ \sum_{i=1}^{N} (Z_r \cdot \psi_i) = m\pi$
NESAP	$\psi_i \neq \frac{2\pi \cdot (i-1)}{N};\ \frac{Z_r \cdot \psi_i}{2\pi} \neq n;\ \sum_{i=1}^{N} (Z_r \cdot \psi_i) \neq m\pi$

In the contents gathered in Table 1 ESIP stands for Equally Spaced In-Phase configurations, as well as ESSP is for Equally Spaced Sequentially Phased configurations. On the other hand, the configurations NESIP are Non-Equally Spaced In-Phase, NESSP Non-Equally Spaced Sequentially Phased and NESAP Non-Equaly Spaced Arbitrarily Phased.

In this case, the defining factors to classify the transmissions are the ring teeth number and the planet spacing. In the expressions above, n and m refer to integer values. For equally spaced transmissions is mathematically impossible

to have an arbitrarily phased transmission, given the fact that the spacing always sums a multiple of π. Therefore, the result of the third equation, the one that proves the arbitrary phasing, is always equal to mπ.

In addition, by analysing the equations, it is possible to conclude that in sequentially phased transmissions, the sequence does not have to be always uniform. This will influence the performance of the transmission. That is the reason why another equation should be included to determine if the sequence is uniform or not. This is commented and derived in depth in 4.5.2.

The sequence in the mesh phasing influences the meshing stiffness in the contacts. Therefore, the phasing will influence the load sharing in the transmission. Afterwards, this will be analysed in more depth and the above statements proved.

In the following section, the influence of the first consideration, planet spacing, will be studied under different conditions.

4.4. PLANET SPACING

The planet spacing refers to the angular positioning of the planets around the sun. Following the above-mentioned classification, there exist two different possible spacings. In the following, each of these options will be observed in depth. For all the possibilities considered, the transmissions will be considered in phase, in terms of mesh phasing. Different mesh phasings will be included later in this document.

4.4.1 Equally spacing

Equally spacing is also implicitly uniform spacing. This spacing is the result of the division of the angular circumference by the number of planets. In addition, it is necessary to prove that the spacing coincides with multiples of the LMA, this way the mounting of the transmission will be assured.

The equal spacing and the lack of any error lead to a uniform behaviour in any planetary transmission beyond any possible mesh phasing. The mesh phasing, in this case, would only delay the same load cycles in each of the planets.

4.4.2 Non-equal spacing

In this case, the possible combinations are endless, always following the LMA verification (17). This non-equal spacing erases the uniformity in the positioning of the planets around the sun. Furthermore, this influences other factors in the transmission performance. For an ideal transmission, where the elements are infinitely rigid, the change in the spacing will not be notable given the fact that this imbalance created by the spacing will be absorbed by the supports; this fact is illustrated in Figure 30.

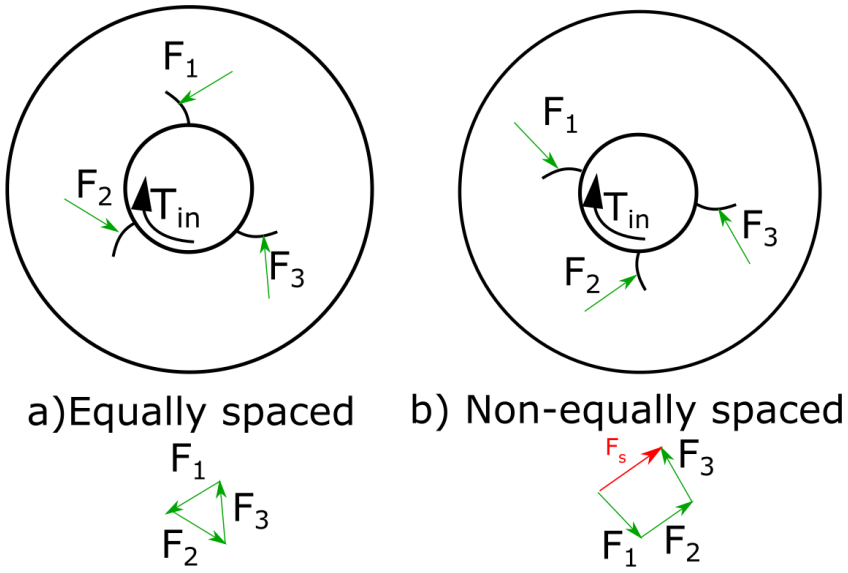

Figure 30. Influence of the spacing in the sun-planet contact forces and the balance in the sun gear

Therefore, in order to observe and, in modelling terms, mimic the behaviour of a planetary transmission with non-equal spacing, it is necessary to decrease

the stiffness in the supports allowing more than just rotating degrees of freedom in the model. These degrees of freedom should include also the translations along the plane of study by the centre of the wheels given the non-infinite stiffness of the supports. In the following, the effect of these floatabilities combined with the planet spacing is analysed.

4.4.3 Floatability

Planetary transmissions can include numerous different solutions for the mounting of its wheels; one of the common solutions includes bearings in the supports of some of their wheels. These could be wheels, cones, balls or barrels bearings. In addition, these wheels can be mounted on shafts using form-fit. All these possibilities, and many other, share the same detail; all of them include some looseness apart from the fact that none of them is infinitely rigid. Given this, there are different ways to model the stiffness in the support. In this case, a lumped-parameter approach has been the chosen option. By this approach, an approximate stiffness is calculated for each of the principal directions and them this rigidity is modelled as a spring that connects the centre of the wheel with the reference to its movement. The latter is important given the fact that for the sun, the reference will be the frame, but for the planet, the reference is the carrier. In the Figure 31, this lumped-parameter approach is illustrated.

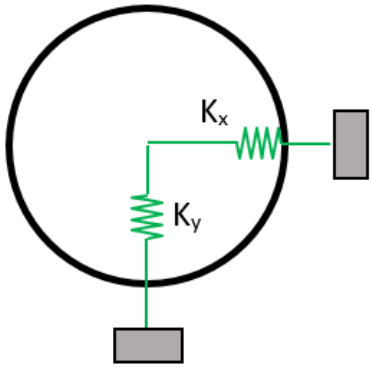

Figure 31. Lumped-parameter approach to the floatability in the sun gear support.

Firstly, the floatability in the sun gear plays a crucial role. In transmissions where the planets are equally spaced and the contacts in phase, there is no force in the support of the sun gear. However, in non-equally spaced transmissions there exist an imbalance in the loads on the sun gear, as seen in Figure 30. This means that a force in the sun support appears. Therefore, this force together with the floatability in the support provides a translation inside the transversal plane and consequently, the sun describes an orbit. Normally, the floatability in the sun gear leads to improve the balance in the load sharing in the transmission and a better behaviour in terms of load for 3-planet transmissions; otherwise, for other number of planets this effect is not assured. On the contrary, the vibratory behaviour of the transmission is worse, given the presence of a higher number of degrees of freedom.

4.5. Mesh phasing

Apart from the planet spacing, the number of teeth in the ring together with the spacing influence the mesh phasing in the transmission. The mesh phasing gathered in Table 1 refers to the timing between the contacts either in every planet with the sun or the contact in each planet with the ring. In more depth, the mesh phasing determines how far along the meshing line each of the contacts in the planets are in comparison to the ones in the other planets. This affects the meshing stiffness in each of the contacts and, therefore, the contact forces. Figure 32 & Figure 33 illustrate the meshing stiffnesses in every contact for different mesh phasing. The differences between them are commented in the following sections.

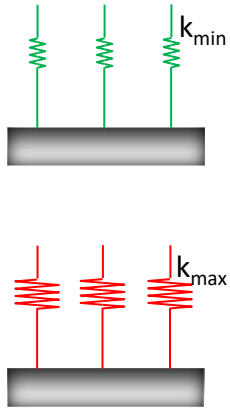

Figure 32. Snapshots of the meshing stiffness in an in-phase transmission

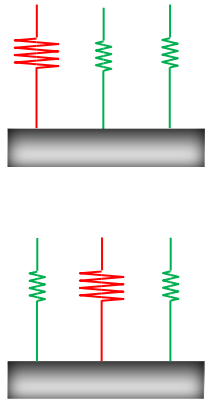

Figure 33. Snapshots of the meshing stiffness in a sequentially phased transmission

4.5.1 In-phase phasing

In-phase mesh phasing refers to the fact that every contact, either sun-planet or planet-ring in every planet, is at the same point of the meshing line at any moment of the transmission performance. To obtain this mesh phasing, taking into account the conditions to sort out the transmissions, the following can be derived for ESIP transmissions.

$$\frac{Z_r \cdot \psi_i}{2\pi} = n \rightarrow \frac{2\pi \cdot (i-1)}{N} \cdot \frac{Z_r}{2\pi} = n \rightarrow \frac{Z_r \cdot (i-1)}{N} = n; \quad i = 1, 2, 3 \ldots N \qquad (21)$$

Therefore, if the ring teeth number is a multiple of the number of planets then the configuration will be in-phase, only for equally spaced transmissions.

This mesh phasing affects the geometry of the contact between teeth flanks. As seen in Figure 32 & Figure 33, the modifications in the geometry of the contacts influences the meshing stiffnesses in every contact and the moment when every contact reaches the maximum stiffness.

Finally, for non-equally spaced transmissions, the previous observation does not stand, given that the spacing is not uniform. Therefore, both conditions will have to be verified.

4.5.2 Sequential phasing

By working with the expressions related to the determination of the phasing in the transmission it is possible to identify a couple of possibilities. These involve sequential phasing where the sequence could be either uniform or non-uniform. In equations (22) & (23) the expressions derived for such a classification are gathered.

$$\frac{Z_r \cdot \psi_i}{2\pi} \neq n \rightarrow \frac{Z_r \cdot \frac{2\pi \cdot (i-1)}{N}}{2\pi} \neq n;\ If\ \psi_i = \frac{2\pi \cdot (i-1)}{N} \rightarrow \frac{\psi_{i+1}}{\psi_i} = integer$$
$$\frac{\psi_{i+1}}{\psi_i} = \frac{n_{i+1}}{n_i}\ \ i = 1, 2, 3\ \ldots\ N \qquad (22)$$

$$\frac{Z_r \cdot \psi_i}{2\pi}; If\ \psi_i \neq \frac{2\pi \cdot (i-1)}{N} \rightarrow \frac{\psi_{i+1}}{\psi_i} \neq integer\ \&\ \frac{\psi_{i+1}}{\psi_i} \neq \frac{n_{i+1}}{n_i}\ \ i = 1, 2, 3\ \ldots\ N \qquad (23)$$

These expressions show a direct relation between the spacing and the uniformity of the sequential spacing. There is no possibility of uniform sequential phasing for transmissions where the planets are not equally spaced. This involves that the meshing stiffness and the load sharing will be affected by this. The lack of uniformity in the phasing affects crucially the behaviour of the transmission, and as far as this thesis is concerned, its load sharing.

4.5.3 Arbitrary phasing

The definition of arbitrary mesh phasing defers to the non-uniform sequential phasing just in mathematical considerations. Thus, the behaviour of both kinds of transmissions will be analogous but the mathematical conditions are different. The difference comes on the last condition gathered in Table 1, which in arbitrarily configuration does not stand.

In behavioural terms, there exists no difference between sequential, with non-uniform sequence, and arbitrarily phased transmissions, at least in their load

sharing. Given that, in the results section the arbitrarily phased configurations have not been considered.

4.6. CONFIGURATIONS OF INTEREST

The configurations presented in this section take into account all the commented above. Firstly, the mounting of the transmissions is checked. Then, the spacing and mesh phasing are calculated and, therefore, the transmissions are classified. These verifications are presented in the following, and further calculations made in this context are included in ANNEX I

Table 2 gathers the characteristics of the proposed transmissions.

Table 2. Detailed number of teeth in the proposed transmissions

Configuration	Number of teeth		
	Z_S	Z_P	Z_R
1º	165	44	75
2º	166	45	74

For both proposed configuration the LMA is the same. Then, by using (17) the LMA is:

$$LMA = \frac{2\pi}{Z_r + Z_s} = \frac{2\pi}{240}$$

Then, this number of teeth are useful for transmissions with a number of planets from 3 to 6. This can be proved by using (19), employed for equally spaced transmissions.

$$\frac{Z_r + Z_s}{N} = \begin{cases} \frac{240}{3} = 80; N = 3 \\ \frac{240}{4} = 60; N = 4 \\ \frac{240}{5} = 48; N = 5 \\ \frac{240}{6} = 40; N = 6 \end{cases}$$

Finally, every configuration proves to be physically big enough for its mounting, this verification is made by using (20).

$$\frac{165 - 75}{2} \geq Z_p = 44$$

$$\frac{166 - 74}{2} \geq Z_p = 45$$

In the following, the transmissions considered are limited to 3 and 5 planet gearboxes, looking for odd number of planets transmissions. Once the number of teeth in each wheel and the mounting of the transmission is verified, then the spacing and mesh phasing have to be set considering the requirements for each of the possible configurations.

Table 3. Classification of the possible transmissions with 3 planets

N=3	Number of teeth			Planet spacing		
	Z_S	Z_P	Z_R	ψ_1	ψ_2	ψ_3
ESIP	165	44	75	0	$\frac{2\pi}{3}$	$\frac{4\pi}{3}$
ESSP	166	45	74	0	$\frac{2\pi}{3}$	$\frac{4\pi}{3}$
NESIP	165	44	75	0	$\frac{2\pi}{3}$	$\frac{22\pi}{15}$
NESSP	165	44	75	0	$\frac{41\pi}{60}$	$\frac{91\pi}{60}$
NESAP	165	44	75	0	$\frac{7\pi}{10}$	$\frac{27\pi}{20}$

Table 4. Classification of the possible transmissions with 5 planets

N=5	Number of teeth			Planet spacing				
	Z_R	Z_P	Z_S	ψ_1	ψ_2	ψ_3	ψ_4	ψ_5
ESIP	165	44	75	0	$\frac{2\pi}{5}$	$\frac{4\pi}{5}$	$\frac{6\pi}{5}$	$\frac{8\pi}{5}$
ESSP	166	45	74	0	$\frac{2\pi}{5}$	$\frac{4\pi}{5}$	$\frac{6\pi}{5}$	$\frac{8\pi}{5}$
NESIP	165	44	75	0	$\frac{2\pi}{5}$	$\frac{2\pi}{3}$	$\frac{6\pi}{5}$	$\frac{26\pi}{15}$
NESSP	165	44	75	0	$\frac{7\pi}{24}$	$\frac{52\pi}{79}$	$\frac{37\pi}{30}$	$\frac{101\pi}{60}$
NESAP	165	44	75	0	$\frac{23\pi}{60}$	$\frac{59\pi}{73}$	$\frac{29\pi}{24}$	$\frac{17\pi}{10}$

The verifications for the classification of the transmissions are included in ANNEX I in detail. Besides, it is important to emphasise the fact that the non-equally spaced configurations, and more precisely, within them, the last two options correspond more to theoretical approaches rather than real industrial applications. Normally in the industry, equally spaced configurations are employed, and as an exception occasionally a diametrically opposed configuration where the spacing is uniform by pairs of planets.

Although the calculations were performed for numerous configurations, for the simulations in this part of the document only transmissions with an odd number of planets have been considered. This is due to the need for addressing in more depth the behaviour of this kind of transmission, mainly the 5-planet transmission. Besides, the lack of symmetries supports the study of the effects of the planet spacing and mesh phasing in detail. In addition, the 3-planet transmission is used as a reference point to start with the analysis and corresponds to the most conventional configuration in planetary transmissions, even having a self-balancing quality non-existent with any other *N*.

4.7. Results

In the following section, the results to all the scenarios taken into account previously are gathered. The effects of each geometrical consideration will be added independently at first and then a combination of more than one at the same time. Thus, the impact of the spacing and the mesh phasing can be understood as well as the floatability.

4.7.1 3-planet configurations

At first, the focus is on the 3-planet configurations, a more classical configuration, at least in the wind turbine industry. Thus, the results to the simulations with this number of planets are gathered in the following sections.

4.7.1.1 Spacing

The influence of the spacing in the behaviour of the transmission, more precisely, in its load sharing is the object of this section. The first scenario to study corresponds to a 3-planet equally spaced transmission with in-phase contacts. A priori, the results to this simulation should be a perfectly balanced LSR, where every planet bears the same amount of load. These results are presented in Figure 34. The results fulfil the expectations.

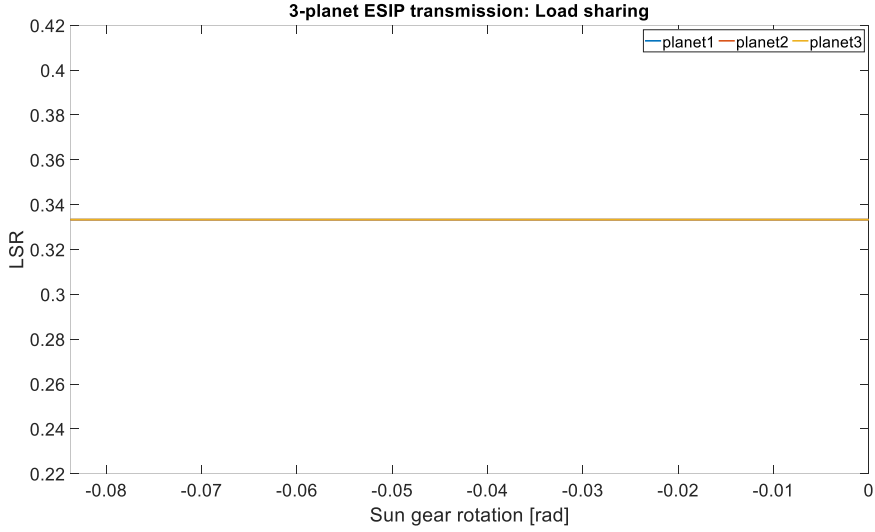

Figure 34. LSR in a 3-planet ESIP transmission.

In order to present more detail of the uniformity of the LSR in this scenario, in Figure 35 the Figure 34 is zoomed in. Thus, it is visible that the only discrepancy in the load in each planet corresponds to negligible computational errors.

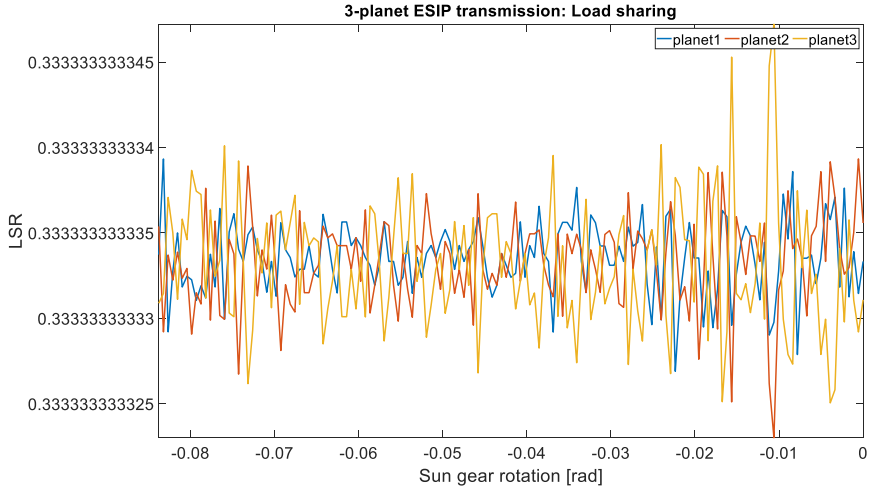

Figure 35. Detail of the LSR in a 3-planet ESIP transmission.

The next step to take consist in eliminating the uniformity in the spacing of the planets. Thus, the spacing correspond to the one for the NESIP configuration gathered in Table 3. However, the lack of floatability in any of the rolling elements impedes the visualization of the imbalance due to the non-equal spacing. The imbalance in the contact forces is absorbed by the infinitely rigid supports, thus, homogenizing the LSR.

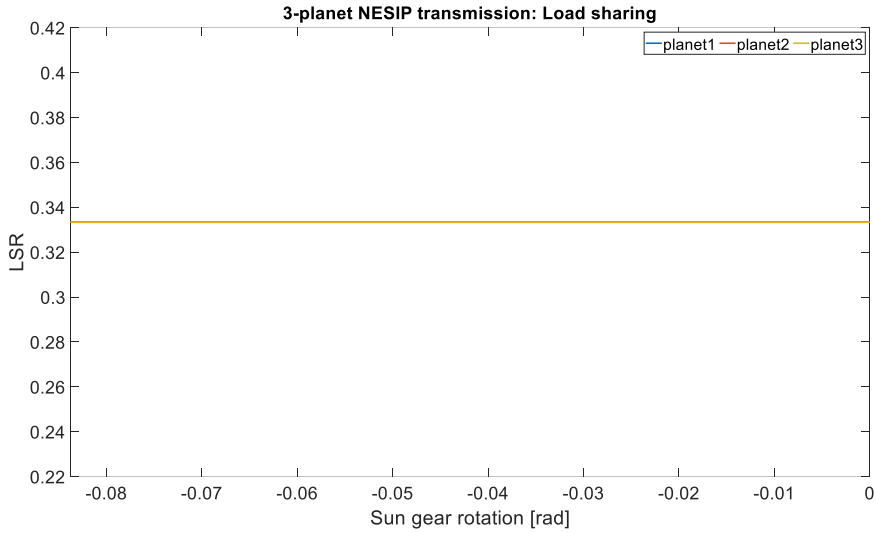

Figure 36. LSR in a 3-planet NESIP transmission.

As it was done in the previous case, the resolution in the LSR graph is augmented in order to see more details. Thus, it is visible how the behaviour of the transmission in this scenario is exactly the same as the previous. Therefore, the uniformity of the spacing in the planets plays no role whatsoever whenever the rigidity in the supports tends to an infinite value.

The next step to take in order to prove what has been stated in this section consists in the inclusion of some degree of floatability in the sun support. However, before it is important to observe the impact of the mesh phasing alone.

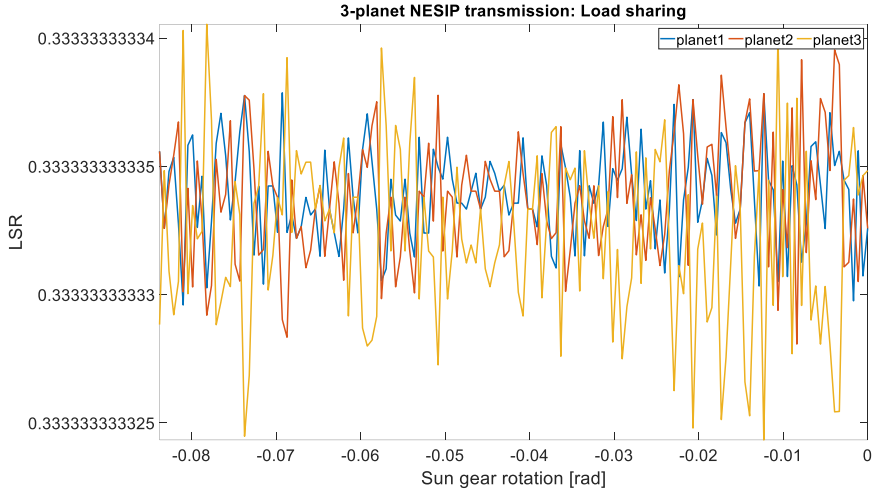

Figure 37. Detail of the LSR in a 3-planet NESIP transmission.

4.7.1.2 Equally spacing various mesh phasing

Apart from the influence of the planet spacing, the geometry of the transmission also determines the mesh phasing. This mesh phasing influences the meshing stiffness in each contact throughout the transmission. A sequential mesh phasing means that every sun-planet or planet-ring contact is at a different point along the meshing line, as commented previously in this document. Thus, as seen before, the transmission equally spaced and in-phase has a perfectly balanced and synchronous behaviour in any of the contacts, whereas the sequentially phased transmission has a different behaviour, as seen in Figure 38.

Given the uniformity in the sequence of the mesh phasing in the ESSP transmission, the LSR shows an n number of maximum values, as many as planets in the transmission, for each meshing cycle in the sun. The equal spacing makes the variation in the loads in each of the planets identical to the rest, but the mesh phasing makes the load level change along the simulation. Nonetheless, the average load level in each of the planets is the same and is equal to the ideal load level and to the one in the ESIP transmission. These

moments where the maximum load is reached coincide with the double contacts, therefore, the highest meshing stiffness.

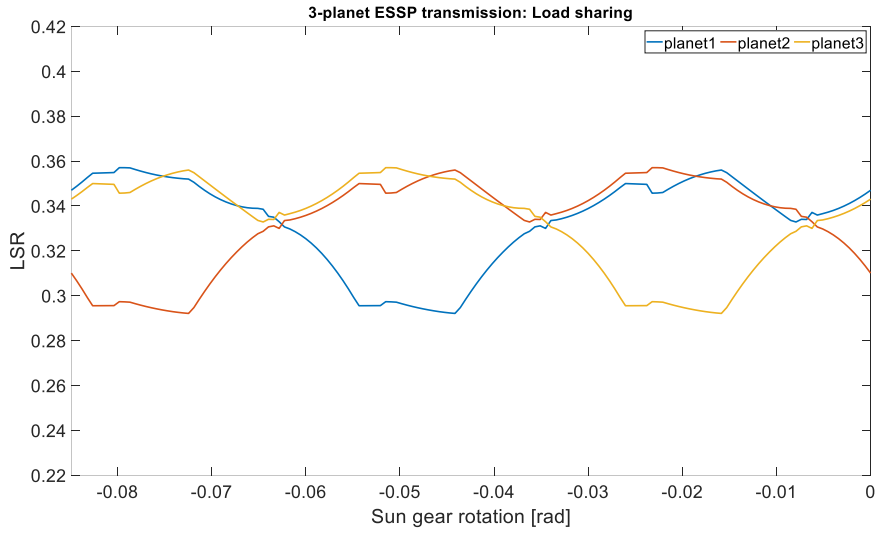

Figure 38. Load sharing in 3-planet ESSP transmission.

4.7.1.3 Nonequally spaced and various mesh phasing

Whenever the effect of the mesh phasing acts together with an unequal spacing in the transmission, the results do not vary for an in-phase transmission due to the lack of floatability in the wheel supports, as mentioned previously and shown in Figure 36.

On the contrary, the unequal spacing affects the uniformity of the sequence and because of that modifies the behaviour of the sequentially phased transmission, which is visible comparing the results in Figure 38 & Figure 39. Thus, the sequence is modified to a point where the highest meshing stiffness is reached by the planet 2, which reaches the highest and the lowest load level along the simulation. Then, the behaviour on the rest of planets is less abrupt given the proximity between them, in terms of spacing.

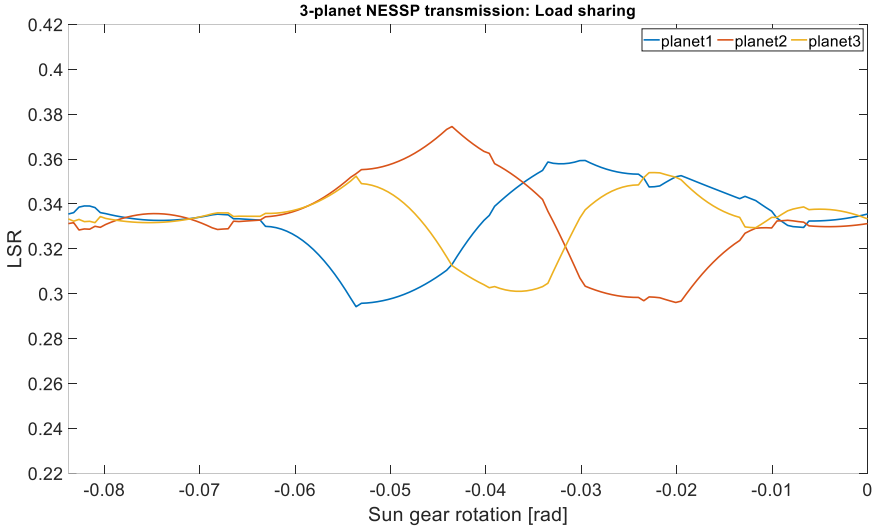

Figure 39. 3-planet NESSP transmission.

4.7.1.4 Configurations with floatability in the sun gear

In the following, some floatability is included in the sun gear support. Given that, the sun centre will be able to modify its position in order to look for balance in the transmission, thus, describing an orbit composed by its every instantaneous position in each of the angular positions studied. The rigidity of the sun support is specified in Table 5, following the lumped-parameter approach explained in 4.4.3.

Table 5. Lumped rigidity in the sun support.

Direction	Rigidity (N/m)
X	1e8
Y	1e8

In the configuration where the planets are equally spaced, the inclusion of floatability in the sun gear support does not make any difference. This is due to the fact of the existence of perfect balance amongst planets due to the

spacing and mesh phasing. If the weight of the wheels and the planet-carrier were considered, this balance would be modified.

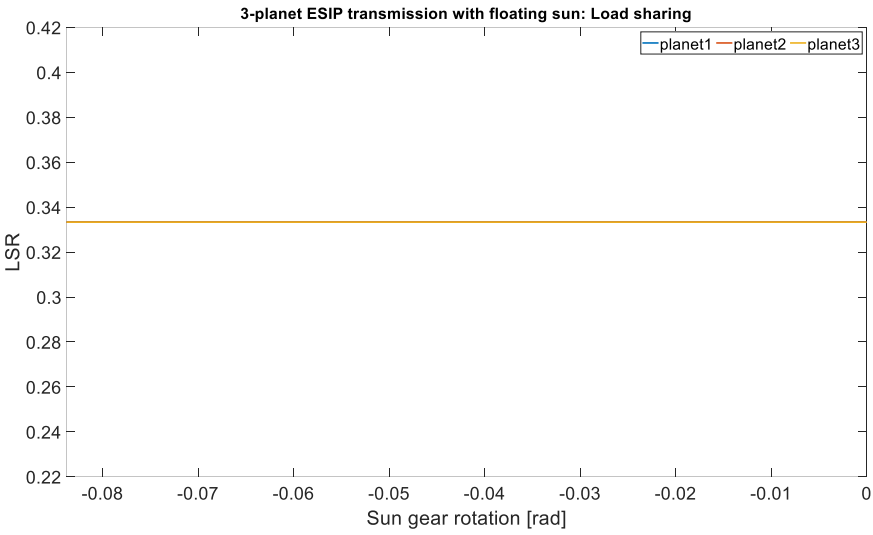

Figure 40. Detail of the LSR in a 3-planet ESIP transmission with floating sun.

Given the perfect balance in the transmission, the centre of the sun-gear does not modify its position from the reference position, located in the centre of the epicyclic transmission.

The detail of the orbit, presented in Figure 41, shows the small translation in the centre of the sun gear. This corresponds to the movement provoked by the small variation in the results due to numerical reasons. This scenario in reality stands for an ideal configuration where the load sharing is perfect and, therefore, there is no orbit described by the sun gear. However, in reality this scenario is far-fetched.

On the contrary, in the same configuration but with a non-equal spacing, the results are dramatically different. Firstly, the spacing in the transmission generates a notable imbalance amongst the planets. Besides, the floatability in the sun support is not enough to compensate this imbalance and uniform the load sharing in the transmission. Thus, the load level in the planet who is

further, in terms of angular spacing, from the other two, will bear more load, as seen in Figure 42. On the other hand, the two planets that are closer to each other are the ones that bear less load. The floatability will tend to move the sun further from those two planets and closer to the other one, in this case planet 2. However, the transmission is notably unbalanced, and this is due to the unequal spacing together with a not enough floatability. The latter refers to the fact that a lower stiffness in the support of the sun gear would allow bigger translations and a bigger orbit. Therefore, this bigger freedom would enable the sun gear to go to the appropriate position to balance the meshing stiffnesses in the contacts and the load sharing in the transmission.

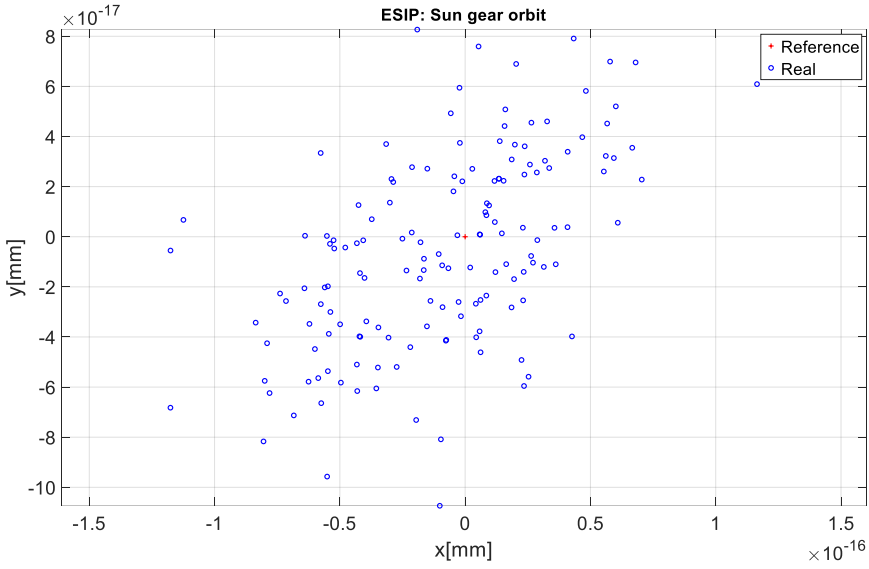

Figure 41. 3-planet ESIP transmission with floating sun: Detail of the sun orbit.

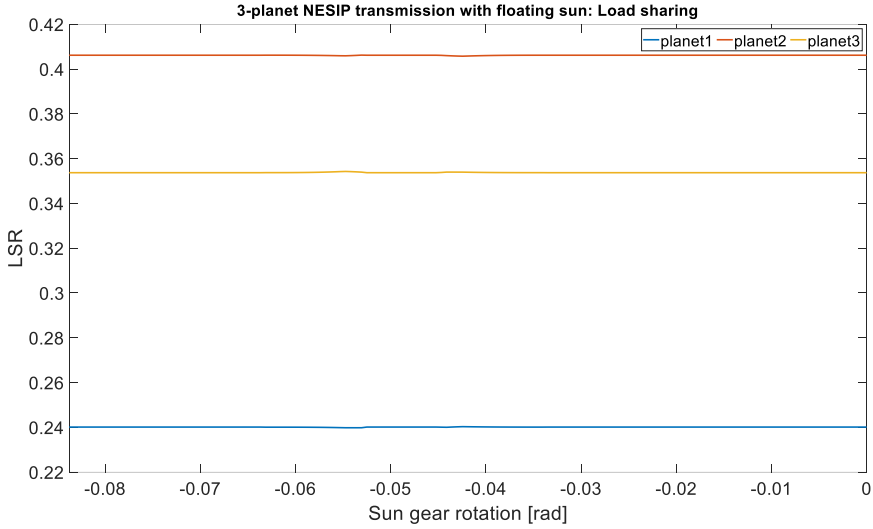

Figure 42. Load sharing in 3-planet NESIP transmission with floating sun.

The movement described by the sun is shown in detail in Figure 43, where a composed movement is visible. Firstly, the translation due to the difference in stiffness in the contacts, commented before. Secondly, there is a loop around that first movement, this loop is described by the sun due to the changes in the meshing stiffnesses in each of the angular positions calculated along the simulation. If the simulation were extended to an entire turn of the carrier, this loop would be repeated a number of times, derived by the transmission ratio, and the translation due to the spacing would describe a circumference alongside the rotation in the carrier, surrounding the reference position.

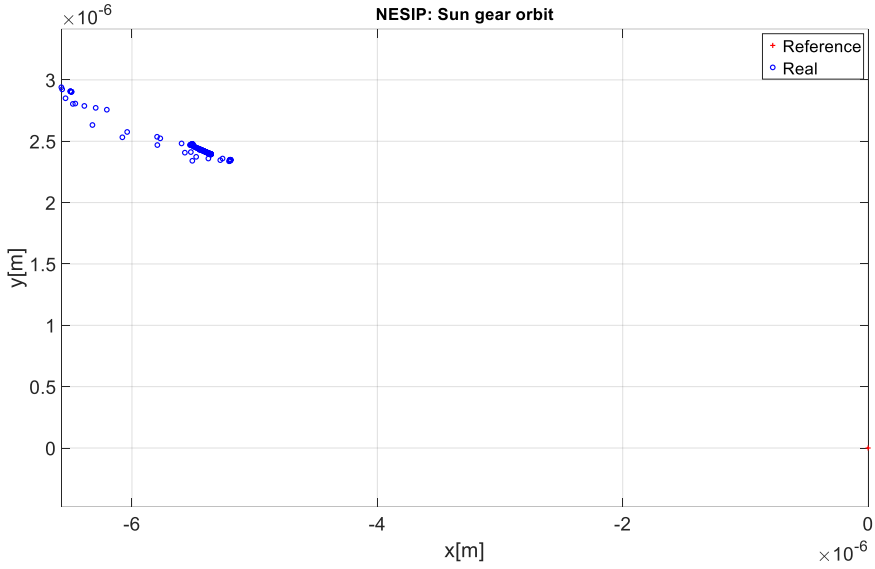

Figure 43. 3-planet NESIP transmission with floating sun: Sun orbit.

After all the scenarios presented before, the next logical step consists in combining every effect that has been analysed separately. Thus, to the previous approach with spacing and mesh phasing combined, the effect of the floatability in the sun gear support is added.

Hereinafter, the scenarios with ESSP and NESSP transmissions are analysed including a floatability in the sun as the one seen in Table 5.

In the ESSP transmission, the floatability in the sun works as expected, reducing the variability of the load on each of the planets, as seen in Figure 44 in the amplitude of the load cycles in each planet. Even with the floatability there are some analogies with the fixed configuration, in this case also, an N number of peaks can be seen, and they are uniformly spaced along the simulation. However, there exists the mentioned attenuation of the load due to the floatability.

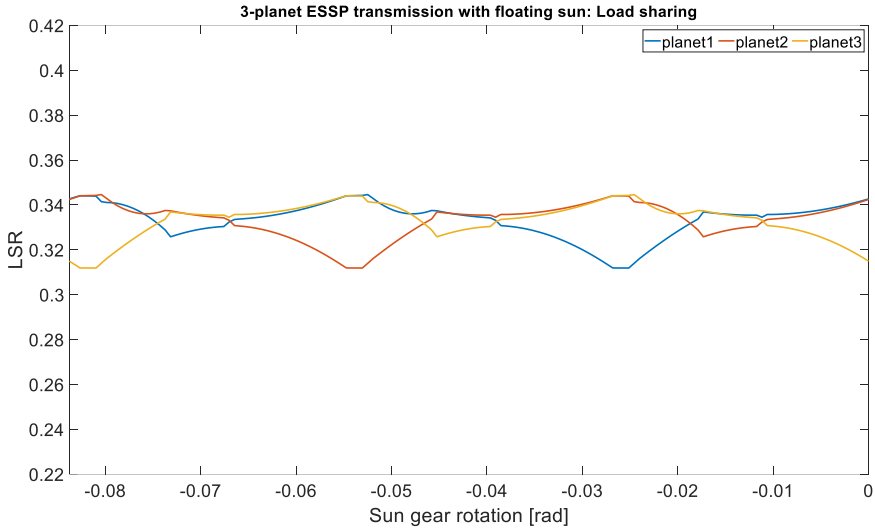

Figure 44. 3-planet ESSP transmission with floating sun: Sun orbit.

The reason to that attenuation is visible in the orbit described by the sun gear, seen in Figure 45. The sun describes an orbit composed by three identical loops around its reference position. Therefore, the sun translates along the plane while the meshing stiffness varies along the simulation. This translation attenuates the variations in the meshing stiffness and decreases the differences amongst planets in terms of load. If this simulation continued, the loops would repeat themselves, however, the next time these loops would include a rotation due to the angular displacement in the carrier and the variation in the positioning of the planets with respect to the sun.

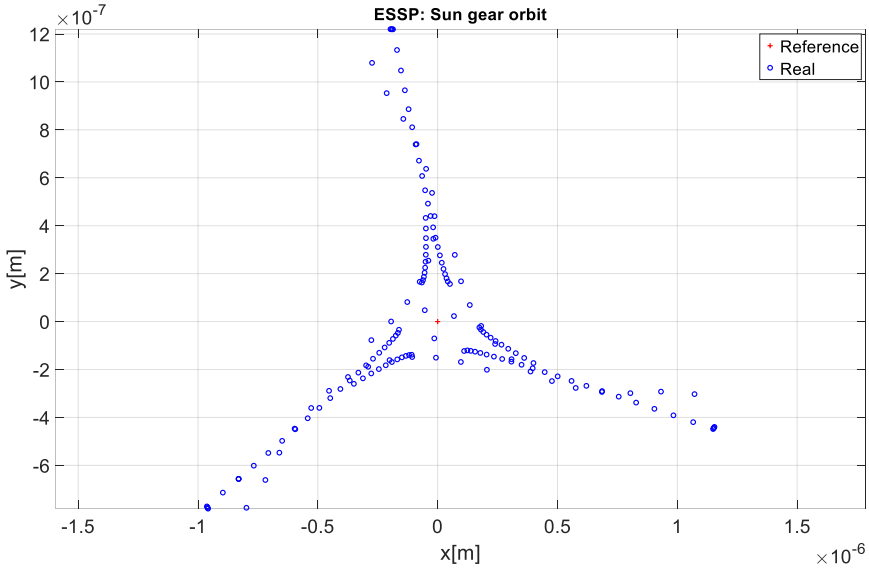

Figure 45. 3-planet ESSP transmission with floating sun: Sun orbit.

Finally, in the NESSP transmission, the combination of the planet spacing and the sequence in the mesh phasing combines their effect with the floatability and everything that was stated before in this section appears together in this last case. Thus, as seen in Figure 46 the load in each planet varies along the meshing cycle due to the mesh phasing, the load level is different in each planet due to the unequal spacing and there exists an attenuation on the variability of the load in each planet due to the floating sun.

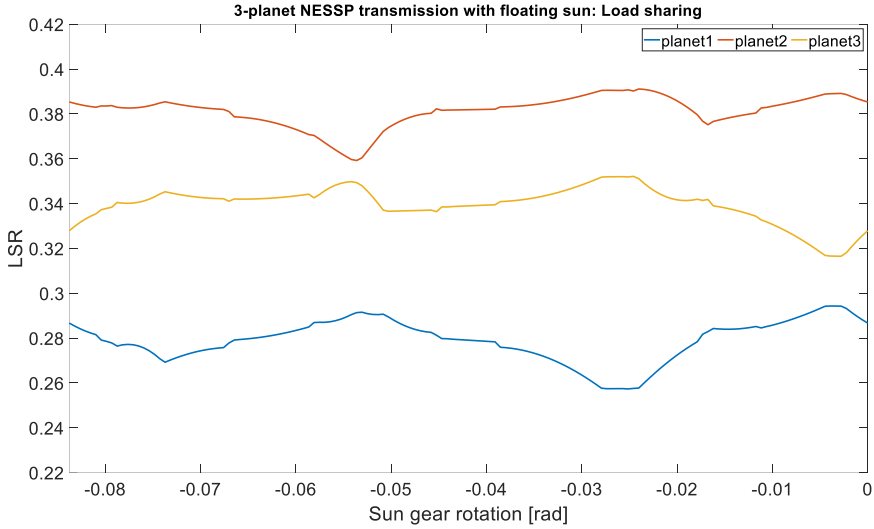

Figure 46. 3-planet ESIP transmission with floating sun: Sun orbit.

The mentioned combination of effects is also visible in the orbit described by the sun, as seen in Figure 47. In this case, the loops described by the sun are similar to the ones in the ESSP transmission, but these are not identical to each other, due to the unequal spacing. In addition, there exists a translation with respect to the reference position, which did not exist for the ESSP transmission. This translation is also due to the spacing. Therefore, the similarities are visible, even though they are affected by the change in the spacing with respect to the previous scenario.

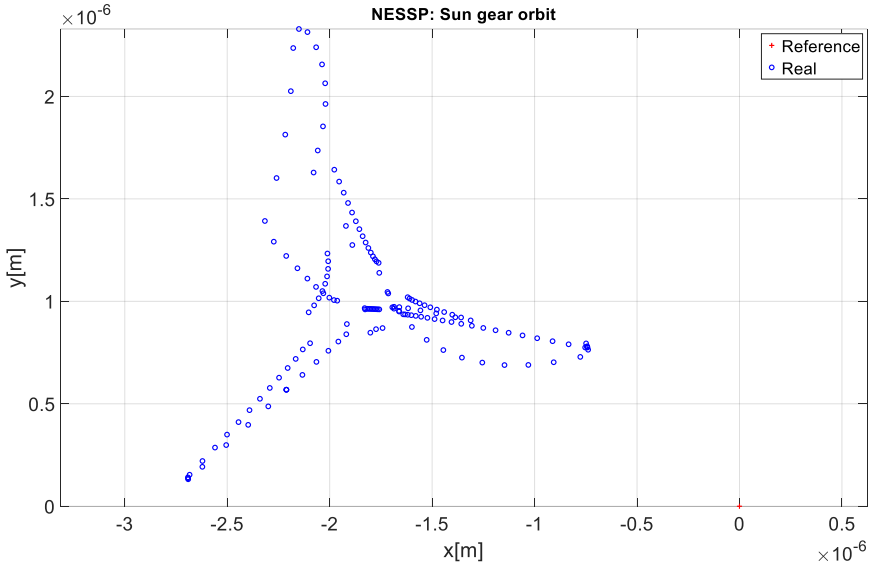

Figure 47. 3-planet ESIP transmission with floating sun: Sun orbit.

4.7.2 5-planet configurations

In the next step, the number of planets is raised to 5, this configuration keeps an odd number of planets as well as augments the stiffness of the entire transmission due to the raise in the number of simultaneous contacts. This raise in the stiffness of the system is expected to augment the sensitivity of the transmission to the changes, as Bodas & Kahraman observed in the case of the errors in (Bodas & Kahraman, 2004).

4.7.2.1 Spacing

At first, in analogy with the 3-planet transmissions the effect of the spacing in the load sharing of the transmissions is studied. However, in this case, looking for conciseness the scenarios with in-phase and sequential mesh phasing are presented together in the same section.

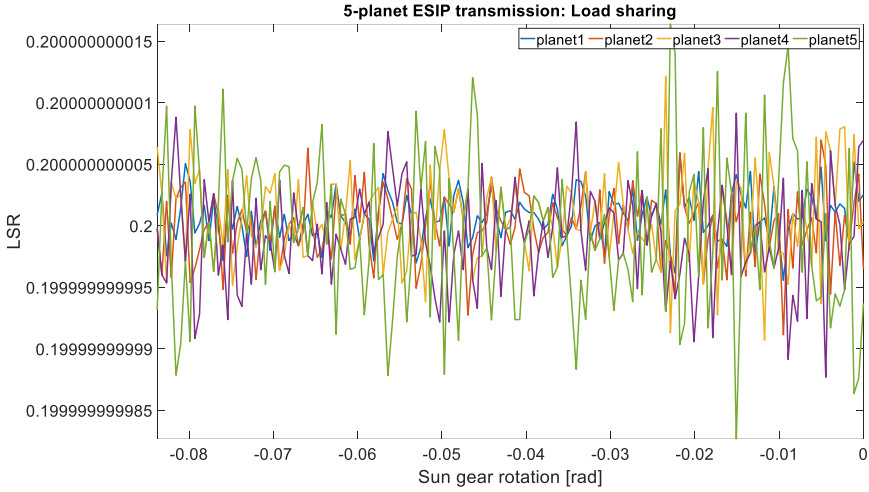

Figure 48. Load sharing in 5-planet ESIP transmission.

In both scenarios, equally and unequally spaced, the results are the same. The lack of floatability in every gear leads to a similar scenario as seen previously for 3 planets, but in this case, the ideal load level is at 20%, given the new number of planets.

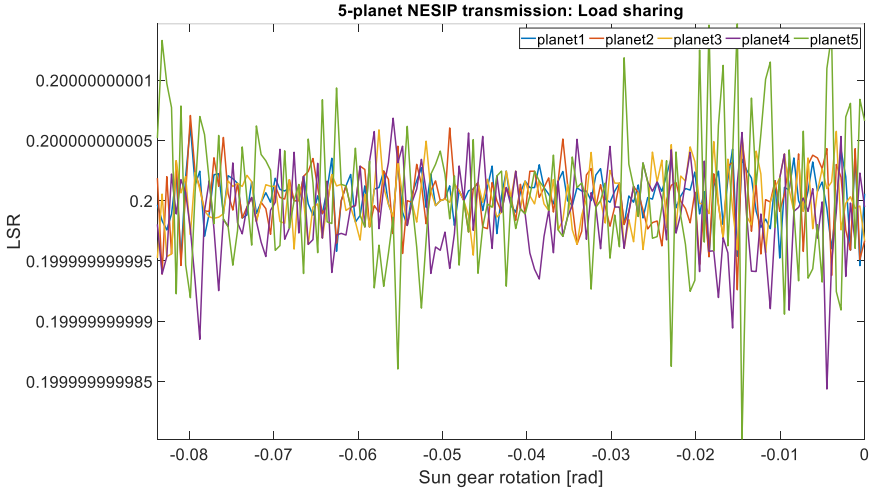

Figure 49. Load sharing in 5-planet NESIP transmission.

In the following, it is visible how the load sharing of a sequentially phased transmission provides an n number of maximum values in the load sharing, as many as the number of planets for each meshing cycle. Each planet describes an identical cycle in terms of load, however, each cycle is delayed a T/5 in time, where T provides the period for each meshing cycle. This statement can be confirmed observing the results in Figure 50.

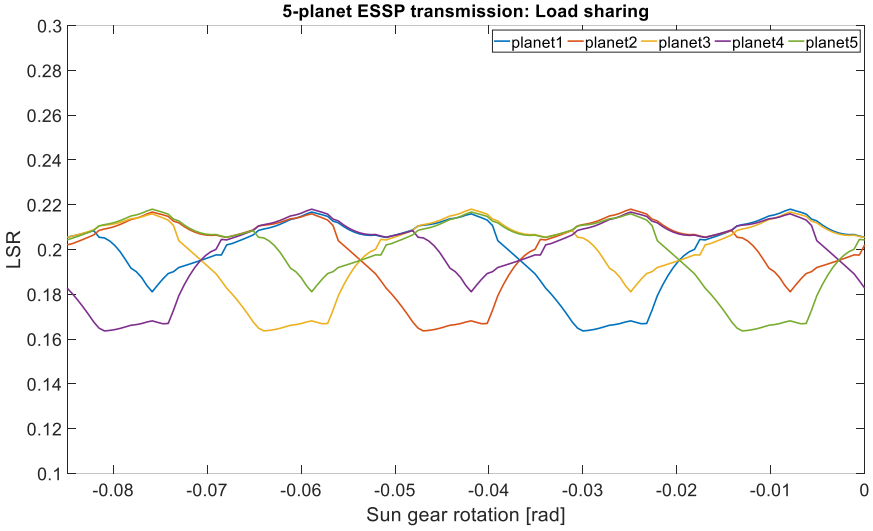

Figure 50. Load sharing in 5-planet ESSP transmission.

On the other hand, the unequal spacing modifies the uniformity of the sequence in the mesh phasing as it happened for the 3-planet transmission, as seen in Figure 39. Thus, the uniformity in the load cycles in each planet is lost, as seen in Figure 51. Besides, this modifies the amount of load in each planet and shows how the spacing makes every maximum value in each planet different, and in this case, the planet 4 is the one that bears more load. In addition, this unequal spacing leads to a higher load level in that planet than in the ESSP scenario. Therefore, in this case, the non-equal spacing not only affects the uniformity on the load sharing, but also provides a less favourable load sharing for some of the planets.

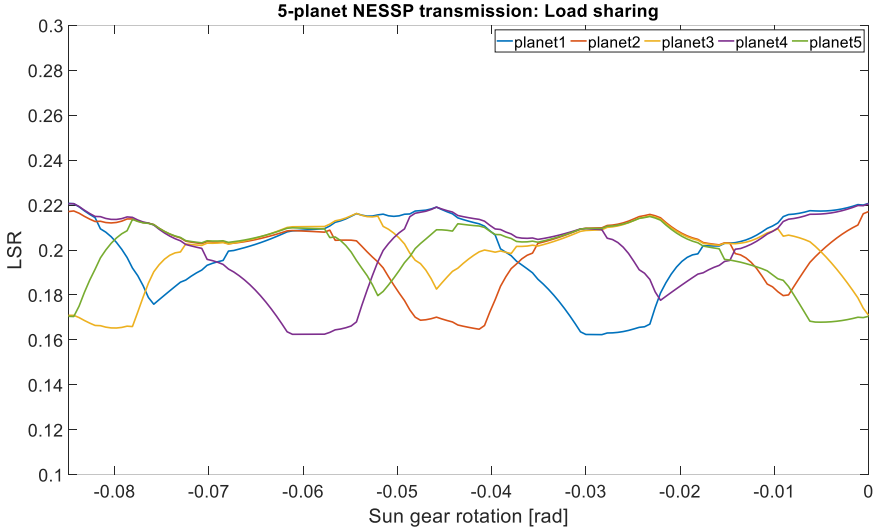

Figure 51. Load sharing in 5-planet NESSP transmission.

These results prove how the non-equal spacing leads always to an irregular sequence in the mesh phasing, as derived in 4.5.2, that corresponds with an unbalanced load sharing. Besides, this lack of regularity in the sequence generates higher load levels in some of the planets with the implications that this could have in the durability of the wheels or other components.

4.7.2.2 Various spacing with floatability

In contrast to the previous results, the floatability included in the sun gear changes the behaviour of the non-equally spaced transmissions. In the ESIP transmission, the results do not change with the floatability as it happened previously for the 3-planet gearbox. These results are expected, but also correspond to an ideally perfectly balanced transmission. On the contrary, the load sharing in the NESIP transmission is a more realistic response, where there exists an imbalance due to the unequal spacing, as seen in Figure 54.

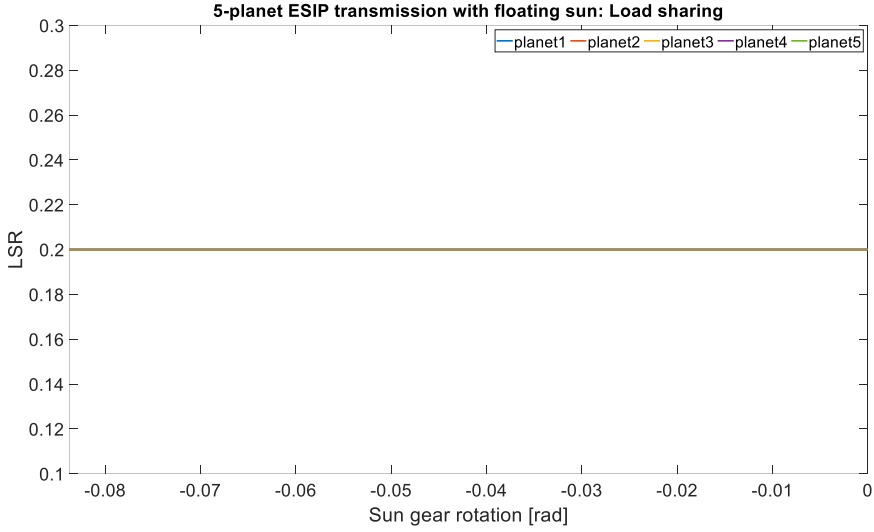

Figure 52. Load sharing in 5-planet ESIP transmission with floating sun.

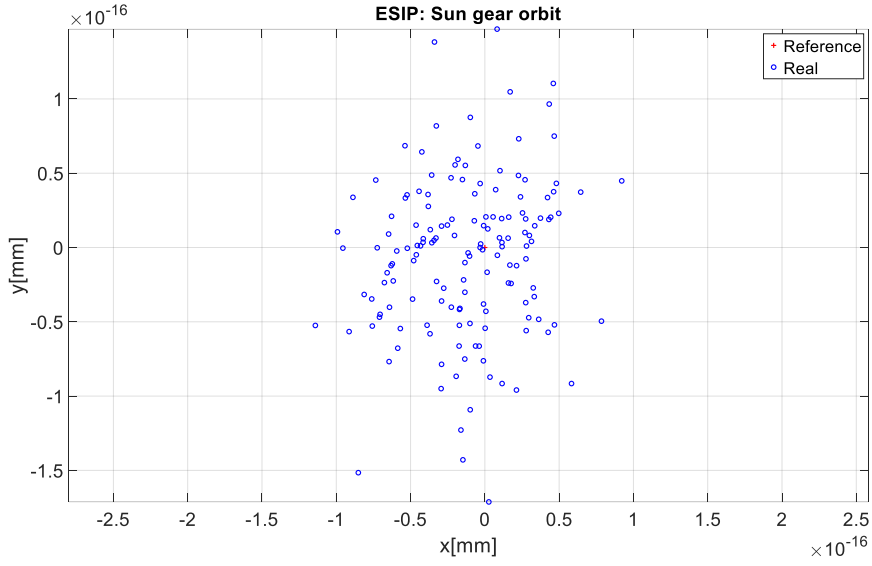

Figure 53. 5-planet ESIP transmission with floating sun: Sun orbit.

The results in Figure 54 provide a better image of the behaviour of a NESIP transmission than the ones obtained with a fixed sun gear. The similarities

with the 3-planet transmission, for both ESIP and NESIP configurations, are evident.

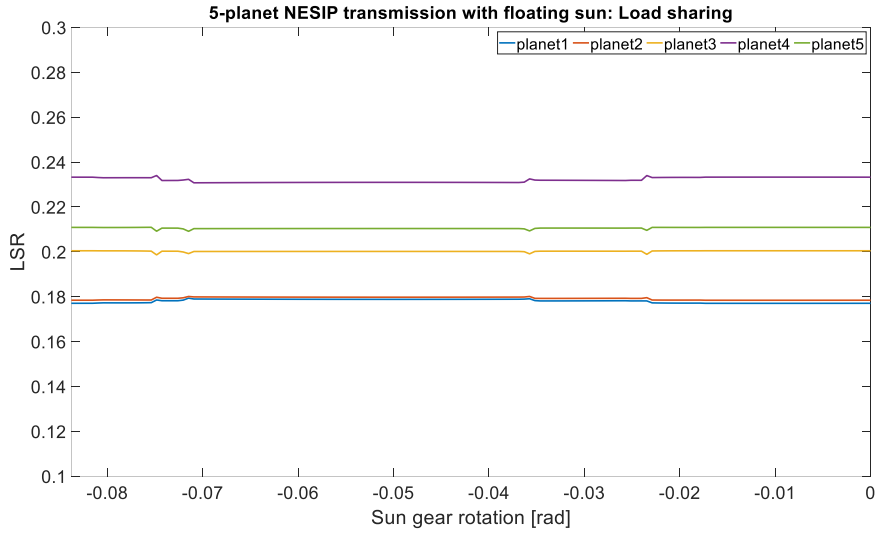

Figure 54. Load sharing in 5-planet NESIP transmission.

Also in analogy with the 3-planet transmission, the sun gear modifies its position looking for balance in the load sharing. However, in 5-planet transmissions this effect does not have the same result as in a 3-planet configuration. In addition, as commented before there exists a joint movement a translation from the reference position together with the loop described due to the changes in the contacts along the meshing cycle, as seen in Figure 55.

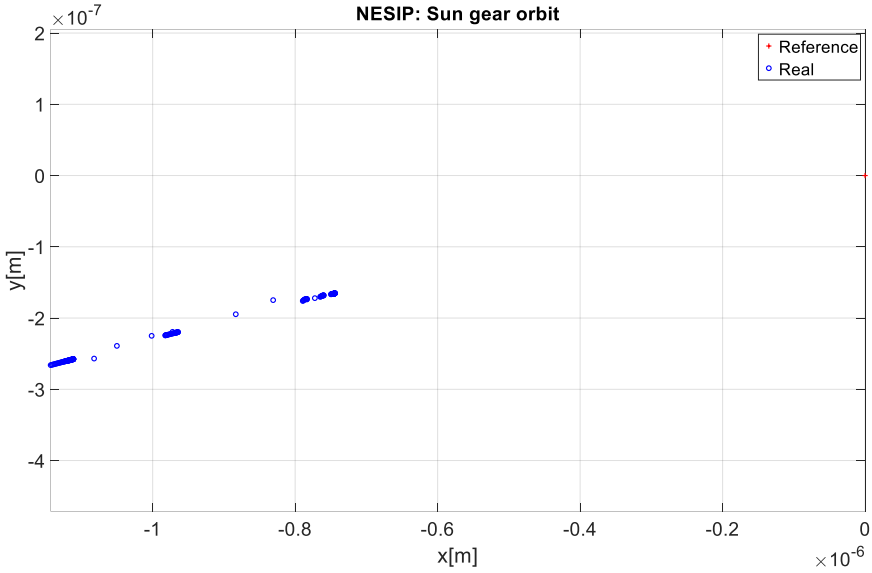

Figure 55. 5-planet NESIP transmission with floating sun: Sun orbit.

Finally, the results for ESSP and NESSP transmissions are also affected by the floating sun. Firstly, it is visible in the ESSP transmission, shown in Figure 56, the floatability in a 5-planet planetary transmission does not have the aim of balancing the load sharing in the transmission. Actually, the results presented in Figure 56 compared to the ones in Figure 50 show a higher level of load in each of the planets. However, the average load level is lower than in the scenario with fixed sun. Apart from that effect, the similarities with the previous scenarios are visible and are logical in the performance in a ESSP transmission.

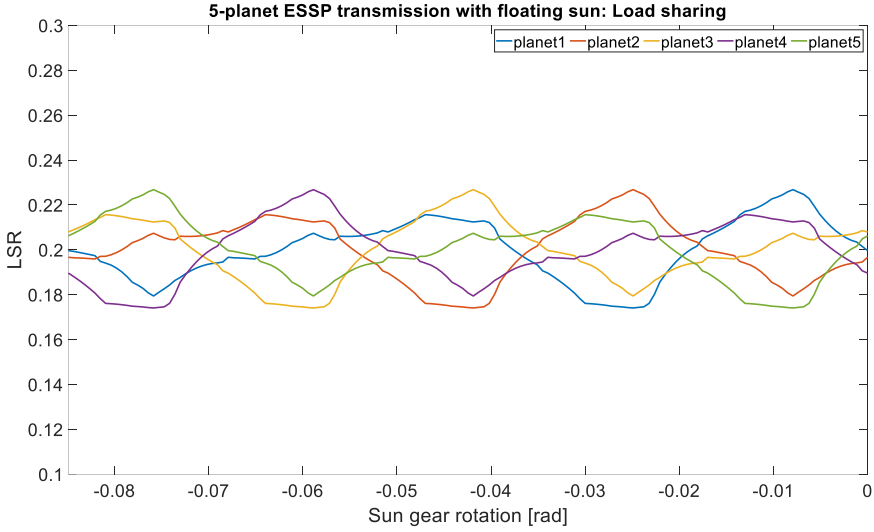

Figure 56. Load sharing in 5-planet ESSP transmission with floating sun.

As it happened with the analogous 3-planet scenario, the sun gear describes an orbit around the reference position composed by an n number of loops, in this case 5, that are identical. Thus, the sun gear modifies its position alongside the changes in the meshing stiffnesses in each contact.

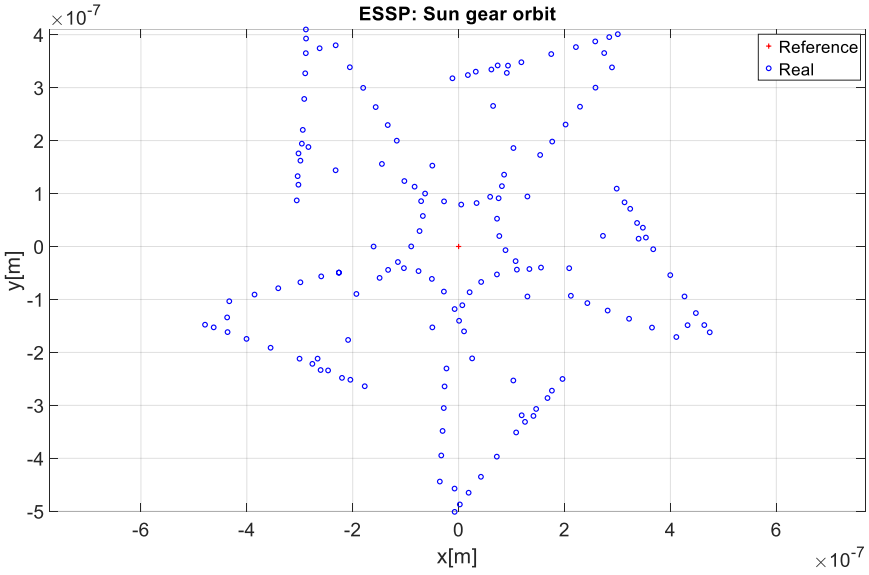

Figure 57. 5-planet ESSP transmission with floating sun: Sun orbit.

Finally, whenever the spacing is non-equal and the phasing sequential, there is no pattern in the behaviour of the load sharing. The inclusion of floatability in the sun gear does not help for the balance in the load sharing, as shown in Figure 58. This effect is only in the 3-planet transmissions.

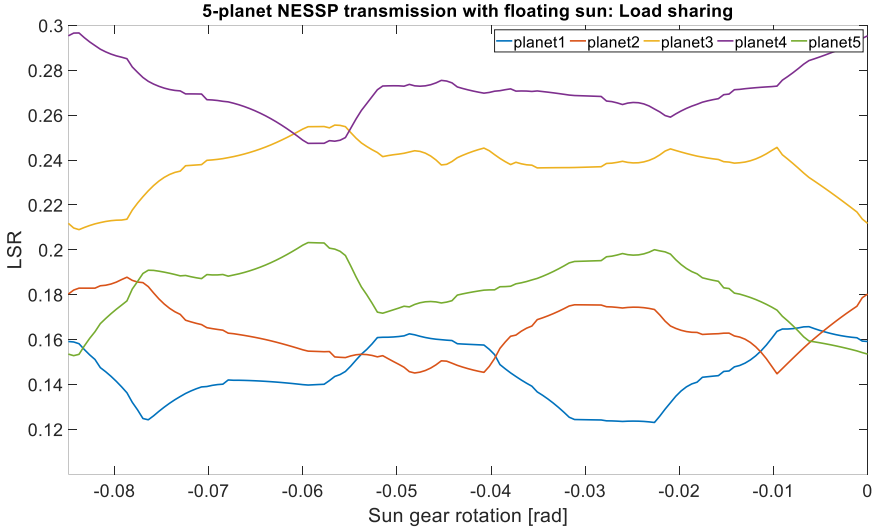

Figure 58. Load sharing in 5-planet NESSP transmission.

In addition, the orbit in Figure 59 shows a completely irregular behaviour compared to the ESSP transmission with the same number of planets.

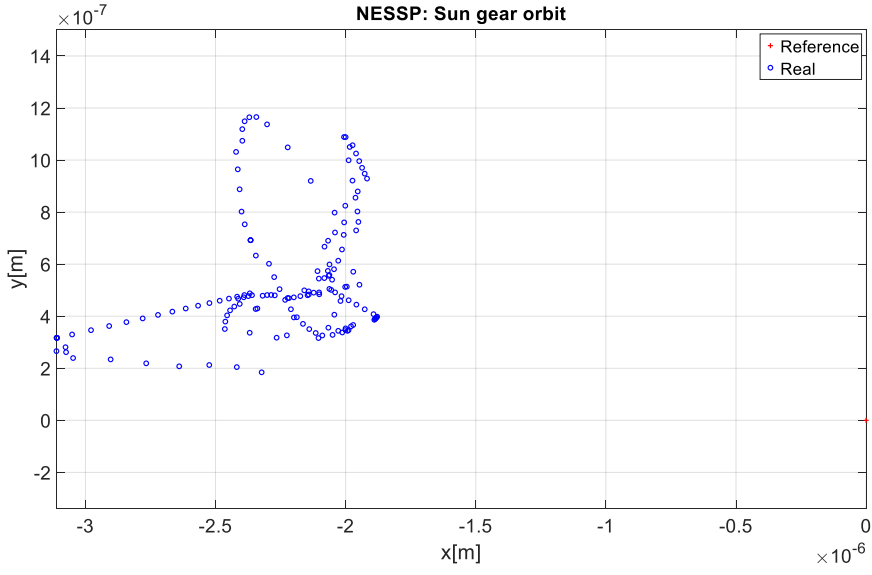

Figure 59. 5-planet NESSP transmission with floating sun: Sun orbit.

4.8. Main effects recap

Once all the results have been presented, it is interesting to gather the main effects that were observed along these results. Firstly, the spacing has no impact in transmissions with in-phase meshing that include no floatability in any of the supports. However, in sequentially phased transmissions the effect of both the spacing and mesh phasing becomes visible under any circumstance.

At the same time, the sequential phasing proves to influence the load sharing generating a load cycle in each planet separated by T/N along the studied meshing cycle. Thus, every planet behaves identically but with a delay.

Regarding the number of planets, there are analogies between 3 and 5 planet configurations. However, the most important difference relies on the influence of the floatability in the load sharing. For 3-planet transmissions, this floatability uniforms the load sharing, whereas in 5-planet transmissions this effect is not seen.

Finally, with respect to the orbits, it is significant to highlight the symmetry in the orbits for equally spaced transmissions affected by a sequential phasing, whereas this behaviour is not visible in any of the other scenarios. It is also relevant the fact of the direct relation between the number of planets and the number of closed loops in the orbit described by the sun gear.

Chapter 5: Error presence in planetary transmissions

5.1. Introduction

Planetary transmissions are complex configurations composed by numerous moving elements. Although the various advantages due to the epicyclic configuration of the gears, there exists also a high probability of error presence in any of the components. At the same time, the manufacturing process of the components is not perfect, even though it has reached a high level of accuracy and repeatability. This makes impossible the avoidance of the error presence in any planetary transmission in the world.

The presence of errors influences directly, and in occasions dramatically, the life expectancy of the components and as a consequence the performance of the transmission. Given their importance, this section focuses on the presence of errors in the main elements (gears and carrier) that compose the gear transmission. A variety of errors is studied. For those, its influence in the performance of the transmission is analysed. However, not only is it important to analyse the sheer effect of the error but also its interaction with other variables such as planet spacing, mesh phasing, interaction between errors and floatability amongst others.

Apart from the above mentioned it is considered important the impact that the load has in such a transmission. The flexibility considered in the

components and the load should a priori work together in the uniformity of the loads and the balancing of the transmission performance.

5.2. Geometrical definition of the studied errors

Before including errors in the employed model, it is necessary to study the geometry of each error, the measurement procedure and the main parameters that describe every error.

Once these errors are analysed, the parameters are included in the model in order to emulate them. Given the definition of the model, for every analysis the geometrical definition of every error is required. In the following, the parameters necessary to include the errors in the model will be specified. Given the wide scope of possible errors in planetary transmissions, this work limits the considered spectra to the pinhole position errors and tooth thickness errors. These have proven to influence significantly the transmission performance, as seen in (Bodas & Kahraman, 2004; M. Iglesias et al., 2017; Ahmet Kahraman, 1999; Singh, 2005)

5.2.1 Pinhole position errors

The concept of pinhole position errors refers to the difference between the ideal and the real positioning of the pinhole. Whenever a transmission is designed, a position tolerance is defined for each of the pinholes in the carrier. However, this tolerance responds to a magnitude that defines a circumference inside of which the centre of the pinhole should be located. Apart from this tolerance, measurements of the radial distance between the centre of the carrier and the centre of the pinhole are made. In addition, angular measurements are performed to establish the angular spacing between consecutive planets and for each planet in relation to an angular reference, common for every pinhole.

In some of the main publications in this topic (Bodas & Kahraman, 2004; Hu et al., 2018; Ahmet Kahraman, 1999; Singh, 2005, 2010) , the pinhole position errors are defined by two parameters, the magnitude of the error and the angle

from a reference position. However, in this work the definition for these errors follows the one presented in (M. Iglesias et al., 2017; Sanchez-Espiga et al., 2020). From now on, this error will be defined in two components, each corresponding to one principal direction inside the transversal plane; every wheel rotates inside this plane.

At first, there is the tangential error, which corresponds to the difference between the ideal and the real position of the pinhole along the direction that is tangential to the carrier circumference with a radius equal to the mounting distance. This error will be the component X of the pinhole position error.

Secondly, the radial error is defined. This refers to the discrepancy along the line that connects the wheel centres between the ideal and the real position of the pinhole. This will be the Y component of the error and together with the tangential are referred as the pinhole position error. In contrast to previous conceptions, in this case the two parameters just refer to the magnitude of the error in each direction. For comparison with the position tolerance, the module of the error should be calculated and compared. This definition is considered the most appropriate solution because it provides information about the magnitude and the direction of the error in a more straightforward way than the other mentioned definition. Finally, Figure 60 illustrates every aspect stated regarding the definition of the pinhole position error in the transmission. It also includes the local reference frames for each of the planets and the global for the transmission.

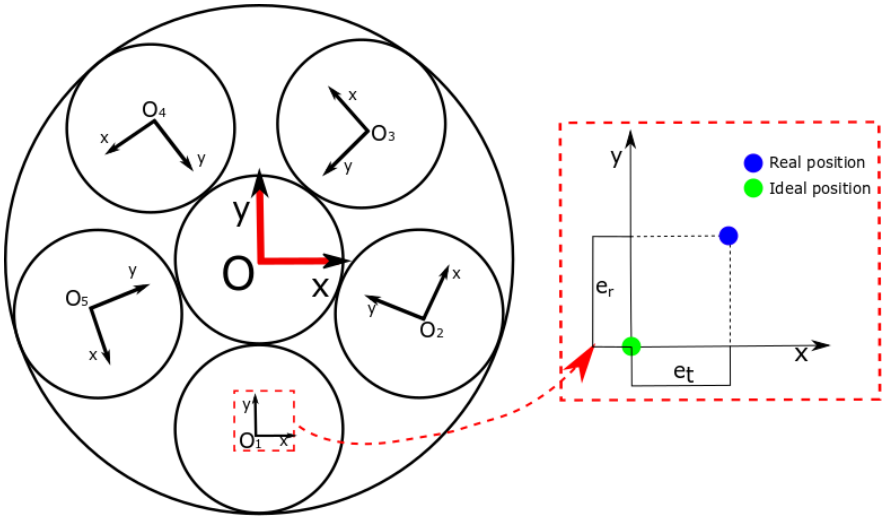

Figure 60. Geometrical definition of the pinhole position error

5.2.2 Tooth thickness errors

This error refers to the difference in thickness between the ideal tooth and the real tooth. In this case, the magnitude of this error depends on the measurement procedure, for the study performed, the measurement procedure proposed by Wildhaber in (Wildhaber, 1923) is taken as reference.

This measuring technique consists in measuring the length of a straight line, tangent to the gear base circle. The points that are the limits of the segment belong to opposite flanks. To measure appropriately, the plates of the tool should be tangent to the involutes. This measured distance is referred as w_k. The drawing in Figure 61 aims to illustrate such procedure.

The main advantage of this measuring technique is the fact that one can measure in any point throughout the involute profile. The tool has to be perpendicular to the profile. Thus, the measured distance will be a straight line tangent to the base circle, and the tool will be perpendicular to the involute profile at the other edge.

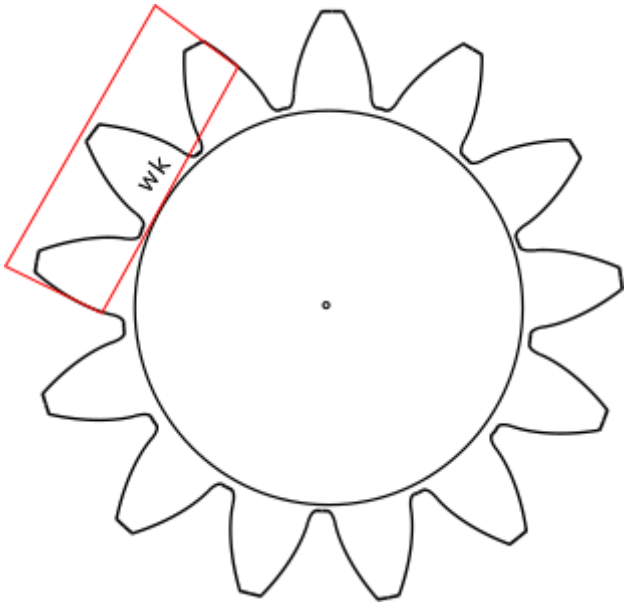

Figure 61. Measurement of the wk

In order to induce the tooth thickness error, the ideal w_k should be calculated, by following the analytical definition in (24). Then, for the calculation of this error, the difference between the ideal value, calculated by the equation (24), and the length measured has to be established. Even though the number of teeth used for the measuring varies, the error does not depend on the number of teeth reached within the tool edges.

$$w_k = \frac{\cos\varphi}{P}\left[(2S+1)\frac{\pi}{2} + N(\tan\varphi - \tan^{-1}\varphi)\right] \qquad (24)$$

In equation (24) P refers to diametral pitch of the gear, S is the number of tooth spaces between the measured profiles, φ is the pressure angle, and N the number of teeth in the gear. It is important to stress the fact that this expression was developed to be employed with imperial units; however, it has been kept as is in order to preserve the way it was written originally.

In order to model this error, there are various approaches. Firstly, given the small magnitude of the error, it is assumed that this error will not modify the

stiffness in the FE models and therefore it is not included in them. However, its impact in the contact problem will be notable; generating an advance or delay in the contact analogous to the effect of the tangential error, and consequently it is included. The chosen way to include it consists in the modification of the overlap calculation. For such procedure, the amount of error is multiplied by the pressure angle to obtain an accurate approximation of the modification of the involute profile by the error and then this distance is sum to the results of the overlap calculation.

Once this point is solved, to observe the influence of such an error it is possible either to assume that the error is symmetrical, therefore the same amount in both flanks, or apply it asymmetrically to both flanks. If this error is considered symmetrical then the procedure to apply consist in obtaining the difference between the ideal thickness of the tooth and the result of the measurement. Once this difference is known, then divide it into both flanks. Not forgetting that the measurement procedure considers the errors in both flanks at the same time and does not make difference between each flank. This is the option chosen in the simulations performed in this chapter.

5.3. Effect of the errors in the load sharing

Beyond the geometrical definition of the errors and its modelling for this work, the most important thing is analysing how they influence the performance of the transmission. This section is aimed to the geometrical study of the contacts, the modifications due to errors, and its impact in the performance of a transmission.

5.3.1 Tangential position error

Based on their geometrical definition, tangential errors in the positioning of the planets in the carrier imply a series of modifications in the geometry of the contacts. Hence, the load sharing in the transmission will experience a subsequent change.

In a first approach, tangential errors produce an advance or delay in the contact between the planet that includes the error and the other gear that is going to contact with it. This advance or delay, depends on the direction of the error and the applied torque. For instance, taking into account the geometrical references shown in Figure 60 a positive error and a Clockwise (CW) torque would result in an advance in the contact of the planet with the positive error.

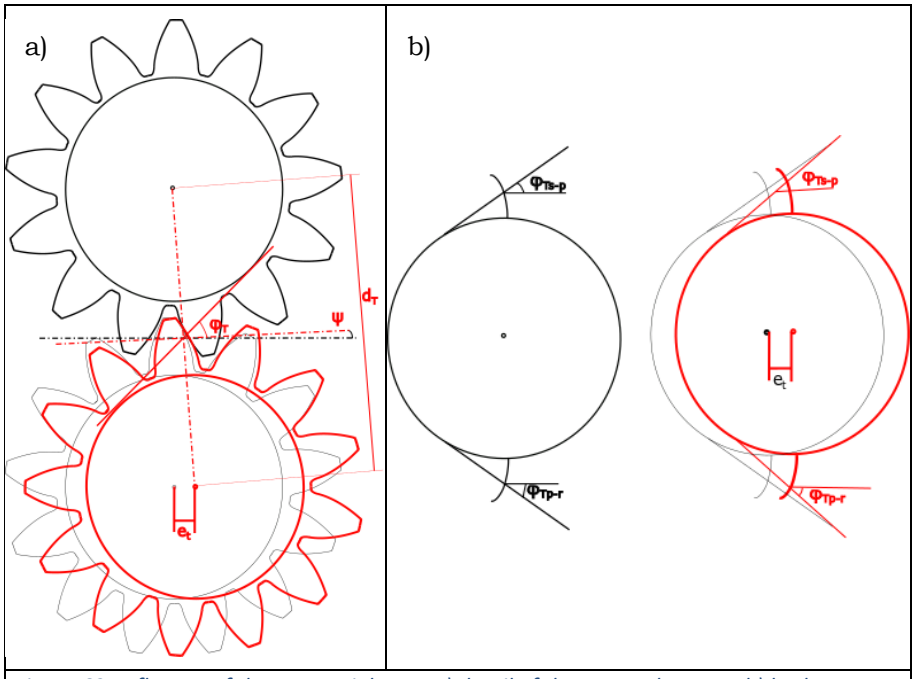

Figure 62. Influence of the tangential error a) detail of the external contact b) both contacts

Figure 62 illustrates the changes in the geometry of the contacts derived from the presence of a, in the picture positive, tangential error. This kind of error will modify the mounting distance between gears and as a consequence or in parallel, the pressure angle between the gears. It is important to highlight, as seen in Figure 62b, that the effect of the error is equal for both contacts. Furthermore, the impact of such modification is a direct function of the size of the error and the transmission. More precisely, the relative size of the error,

in comparison to the dimensions of the transmission influences crucially the effect of the error in the mounting distance and pressure angle.

At this point, it is interesting to remind the equations presented before in (Iglesias Santamaría, 2013), where the overlaps are calculated for any of the possible contacts. These equations prove that these changes affect the overlaps between flanks and, given the definition of the contact problem, will affect the amount of load borne by each planet. These groups of equations (25) & (26) are for external and internal contact, respectively.

$$\begin{cases} \delta_{iv-iv} = (\rho_1+\rho_2)(\tan\varphi_0+\varphi_T-\varphi_0+\psi)-(\rho_1\theta_1+\rho_2\theta_2)-d_T\sin\varphi_T \\ \delta_{iv-r1} = \rho_2\left(\tan\varphi_0+\varphi_T^{r1}-\varphi_0+(\psi-\theta_1)\right)-(R_{ext1}-r_{o1})\sin(\varphi_T^{r1}-\lambda_1)-r_{o1}+d_T\sin\varphi_T^{r1} \\ \delta_{iv-r2} = \rho_1\left(\tan\varphi_0+\varphi_T^{r2}-\varphi_0+(\psi-\theta_2)\right)-(R_{ext2}-r_{o2})\sin(\varphi_T^{r2}-\lambda_2)-r_{o2}+d_T\sin\varphi_T^{r2} \end{cases} \quad (25)$$

$$\begin{cases} \delta_{iv-iv} = d_T+(\rho_1+\rho_2)(tan\,\varphi_0+\varphi_T-\varphi_0+\psi)-(\rho_1\theta_1+\rho_2\theta_2) \\ \delta_{iv-rext} = d_T\,sin\,\varphi_T^{r1}+\rho_2\left(\varphi_T^{r1}-tan\,\varphi_0-\varphi_0+(\psi-\theta_1)\right)+(R_{ext}-r_{o1})\,sin(\varphi_T^{r1}-\lambda_1)+r_{o1} \\ \delta_{iv-rint} = d_T\,sin\,\varphi_T^{r2}+\rho_1\left(tan\,\varphi_0+\varphi_T^{r2}-\varphi_0+(\psi-\theta_2)\right)-(R_{min}+r_{o2})\,sin(\varphi_T^{r2}-\lambda_2)+r_{o2} \end{cases} \quad (26)$$

In conclusion, for an error such as the commented as an example, an advance in the contact and the geometrical impact that this has, produces an imbalance that overloads the planet with the error and underloads the rest. The amount of overload in the planet with error splits in N-1 parts and gives the amount of load that every planet with no error is sparing. Consequently, the total of load is the same, but splitted in a non-equal manner.

This stands for any mesh phasing. The mesh phasing will affect the variation of the load in the planet, but the average load in that planet will always be over the rest.

Consequently, the opposite effect can be expected if the error is negative. Then, the load that will be spared by the planet with error will be distributed amongst the rest of planets. This stands due to the non-symmetrical geometry of the error for both torque directions.

5.3.2 Radial error

Hereinafter, the focus is placed on the effects of the radial error, which are expected to be different and less significant than for tangential errors, as

proved in previous works (M. Iglesias et al., 2017), but not negligible as stated in (Bodas & Kahraman, 2004; Ahmet Kahraman, 1999). At first, the advance or delay in the contact does not appear due to the presence of the error. Consequently, the imbalance derived of this effect does not exist under these new conditions.

Despite their differences, there are also some similarities in the effect of both components in the pinhole position error. Figure 63 illustrates the modification of the geometry induced by the radial error. This error modifies the mounting distance as well as the pressure angles, as it happens with the tangential error. However, these changes are not equal for external and internal contact, in contrast to what happens with the tangential error.

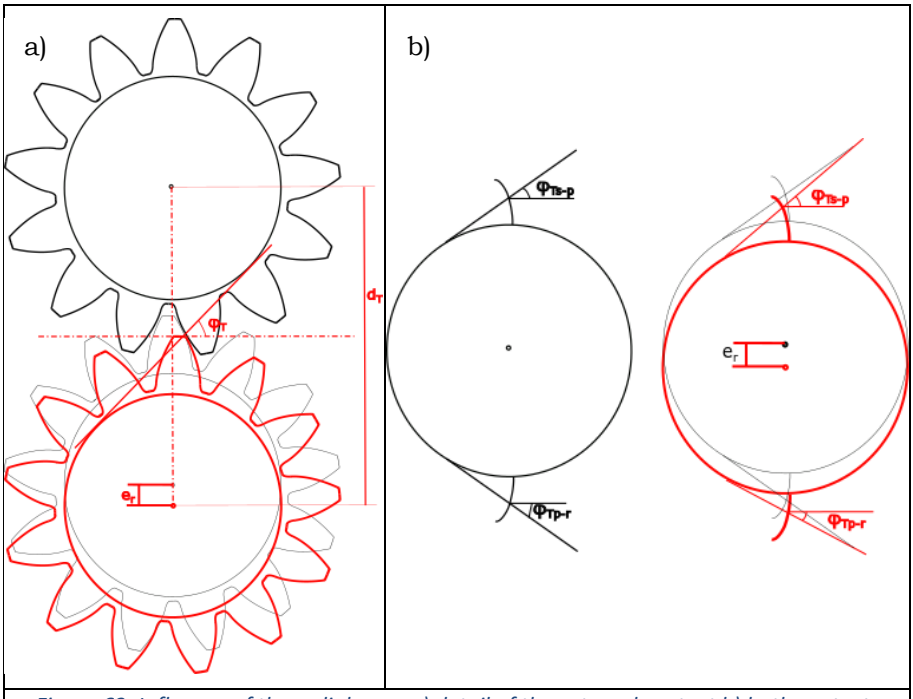

Figure 63. Influence of the radial error a) detail of the external contact b) both contacts

The unequal modification on the pressure angles, contrary to what happens in the tangential errors, will provoke an imbalance in the contact forces in the

planet. Even with this imbalance the equilibrium in moments in the planet stands, given the lack of friction, viscous forces or acceleration, but the vertical component of the contact forces will be different and due to it there will exists an imbalance and a force will appear in the gear support. As a reminder, at this point Figure 64 is included, which is identical to Figure 21; however, in this case the imbalance is generated by the radial error.

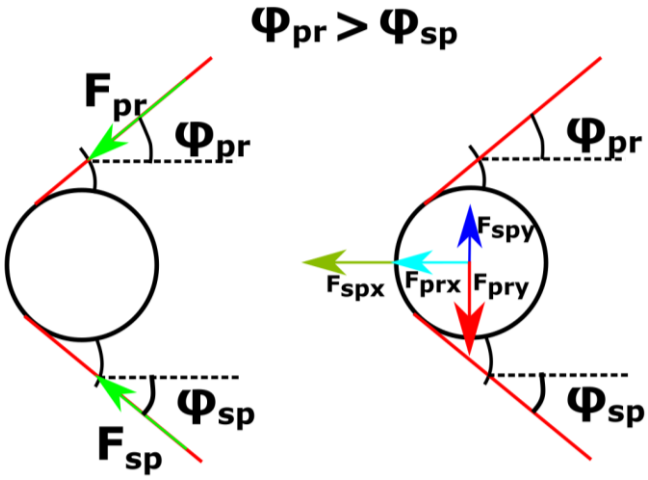

Figure 64. Contact forces and its imbalance due to the mounting distance.

In conditions of high stiffness in the gear support, this imbalance will continue in the carrier and expectedly will generate a deflection in it. This deflection will tend to open or close the carrier, depending on the sign of the radial error.

Observing the formulation for the contact together with the Figure 63, it is possible to induce the implications of the modification of the mounting distance and the pressure angle, but no advance or delay exist whatsoever in the contact. Therefore, this error modifies the geometry of the contact and moves the contact point along the meshing line, but every planet contacts at the same time. This shift along the meshing line of the contact point will modify slightly the meshing stiffness in that contact. Consequently, the effect of this error is less crucial than the tangential, in load sharing terms. Hence, there could exists a higher tolerance for this error. Apart from that, the effect

of this error is independent to the torque direction in contrast to what happens with the tangential component of the pinhole position error.

5.3.3 Tooth thickness errors

As mentioned in the modelling of this error, there is a big difference between considering the error symmetrical or not. In this section, only the symmetrical scenario is going to be studied.

The tooth thickness error is analogous to a tangential pinhole position error up to a point. This error will generate an advance or delay in the contact, but will not modify neither the mounting distance nor the pressure angle.

As it happens in the case of the tangential error, this advance or delay generates a modification in the number of pairs of teeth in contact and consequently, in the meshing stiffness that translates in an imbalance in the load sharing. According to the previously stated, under some conditions it is possible that opposed tangential and tooth thickness errors have opposite effects and sometimes neutralize each other.

If the tooth thickness error is considered symmetrical in both flanks of the tooth, then, the effect will not change with the torque direction. However, its effect is likely to change with the change in the number of planets.

5.4. Considered configurations

The configurations considered cover the scope of the common configurations in industrial applications, except for diametrically opposed configurations. As a result, not only are the errors are considered but also different mesh phasings are considered for equally spaced transmissions. In addition, the number of planets is modified considering three and five planet configurations. Furthermore, a couple of load levels are tested.

In more detail, equally spaced configurations both in-phase and sequentially phased are simulated. Furthermore, three possible errors are considered and

the combination of them. Likewise, two levels of load are considered. Overall, the relevant information for the performed simulations is gathered in Table 6.

Table 6. Considerations for studied cases.

Number of planets: 3 and 5 Mesh phasing: ESIP and ESSP				
Case	e_t(μm)	e_t(μm)	e_t(μm)	Torque direction
1	2.5	0	0	CW & CCW
2	0	20	0	CW & CCW
3	0	0	2.5	CW & CCW
4	2.5	20	0	CW & CCW
5	2.5	0	2.5	CW & CCW
6	2.5	20	2.5	CW & CCW
Input torque (Nm): 1200 and 3600				

In conclusion, all the details considered and the combinations of them, lead to as many as 96 cases of study that will provide an accurate enough image of the influence that these errors have on the performance of planetary transmissions under different mesh phasing conditions.

Besides, it is important to observe the change in the performance on the transmission with its stiffness; in this case, this stiffness is modified by changing the dimensions of the shaft mounting in the wheels. Thus, for all the considered cases, mentioned above, there will be two different configurations with different shaft mounting dimensions. The characteristics of these two are gathered in Table 7.

Table 7. Dimensions of the shaft mountings in the considered configurations

Configuration	Spacing & phasing	Sun	Planets	Ring*
1	ESIP	40	20	1.3·rint
	ESSP	40	20	1.3·rint
2	ESIP	143	80	1.2·R
	ESSP	145	82	1.2·R

*For the ring gear this dimension refers to its outer radius.

The change in the definition of the shaft mounting in the configuration 2 corresponds to the guidance made in (ISO 6336-1, 2006) regarding the back-up ratio in the external gears. On the contrary, configuration 1 corresponds to the geometry of the wheels for a project developed previously. It can be expected that in view of this geometry, the wheels in configuration 2 and the boundary conditions considered in the FE models, the entire transmission will be more rigid and sensitive to the errors (Bodas & Kahraman, 2004).

5.5. Results

From this point, the mentioned errors are included consecutively to obtain the sheer effect of each error. In these cases, floatability is not included in any of the supports.

5.5.1 Crucial values of the LSR: Configurations 1 & 2

The values that are considered crucial to define the impact of the errors in the transmission performance are the maximum and minimum reached along the simulation by the Load Sharing Ratio. These show the imbalances generated by any of the errors in the transmission and quantify how significant is the size of the error in relation with the imbalance generated. Hereinafter, these

results are presented for the gearboxes named configuration 1 & 2 previously in this document.

For starters, in Figure 65 & Figure 66 the results for configuration 1 & 2 under a 1200 Nm input torque are gathered for the 6 cases of study. At first, it is visible that the effect of the tangential error (Case 1) is significantly higher than the radial one (Case 2). This can be stated given the fact that the size of radial error is even higher, therefore, leaving no doubt to the difference in influence between both errors. However, as expected and mentioned before, the influence of the radial error is not negligible. Even though its influence is small, it has to be taken into consideration.

Then, for a tooth thickness error as big as the tangential, the influence is almost the same. To get more accuracy in these comparisons, in ANNEX I the numerical data of the values are gathered for every case. Comparing cases 1 and 3, one can see the same effect both for the tangential and tooth thickness error, also having the same size. This stands at least for a three-planet configuration where the size of the tangential error is small and does not produce a notable modification in the mounting distance and pressure angle.

For the last three cases, the joint action of different errors augments the imbalances. The torque direction makes errors to sum their effects and together produce a bigger imbalance. However, the result of the imbalance in the LSR is not the analytic summation of both effects. This proves that the joint action of different errors can be beneficial or detrimental depending on the circumstances.

Given the geometrical definition of the errors considered, the change in the direction of the torque affects them differently. On the one hand, the tangential error approximately has the same effect in both cases, just changes the sign in the imbalance that produces. On the other hand, the tooth thickness error is not influenced by the torque direction; a thicker tooth is more loaded than a slimmer one under any torque direction. Likewise, radial error effects stay unchanged by the turn in the torque direction.

It is relevant to highlight the behaviour in case 5, where the effect of both tangential and tooth thickness errors null each other, giving a result of no imbalance in the LSR. Given the geometry of the transmission, this occurs due to the small size of the tangential error that generates insignificant changes in the mounting distance and the angle pressure. Given that, the influence of both errors is exactly the same, but with opposite signs, as a result, the imbalance is null.

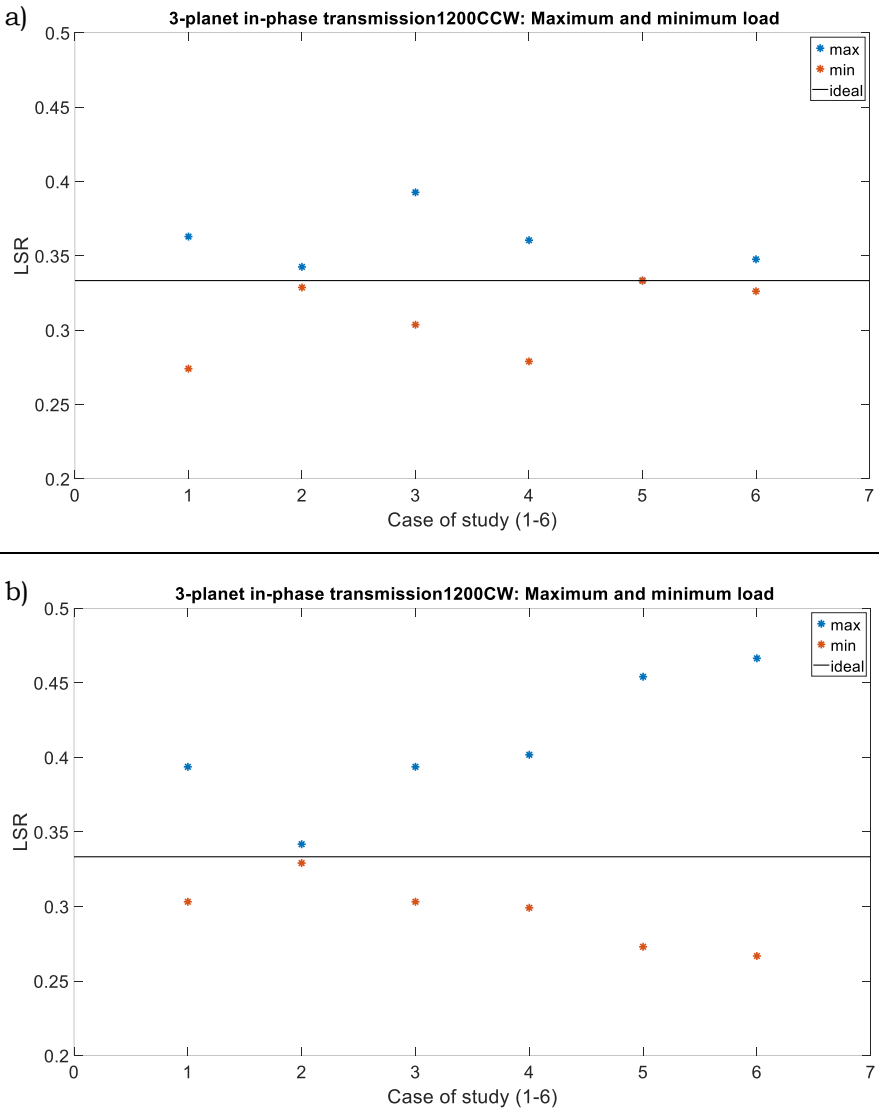

Figure 65. Max. and min. in the LSR for three-planet ESIP a) 1200 Nm CCW b) 1200 Nm CW (Conf. 1)

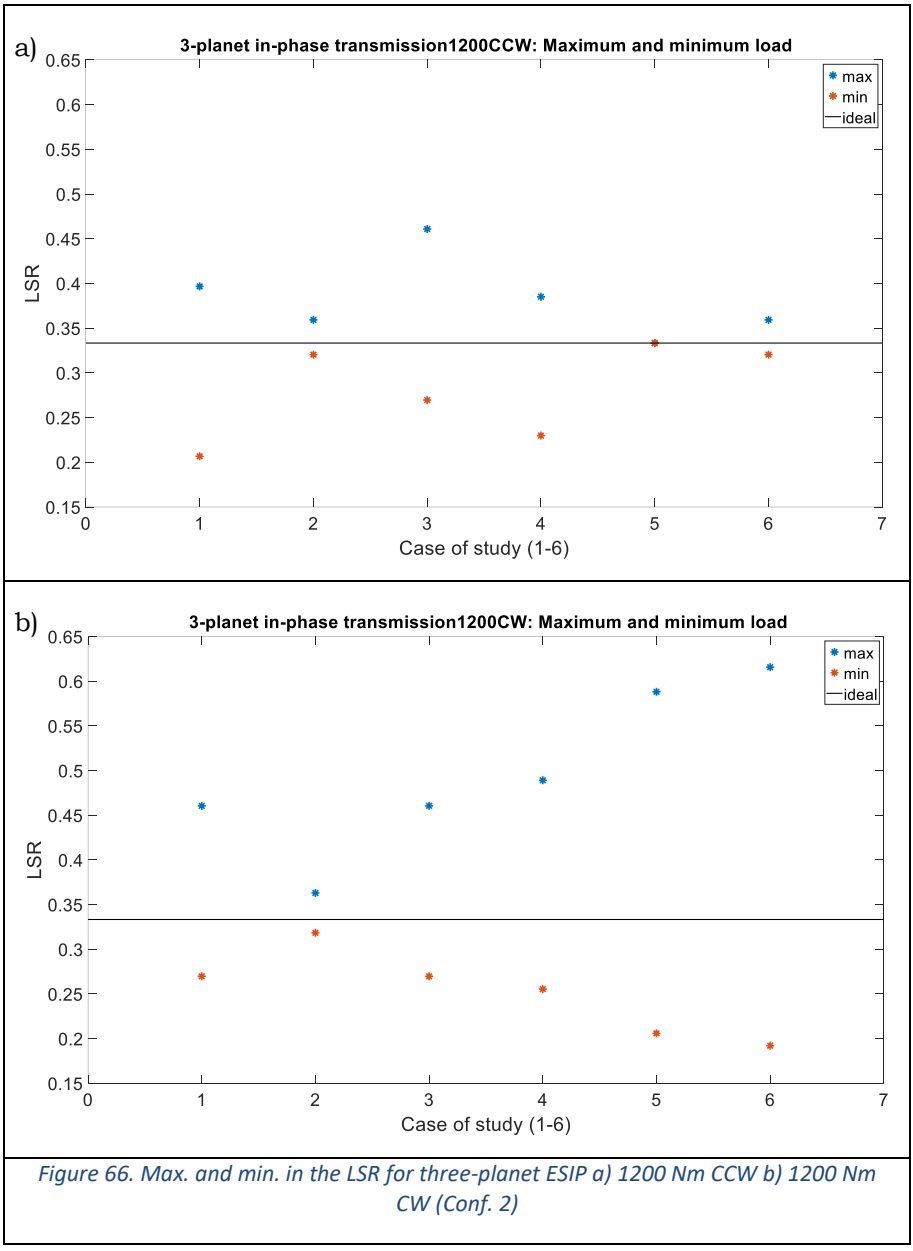

Figure 66. Max. and min. in the LSR for three-planet ESIP a) 1200 Nm CCW b) 1200 Nm CW (Conf. 2)

As seen in the results, these are almost identical for the two configurations except for the fact of the magnitude of the imbalance generated by the error, which, as expected, is bigger in the configuration 2 due to its higher stiffness.

In Figure 67 & Figure 68, the results belong to the same scenarios as before but under a 3600 Nm input torque. At first sight, something that stands out is the fact that the imbalances due to the same errors in the transmission under a higher load are smaller. In case 2, it is visible how for high level of loads the influence of the radial error is close to null, whereas for a lower load this did not happen. Furthermore, the analogy in the effects of the tangential and tooth thickness error stays under higher load, this is due to the fact that the tooth thickness error is not big enough to significantly change the teeth stiffness.

Once both the higher load and the CW direction for the torque act together, the imbalances in the transmission are significantly smaller than in any of the previously studied scenarios. It even reaches levels close to zero in three of the cases (2, 5 & 6) as seen in Figure 67a & Figure 68a.

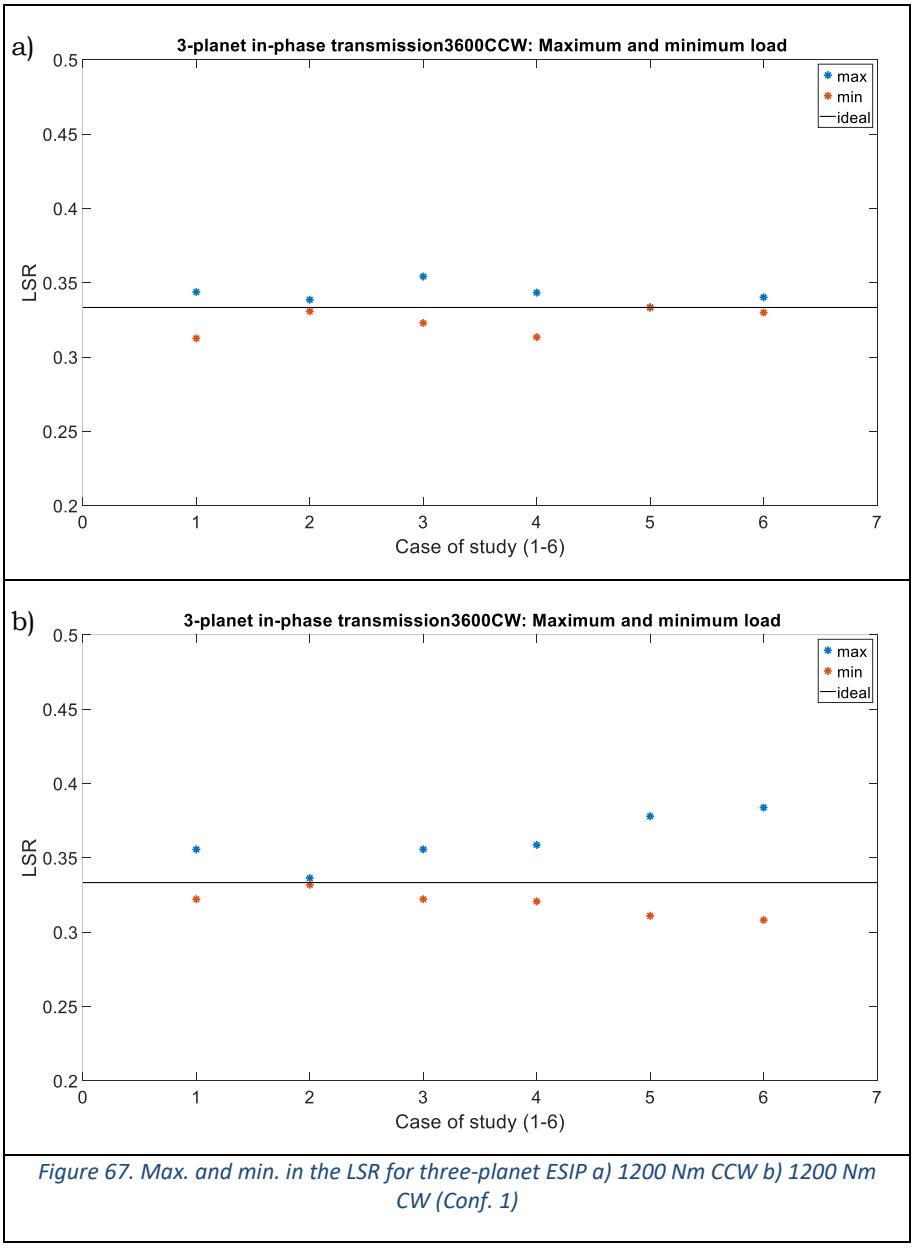

Figure 67. Max. and min. in the LSR for three-planet ESIP a) 1200 Nm CCW b) 1200 Nm CW (Conf. 1)

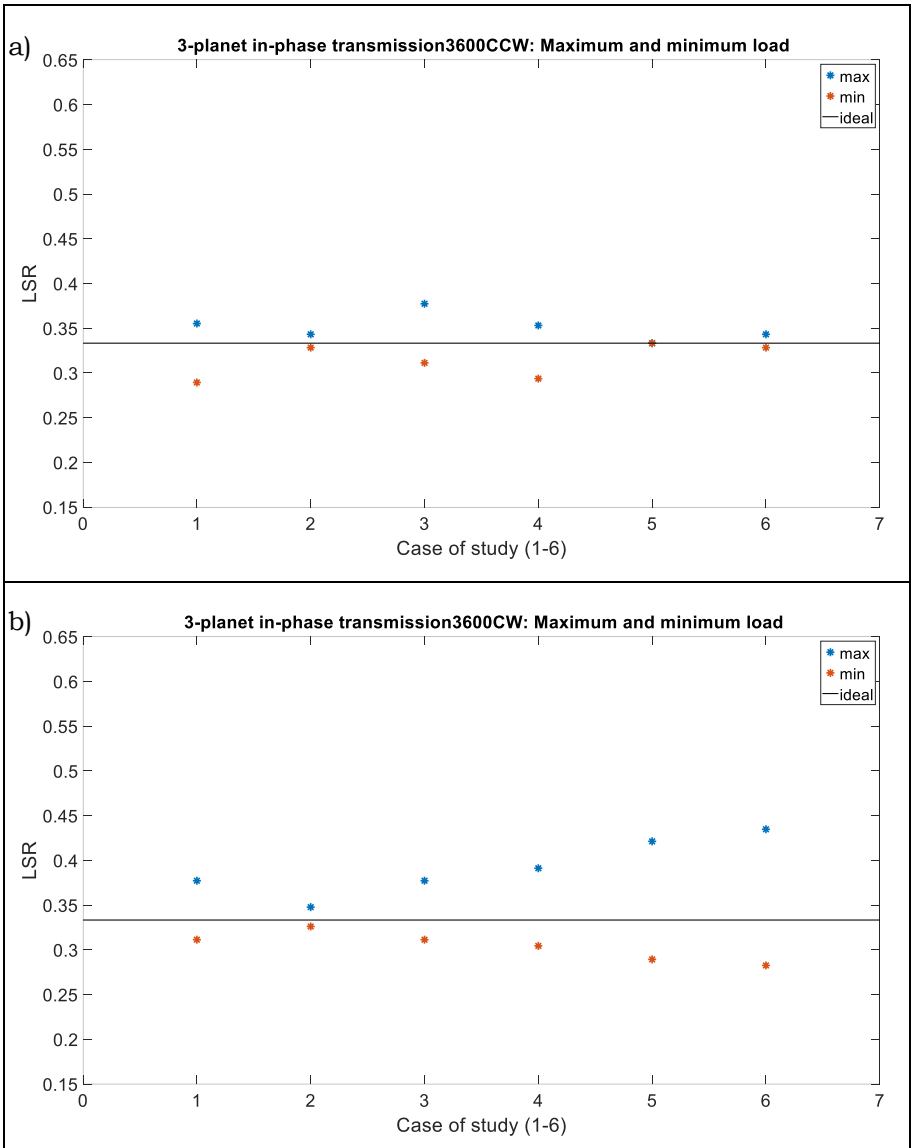

Figure 68. Max. and min. in the LSR for three-planet ESIP a) 3600 Nm CCW b) 3600 Nm CW (Conf. 2)

From this point on, the results refer to the transmission with sequential phasing. At first, in Figure 69 & Figure 70, it is visible the increment in both the maximum and minimum values due to the sequence in the mesh phasing. Furthermore, it is relevant to address the fact that the radial error impact increases significantly under in this new configuration. This proves what was stated previously that the radial error effect is not negligible. In addition, it is necessary to acknowledge the fact that the maximum and minimum values are not directly related, opposite to what happened with the in-phase results. Sequential mesh phasing includes delay amongst teeth meshings and maximum and minimum values are asynchronous. Therefore, the summation of the maximum and the N-1 minimum values is not equal to the total input load.

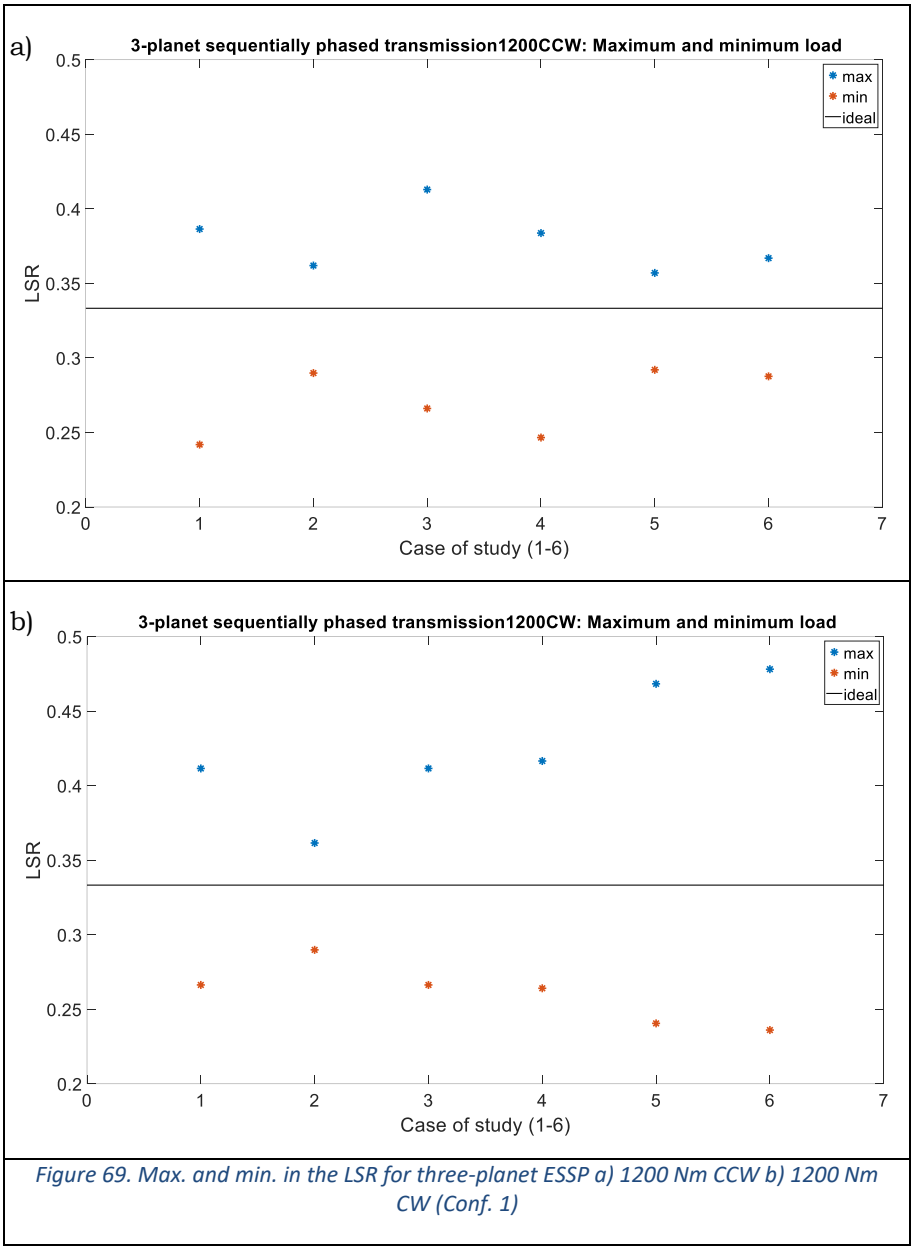

Figure 69. Max. and min. in the LSR for three-planet ESSP a) 1200 Nm CCW b) 1200 Nm CW (Conf. 1)

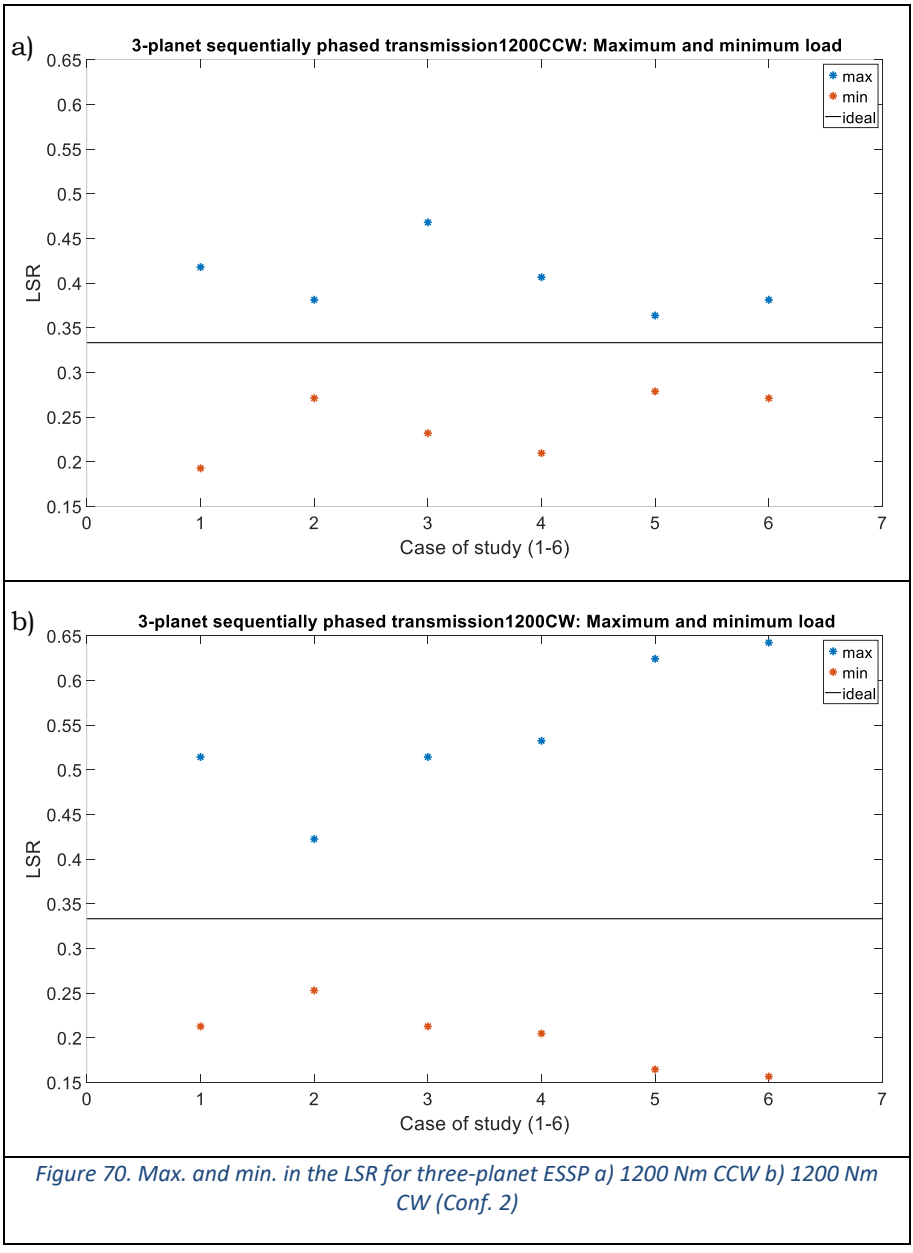

Figure 70. Max. and min. in the LSR for three-planet ESSP a) 1200 Nm CCW b) 1200 Nm CW (Conf. 2)

Despite the raise in the working load, in Figure 71 & Figure 72 the increase in the imbalances stays due to the effect of the sequential phasing. However,

there exists still a reduction due to the higher working load. As it can be seen for case 4.

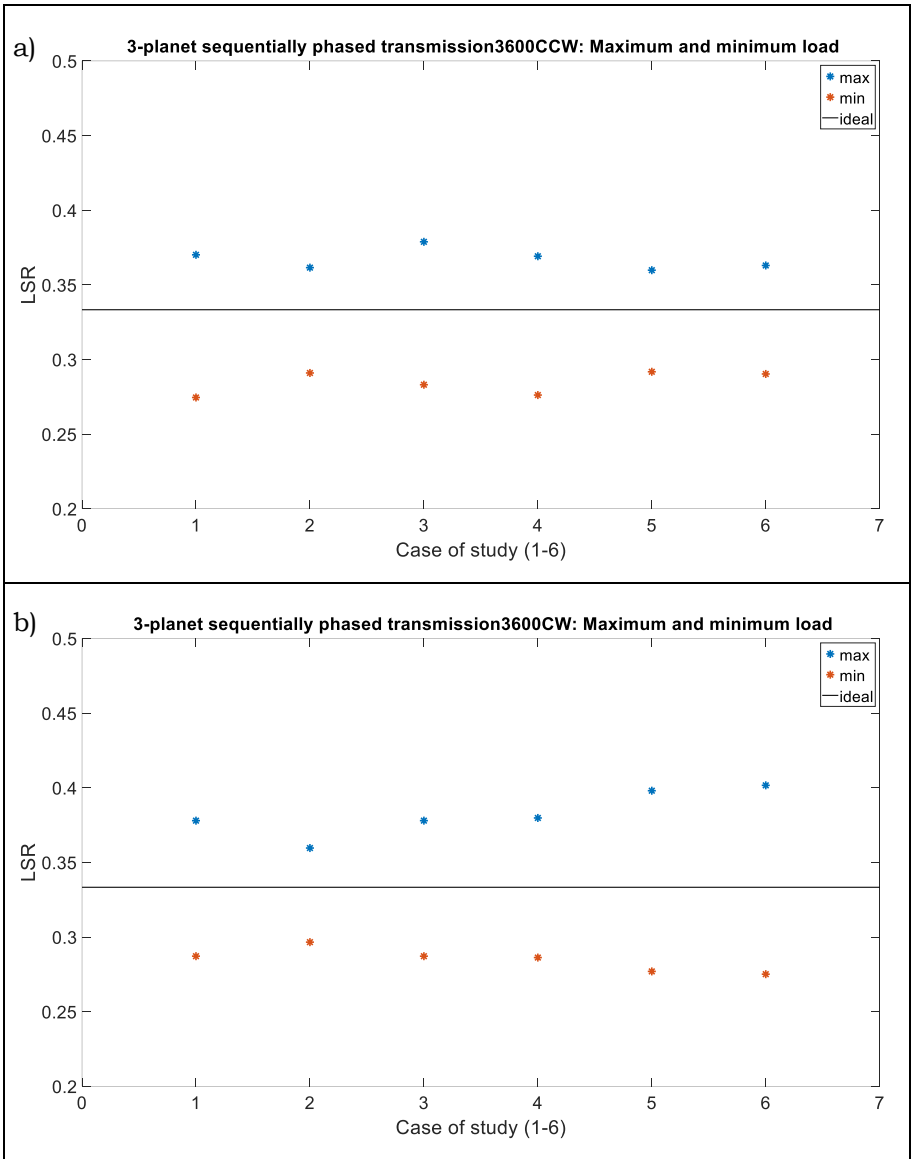

Figure 71. Max. and min. in the LSR for five-planet ESIP a) 3600Nm CCW b) 3600Nm CW (Conf. 1)

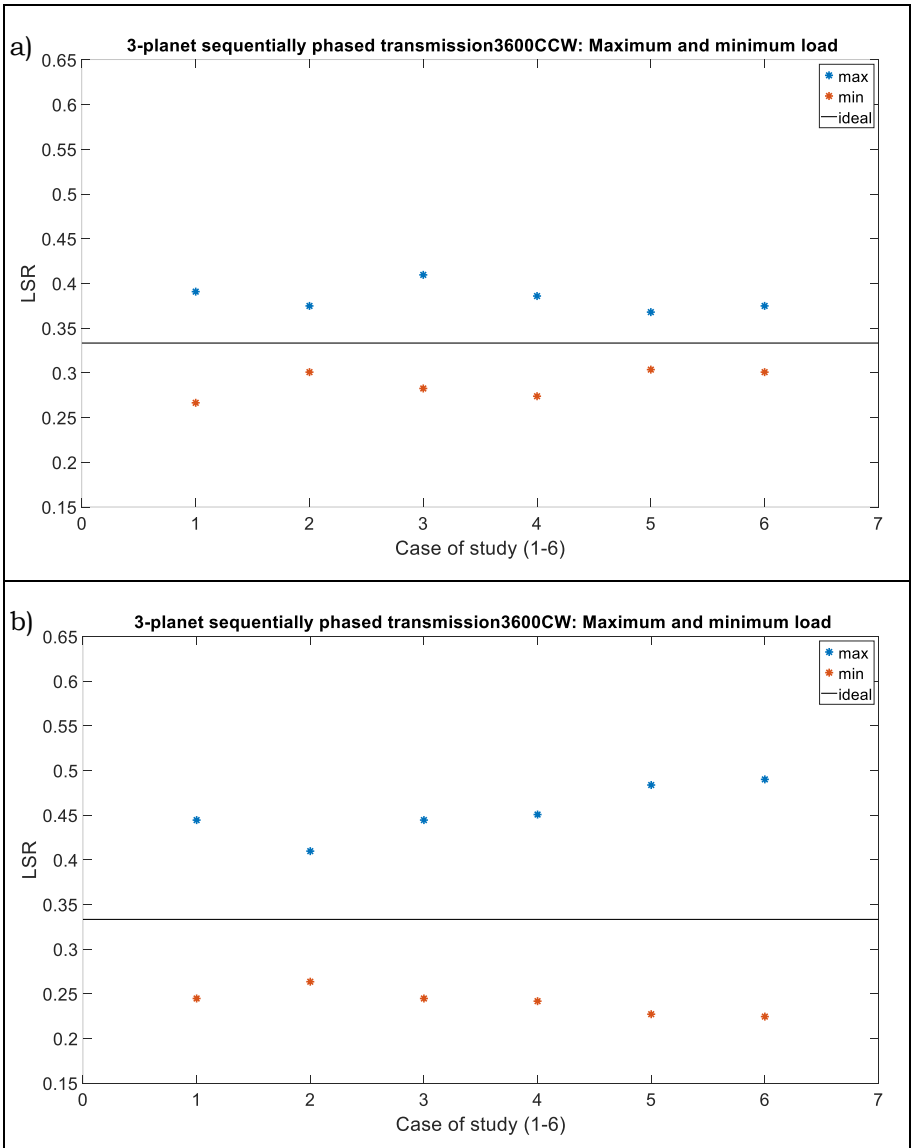

Figure 72. Max. and min. in the LSR for three-planet ESIP a) 3600Nm CCW b) 3600Nm CW (Conf. 2)

The increment in the number of planets augments the sensitivity of the transmission to the presence of errors, as shown in (Bodas & Kahraman, 2004). On these grounds, the inclusion of the same error on a transmission with 5 planets instead of 3 will lead to bigger imbalances in relative terms.

In this new 5-planet planetary transmission, the scenarios simulated are the same as for the 3-planet configuration. For starters, in Figure 73 & Figure 74 the results for a configuration as commented under 1200Nm load are gathered. Something that stands out is the increase in the impact of the radial error, just by increasing the number of planets. For this configuration, what was stated previously about the relevance of the radial error becomes even more a reality.

Apart from the radial error (Case 2) it is significant the decrease on the impact of the tooth thickness error (Case 3), even more in comparison to the tangential error (Case 1). For a 3-planet configuration, these errors had similar impacts, this does not continue for 5-planet transmissions. Because of this, the summation of the tangential and tooth thickness errors (Case 5) does not provide a null effect for any of the load directions. Finally, for in-phase scenarios the imbalances observed in Figure 73 & Figure 74 are significantly higher than the ones in the in-phase transmission with 3 planets. This confirms what was expected beforehand. The parallelism between the configurations is also visible and having just the change in the size of the imbalance as stated before for the 3-planet transmissions.

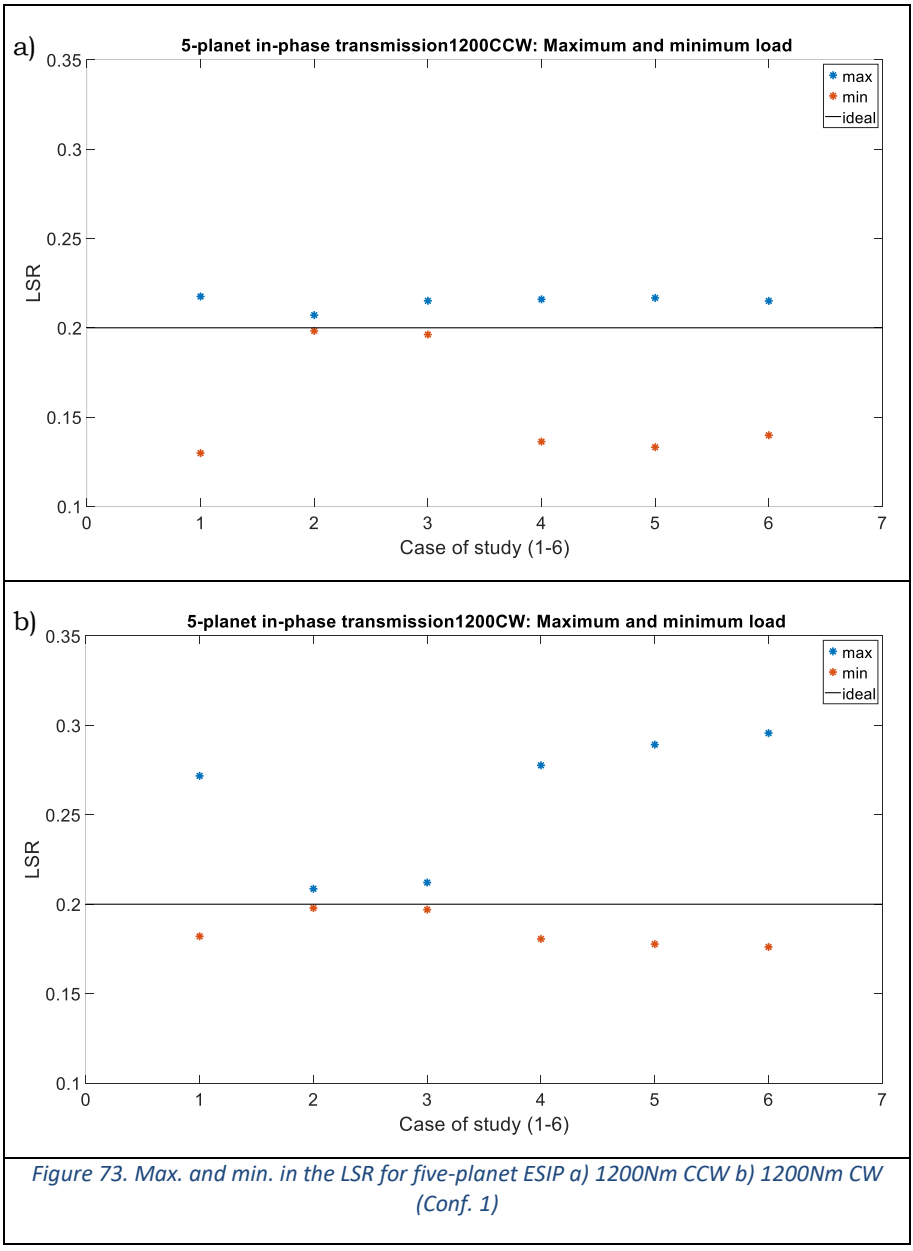

Figure 73. Max. and min. in the LSR for five-planet ESIP a) 1200Nm CCW b) 1200Nm CW (Conf. 1)

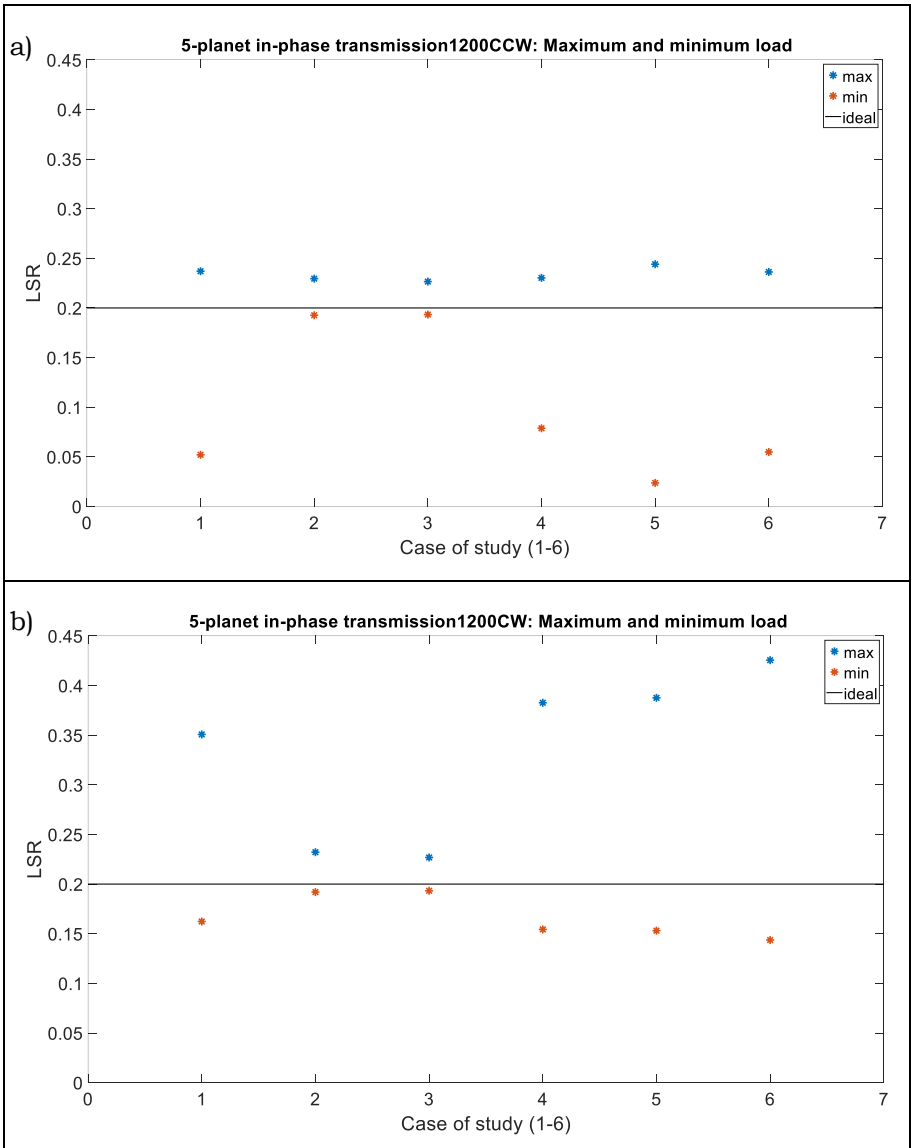

Figure 74. Max. and min. in the LSR for five-planet ESIP a) 1200Nm CCW b) 1200Nm CW (Conf. 2)

In the following, the load is increased to 3600 Nm. Thus, as seen in Figure 75 & Figure 76 the expected decrease in the imbalances appears as it happened in the analogous 3-plant configuration. For the cases that were highlighted in the scenarios under 1200 Nm, the decrease in the imbalances due to the higher load is notable. Furthermore, under this load the impact of the radial error and the tooth thickness error become almost identical. With this reduction in the impact of every other kind of error, the influence of the tangential error dominates the behaviour of the transmissions and their load sharing.

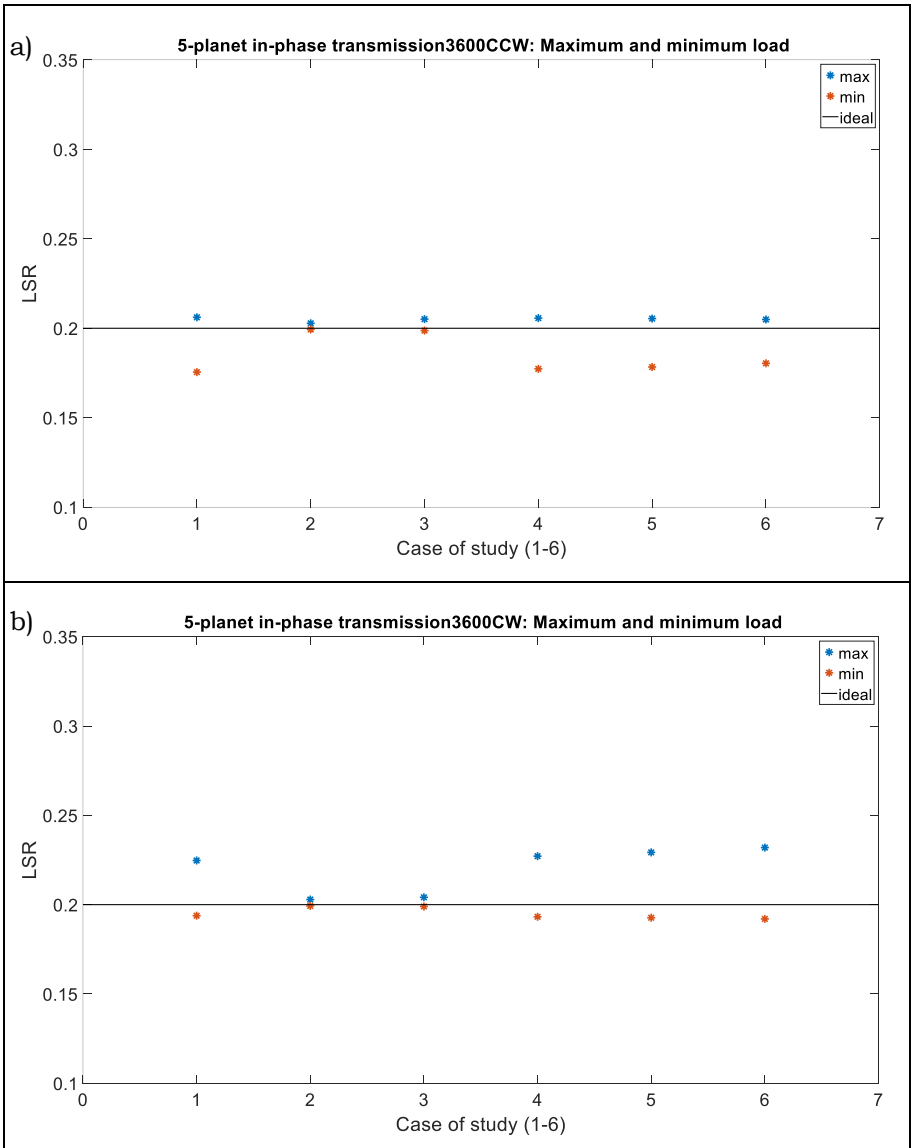

Figure 75. Max. and min. in the LSR for five-planet ESIP a) 3600Nm CCW b) 3600Nm CW (Conf. 1)

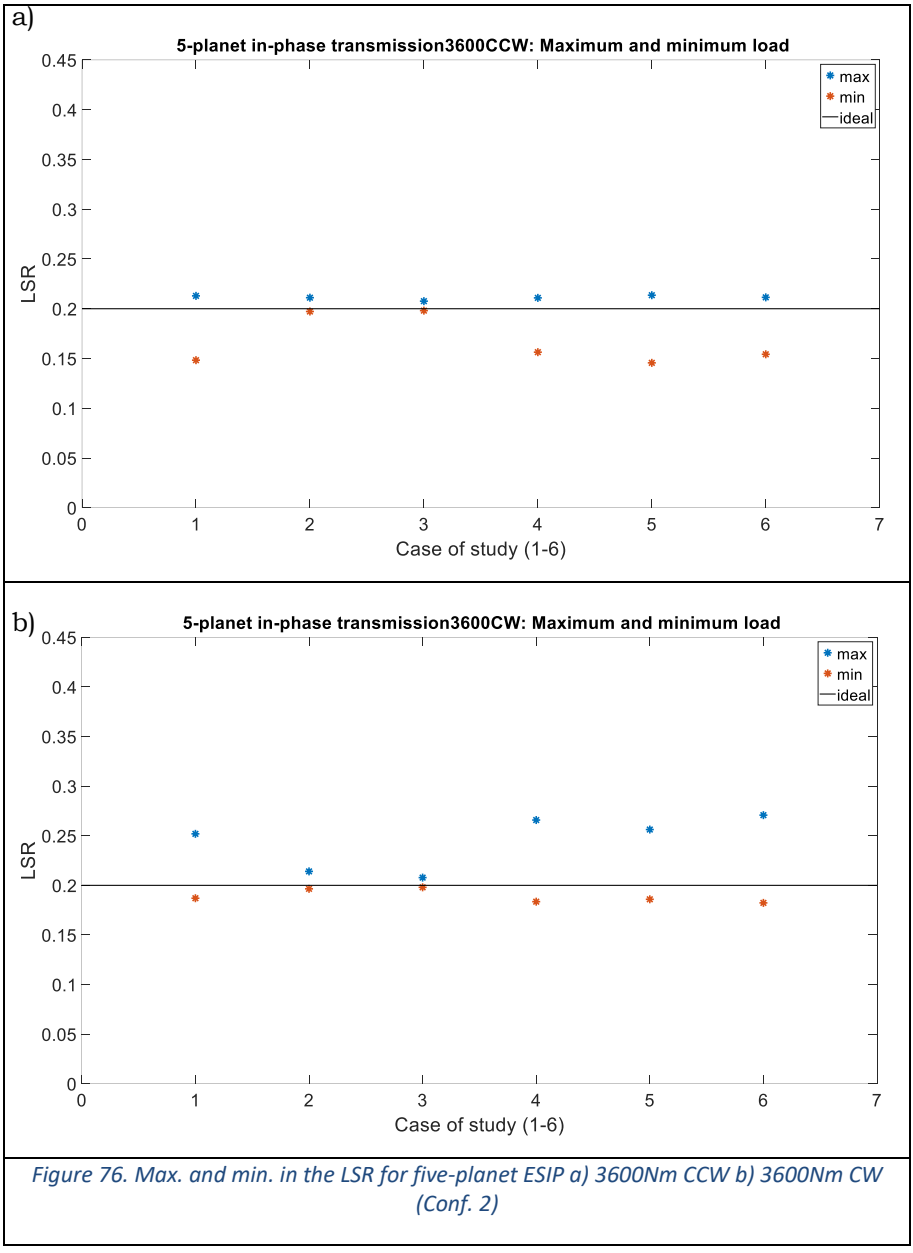

Figure 76. Max. and min. in the LSR for five-planet ESIP a) 3600Nm CCW b) 3600Nm CW (Conf. 2)

Finally, last but not least, the 5-planet transmissions with sequential phasing. In these last simulations, the joint effect of the sequential phasing and the increment of the planets will expectedly lead to a notable increase in the imbalances. Firstly, in Figure 77 & Figure 78 it is visible that the similitude between the radial and the tooth thickness errors continues. Due to the sequential phasing, their impact grows, but it does equally for both. Although their influence is higher, the impact of the tangential error continues to be significantly higher. Consequently, in the last three, where the tangential error joints with others, the imbalance is similar to the one in the Case 1, where there is just tangential error.

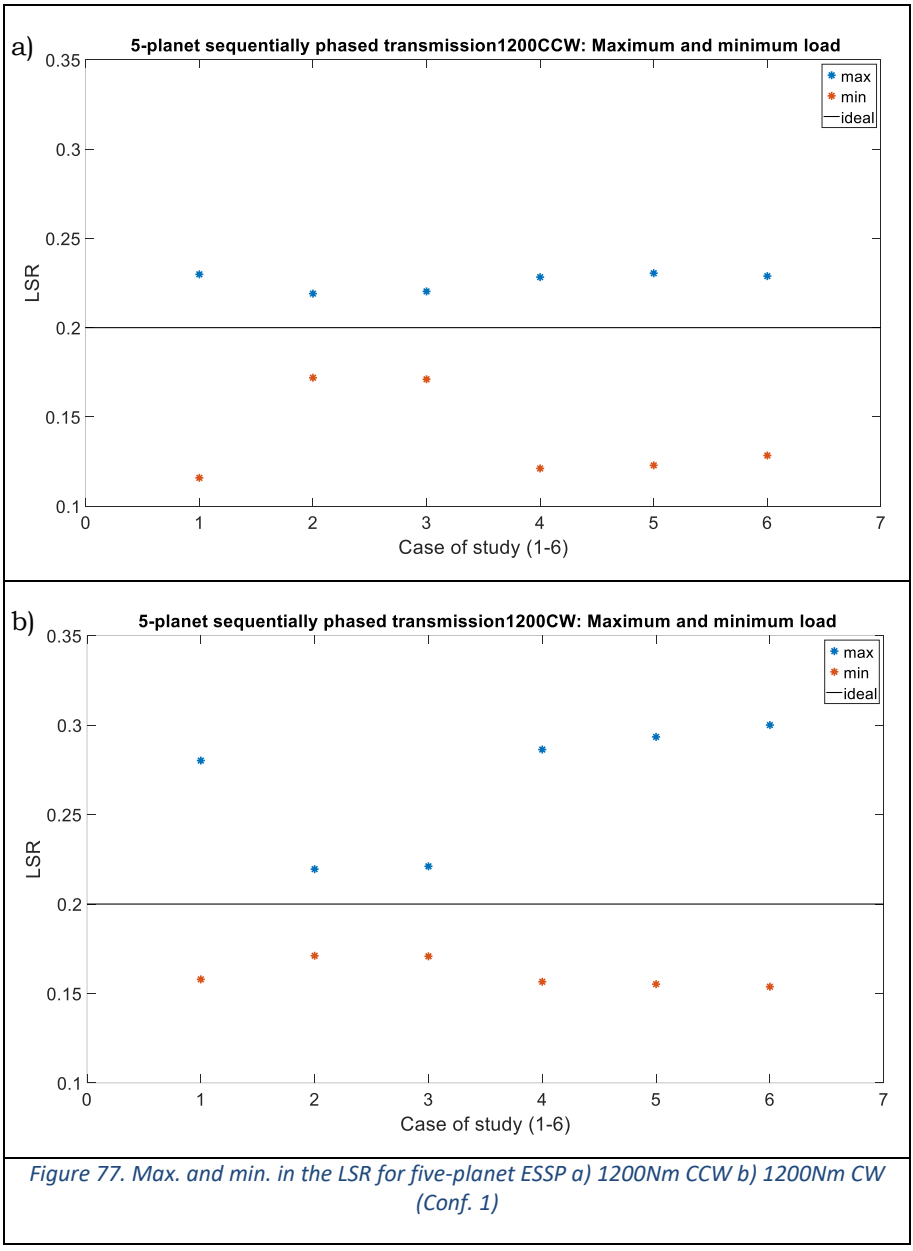

Figure 77. Max. and min. in the LSR for five-planet ESSP a) 1200Nm CCW b) 1200Nm CW (Conf. 1)

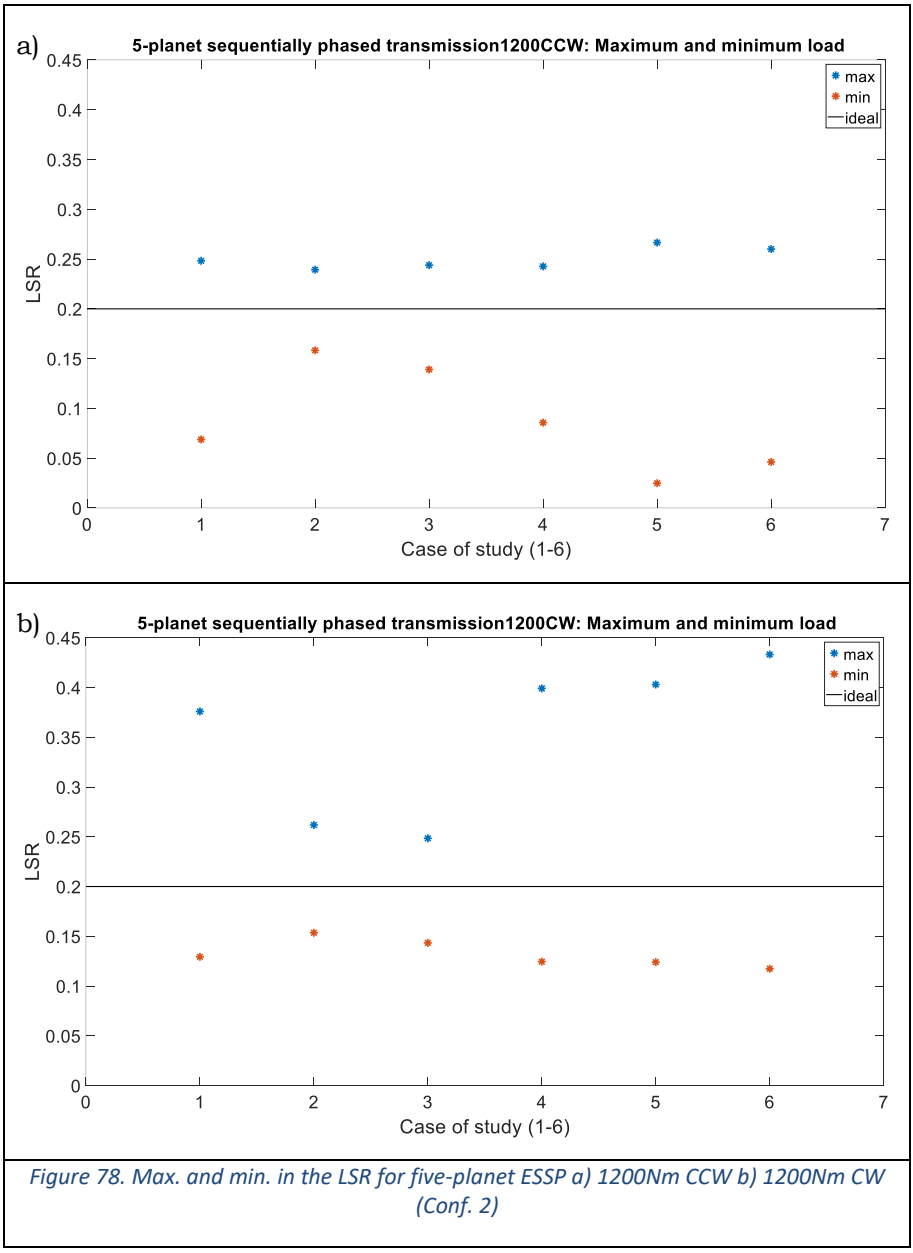

Figure 78. Max. and min. in the LSR for five-planet ESSP a) 1200Nm CCW b) 1200Nm CW (Conf. 2)

Finally, whenever the load level is increased, as seen in Figure 79 & Figure 80, the impact of the errors lowers. The decrease in the Case 1 should be highlighted, given the fact that it is notably higher than for Cases 2 & 3. This

proves the importance of the geometry of the errors in the impact they have on the transmission and its load sharing.

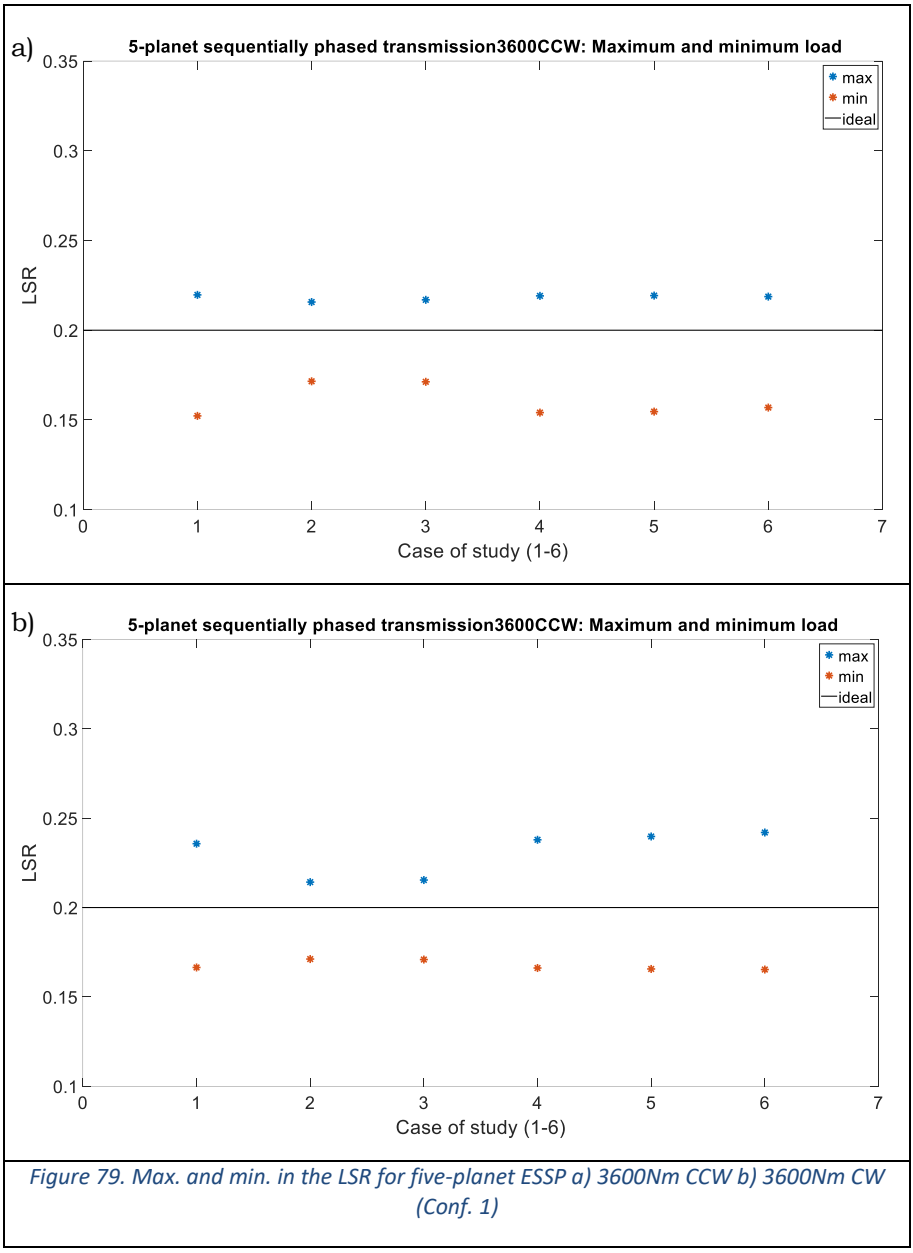

Figure 79. Max. and min. in the LSR for five-planet ESSP a) 3600Nm CCW b) 3600Nm CW (Conf. 1)

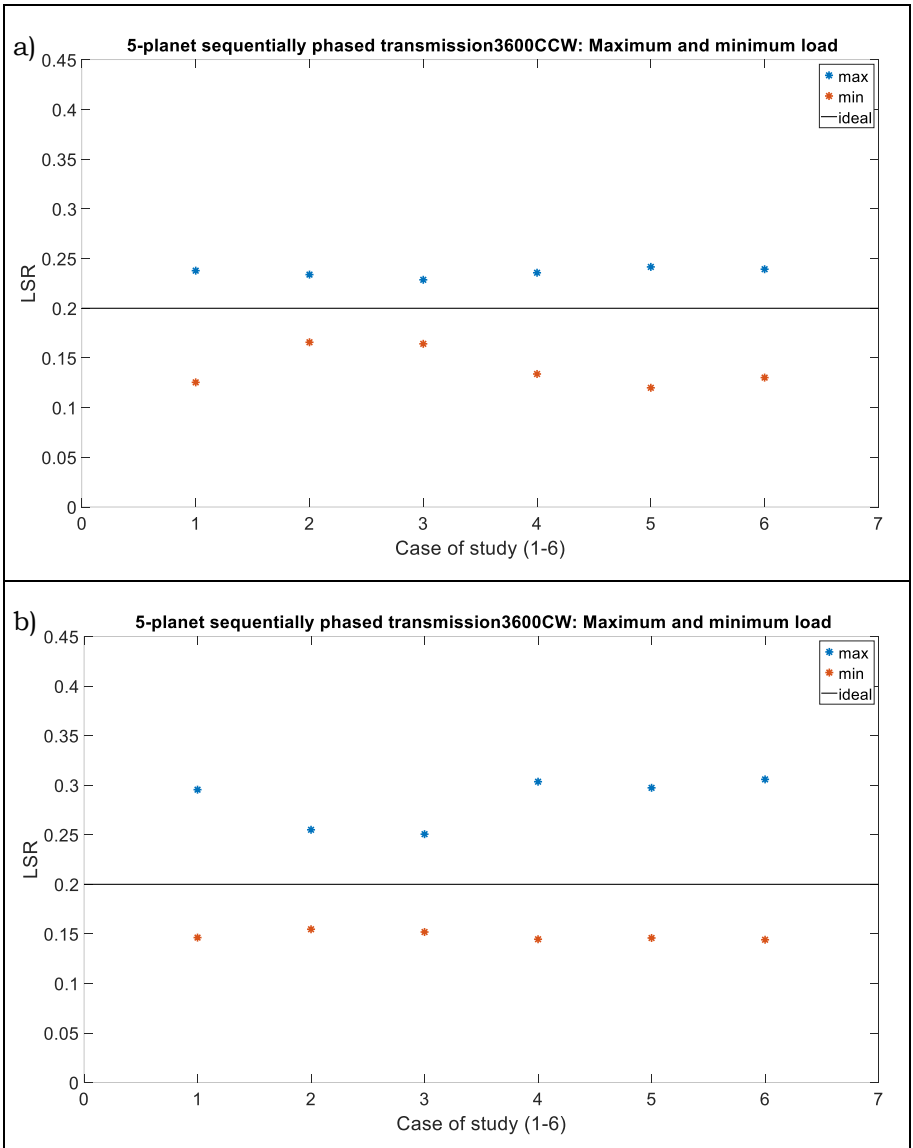

Figure 80. Max. and min. in the LSR for five-planet ESSP a) 3600Nm CCW b) 3600Nm CW (Conf. 2)

5.5.2 Imbalance created in the LSR: Configuration 1

After all the cases presented, it is even more interesting to present the imbalances generated in relative terms to the ideal load level. However, given the similarities in the functioning of both configurations, this analysis is going to be performed only for the configuration 1 in look for conciseness.

By using this procedure, the results for transmissions with different number of planets can be compared at the same level. To such comparison the magnitude ΔLSR. This magnitude is analytically expressed in (27).

$$\Delta LSR = \frac{\left(LSR_i - \left(\frac{1}{N}\right)\right)}{1/N} \qquad (27)$$

By this comparison, it is possible to observe the imbalances generated in each transmission by the maximum/minimum load values.

In Figure 81, the maximum and minimum values for the ΔLSR in the ESIP configurations are presented. Firstly, the decrease in the imbalances with the raise in the load is notable for any case and it can reach up to 40% for some of the considered scenarios. Normally, the imbalances in a 3-planet configuration are lower than in a 5-planet one, except for the tooth thickness error where the results prove the opposite behaviour. Furthermore, the increase of the number of planets raises the imbalances in the maximum values, compared to the analogous 3-planet transmission, but decreases or maintains the minimum values for CCW load. This translates on an increment of the overload, but a maintenance of the underloads. This is due to the decrease in the ideal load level as the number of planets augments.

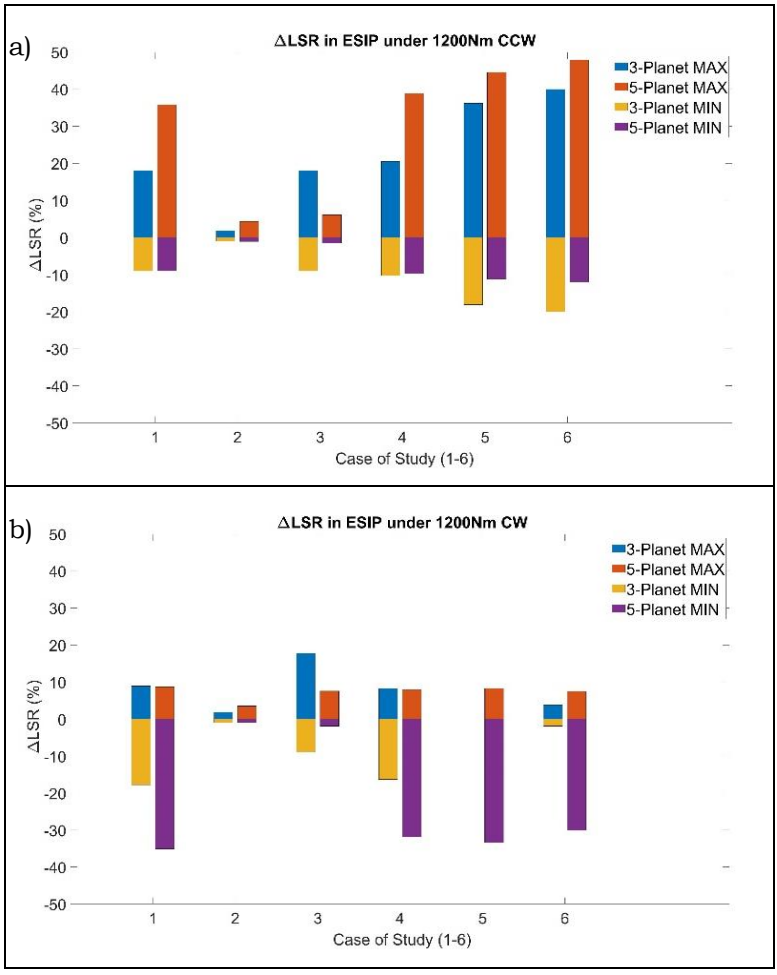
a)
ΔLSR in ESIP under 1200Nm CCW
3-Planet MAX
5-Planet MAX
3-Planet MIN
5-Planet MIN
ΔLSR (%)
Case of Study (1-6)
b)
ΔLSR in ESIP under 1200Nm CW
3-Planet MAX
5-Planet MAX
3-Planet MIN
5-Planet MIN
ΔLSR (%)
Case of Study (1-6)

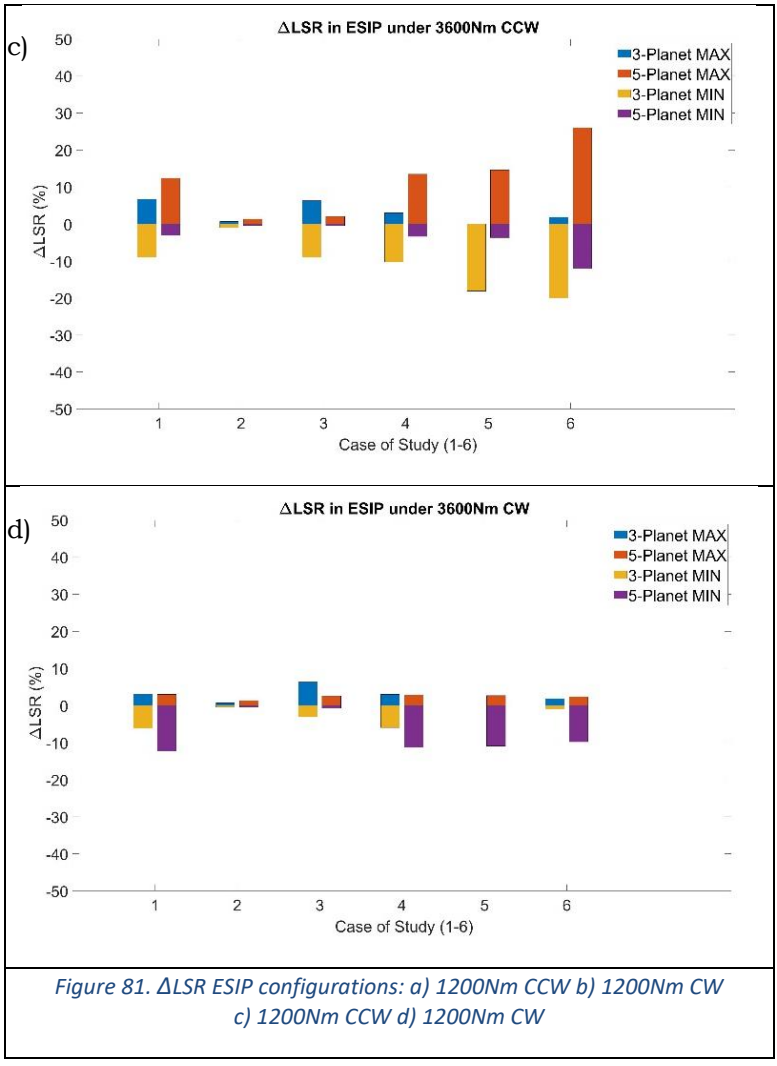

Figure 81. ΔLSR ESIP configurations: a) 1200Nm CCW b) 1200Nm CW c) 1200Nm CCW d) 1200Nm CW

For ESSP configurations, there are many similarities in the results with the previous, as seen in Figure 82. For every error but the tooth thickness error, the imbalance in the maximum value is bigger for the configurations with 5 planets. For the scenarios where the load is CCW, there exists an increment of the imbalance in the minimum values due to the sequential phasing, even though the imbalance in the maximum value stays similar to the one in ESIP transmissions.

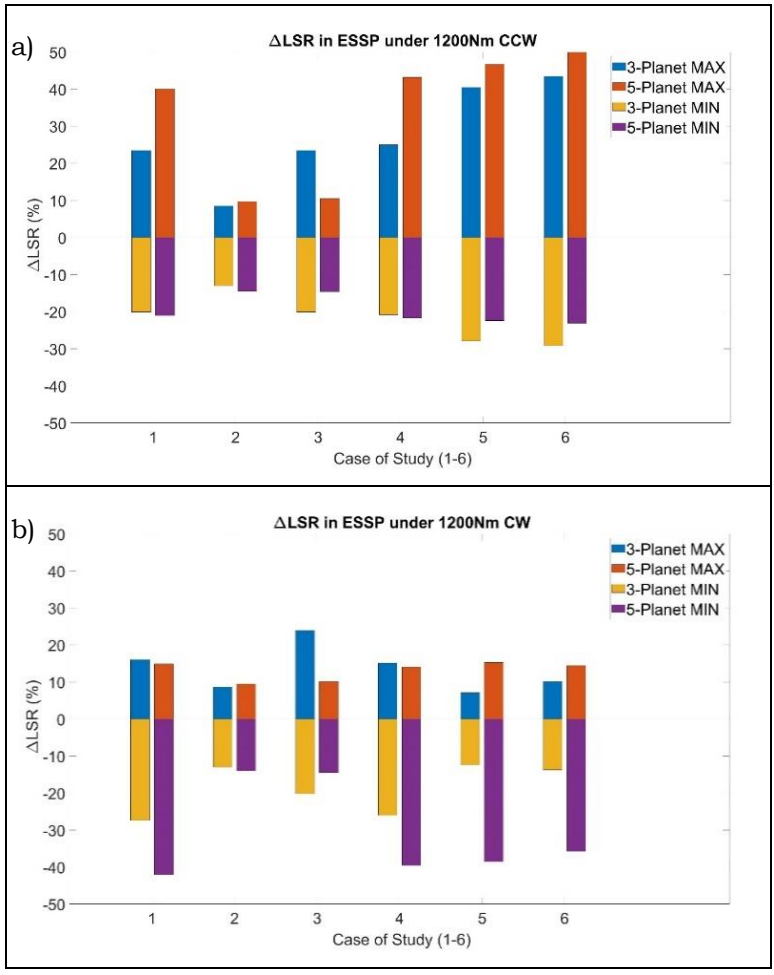
a)
ΔLSR in ESSP under 1200Nm CCW
3-Planet MAX
5-Planet MAX
3-Planet MIN
5-Planet MIN
ΔLSR (%)
50
40
30
20
10
0
-10
-20
-30
-40
-50
1
2
3
4
5
6
Case of Study (1-6)
b)
ΔLSR in ESSP under 1200Nm CW
3-Planet MAX
5-Planet MAX
3-Planet MIN
5-Planet MIN
ΔLSR (%)
50
40
30
20
10
0
-10
-20
-30
-40
-50
1
2
3
4
5
6
Case of Study (1-6)

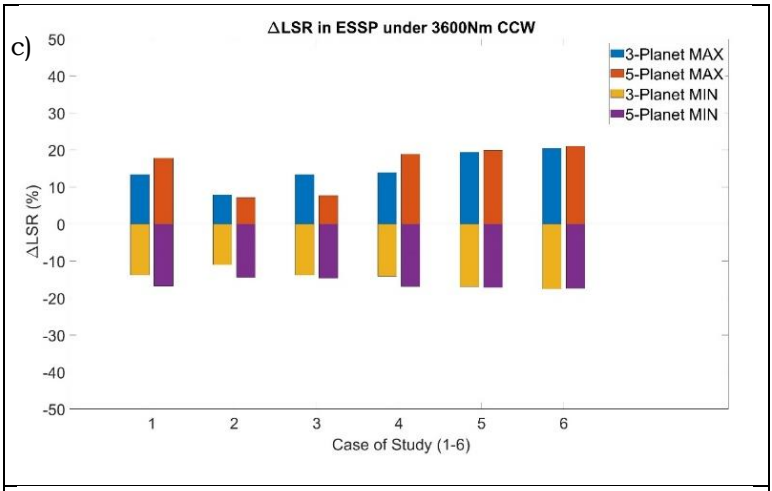

Figure 82. ΔLSR ESSP configurations: a) 1200Nm CCW b) 1200Nm CW c) 1200Nm CCW d) 1200Nm CW

For every case, as stated before, the imbalance created by the radial error is neither negligible nor small. Actually, it reaches levels close to the ones generated by the tooth thickness error. The existence of uniformity in the results obtained in Figure 82 d is quite significant, showing how the working conditions can equalize the impact of various errors with different sizes. Finally, the increment in the load decreases the impact of the errors, but the

sequential phasing makes this decrease less significant than in the ESIP configurations.

Chapter 6: Load sharing calculation by measuring root strains

6.1. Introduction

Gear transmissions are a recurrent solution in different ambits of life. These transmissions provide a wide variety of advantages that makes them the most appropriate solution for various applications.

The research and industry fields in gears have experienced a still ongoing development in the virtual world. Therefore, as years passed by, more and more models to recreate planetary gear transmissions have been presented, as presented in section 2.3. Despite its reduced cost and outstanding development, virtual modelling has not completely substituted experimental works in gears. There still exist numerous research works in gears from the experimental point of view that prove to facilitate more accurate results in relation to the real performance of the transmission. In this scope, the study of the load sharing in planetary transmissions plays an important role, given the importance of the study of the component resistance and durability.

In spite of all the studies presented in Chapter 2:, there seems to be a lack of numerical approaches to analyse the implications of both mesh phasing and tangential errors in the calculation of the load sharing by experimentally measuring the strains in planetary transmissions. The measuring of strains in gearboxes is a procedure employed to certify gearboxes in wind turbines

("IEC61400 – 4: Design Requirements for wind turbine gearboxes," n.d.), which gives the magnitude of the importance of an accurate measuring procedure. In this case, these strains will be measured in the root of the teeth in the sun gear, following the observation made by Hidaka, as commented in section 2.7. Besides, given the lack of flexibility in the body of the ring gear and the big size of the sun gear, which enables placing the strain gauges and the telemetry module, this location seems appropriate. Therefore, this chapter is oriented to mimic the behaviour of a strain gauge located in the root of one tooth in the sun gear and its behaviour due to the contact between the sun and the planets. Later, the strain data is employed to calculate the load sharing in the transmission and these results will be compared with the ones obtained from the LSR, which provides the real load sharing in the transmission. This comparison has been proved to be inaccurate in a previous work presented by Aurrekoetxea & Ruiz de Ocenda in (Aurrekoetxea et al., n.d.), therefore, this section if aimed to clarify the nature of these discrepancies.

6.2. Methods

6.2.1 Finite-element models

As mentioned before in section 3.3.1, the contact problem in the model employs a hybrid point of view. The FE models employed in this approach consist of a global and a local FE models shown in section 3.3.1.1. For this work, the information is extracted from the global model, presented in Figure 83a. The measuring of strains in the sun gear root is a technique employed in some cases (Aurrekoetxea et al., n.d.; Dai et al., 2016), this is the preferred procedure whenever the sun gear is big enough to dispose the gauges and necessary telemetry module. In addition, these measurements are necessary in order to certify the gearbox, at least in the wind generator business. However, this represents one possibility, another possible technique consists in

measuring the strains in the ring gear, at least for flexible rings such as the ones presented in (Ligata et al., 2008; Singh et al., 2008) .

In order to evaluate numerically the accuracy of the experimental measurements, the focus for virtually mimicking the measurement is on the FE models. These models are described in section 3.3.1.1. Amongst all the defined finite-element models, the sun gear global model will be the target in this section.

As a reminder from section 3.3.1.1, the mentioned model consist of a definition of a Z number of teeth and the body of the sun gear. In terms of boundary conditions, the nodes along the inner circle, where the gear is mounted on the shaft, are embedded. The rest of nodes are free in the plane.

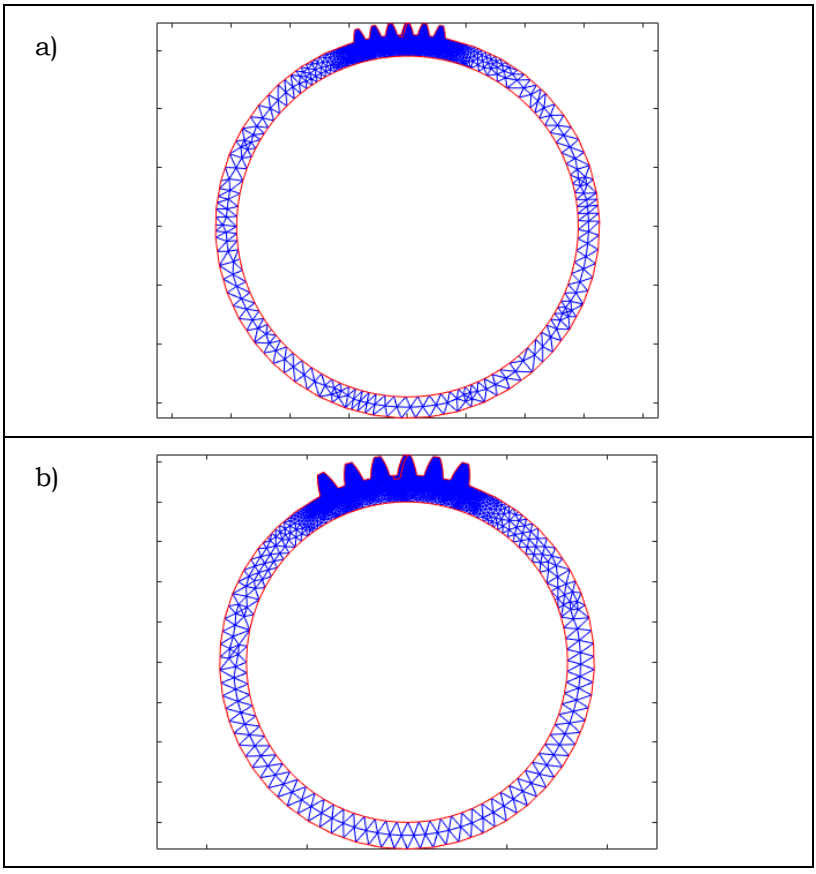

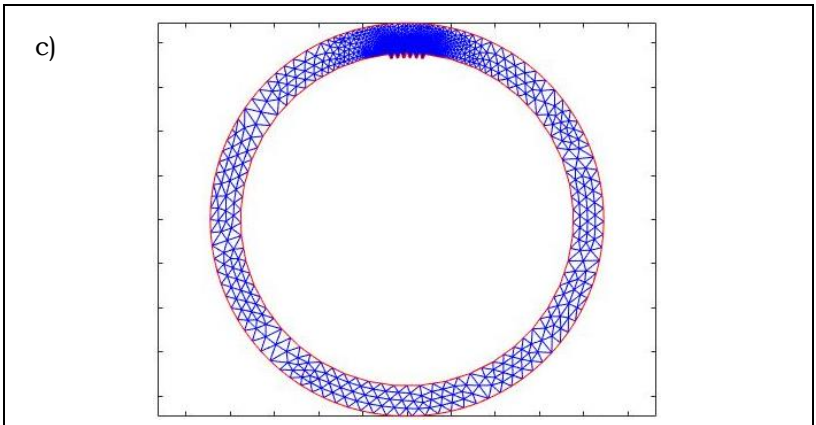

Figure 83. Global FE models for the configuration 2: a) Sun, b) planet, and c) ring

The Z number of teeth in every global FE model is obtained by using (28). This Z number considers all the possible contacts given the contact ratio (Figure 85), with the possibility of high contact ratio spur gears and the teeth that suffer strains due to the contact in adjacent teeth.

$$Z = 2 \cdot ceil(\varepsilon + 1) \qquad (28)$$

In equation (28) the function ceil rounds the contact ratio ε+1 to the next integer in the positive direction. For the simulations performed in this work, Z will be equal to 6, given the contact ratios specified in Table 8.

Table 8. Theoretical contact ratios in the studied configurations

Configuration	Parameter	Value
ESIP	Contact ratio (sun-planet)	1.294
	Contact ratio (planet ring)	1.395
ESSP	Contact ratio (sun-planet)	1.295
	Contact ratio (planet ring)	1.397

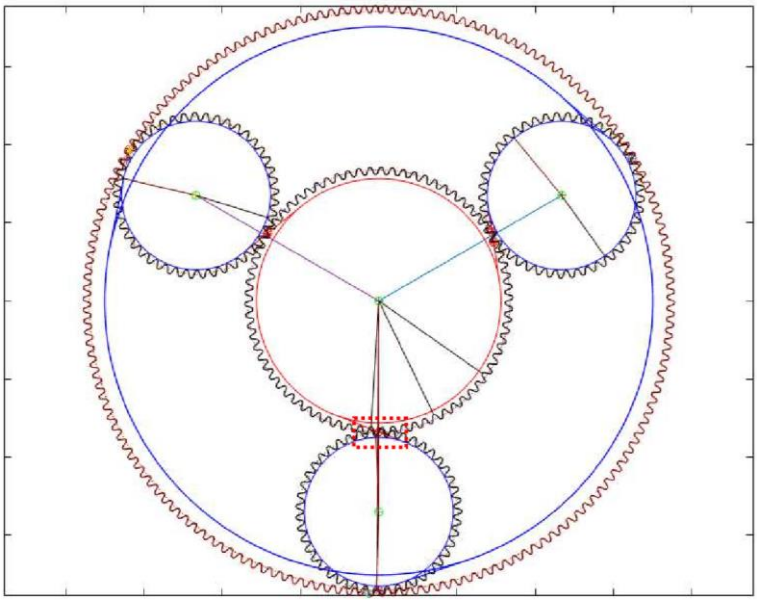

Figure 84. 3-planet transmission after mounting

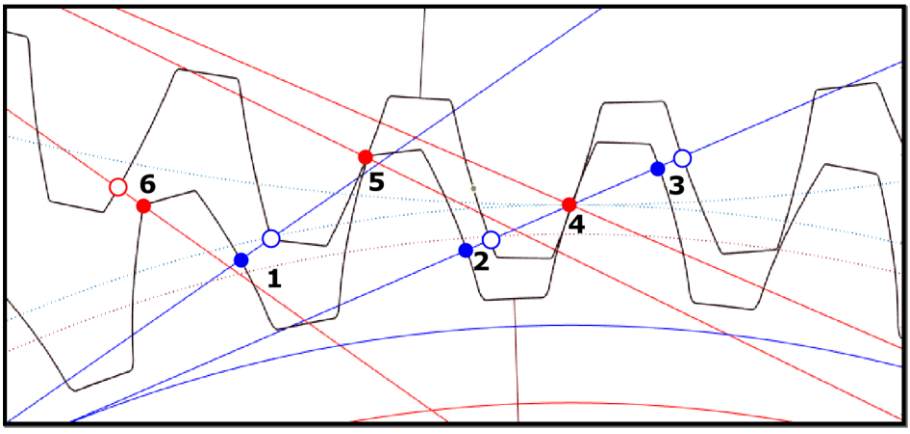

Figure 85. Detail of the possible contacts in the marked section in Figure 84

6.2.2 Definition of the virtual strain gauges

In the following, the modelling of the virtual strain gauges is described. This approach obtains the strains in the root of the sun gear teeth by processing the already existing information in the global FE model. Thus, the change in

the distance between adjacent nodes in different sections will be obtained. The first step to take consists in identifying in the FE model the relevant nodes, select them, and gather the coordinates of their initial position. For this, three conditions are established:

- The nodes have to belong to the root circumference.
- They must be in the arc that connects the trochoids of consecutive teeth, but avoiding the nodes along the trochoid.
- At the first and last teeth this number of nodes just have to be on the root circumference.

Avoiding the trochoid of the teeth profile, the stress concentration effect that appears in this zone with the load would be avoided. Therefore, the strain gauge data will not be distorted by such effect. Taking all the previous into account, the nodes selected appear in Figure 86 and their coordinates are stored. Thus, the initial position of the nodes of interest is monitored. In this initial configuration, no load is applied in any of the Z teeth. By this procedure, the number of noded sections where the strains are measured will be Z+1, always.

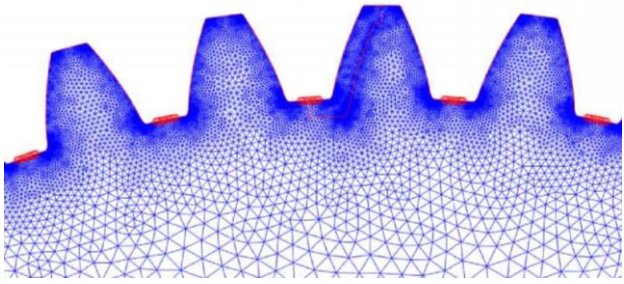

Figure 86. Detail of the noded sections in the global FE model.

Secondly, in order to establish the initial length of the strain gauge each section of nodes is analysed separately. In every section, the distance between each pair of consecutive nodes is calculated by using (29). This equation approximates the distance as a straight line, a good enough approximation given the reduced length and therefore the negligible curvature.

$$\overline{No_{J,\iota}No_{J,(\iota+1)}} = \sqrt{\left(No_{j,(i+1)x} - No_{j,ix}\right)^2 + \left(No_{j,(i+1)y} - No_{j,iy}\right)^2} \qquad (29)$$

$No_{j,i}$ refers to the node i in the j section of nodes. The subindexes x and y identify the horizontal and vertical components of the nodes Cartesian coordinates.

The summation of the distances between the nodes that belong to each of the sections provides the length of the strain gauge. Equation (30) provides the reference value of that length, whenever there is no load in the model.

$$Lo_j = \sum_{i=1}^{wk(j)-1} \overline{No_{J,\iota}No_{J,\iota+1}} \qquad (30)$$

Then, equation (31) provides the results for the same calculation when load is applied in the model. The lack of the subindex o in the equation identifies this detail.

$$L_j = \sum_{i=1}^{wk(j)-1} \overline{N_{J,\iota}N_{J,\iota+1}} \qquad (31)$$

Once these values are known, the strain in each of the monitored sections will correspond to the difference in length of each section between the unloaded and the loaded configuration (32).

$$\Delta L_j = L_j - Lo_j \qquad (32)$$

With the previous steps, the strains in a supposed strain gauge could be modelled, and the strain gauge positioned in any of the monitored sections. However, in order to obtain the measurements of a strain gauge placed in one of the sections of nodes monitored, it is important to define the acquisition sequence, and to take into account the effect of any contact on such strain gauge. In the following section, all of these points are explained.

6.2.3 Contact sequence

In order to manage the information acquired by the strain gauge, its location is greatly relevant. The strain gauge is considered to be positioned in the (Z/2)+1 section, which is the midst of the model. Thus, the initial single contact in the first tooth will have a small, but notable influence on the gauge. As commented before, the number Z of teeth show all the teeth that are notably influenced by a contact on the middle tooth. Consequently, the gauge placement assures the measuring of the strains produced by any contact in any of the considered teeth.

Thus, the contact sequence starts with a single contact in the first tooth, which will produce a small strain in the gauge. After this, the contact will continue to the point that there will appear a double contact both in the first and second tooth. In such scenario, firstly, the strains due to the first contact will be monitored and then the ones due to the second. Finally, the superposition principle will sum up the effects of both contacts. This strategy will be applied continuously during the Z meshing cycles in the Z teeth, considering every possible contact that affect the strain gauge.

In Figure 87, the contact sequence for the cases considered in this section is presented. The snapshots for simple and double contacts are represented. Every snapshot includes the strain gauge representation by a thick red line between teeth 3 and 4.

In order to recreate virtually what is presented in Figure 87, the strains in every section between teeth are calculated in every contact position, by using equations (29)-(32). Then, due to the employed model, the relative position of the contact has to be taken into consideration to obtain the strain in the gauge. For starters, the position of the contact in the middle tooth in the FE model has to be taken into account. In any case, the contact appears in the middle tooth in the FE model, as shown in Figure 88. Thus, it is important to consider the sequence in the contacts to be able to allocate the relative position of the strain gauge with respect to the contact. Therefore, whenever the contact is

on the first tooth, in the FE model this tooth is the (Z/2)+1 tooth. Then, the strain in the gauge corresponds to the last measured section. Continuing with the sequence previously commented a double contact would appear. For both contacts, in the FE model, they will happen in the (Z/2)+1 tooth. For the contact in the tooth number 1, the previously explained still stands. Then, for the contact in the second tooth, the strains belonging to the gauge will be found in the strains the Z noded section.

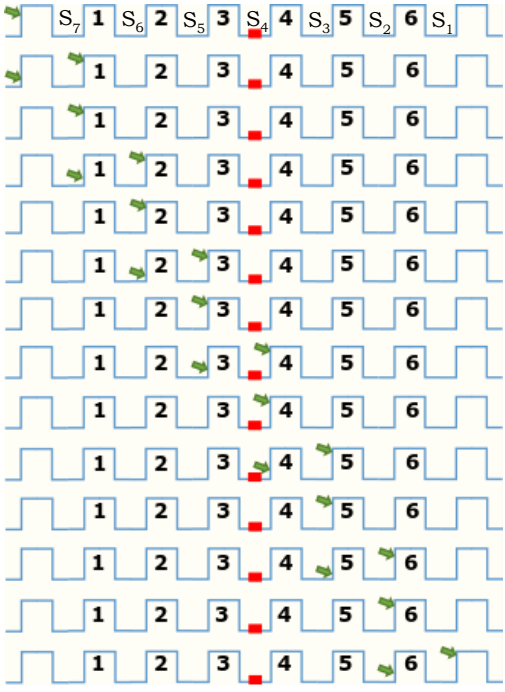

Figure 87. Snapshots of the contact sequence

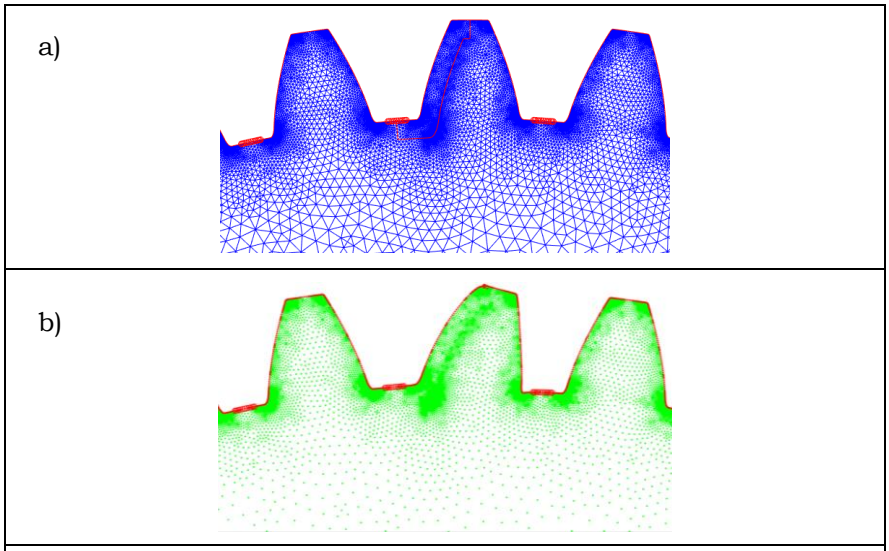

Figure 88. Detail of the global FE model a) under no load b) under one of the load cases.

For the example illustrated in Figure 87, the procedure commented above would start with a contact in the tooth 1, this in FE model will be the 4th tooth, as seen in Figure 88b. Thus, the strains in the gauge would be the ones in section S_7. Then, the double contact would add to that the contact in the 2nd tooth. This contact also in the FE model happens in the 4th tooth. By the relative positioning of the gauge to the contact and the FE model, the strains in the gauges due to this contact are the ones in the section S_6 in the FE model. By this procedure and following the sequence in the contacts, the strains in the gauge can be recreated for any of the contact cases. The matrix gathered in (33) determines the section whose strains have to be considered for each contact case. For each meshing cycle, the row changes to the next one. In this matrix only the 8 meshing cycles considered for the simulations are studied. Whenever there is a single contact only the 4th column has to be considered, but whenever there is a double contact then the 5th column sets the section to consider. There are more columns to consider in case of high spur contact ratio.

$$S_i = \begin{matrix} \\ \\ \\ \\ \\ \\ \\ \\ \end{matrix} \overset{\begin{matrix} 1^{st}\text{ contact} \end{matrix}}{\begin{bmatrix} 0 & 0 & 0 & 0 & 7 & 6 & 5 \\ 0 & 0 & 0 & 7 & 6 & 5 & 4 \\ 0 & 0 & 7 & 6 & 5 & 4 & 3 \\ 0 & 7 & 6 & 5 & 4 & 3 & 2 \\ 7 & 6 & 5 & 4 & 3 & 2 & 1 \\ 6 & 5 & 4 & 3 & 2 & 1 & 0 \\ 5 & 4 & 3 & 2 & 1 & 0 & 0 \\ 4 & 3 & 2 & 1 & 0 & 0 & 0 \end{bmatrix}} \begin{matrix} \\ \\ \\ \\ \\ \\ \\ \\ 2^{nd}\text{ contact} \end{matrix} \quad (33)$$

This procedure leads to the mimicking of the measurements by an ideal strain gauge located in the arc along the root of the sun teeth. In the section 6.5 the results of these virtual measurements are presented, showing how the gauge first is under compression and, whenever the contact overtakes it, it gets under traction.

6.3. Load sharing calculation

In this work, the load sharing amongst planets will be calculated employing different definitions.

Firstly, for the immediate calculation of the load sharing, the Load Sharing Ratio (LSR) is the magnitude chosen. This was employed previously in Chapter 3: & Chapter 4: as well as in publications (M. Iglesias et al., 2017; Miguel Iglesias et al., 2013; Sanchez-Espiga et al., 2020), also referred as Load Sharing Factor (LSF) in (Boguski et al., 2012; Ahmet Kahraman, 1999; Ahmet Kahraman & Vijayakar, 2001). This LSR allows to observe the amount of load in each planet, compared to the inlet torque at any moment of the simulation. The analytical definition of the LSR is reminded in equation (34) given its importance for the following analysis.

$$LSR_s = \frac{F_s}{\sum_{t=1}^{N} F_t} \quad (34)$$

In order to address the differences between the calculation of the load sharing by using the LSR, which represents the actual load sharing, and the strain measurements Figure 89 & Figure 90 are included. These represent ideal scenarios of the behaviour of both ESIP and ESSP transmissions without any

tangential error in the pinhole of the planets. A sketch of the LSR and the strains in the gauges shows this behaviour. In both figures, the LSR is a continuous calculation. On the contrary, the strains in the contact with each planet are measured during a period of time. In each of the measurements of strains, the peak-to-peak value in the strains is obtained.

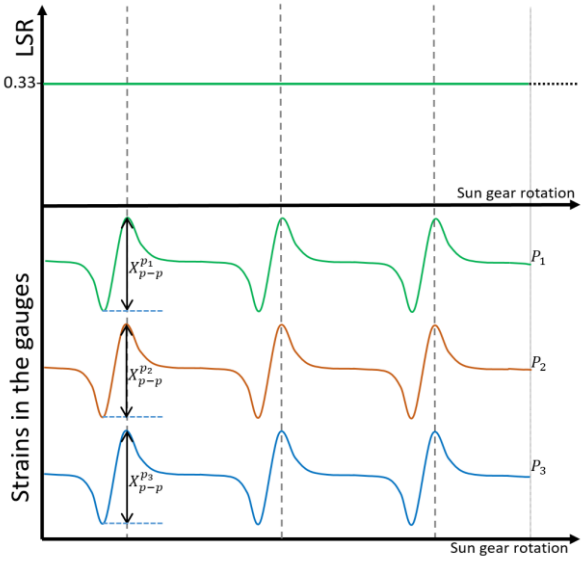

Figure 89. Comparison of the LSR and the strain measurements in the ESIP transmissions

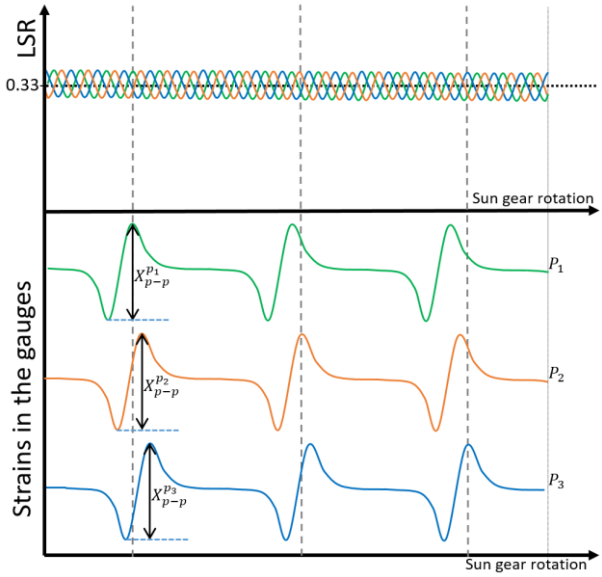

Figure 90. Comparison of the LSR and the strain measurements in the ESSP transmissions

As seen in Fig.7, there exists a synchronicity between the peaks in the LSR and the strains. The maximum level of load, signalled by the maximum in the LSR, coincides with the peak of peak-to-peak value in the strains. After this, the calculation of the load sharing from the strains, which will be referred in the following as SGLR, is calculated. This magnitude refers to the size of each peak-to-peak value compared to the total of summation of every peak-to-peak value. Thus, the peak-to-peak value corresponding to each planet will be the same and will lead to a uniform result in the SGLR. On the contrary, a transmission with a sequential mesh phasing will have a fluctuant LSR, different to the SGLR as seen in Fig.6. Thus, the SGLR will only coincide with the real load sharing in the transmission in the ideal scenario of an ESIP transmission without any error, as seen in Fig.6. In order to obtain the SGLR (7) is used.

$$SGLR_{p_e} = \frac{X_{p-p}^{p_e}}{\sum_{f=1}^{N} X_{p-p}^{p_f}} \qquad (35)$$

In equations (34) & (35) the N refers to the total number of planets. Furthermore, the subindex t is used as an auxiliary subindex to sum up the contributions of every planet in the transmission.

6.4. Cases of study

Firstly, for the measurements of the strains two cases of mesh phasing are considered. In the same manner as in the previous sections 4.6 & 5.4.

The strain measurements are performed in the sun gear. By the definition of this technique, it is expected that the results obtained will be crucially affected by the mesh phasing in the transmission. Not only will phasing influence but also the manufacturing errors will play a crucial role. Thus, after the results observed for the manufacturing errors considered in section 5.5, the tangential pinhole position errors prove to have the highest impact. Therefore, these will be considered also for this new approach, however, with a wider scope of cases.

The various cases considered, in terms of errors and mesh phasing are gathered in Table 9. The two configurations considered in the dimension of the teeth and the shaft mounting correspond to the ones presented in 5.4.

Table 9. Pinhole position errors considered to study for both configurations.

Configuration	Tangential error						
ESIP	0 μm	1.25 μm	2.5 μm	3.75 μm	5 μm	6.25 μm	7.5 μm
ESSP	0 μm	1.25 μm	2.5 μm	3.75 μm	5 μm	6.25 μm	7.5 μm

None of the mentioned configurations includes flexibility in the shafts that support the wheels. This decision is due to the need of observing the pure effect of the load in the transmission and in the strain measurements, to which aim, the lack of floatability is a great asset. Nonetheless, in a future further step, the focus should be on the inclusion of floatability in the gear supports, increasing the realism of the simulations. However, it is important to highlight the importance of this consideration knowing that a more rigid system is more

sensitive to any error, as it can be seen in (Bodas & Kahraman, 2004) where the stiffness is increased by augmenting the N. This effect will probably be seen whenever the radius of the shaft mounting is modified, or the geometry of the teeth, or even the number of teeth. Thus, leading to a more rigid system more sensitive to errors, which translate in higher imbalances for a given error.

6.5. Results

Hereinafter, the results to the cases of study are summarised. As a first step to comprehend the obtained results, Figure 91 & Figure 92 present the detail of sun-planet contacts, where the contacts are highlighted by a red circle and numbered as presented in Figure 85. In the in-phase configuration, only one figure is presented given the fact that every contact is at the same situation for any of the planets. These figures prove the differences in the contacts due to the mesh phasing. Both configurations are ideally perfect; therefore, the difference in the pairs of teeth in contact is caused by the mesh phasing.

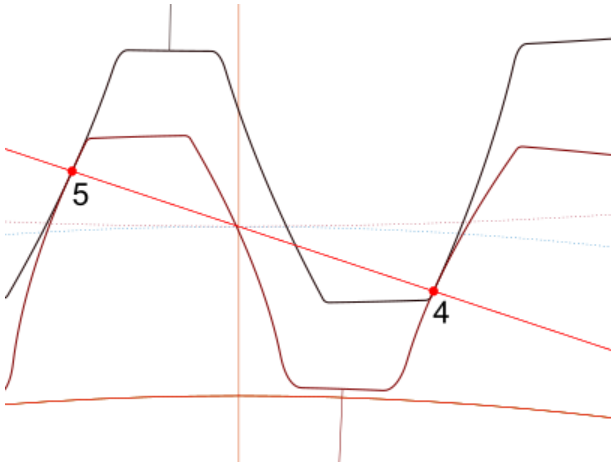

Figure 91. Detail of the contacts between sun and planets for 3-planet ESIP transmission.

On the contrary, in a sequentially phased transmission every contact is at a different point along the meshing line, as seen in Figure 92 Thus, the number of teeth pairs in contact varies from one planet to the other. Likewise, the

meshing stiffness varies in each of the contacts, and this will influence the load sharing and the strains.

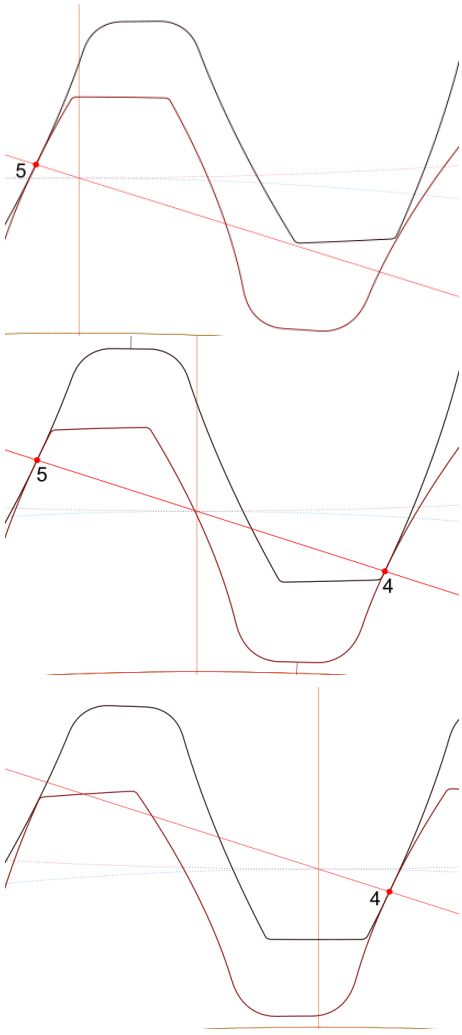

Figure 92. Detail of the contacts between sun and planets for 3-planet ESSP transmission.

As a consequence of those differences in the contacts, in Figure 93 a series of mechanical scenarios are plotted in order to introduce the physical explanation for the obtained results. Thus, the figure shows snapshots of 3 instants throughout the simulations. In every instant, a blue dotted box shows the

stiffness observed in the contact on each planet. This stiffness is related directly with the contact forces and the strains suffered by the strain gauge. Besides, this stiffness is affected by the mesh phasing. Then, given the data in each of these instants, considering the peak-to-peak value proportional to that stiffness, the SGLR is induced.

As shown in Figure 93, the springs present differences in stiffness due to the mesh phasing in the sequentially phased scenario. For the strains experienced by the strain gauge, the differences due to the mesh phasing are not visible given the fact that the same cycle is repeated for every contact at different moments along the simulation. Although the cycles in the strains are not affected by the mesh phasing, it is notable for the LSR in each of the instants. Given that, discrepancies are expected between the results obtained by using each of the proposed techniques. This is a consequence of the fact that the strain gauge only observes what happens in each planet, and not on the rest, for a period of time, but whenever the sun will reach every different planet will observe analogous conditions. However, the LSR observes the circumstances in every planet at the same time, and therefore, it is affected directly by the conditions in the whole transmission and not only in one of the planets as it happens with the SGLR.

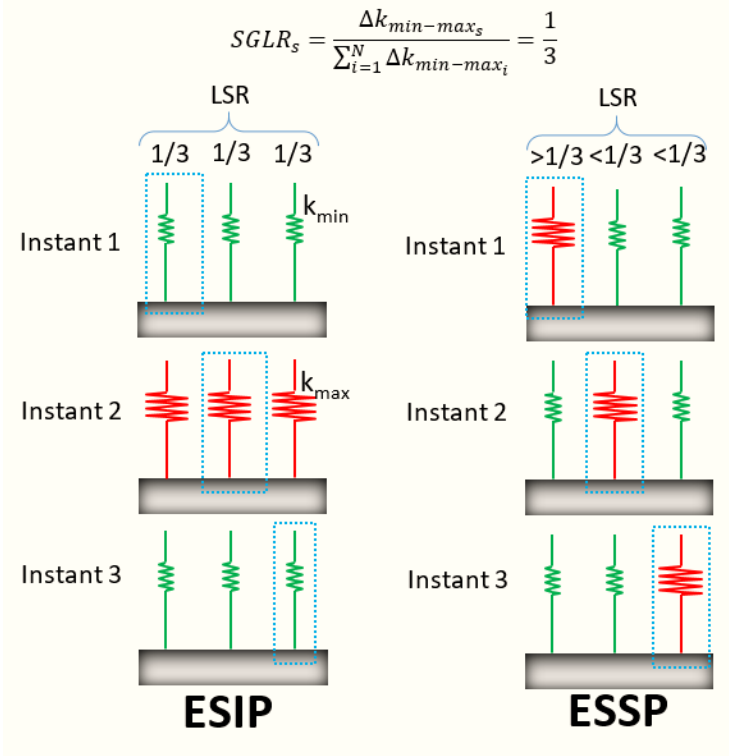

Figure 93. Mechanical analogy for the load sharing calculation discrepancies.

In order to observe in detail the magnitudes mentioned in section 2.4, the LSR is presented, together with the strain measurements. This is presented for the case where there is a tangential position error of 1.25 μm. These magnitudes are shown both for the in-phase (Figure 94) and sequentially phased (Figure 99) transmissions. By using this scenario, all the effects can be analysed. Looking for conciseness and given the parallelisms in the behaviour of both configurations, this detailed analysis has been limited to the configuration 2. However, the numerical data is extracted and analysed for every case in both configurations.

Later, the results for all the other cases studied are presented together in order to show the tendencies that can be identified both in the LSR and the strains measurements.

Regarding the strains measured in the root of the teeth in the sun gear, these are shown in Figure 94 for the ESIP transmission with a 1.25 μm tangential error. Given the applied torque and the direction of the rotation in the sun gear, the contacts in the successive teeth start by compressing the gauge. The closer the contact gets to the gauge, the higher the measured compressing strain. However, whenever the contact becomes a double contact both in the tooth before and after the strain gauge, there is a combination of traction and compression that leads to the tipping point located right after the 4^{th} meshing cycle in the sun. In the meshing cycles afterwards, the strains are tractions in the gauge whose amplitude diminishes as the meshing continues, given the fact that the contacts happen further from the gauge. As seen in the lower graph in Figure 94, due to the tangential error included in the mounting of the planet 1, the amount of load in this planet is lower than in the other planets, as it can be expected in these conditions. For in-phase transmissions, this error affects equally the planet 2 & 3, therefore, the behaviour of the LSR and strains in planets 2 & 3 are identical, that is the reason why these lines overlap. Besides, the error in the planet 1 translates also in a lower peak-to-peak value in the strains, due to the contact with this planet. At the same time, the error narrows the width of the different strain sections in the strain graph in the planet 1. This narrowing is visible in the moment when the slope in the graph changes. This narrowing is due to the lower load in that planet together with the flexibility of the tooth, which leads to a lower effective contact ratio in that planet compared to the rest.

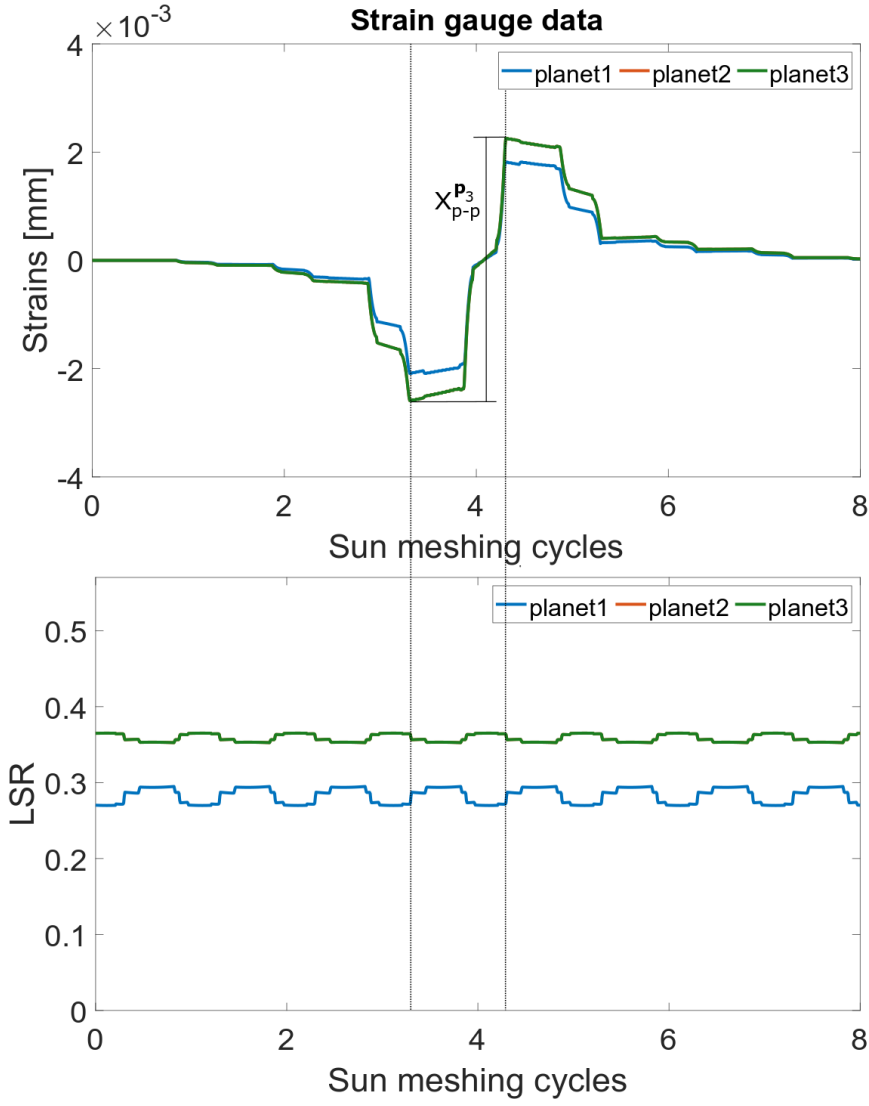

Figure 94. LSR and strains in the gauge in ESIP with 1.25 µm error (Conf. 2).

Whenever the results in the strain measurements are observed together with the LSR results more effects can be identified. In Figure 94 some dotted lines are included in order to show the synchronicity in a relevant event such as the peak values in the strains and in the LSR. The changes in the LSR are related with the changes in the meshing stiffness, as well as the change of the pairs of

teeth in contact. The inexistence of mesh phasing makes these changes synchronous in each planet except for the small delay in the planet 1 due to the tangential error. In terms of the LSR, the variations in the planet 1 inside a meshing cycle are bigger than in the other planets. However, the average load in this planet is lower than in the rest of planets and, thus, the strains are smaller.

These effects are studied in more depth varying the size of the tangential error in the mounting of the planet 1, as seen in Figure 95, Figure 96, Figure 97 & Figure 98. Thus, the variation of this error creates a tendency that continues along the simulations and prove the effects commented before. The higher the error, the bigger the imbalance in the LSR, and the lower the load in the planet with the error.

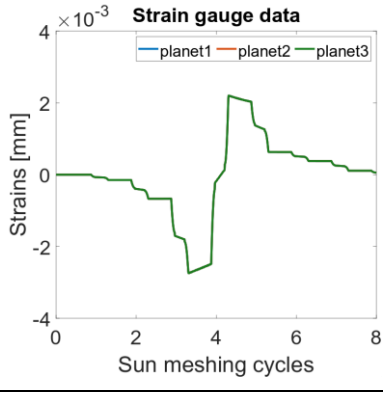

a) 0 µm

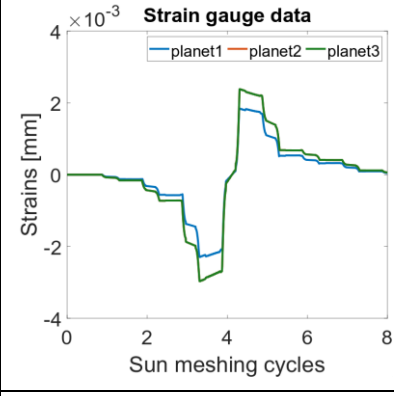

b) 2.5 µm

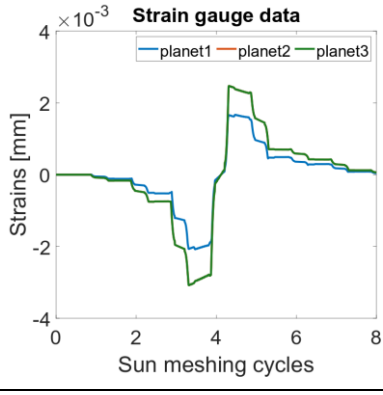

c) 3.75 µm

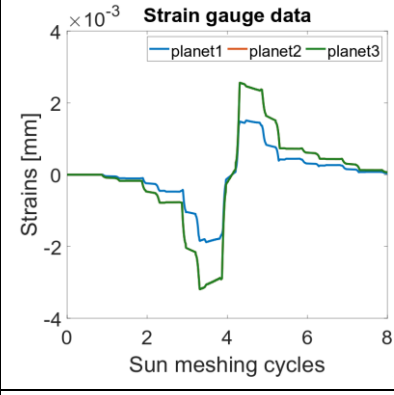

d) 5 µm

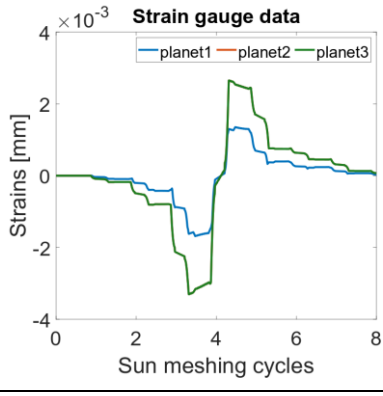

e) 6.25 µm

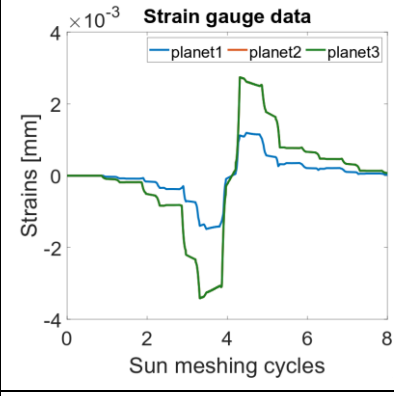

f) 7.5 µm

Figure 95. Strains in the gauge in ESIP with various errors for configuration 1.

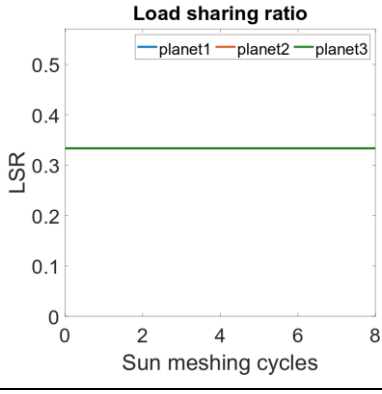

a) 0 µm

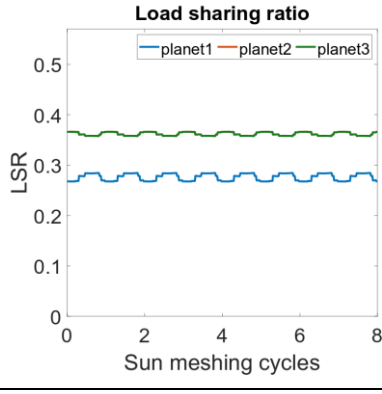

b) 2.5 µm

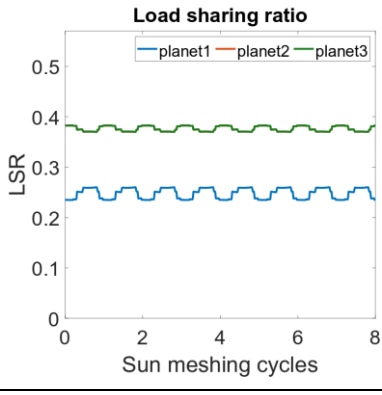

c) 3.75 µm

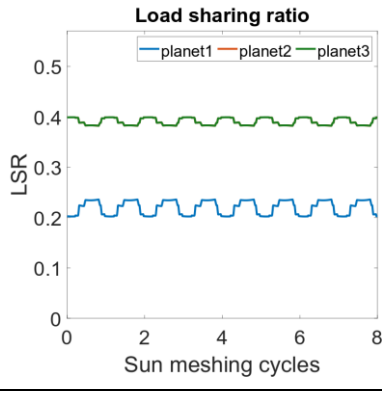

d) 5 µm

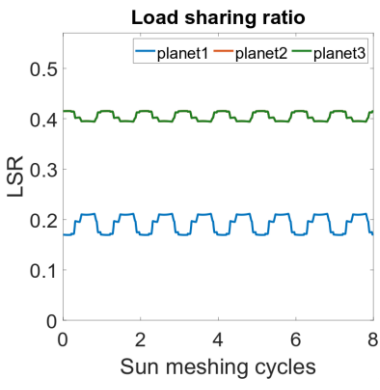

e) 6.25 µm

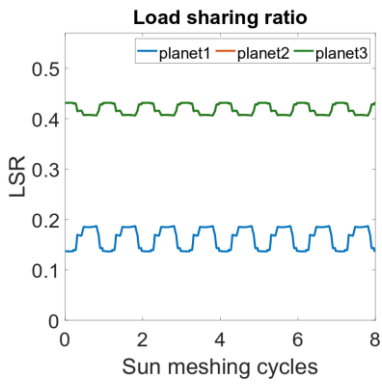

f) 7.5 µm

Figure 96. LSR in ESIP with various errors in configuration 1.

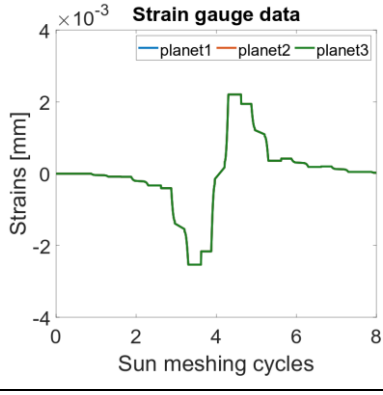

a) 0 µm

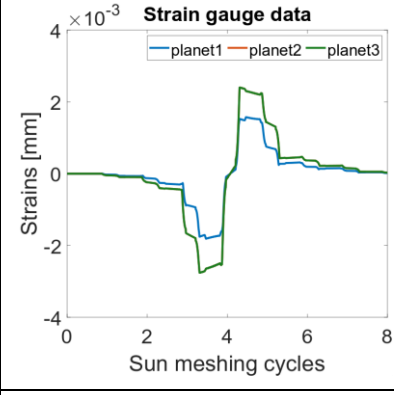

b) 2.5 µm

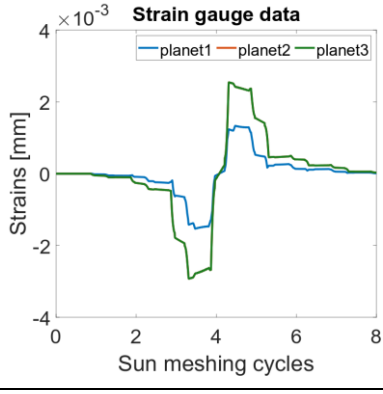

c) 3.75 µm

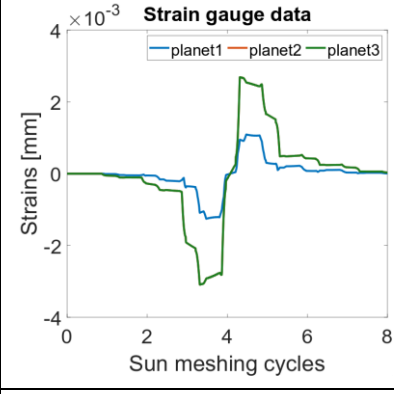

d) 5 µm

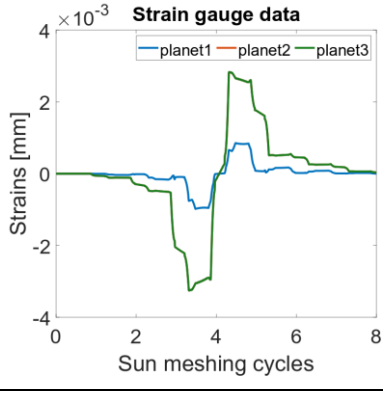

e) 6.25 µm

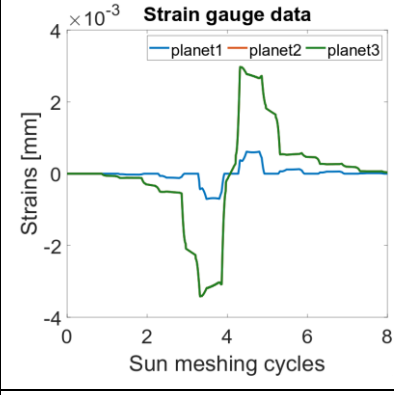

f) 7.5 µm

Figure 97. Strains in the gauge in ESIP with various errors for configuration 2.

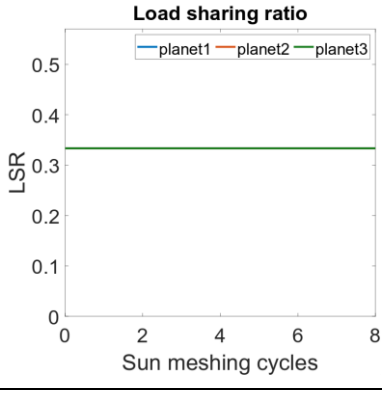

a) 0 µm

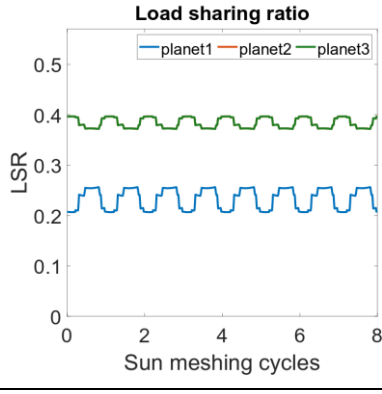

b) 2.5 µm

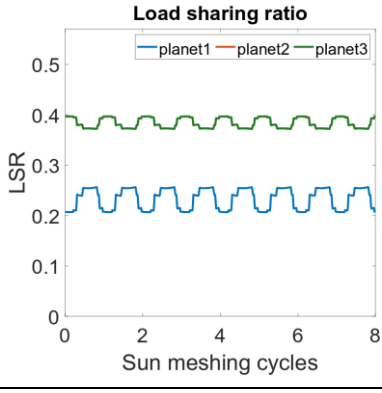

c) 3.75 µm

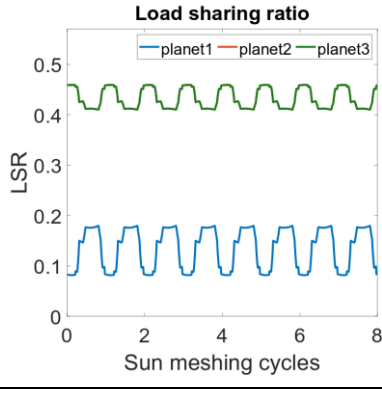

d) 5 µm

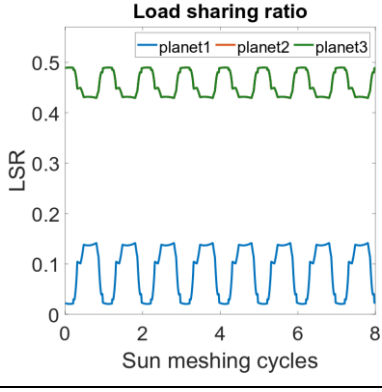

e) 6.25 µm

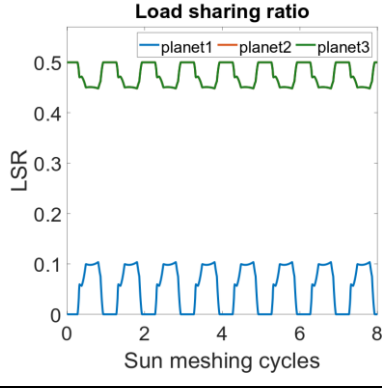

f) 7.5 µm

Figure 98. LSR in ESIP with various errors for configuration 2.

Because of that, the lower the strains in the contact with that planet. At the same time, the impact of the error in the width of the events in the strains and LSR becomes more visible the higher the error, proving what was commented but was difficult to spot for the case with 1.25 m error.

In Table 10 & Table 11, the numerical results to the magnitudes of interest are gathered. In this case, the lack of mesh phasing uniforms the results in the maximum LSR (Max. LSR) and in the SGLR. This uniformity continues in the cases where there is tangential error in the planet 1. Even though there is an error, planets 2 & 3 conserve the uniformity in the mentioned results. Apart from that, the numerical results prove that the measuring of the strains to calculate the load sharing tend to minimise the impact of the tangential error. Thus, the SGLR in the planet 1 is higher than the average LSR, as well as the SGLR in planets 2 & 3 is lower than the average LSR. Therefore, the load sharing obtained in the SGLR is more uniform and diminishes the impact of the tangential error.

Table 10. Numerical results for the ESIP configuration 1 in every case of study for configuration 1.

	Planet 1			Planet 2			Planet 3		
e_t (μm)	Avg. LSR	Max. LSR	SGLR	Avg. LSR	Max. LSR	SGLR	Avg. LSR	Max. LSR	SGLR
0	0.333	0.333	0.333	0.333	0.333	0.333	0.333	0.333	0.333
1.25	0.3047	0.3089	0.3060	0.3477	0.3498	0.3470	0.3477	0.3498	0.3470
2.5	0.2761	0.2845	0.2787	0.3619	0.3662	0.3607	0.3619	0.3662	0.3607
3.75	0.2477	0.2601	0.2523	0.3762	0.3826	0.3738	0.3762	0.3826	0.3738
5	0.2193	0.2357	0.2276	0.3904	0.3990	0.3862	0.3904	0.3990	0.3862
6.25	0.1910	0.2113	0.2031	0.4045	0.4153	0.3984	0.4045	0.4153	0.3984
7.5	0.1628	0.1871	0.1788	0.4186	0.4316	0.4106	0.4186	0.4316	0.4106

Table 11. Numerical results for the ESIP configuration 2 in every case of study for configuration 2.

	Planet 1			Planet 2			Planet 3		
e_t (μm)	Avg. LSR	Max. LSR	SGLR	Avg. LSR	Max. LSR	SGLR	Avg. LSR	Max. LSR	SGLR
0	0.333	0.333	0.333	0.333	0.333	0.333	0.333	0.333	0.333
1.25	0.2829	0.2949	0.2872	0.3586	0.3651	0.3564	0.3586	0.3651	0.3564
2.5	0.2328	0.2564	0.2465	0.3836	0.3967	0.3767	0.3836	0.3967	0.3767
3.75	0.1834	0.2179	0.2076	0.4083	0.4281	0.3962	0.4083	0.4281	0.3962
5	0.1346	0.1796	0.1688	0.4327	0.4592	0.4156	0.4327	0.4592	0.4156
6.25	0.0869	0.1413	0.1309	0.4566	0.4897	0.4345	0.4566	0.4897	0.4345
7.5	0.0516	0.1035	0.0935	0.4742	0.5	0.4533	0.4742	0.5	0.4533

On the other hand, for ESSP configurations, as shown before in Figure 93 the contacts in each of the planets differ. Thus, the meshing stiffness is different and also will be the LSR and the strains, as shown in Figure 99. The mesh phasing provokes a delay between the peak values in the LSR. Then, the error adds a little difference in the behaviour of the planets, a tangential error equals to a small delay in the mesh phasing, thus, the peak values in the LSR are not equal to each other. However, in the configuration without error, the peak values are identical. Later, relating the strain measurements and the LSR, it is visible how there is a synchronicity between the peak values in the LSR and in the strains, and how these peaks are separated by the mesh phasing. Besides, the peak values of the strains in each planet are not identical either. Thus, the error modifies the geometry of the contact and the situation where the highest strain appears in any planet is not equal to the others.

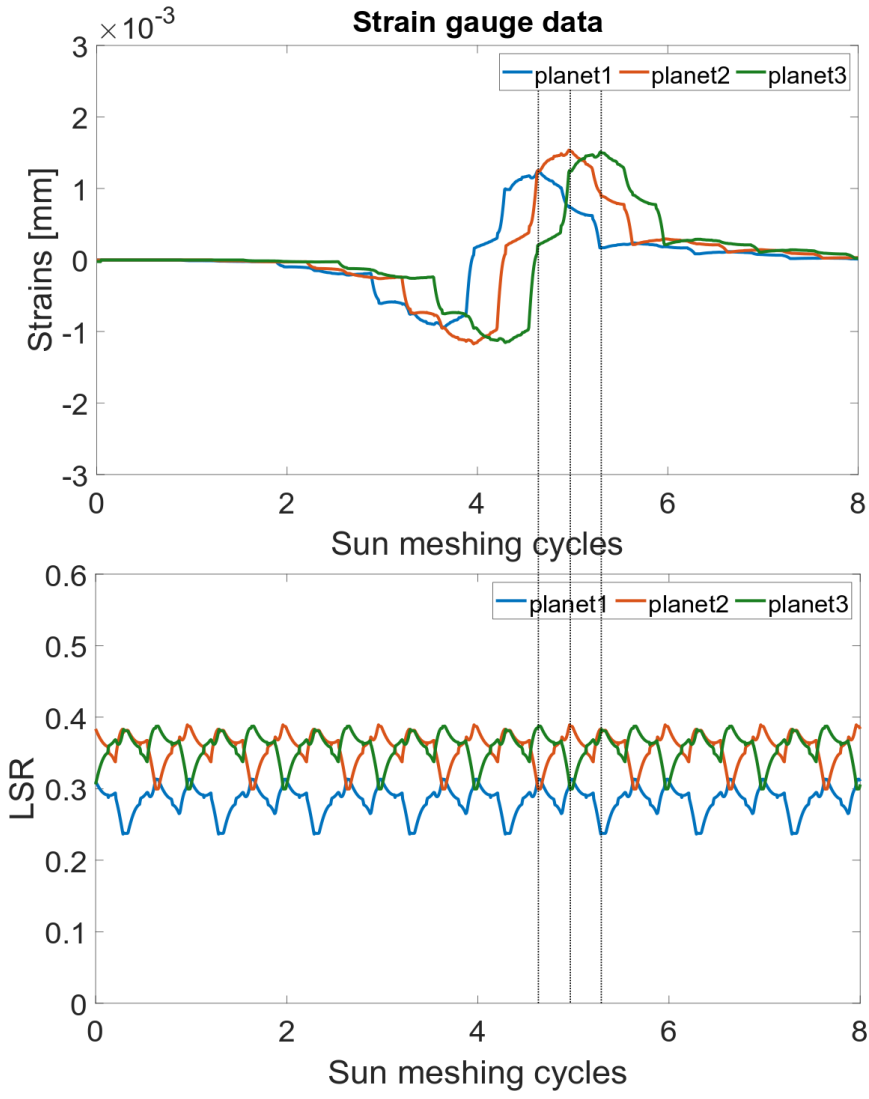

Figure 99. LSR and strains in the gauge in ESSP with 1.25 µm error (Conf. 2).

However, this difference is purely due to the tangential error. In Figure 100, Figure 101, Figure 102 & Figure 103 in the case without error every peak is identical to the rest, but the bigger the error, the bigger the difference between these peaks. This effect is due to the modification of the sequential phasing. The mesh phasing in a sequential configuration is uniformly divided in N parts.

A tangential error modified this division and, thus, each contact affects the rest but not equally, therefore, an imbalance is created and the load in each of the planets will not be the same. This stands also for the strains, given the fact that they are a direct consequence of the contact forces. The numerical values extracted from these results are gathered in Table 12 & Table 13.

The numerical results gathered prove how these measurements tend to diminish the influence of both the mesh phasing and the tangential error. Thus, the results of the SGLR prove to be more uniform than the maximum values in the LSR. Thus, SGLR overestimates the uniformity in the load balance in the ESSP transmission studied.

Table 12. Numerical results for the ESSP configuration 1 in every case of study for configuration 1.

	Planet 1			Planet 2			Planet 3		
e_t (μm)	Avg. LSR	Max. LSR	SGLR	Avg. LSR	Max. LSR	SGLR	Avg. LSR	Max. LSR	SGLR
0	0.333	0.3506	0.333	0.333	0.3506	0.333	0.333	0.3506	0.333
1.25	0.3053	0.3231	0.3070	0.3474	0.3649	0.3470	0.3473	0.3652	0.3460
2.5	0.2774	0.2957	0.2810	0.3613	0.3796	0.3613	0.3613	0.3802	0.3577
3.75	0.2495	0.2684	0.2544	0.3753	0.3942	0.3755	0.3753	0.3955	0.3700
5	0.2218	0.2410	0.2281	0.3892	0.4089	0.3891	0.3891	0.4109	0.3828
6.25	0.1941	0.2138	0.2015	0.4030	0.4235	0.4022	0.4029	0.4262	0.3963
7.5	0.1665	0.1864	0.1749	0.4168	0.4381	0.4153	0.4167	0.4415	0.4098

Table 13. Numerical results for the ESSP configuration 2 in every case of study.

	Planet 1			Planet 2			Planet 3		
e_t (μm)	Avg. LSR	Max. LSR	SGLR	Avg. LSR	Max. LSR	SGLR	Avg. LSR	Max. LSR	SGLR
0	0.333	0.363	0.333	0.333	0.363	0.333	0.333	0.363	0.333
1.25	0.2844	0.3136	0.2888	0.3579	0.3893	0.3585	0.3578	0.3875	0.3527
2.5	0.2358	0.266	0.2446	0.3822	0.4142	0.3833	0.3821	0.4179	0.372
3.75	0.1877	0.2188	0.2011	0.4062	0.4407	0.4078	0.4062	0.4485	0.3911
5	0.1401	0.1719	0.1562	0.4299	0.467	0.4303	0.43	0.4776	0.4135
6.25	0.0933	0.1251	0.1106	0.4533	0.4931	0.453	0.4534	0.5061	0.4364
7.5	0.0475	0.0769	0.0656	0.4761	0.517	0.4753	0.4764	0.5344	0.459

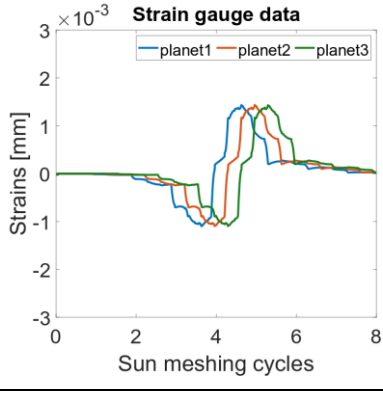

a) 0 µm

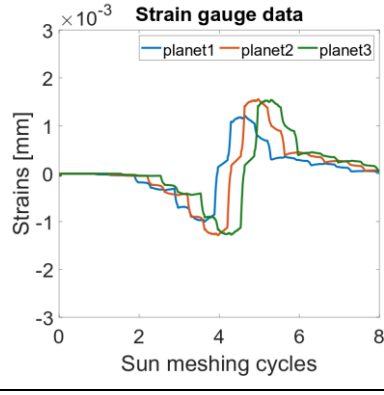

b) 2.5 µm

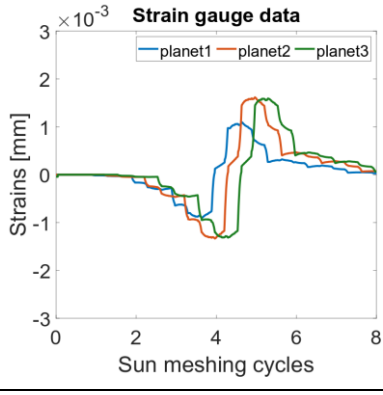

c) 3.75 µm

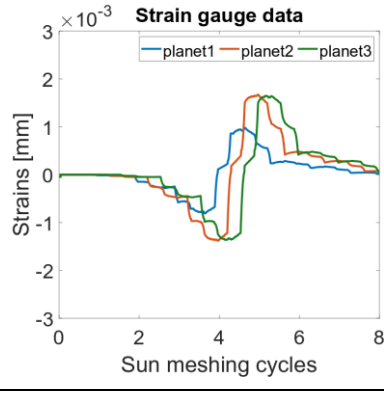

d) 5 µm

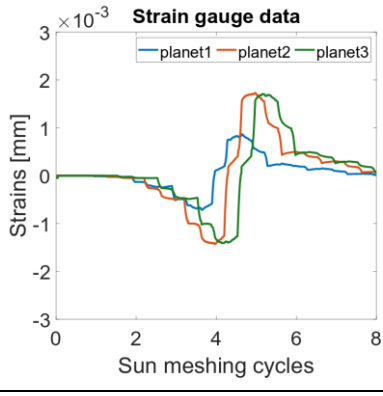

e) 6.25 µm

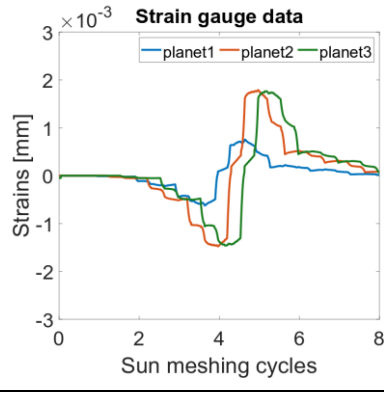

f) 7.5 µm

Figure 100. Strains in the gauge in ESSP with various errors for configuration 1.

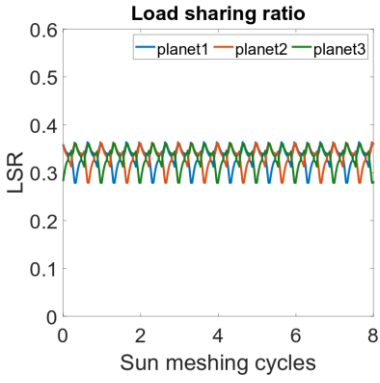

a) 0 µm

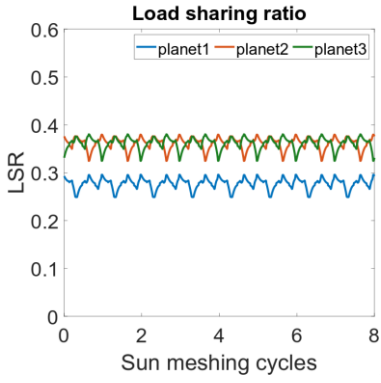

b) 2.5 µm

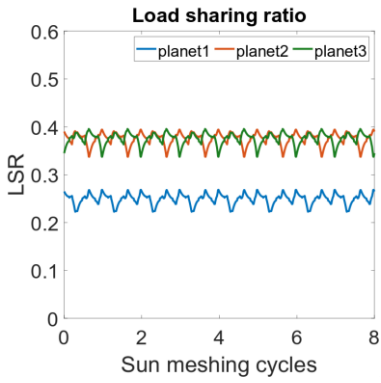

c) 3.75 µm

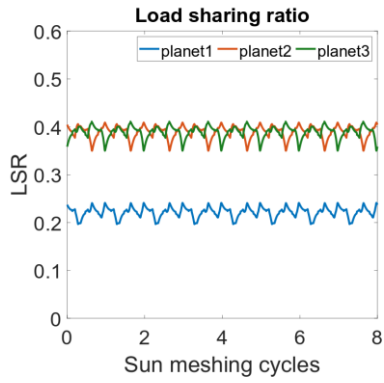

d) 5 µm

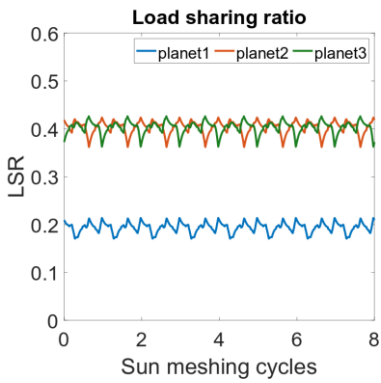

e) 6.25 µm

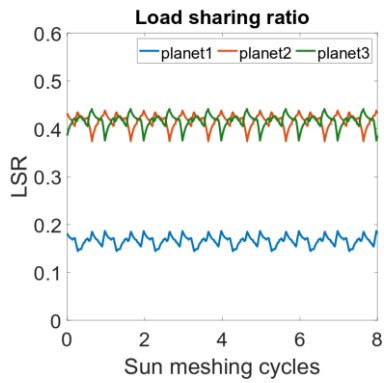

f) 7.5 µm

Figure 101. LSR in ESSP with various errors for configuration 1.

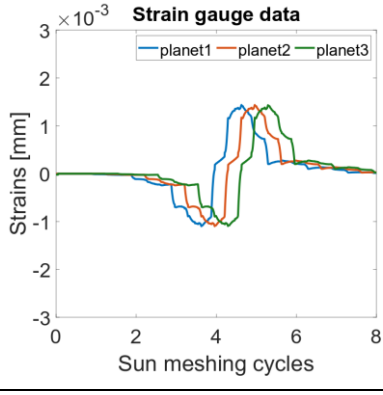

a) 0 µm

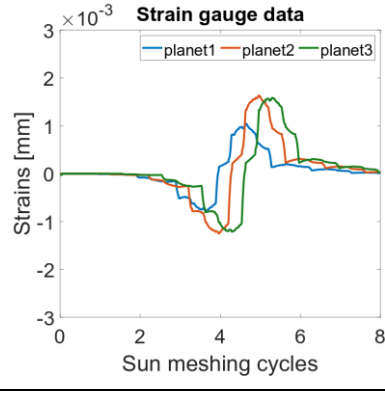

b) 2.5 µm

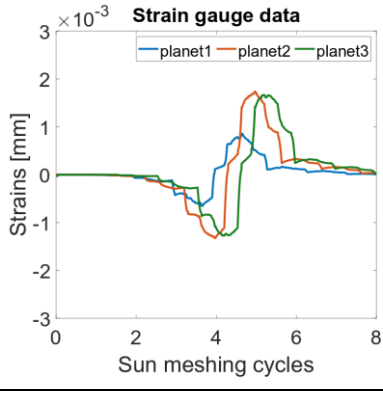

c) 3.75 µm

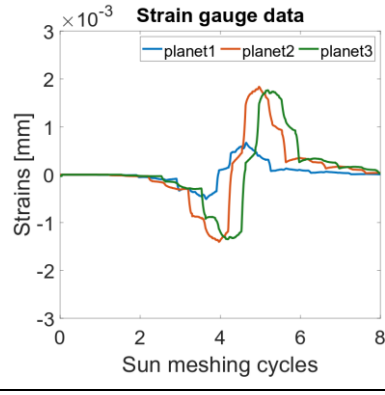

d) 5 µm

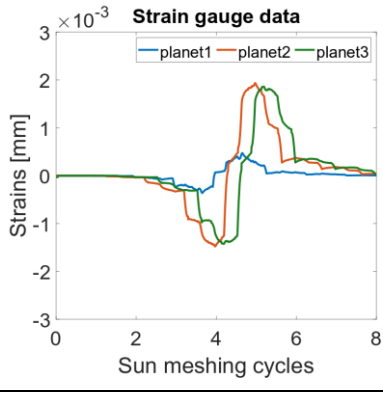

e) 6.25 µm

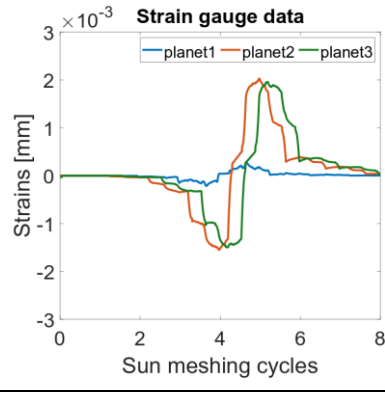

f) 7.5 µm

Figure 102. Strains in the gauge in ESSP with various errors for configuration 2.

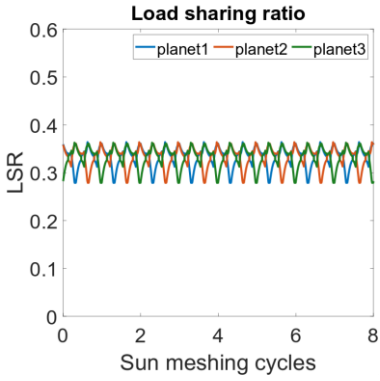

a) 0 µm

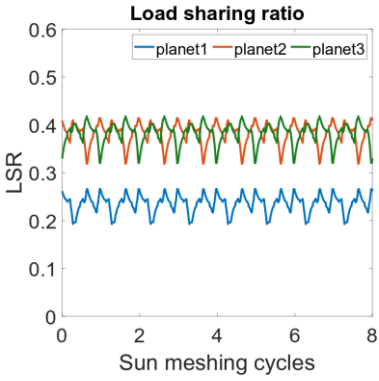

b) 2.5 µm

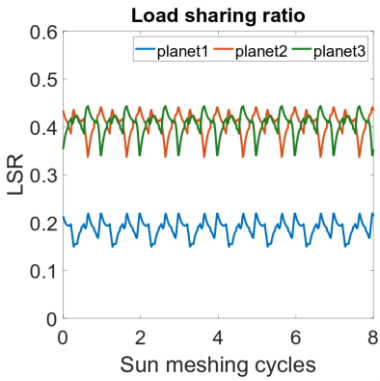

c) 3.75 µm

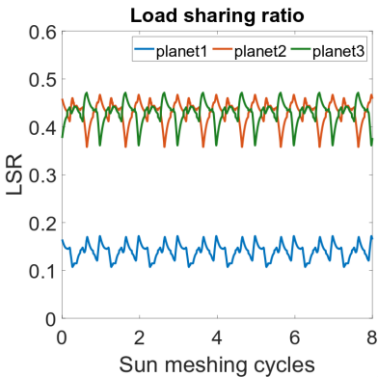

d) 5 µm

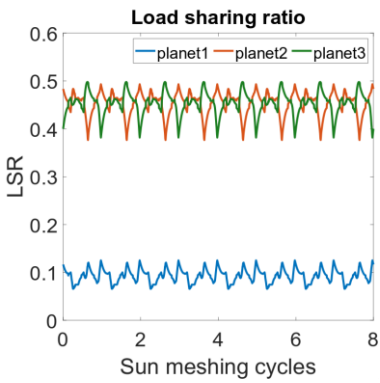

e) 6.25 µm

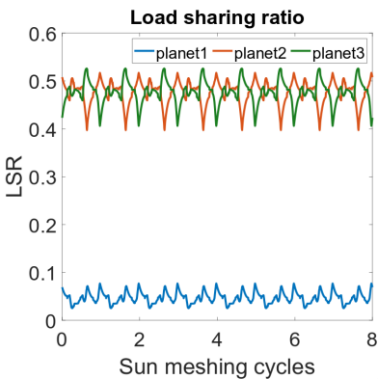

f) 7.5 µm

Figure 103. LSR in ESSP with various errors for configuration 2.

In a further step, the tendencies of the inaccuracies between the real maximum of the load sharing, obtained from the LSR, and the load sharing obtained by the SGLR are represented in Figure 104 & Figure 105. These figures gather the maximum value of these discrepancies. In this scenario, it is important to observe the fact that in the in-phase transmission without any error, the existing ideal balance leads to an accurate calculation of the load sharing with the SGLR. However, in the same scenario but with sequential phasing, there exists a discrepancy between the LSR and the SGLR. Thus, the accuracy of the load sharing calculated from the strain measurements is quantified. Then, the increment of the tangential error in the planet 1 mounting increases these inaccuracies. In terms of the growth of the inaccuracy in the calculation of the load sharing, in the ESIP configuration this pace seems to be uniform for any tangential error until the 7.5 m tangential error that produces moments where the contact in the planet 1 is lost, as seen in Fig.13f. On the contrary, in the ESSP transmission this pace varies with the tangential error and different slopes can be identified in the graph. The variation between the scenarios with 0 error and 1.25 present a slight variation, however, in the scope from 1.25-5 there is a higher slope, which changes from then on to a lower slope, even lower than the one in the ESIP transmission's results. Finally, in the last case, for the configuration 2, where there is loss of contact in the planet with error the development of the discrepancy is highly affected, losing any kind of linear proportion with any of the previous values. However, in configuration 1 the higher flexibility in the sun gear avoids the loss of contact.

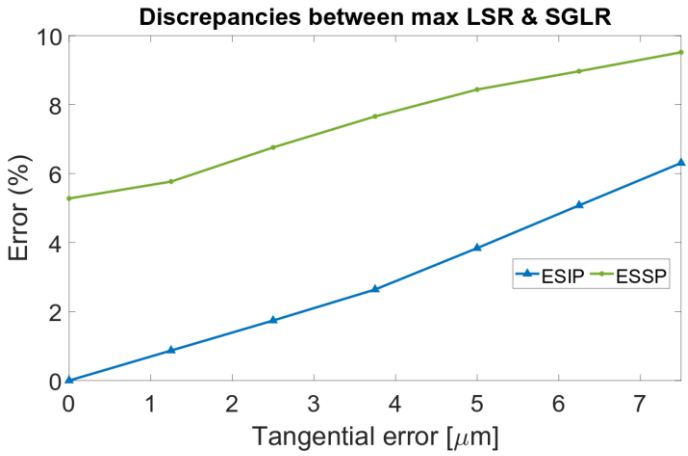

Figure 104. Discrepancies between the maximum LSR and SGLR results for configuration 1(Graph).

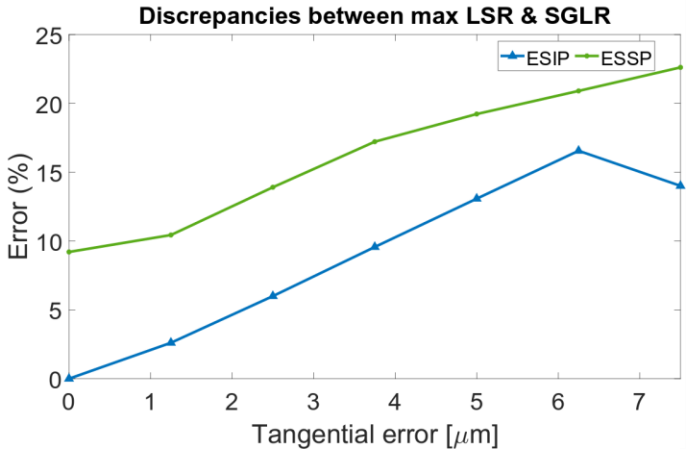

Figure 105. Discrepancies between the maximum LSR and SGLR results for configuration 2(Graph).

In more depth, in Table 14 & Table 15 the numerical values of the mentioned discrepancies for every case of study in each planet are gathered. These values prove how the phasing creates a discrepancy in the results, but this discrepancy is uniform for the 3 planets. Then, the tangential error modifies this uniformity. In the ESIP configuration planet 1 behaves differently to planets 2 & 3, who have identical behaviour. On the contrary, in the ESSP

transmission the impact of the error is higher and modifies the behaviour of every planet, being the planet 3 the most affected. By this, this planet will be the one that provides the highest inaccuracy in the results obtained by this measuring technique.

Table 14. Discrepancies between the maximum LSR and SGLR results for configuration 2 (numerical results).

Case	Planet 1(%)	Planet 2(%)	Planet 3(%)
ESIP@et[0]	0	0	0
ESSP@et[0]	5.28	5.28	5.28
ESIP@et[1.25]	0.87	0.84	0.84
ESSP@et[1.25]	4.83	5.38	5.77
ESIP@et[2.5]	1.74	1.65	1.65
ESSP@et[2.5]	4.41	5.50	6.76
ESIP@et[3.75]	2.34	2.64	2.64
ESSP@et[3.75]	4.20	5.62	7.66
ESIP@et[5]	2.43	3.84	3.84
ESSP@et[5]	3.87	5.95	8.44
ESIP@et[6.25]	2.46	5.08	5.08
ESSP@et[6.25]	3.69	6.40	8.97
ESIP@et[7.5]	2.49	6.31	6.31
ESSP@et[7.5]	3.45	6.85	9.52

Table 15. Discrepancies between the maximum LSR and SGLR results for configuration 2 (numerical results).

Case	Planet 1(%)	Planet 2(%)	Planet 3(%)
ESIP@et[0]	0	0	0
ESSP@et[0]	9	9	9
ESIP@et[1.25]	2.31	2.61	2.61
ESSP@et[1.25]	7.44	9.24	10.44
ESIP@et[2.5]	2.97	6	6
ESSP@et[2.5]	6.48	9.36	13.91
ESIP@et[3.75]	3.09	9.57	9.57
ESSP@et[3.75]	5.31	9.87	17.22
ESIP@et[5]	3.24	13.08	13.08
ESSP@et[5]	4.71	11.01	19.23
ESIP@et[6.25]	3.12	16.56	16.56
ESSP@et[6.25]	4.35	12.03	20.91
ESIP@et[7.5]	3	14.01	14.01
ESSP@et[7.5]	3.39	12.51	22.62

Part IV

Chapter 7: Contributions, conclusions and future work

7.1. Contributions

In the context of this Ph.D. work several topics have been analysed in the context of the planetary gear transmissions employed in industrial applications. In all these different topics the common factor relies on the impact of the transmission geometry in its behaviour under different working conditions. In this work, the transmission geometry refers to the planet spacing and the mesh phasing, and the study of its behaviour is focused on the load sharing. In more detail, the following points can be highlighted:

- An analytical study of the conditions that classify the transmissions depending on their geometry has been performed in order to expand the previous conditions and understanding.
- The influence of the geometry in the behaviour of the planetary transmissions has been studied for different numbers of planets. Thus, the direct relation between the geometry and the load sharing in the transmission has been studied in depth, determining the impact that the geometry has on the load sharing.
- The impact that having floatability in the sun gear has in its behaviour was analysed either for the scenarios that are defined by the transmission geometry.

- Manufacturing errors in a context such as planetary transmissions are impossible to avoid, thus, this topic has been the subject of numerous studies. However, this work focuses on the impact of some of those errors in a variety of transmissions where the mesh phasing and the number of planets are modified.
- Finally, this work analyses in depth the use of strains measured in the root of the teeth in the sun gear, which is a measuring technique suggested in ("IEC61400 – 4: Design Requirements for wind turbine gearboxes," n.d.) in order to certify gearboxes for wind turbines. In this context, a numerical evaluation is made to establish the differences between the real load sharing, represented by the LSR, and the calculation of the load sharing from those strains. Consequently, the error made by such measuring technique with respect to the real load sharing were quantified in different scenarios.

7.2. Conclusions

After all the ideas presented in this work, several conclusions can be extracted in regards to the behaviour of planetary transmissions under different working conditions determined by its geometry. Also, the measuring techniques have been analysed and in view of the results obtained some conclusions are extracted in the following:

- Infinitely rigid systems with fixed elements are affected by the mesh phasing but not by the planet spacing. Thus, the load sharing of non-equally spaced transmissions is perfectly balanced for any in-phase transmission. On the contrary, the non-equal spacing modifies the sequence in the mesh phasing and makes a difference between the ESSP and NESSP transmissions.

- For any ESSP transmission with a floating sun, this will describe an orbit around the reference position with a number of closed loops equal to the number of planets.
- The change in the number of planets in a planetary transmission affects the influence of the floatability included in the support of the sun gear.
- Sequentially phased transmissions have a worse behaviour, in terms of load sharing, than the equal in-phase transmission, both for equally and non-equally spaced transmissions.
- Whenever an error exists, sequentially phased transmissions are more influenced by an equal error than an in-phase transmission. Thus, the imbalance created by such error is bigger in the sequentially phased transmission than in the in-phase one.
- Systems that are more rigid are more sensitive to any kind of error. This rigidity could be in the shape of a higher number of planets, higher stiffness in the wheels, or less load in the system given the fact that with a higher load the teeth will bend more and the load sharing becomes less abrupt.
- The results obtained prove that the influence of the radial pinhole position error is neither null nor negligible. It even gains in importance with the inclusion of sequential mesh phasing and the raise in the number of planets. However, the magnitude of the radial error studied is significantly bigger than the rest, thus, the tolerance for this error can be higher than for the tangential one.
- Higher loads provide a more uniform load sharing from the transmissions, due to the raise in the effective contact ratio, analogously to what happens with helical gears.
- The role of the tangential error as an imbalance-creator factor gains in importance with the increase of the number of planets. On the

contrary, the higher the number of planets, the less important the tooth thickness error is.

- For some errors size and a torque direction, there exists a nulling effect between tooth thickness and tangential errors for 3-planet planetary transmissions. This is just for in-phase configurations, whenever the error is small enough that the change in the mounting distance and pressure angle are negligible.
- The use of strain gauges in the sun gear tooth root to measure the load sharing in planetary transmissions prove to be inaccurate compared to the real load sharing in the transmissions.
- The accuracy of these measuring techniques is directly affected by the lack of continuous monitoring. This technique obtains a brief amount of the strains suffered on the teeth due to the contacts given the measuring during a time window.
- The mesh phasing proves to play a crucial role in the measuring procedure given the lack of synchronicity. The synchronization between the strain gauge acquisition and the imbalance-creating factor is crucial. In case of lack of synchronization, the gauge would miss the effect of temporary flaw.
- The error made by the measurements in the strain gauge raises with the growth of the tangential pinhole position error. The growth of this error proves to have different speeds depending on the size of the tangential error.
- Under any working condition, there exists an error in the calculation of the load sharing of a planetary transmission from the strains in the root of the sun gear teeth, just with the exception of any ideal ESIP transmission. The change in the working conditions will change the magnitude of the errors, but will not make it disappear.

7.3. Future works

Finally, this work is another step taken in a real complex topic that requires more study, both for its complexity and the interest that these transmissions have in the current society and in the near future. Thus, this work should be continued in order to understand better all the points made along this document and to enhance the understanding

- Virtual modelling: Some of the approaches presented in this work are also interesting in a context of helical gears. To this end, the model presented should be extended to a 3-D formulation.
- Study planetary transmissions with a number of planets higher than 5. Thus, different possibilities appear in terms of the sequential mesh phasing with an even number of planets.
- Geometrical influence: Analyse the impact of the planet spacing and mesh phasing in a dynamic model. Thus, the vibrational response of the transmission can be analysed.
- Manufacturing errors: Extend the scope of errors and include errors whose influence changes in time, thus, every contact would be modified.
- Inclusion of floatability in the gear supports to reduce the stiffness in the models and observe the influence of the orbits.
- Experimental measuring: The numerical analysis of experimental procedures by measuring strains should be expanded to more approaches, such as gauges in the ring gear or in the planet pins. To this aim, the approach for the FE model of the ring gear has to be changed in order to modify the boundary conditions and study the deflections in the body of the gear.
- Experimental measurements of strains in different locations along the planetary gearbox.

References

Abousleiman, V., & Velex, P. (2006). A hybrid 3D finite element/lumped parameter model for quasi-static and dynamic analyses of planetary/epicyclic gear sets. *Mechanism and Machine Theory*, *41*(6), 725–748. https://doi.org/10.1016/j.mechmachtheory.2005.09.005

Ajmi, M., & Velex, P. (2005). A model for simulating the quasi-static and dynamic behaviour of solid wide-faced spur and helical gears. *Mechanism and Machine Theory*, *40*(2), 173–190. https://doi.org/10.1016/j.mechmachtheory.2003.06.001

Ambarisha, V. K., & Parker, R. G. (2007). Nonlinear dynamics of planetary gears using analytical and finite element models. *Journal of Sound and Vibration*, *302*(3), 577–595. https://doi.org/10.1016/j.jsv.2006.11.028

Antolick, L. J., Branning, J. S., Wade, D. R., & Dempsey, P. J. (2010). Evaluation of gear condition indicator performance on rotorcraft fleet. In *Annual Forum Proceedings - AHS International* (Vol. 2, pp. 1110–1121).

Argyris, J., Fuentes, A., & Litvin, F. L. (2002). Computerized integrated approach for design and stress analysis of spiral bevel gears. *Computer Methods in Applied Mechanics and Engineering*, *191*(11–12), 1057–1095. https://doi.org/10.1016/S0045-7825(01)00316-4

Attia, A. Y. (1959). Dynamic Loading of Spur Gear Teeth. *Journal of Manufacturing Science and Engineering*, *81*(1), 1–7. https://doi.org/10.1115/1.4008220

August, R., & Kasuba, R. (1986a). Torsional vibrations and dynamic loads in a basic planetary gear system. *Journal of Vibration and Acoustics, Transactions of the ASME*, *108*(3), 348–353.

https://doi.org/10.1115/1.3269349

August, R., & Kasuba, R. (1986b). Torsional Vibrations and Dynamic Loads in a Basic Planetary Gear System. *Journal of Vibration, Acoustics, Stress, and Reliability in Design*, *108*(3), 348–353. https://doi.org/10.1115/1.3269349

Aurrekoetxea, H., Eng, M., Gearbox, G., Ocenda, I. R. De, Eng, E., & Gearbox, G. (n.d.). Experimental and theoretical study of Load mesh factor for different boundary conditions in wind gearbox planetary stages.

Bajpai, P., Kahraman, A., & Anderson, N. E. (2004). A surface wear prediction methodology for parallel-axis gear pairs. *Journal of Tribology*, *126*(3), 597–605. https://doi.org/10.1115/1.1691433

Bodas, A., & Kahraman, A. (2004). Influence of Carrier and Gear Manufacturing Errors on the Static Load Sharing Behavior of Planetary Gear Sets. *JSME International Journal Series C*, *47*(3), 908–915. https://doi.org/10.1299/jsmec.47.908

Boguski, B., Kahraman, A., & Nishino, T. (2012). A New Method to Measure Planet Load Sharing and Sun Gear Radial Orbit of Planetary Gear Sets. *Journal of Mechanical Design*, *134*(7), 071002. https://doi.org/10.1115/1.4006827

Botman, M. (1976). Epicyclic gear vibrations. *Journal of Manufacturing Science and Engineering, Transactions of the ASME*, *98*(3), 811–815. https://doi.org/10.1115/1.3439034

Brauer, J. (2002). Analytical geometry of straight conical involute gears. *Mechanism and Machine Theory*, *37*(1), 127–141. https://doi.org/10.1016/S0094-114X(01)00062-3

Brauer, J. (2005). Transmission error in anti-backlash conical involute gear transmissions: A global-local FE approach. *Finite Elements in Analysis and Design*, *41*(5), 431–457. https://doi.org/10.1016/j.finel.2004.04.007

Brauer, Jesper. (2004). A general finite element model of involute gears. *Finite Elements in Analysis and Design*, *40*(13–14), 1857–1872. https://doi.org/10.1016/j.finel.2004.02.002

Caso, E., Fernandez-del-Rincon, A., Garcia, P., Iglesias, M., & Viadero, F. (2020). Monitoring of misalignment in low speed geared shafts with acoustic emission sensors. *Applied Acoustics*, *159*, 107092. https://doi.org/10.1016/j.apacoust.2019.107092

Chaari, F., Fakhfakh, T., Hbaieb, R., Louati, J., & Haddar, M. (2006). Influence of manufacturing errors on the dynamic behavior of planetary gears. *The International Journal of Advanced Manufacturing Technology*, *27*(7–8), 738–746. https://doi.org/10.1007/s00170-004-2240-2

Chung, M. Y., & Shaw, D. (2007). Parametric study of dynamics of worm and worm-gear set under suddenly applied rotating angle. *Journal of Sound and Vibration*, *304*(1–2), 246–262. https://doi.org/10.1016/j.jsv.2007.02.022

Colmenar-Santos, A., Perera-Perez, J., Borge-Diez, D., & Depalacio-Rodríguez, C. (2016). Offshore wind energy: A review of the current status, challenges and future development in Spain. *Renewable and Sustainable Energy Reviews*, *64*, 1–18. https://doi.org/10.1016/j.rser.2016.05.087

Cooley, C. G., & Parker, R. G. (2014). A Review of Planetary and Epicyclic Gear Dynamics and Vibrations Research. *Applied Mechanics Reviews*, *66*(4), 040804. https://doi.org/10.1115/1.4027812

Cunliffe, F., Smith, J. D., & Welbourn, D. B. (1974). Dynamic tooth loads in epicyclic gears. *Journal of Manufacturing Science and Engineering, Transactions of the ASME*, *96*(2), 578–584. https://doi.org/10.1115/1.3438367

Dai, X., Cooley, C. G., & Parker, R. G. (2016). Dynamic tooth root strains

and experimental correlations in spur gear pairs. *Mechanism and Machine Theory*, (101), 60–74. https://doi.org/10.1016/j.mechmachtheory.2016.03.010

Delgado, I. R., Dempsey, P. J., Antolick, L. J., & Wade, D. R. (2013). Continued evaluation of gear condition indicator performance on rotorcraft fleet. In *American Helicopter Society International - Airworthiness, CBM and HUMS Specialists' Meeting 2013* (pp. 344–365).

Diez-Ibarbia, A. (2016). *Estudio de la eficiencia y fenomenos disipativos de engranajes con correcciones de tallado y modificaciones del perfil.*

Du, W., Zhao, S., Jin, L., Gao, J., & Zheng, Z. (2021). Optimization design and performance comparison of different powertrains of electric vehicles. *Mechanism and Machine Theory*, *156*, 104143. https://doi.org/10.1016/j.mechmachtheory.2020.104143

Erltenel, T., & Parker, R. G. (2005). A static and dynamic model for three-dimensional, multi-mesh gear systems. In *Proceedings of the ASME International Design Engineering Technical Conferences and Computers and Information in Engineering Conference - DETC2005* (Vol. 5, pp. 945–956).

Fang, S., Song, J., Song, H., Tai, Y., Li, F., & Sinh Nguyen, T. (2016). Design and control of a novel two-speed Uninterrupted Mechanical Transmission for electric vehicles. *Mechanical Systems and Signal Processing*, *75*, 473–493. https://doi.org/https://doi.org/10.1016/j.ymssp.2015.07.006

Faulstich, S., Hahn, B., & Tavner, P. J. (2011). Wind turbine downtime and its importance for offshore deployment. *Wind Energy*, *14*(3), 327–337. https://doi.org/10.1002/we.421

Fernández del Rincón, A. (2010). Modelo Avanzado Para El Estudio Del Comportamiento Vibratorio De Sistemas De Transmisión Mediante Engranajes.

Fernandez del Rincon, A., Viadero, F., Iglesias, M., García, P., & Sancibrian,

R. (2013). A model for the study of meshing stiffness in spur gear transmissions. *Mechanism and Machine Theory*, *61*, 30–58. https://doi.org/10.1016/j.mechmachtheory.2012.10.008

Ferrando-Chacon, J. L. (2015). Fault Detection in Rotating Machinery Using Acoustic Emission, (October).

Fischer, K., & Coronado, D. (2015). Condition Monitoring of Wind Turbines : State of the Art , User Experience and Recommendations, (January), 89.

Fox, R. G. (2005). The History Of Helicopter Safety. *International Helicopter Safety Symposium*, 1–19.

Gallego-Calderon, J., & Natarajan, A. (2015). Assessment of wind turbine drive-train fatigue loads under torsional excitation. *Engineering Structures*, *103*, 189–202. https://doi.org/10.1016/j.engstruct.2015.09.008

García, P., Sanchez-Espiga, J., Fernandez-del-Rincon, A., De-Juan, A., Iglesias, M., Diez-Ibarbia, A., & Viadero, F. (2019). *Access systems to marine energy production units. Review and new challenges. Mechanisms and Machine Science* (Vol. 59). https://doi.org/10.1007/978-3-319-98020-1_21

Gill-Jeong, C. (2010). Numerical study on reducing the vibration of spur gear pairs with phasing. *Journal of Sound and Vibration*, *329*(19), 3915–3927. https://doi.org/10.1016/j.jsv.2010.04.005

Gioia, N., Peeters, C., Guillaume, P., & Helsen, J. (2019). Identification of noise, vibration and harshness behavior of wind turbine drivetrain under different operating conditions. *Energies*, *12*(17). https://doi.org/10.3390/en12173401

GLOBAL EV OUTLOOK 2020. (n.d.). Retrieved November 25, 2020, from https://www.iea.org/reports/global-ev-outlook-2020

Global Wind Energy Council. (2020). Global Offshore Wind: Annual Market

Report 2020. *Global Offshore Wind Report 2020*, (February), 130. Retrieved from https://gwec.net/wp-content/uploads/dlm_uploads/2020/08/GWEC-offshore-wind-2020-5.pdf

Gu, X., & Velex, P. (2011). *A lumped parameter model to analyse the dynamic load sharing in planetary gears with planet errors. Applied Mechanics and Materials* (Vol. 86). https://doi.org/10.4028/www.scientific.net/AMM.86.374

Gu, X., & Velex, P. (2012). A dynamic model to study the influence of planet position errors in planetary gears. *Journal of Sound and Vibration*, *331*(20), 4554–4574. https://doi.org/10.1016/j.jsv.2012.05.007

GWEC. (2019). GWEC, Global wind power report; 2018, (April).

Helsen, J., Vanhollebeke, F., Marrant, B., Vandepitte, D., & Desmet, W. (2011). Multibody modelling of varying complexity for modal behaviour analysis of wind turbine gearboxes. *Renewable Energy*, *36*(11), 3098–3113. https://doi.org/10.1016/j.renene.2011.03.023

Hidaka, T. (1979). Dynamic behavior of planetary gear bulletin 6. *JSME International Journal Series C*, *1*(3), 1026–1033. https://doi.org/10.1061/ASCE1090-0241200312911212

Hidaka, Teruaki, & Terauchi, Y. (1976). Dynamic Behavior of Planetary Gear : 1st Report Load Distribution in Planetary Gear. *Bulletin of JSME*, *19*(132), 690–698. https://doi.org/10.1299/jsme1958.19.690

Hidaka, Teruaki, Terauchi, Y., & Ishioka, K. (1976). Dynamic Behavior of Planetary Gear : 2nd Report, Displacement of Sun Gear and Ring Gear. *Bulletin of JSME*, *19*(138), 1563–1570. https://doi.org/10.1299/jsme1958.19.1563

Hidaka, Teruaki, Terauchi, Y., & Nagamura, K. (1979a). Dynamic Behavior of Planetary Gear : 6th Report, Influence of Meshing-Phase. *Bulletin of JSME*, *22*(169), 1026–1033. https://doi.org/10.1299/jsme1958.22.1026

Hidaka, Teruaki, Terauchi, Y., & Nagamura, K. (1979b). Dynamic Behavior of Planetary Gear : 7th Report, Influence of the Thickness of the Ring Gear. *Bulletin of JSME*, *22*(170), 1142–1149. https://doi.org/10.1299/jsme1958.22.1142

Hidaka, Teruaki, Terauchi, Y., Nohara, M., & Oshita, J. (1977). Dynamic Behavior of Planetary Gear : 3rd Report, Displacement of Ring Gear in Direction of Line of Action. *Bulletin of JSME*, *20*(150), 1663–1672. https://doi.org/10.1299/jsme1958.20.1663

Howard, I., Jia, S., & Wang, J. (2001). The dynamic modelling of a spur gear in mesh including friction and a crack. *Mechanical Systems and Signal Processing*, *15*(5), 831–853. https://doi.org/10.1006/mssp.2001.1414

Hu, Y., Talbot, D., & Kahraman, A. (2018). A Load Distribution Model for Planetary Gear Sets. *Journal of Mechanical Design*, *140*(5), 053302. https://doi.org/10.1115/1.4039337

IEC61400 – 4: Design Requirements for wind turbine gearboxes. (n.d.).

Iglesias, M., Fernandez del Rincon, A., de-Juan, A., Diez-Ibarbia, A., Garcia, P., & Viadero, F. (2015). Advanced model for the calculation of meshing forces in spur gear planetary transmissions. *Meccanica*, *50*(7), 1869–1894. https://doi.org/10.1007/s11012-015-0130-3

Iglesias, M., Fernandez del Rincon, A., de-Juan, A., Garcia, P., Diez-Ibarbia, A., & Viadero, F. (2017). Planetary transmission load sharing: Manufacturing errors and system configuration study. *Mechanism and Machine Theory*, *111*, 21–38. https://doi.org/10.1016/j.mechmachtheory.2016.12.010

Iglesias, Miguel, Fernández, A., De-Juan, A., Sancibrián, R., & García, P. (2013). Planet position errors in planetary transmission: Effect on load sharing and transmission error. *Frontiers of Mechanical Engineering*, *8*(1), 80–87. https://doi.org/10.1007/s11465-013-0362-7

Iglesias Santamaría, M. (2013). Modelo para el estudio del comportamiento

vibratorio de transmisiones planetarias.

Inalpolat, M., & Kahraman, A. (2009). A theoretical and experimental investigation of modulation sidebands of planetary gear sets. *Journal of Sound and Vibration*, *323*(3–5), 677–696. https://doi.org/10.1016/j.jsv.2009.01.004

Inalpolat, Murat, & Kahraman, A. (2010). A dynamic model to predict modulation sidebands of a planetary gear set having manufacturing errors. *Journal of Sound and Vibration*, *329*(4), 371–393. https://doi.org/10.1016/j.jsv.2009.09.022

ISO 6336-1. (2006). Calculation of load capacity of spur and helical gears, *2006*, 13.

Joshi, R., & Darpe, A. K. (2019). *Detection of Gear Tooth Crack in a Wind Turbine Planetary Gearbox. Mechanisms and Machine Science* (Vol. 62). https://doi.org/10.1007/978-3-319-99270-9_38

Kahnamouei, J. T., & Yang, J. (2021). Development and verification of a computationally efficient stochastically linearized planetary gear train model with ring elasticity. *Mechanism and Machine Theory*, *155*. https://doi.org/10.1016/j.mechmachtheory.2020.104061

Kahraman, A. (1993). Effect of axial vibrations on the dynamics of a helical gear pair. *Journal of Vibration and Acoustics, Transactions of the ASME*, *115*(1), 33–39. https://doi.org/10.1115/1.2930311

Kahraman, A. (1994). Natural Modes of Planetary Gear Trains. *Journal of Sound and Vibration*, *173*(1), 125–130. https://doi.org/10.1006/jsvi.1994.1222

Kahraman, A. (1994a). Dynamic Analysis of a Multi-Mesh Helical Gear Train. *Journal of Mechanical Design*, *116*(3), 706–712. https://doi.org/10.1115/1.2919440

Kahraman, A. (1994b). Planetary gear train dynamics. *Journal of Mechanical*

Design, Transactions of the ASME, *116*(3), 713–720. https://doi.org/10.1115/1.2919441

Kahraman, A, Kharazi, A. A., & Umrani, M. (2003). A deformable body dynamic analysis of planetary gears with thin rims. *Journal of Sound and Vibration*, *262*(3), 752–768. https://doi.org/10.1016/S0022-460X(03)00122-6

Kahraman, A, & Vijayakar, S. (2001). Effect of internal gear flexibility on the quasi-static behavior of a planetary gear set. *Journal of Mechanical Design, Transactions of the ASME*, *123*(3), 408–415. https://doi.org/10.1115/1.1371477

Kahraman, Ahmet. (1994). Load sharing characteristics of planetary transmissions. *Mechanism and Machine Theory*, *29*(8), 1151–1165. https://doi.org/10.1016/0094-114X(94)90006-X

Kahraman, Ahmet. (1999). Static Load Sharing Characteristics of Transmission Planetary Gear Sets : Model and Experiment. *Transmission and Driveline Systems Symposium*, (1), 1–10. https://doi.org/10.4271/1999-01-1050

Kahraman, Ahmet, & Vijayakar, S. (2001). Effect of Internal Gear Flexibility on the Quasi-Static Behavior of a Planetary Gear Set. *Journal of Mechanical Design*, *123*(3), 408. https://doi.org/10.1115/1.1371477

Kalogeri, C., Galanis, G., Spyrou, C., Diamantis, D., Baladima, F., Koukoula, M., & Kallos, G. (2017). Assessing the European offshore wind and wave energy resource for combined exploitation. *Renewable Energy*, *101*, 244–264. https://doi.org/10.1016/j.renene.2016.08.010

Karki, R. (2017). *Reliability of Renewable Power Systems. Encyclopedia of Sustainable Technologies* (Vol. 4). Elsevier. https://doi.org/10.1016/B978-0-12-409548-9.10147-2

Kasuba, R., & Evans, J. W. (1981). An extended model for determining dynamic loads in spur gearing. *Journal of Mechanical Design,*

Transactions of the ASME, *103*(2), 398–409. https://doi.org/10.1115/1.3254920

Li, S. (2007). Finite element analyses for contact strength and bending strength of a pair of spur gears with machining errors, assembly errors and tooth modifications. *Mechanism and Machine Theory*, *42*(1), 88–114. https://doi.org/10.1016/j.mechmachtheory.2006.01.009

Ligata, H., Kahraman, A., & Singh, A. (2008). An Experimental Study of the Influence of Manufacturing Errors on the Planetary Gear Stresses and Planet Load Sharing. *Journal of Mechanical Design*, *130*(4), 041701. https://doi.org/10.1115/1.2885194

Ligata, H., Kahraman, A., & Singh, A. (2009). A Closed-Form Planet Load Sharing Formulation for Planetary Gear Sets Using a Translational Analogy. *Journal of Mechanical Design*, *131*(2), 021007. https://doi.org/10.1115/1.3042160

Lin, J., & Parker, R. G. (2002). Planetary gear parametric instability caused by mesh stiffness variation. *Journal of Sound and Vibration*, *249*(1), 129–145. https://doi.org/10.1006/jsvi.2001.3848

Lin, J., & Parker, R. G. (2007). Planetary gear parametric instability, (September).

Lin, J, & Parker, R. G. (1999). Sensitivity of Planetary Gear Natural Frequencies and Vibration Modes to Model Parameters. *Journal of Vibration and Acoustics*, *132*(1), 11006. https://doi.org/10.1115/1.4000461

Lin, Jian, & Parker, R. G. (1999). Analytical Characterization of the Unique Properties of Planetary Gear Free Vibration. *Journal of Vibration and Acoustics*, *121*(3), 316–321. https://doi.org/10.1115/1.2893982

Litvin, F.L., Fuentes, A., Gonzalez-Perez, I., Carvenali, L., Kawasaki, K., & Handschuh, R. F. (2003). Modified involute helical gears: Computerized design, simulation of meshing and stress analysis. *Computer Methods in*

Applied Mechanics and Engineering, *192*(33–34), 3619–3655. https://doi.org/10.1016/S0045-7825(03)00367-0

Litvin, F.L., Gonzalez-Perez, I., Yukishima, K., Fuentes, A., & Hayasaka, K. (2007). Design, simulation of meshing, and contact stresses for an improved worm gear drive. *Mechanism and Machine Theory*, *42*(8), 940–959. https://doi.org/10.1016/j.mechmachtheory.2006.08.005

Litvin, F.L., Tsung, W. J., Coy, J. J., Handschuh, R. F., & Tsay, C. B. P. (1986). New generation methods for spur, helical, and spiral-bevel gears.

Litvin, Faydor L., & Fuentes, A. (2004). *Gear Geometry and Applied Theory*. Cambridge University Press. https://doi.org/10.1017/CBO9780511547126

Liu, J., Pang, R., Ding, S., & Li, X. (2020). Vibration analysis of a planetary gear with the flexible ring and planet bearing fault. *Measurement*, *165*, 108100. https://doi.org/10.1016/j.measurement.2020.108100

Liu, X., Yang, Y., & Zhang, J. (2018). Resultant vibration signal model based fault diagnosis of a single stage planetary gear train with an incipient tooth crack on the sun gear. *Renewable Energy*, *122*, 65–79. https://doi.org/10.1016/j.renene.2018.01.072

Ma, P., & Botman, M. (1985). Load sharing in a planetary gear stage in the presence of gear errors and misalignment. *Journal of Mechanical Design, Transactions of the ASME*, *107*(1), 4–10. https://doi.org/10.1115/1.3258694

McFadden, P. D., & Smith, J. D. (1985). An Explanation for the Asymmetry of the Modulation Sidebands about the Tooth Meshing Frequency in Epicyclic Gear Vibration. *Proceedings of the Institution of Mechanical Engineers, Part C: Journal of Mechanical Engineering Science*, *199*(1), 65–70. https://doi.org/10.1243/PIME_PROC_1985_199_092_02

Meltzer, G., & Ivanov, Y. Y. (2003). Fault detection in gear drives with non-stationary rotational speed PartI: The time frequency approach.

Mechanical Systems and Signal Processing, *17*(5), 1033–1047. https://doi.org/10.1006/mssp.2002.1530

Parker, R. G., & Lin, J. (2004). Mesh Phasing Relationships in Planetary and Epicyclic Gears. *Journal of Mechanical Design*, *126*(2), 365. https://doi.org/10.1115/1.1667892

Parker, R G, Agashe, V., & Vijayakar, S. M. (2000). Dynamic response of a planetary gear system using a finite element/contact mechanics model. *Journal of Mechanical Design, Transactions of the ASME*, *122*(3), 304–310. https://doi.org/10.1115/1.1286189

Parker, Robert G. (2000). Physical explanation for the effectiveness of planet phasing to suppress planetary gear vibration. *Journal of Sound and Vibration*, *236*(4), 561–573. https://doi.org/10.1006/jsvi.1999.2859

Parker, Robert G., Agashe, V., & Vijayakar, S. M. (2000). Dynamic Response of a Planetary Gear System Using a Finite Element/Contact Mechanics Model. *Journal of Mechanical Design*, *122*(3), 304. https://doi.org/10.1115/1.1286189

Parker, Robert G., & Wu, X. (2010). Vibration modes of planetary gears with unequally spaced planets and an elastic ring gear. *Journal of Sound and Vibration*, *329*(11), 2265–2275. https://doi.org/10.1016/j.jsv.2009.12.023

Peng, D., Smith, W. A., Randall, R. B., & Peng, Z. (2019). Use of mesh phasing to locate faulty planet gears. *Mechanical Systems and Signal Processing*, *116*, 12–24. https://doi.org/10.1016/j.ymssp.2018.06.035

Peng, H., Qin, D., Hu, J., & Fu, C. (2020). Synthesis and analysis method for powertrain configuration of single motor hybrid electric vehicle. *Mechanism and Machine Theory*, *146*, 103731. https://doi.org/10.1016/j.mechmachtheory.2019.103731

Qiu, X., Han, Q., & Chu, F. (2015). Load-sharing characteristics of planetary gear transmission in horizontal axis wind turbines. *Mechanism and Machine Theory*, *92*, 391–406.

https://doi.org/10.1016/j.mechmachtheory.2015.06.004

Qiu, Xinghui, Han, Q., & Chu, F. (2015). Load-sharing characteristics of planetary gear transmission in horizontal axis wind turbines. *Mechanism and Machine Theory*, *92*, 391–406. https://doi.org/10.1016/J.MECHMACHTHEORY.2015.06.004

Sainsot, P., Velex, P., & Duverger, O. (2004). Contribution of gear body to tooth deflections - A new bidimensional analytical formula. *Journal of Mechanical Design, Transactions of the ASME*, *126*(4), 748–752. https://doi.org/10.1115/1.1758252

Sanchez-Espiga, J., Fernandez-del-Rincon, A., Iglesias, M., & Viadero, F. (2019). *Influence of the phase in planetary gears load sharing and transmission error. Mechanisms and Machine Science* (Vol. 73). https://doi.org/10.1007/978-3-030-20131-9_105

Sanchez-Espiga, J., Fernandez-del-Rincon, A., Iglesias, M., & Viadero, F. (2020). Influence of errors in planetary transmissions load sharing under different mesh phasing. *Mechanism and Machine Theory*, *153*. https://doi.org/10.1016/j.mechmachtheory.2020.104012

Saxena, A., Chouksey, M., & Parey, A. (2017). Effect of mesh stiffness of healthy and cracked gear tooth on modal and frequency response characteristics of geared rotor system. *Mechanism and Machine Theory*, *107*(May 2016), 261–273. https://doi.org/10.1016/j.mechmachtheory.2016.10.006

Seol, I. H., & Litvin, F. L. (1996). Computerized design, generation and simulation of meshing and contact of worm-gear drives with improved geometry. *Computer Methods in Applied Mechanics and Engineering*, *138*(1–4), 73–103. https://doi.org/10.1016/0045-7825(95)00976-0

Sheveleva, G. I., Volkov, A. E., & Medvedev, V. I. (2007). Algorithms for analysis of meshing and contact of spiral bevel gears. *Mechanism and Machine Theory*, *42*(2), 198–215.

https://doi.org/10.1016/j.mechmachtheory.2006.02.009

Shimizu, H., Harada, J., Bland, C., Kawakami, K., & Chan, L. (1997). Advanced concepts in electric vehicle design. *IEEE Transactions on Industrial Electronics*, *44*(1), 14–18. https://doi.org/10.1109/41.557494

Shweiki, S., Mundo, D., Korta, J., Oranges, P., & Palermo, A. (2016). Investigation of mesh phasing in a planetary gear train using combined FE and multibody simulations. *Isma*, 1407–1416.

Singh, A. (2005). Application of a System Level Model to Study the Planetary Load Sharing Behavior. *Journal of Mechanical Design*, *127*(3), 469. https://doi.org/10.1115/1.1864115

Singh, A. (2010). Load sharing behavior in epicyclic gears: Physical explanation and generalized formulation. *Mechanism and Machine Theory*, *45*(3), 511–530. https://doi.org/10.1016/j.mechmachtheory.2009.10.009

Singh, A. (2011). Epicyclic Load Sharing Map - Development and validation. *Mechanism and Machine Theory*, *46*(5), 632–646. https://doi.org/10.1016/j.mechmachtheory.2011.01.001

Singh, A., Kahraman, A., & Ligata, H. (2008). Internal Gear Strains and Load Sharing in Planetary Transmissions: Model and Experiments. *Journal of Mechanical Design*, *130*(7), 072602. https://doi.org/10.1115/1.2890110

Sirichai, S. (1999). Torsional properties of spur gears in mesh using nonlinear finite element analysis.

Teng, W., Ding, X., Cheng, H., Han, C., Liu, Y., & Mu, H. (2019). Compound faults diagnosis and analysis for a wind turbine gearbox via a novel vibration model and empirical wavelet transform. *Renewable Energy*, *136*, 393–402. https://doi.org/10.1016/j.renene.2018.12.094

Theodossiades, S., & Natsiavas, S. (2001). Geared rotordynamic systems on hydrodynamic bearings. In *Proceedings of the ASME Design Engineering*

Technical Conference (Vol. 6 A, pp. 1099–1107).

Tian, Y., Zhang, N., Zhou, S., & Walker, P. D. (2020). Model and gear shifting control of a novel two-speed transmission for battery electric vehicles. *Mechanism and Machine Theory*, *152*. https://doi.org/10.1016/j.mechmachtheory.2020.103902

Umezawa, K., Sato, T., & Ishikawa, J. (1984). Simulation on rotational vibration of spur gears. *Bulletin of the JSME*, *27*(223), 102–109. https://doi.org/10.1299/jsme1958.27.102

Velex, P., & Maatar, M. (1996). A mathematical model for analyzing the influence of shape deviations and mounting errors on gear dynamic behaviour. *Journal of Sound and Vibration*, *191*(5), 629–660. https://doi.org/10.1006/jsvi.1996.0148

Velex, Ph., & Flamand, L. (1996). Dynamic Response of Planetary Trains to Mesh Parametric Excitations. *Journal of Mechanical Design*, *118*(1), 7. https://doi.org/10.1115/1.2826860

Viadero, F., Fernández, A., Iglesias, M., De-Juan, A., Liaño, E., & Serna, M. A. (2014). Non-stationary dynamic analysis of a wind turbine power drivetrain: Offshore considerations. *Applied Acoustics*, *77*, 204–211. https://doi.org/10.1016/j.apacoust.2013.10.006

Vijayakar, S. (1991). A combined surface integral and finite element solution for a three-dimensional contact problem. *International Journal for Numerical Methods in Engineering*, *31*(3), 525–545. https://doi.org/10.1002/nme.1620310308

Wang, Jainde. (n.d.). 14464_Wang, Jiande 2003.pdf.

Wang, Jungang, Yang, S., Liu, Y., & Mo, R. (2019). Analysis of load-sharing behavior of the multistage planetary gear train used in wind generators: Effects of random wind load. *Applied Sciences (Switzerland)*, *9*(24). https://doi.org/10.3390/app9245501

Weber, C. Banaschek, K. (1951). *The deformation of loaded gears and the effect on their load carrying capacity.* (D. of Scientific & and I. Research, Eds.). London.

Wesley Blankenship, G., & Singh, R. (1995a). A new gear mesh interface dynamic model to predict multi-dimensional force coupling and excitation. *Mechanism and Machine Theory*, *30*(1), 43–57. https://doi.org/10.1016/0094-114X(94)00018-G

Wesley Blankenship, G., & Singh, R. (1995b). Dynamic force transmissibility in helical gear pairs. *Mechanism and Machine Theory*, *30*(3), 323–339. https://doi.org/10.1016/0094-114X(94)00048-P

Wildhaber, E. (1923). Measuring Tooth Thickness of Involute Gears, 1923.

Wink, C. H., & Serpa, A. L. (2005). Investigation of tooth contact deviations from the plane of action and their effects on gear transmission error. *Proceedings of the Institution of Mechanical Engineers, Part C: Journal of Mechanical Engineering Science*, *219*(5), 501–509. https://doi.org/10.1243/095440605X16983

Wink, C. H., & Serpa, A. L. (2008). Performance assessment of solution methods for load distribution problem of gear teeth. *Mechanism and Machine Theory*, *43*(1), 80–94. https://doi.org/10.1016/j.mechmachtheory.2006.12.010

Wojnarowski, J., & Onishchenko, V. (2003). Tooth wear effects on spur gear dynamics. *Mechanism and Machine Theory*, *38*(2), 161–178. https://doi.org/10.1016/S0094-114X(02)00091-5

Wu, X., & Parker, R. G. (2008). Modal properties of planetary gears with an elastic continuum ring gear. *Journal of Applied Mechanics, Transactions ASME*, *75*(3), 310141–3101412. https://doi.org/10.1115/1.2839892

Yuksel, C., & Kahraman, A. (2004). Dynamic tooth loads of planetary gear sets having tooth profile wear. *Mechanism and Machine Theory*, *39*(7), 695–715. https://doi.org/10.1016/j.mechmachtheory.2004.03.001

Zhang, C., Zhang, S., Han, G., & Liu, H. (2017). Power Management Comparison for a Dual-Motor-Propulsion System Used in a Battery Electric Bus. *IEEE Transactions on Industrial Electronics*, *64*(5), 3873–3882. https://doi.org/10.1109/TIE.2016.2645166

Zhang, J., Fang, Z., Cao, X., & Deng, X. (2007). The modified pitch cone design of the hypoid gear: Manufacture, stress analysis and experimental tests. *Mechanism and Machine Theory*, *42*(2), 147–158. https://doi.org/10.1016/j.mechmachtheory.2006.09.008

Zhu, C., Xu, X., Liu, H., Luo, T., & Zhai, H. (2014). Research on dynamical characteristics of wind turbine gearboxes with flexible pins. *Renewable Energy*, *68*, 724–732. https://doi.org/10.1016/j.renene.2014.02.047

Zountouridou, E. I., Kiokes, G. C., Chakalis, S., Georgilakis, P. S., & Hatziargyriou, N. D. (2015). Offshore floating wind parks in the deep waters of Mediterranean Sea. *Renewable and Sustainable Energy Reviews*, *51*, 433–448. https://doi.org/10.1016/j.rser.2015.06.027

ANNEX: Numerical results

A.I. GEOMETRY

Geometrical verifications of the conditions for the classification of the transmissions.

A.I.1. 3-planet transmissions

Table 16. Numerical verification of the angular spacing (3-planet transmission).

N=3	k_1	k_2	k_3
ESIP	0	80	160
ESSP	0	80	160
NESIP	0	80	176
NESSP	0	82	182
NESAP	0	84	162

Table 17. Numerical results to the mesh phasing (3-planet transmission).

N=3	n_1	n_2	n_3
ESIP	0	55	110
ESSP	0	53.333	110.667
NESIP	0	55	121
NESSP	0	56.375	125.125
NESAP	0	57.75	111.375

A.I.2. 5-planet transmissions

Table 18. Numerical verification of the angular spacing (5-planet transmission).

N=5	k_1	k_2	k_3	k_4	k_5
ESIP	0	48	96	144	192
ESSP	0	48	96	144	192
NESIP	0	48	80	144	208
NESSP	0	35	79	148	202
NESAP	0	46	97	145	204

Table 19. Numerical results to the mesh phasing (5-planet transmission).

N=5	n_1	n_2	n_3	n_4	n_5
ESIP	0	33	66	99	132
ESSP	0	33.2	66.4	99.6	132.8
NESIP	0	33	55	99	143
NESSP	0	24.0625	54.3125	101.75	138.875
NESAP	0	31.625	66.6875	99.6875	140.25

A.II. Errors

Numerical values of the LSR results presented in section 5.5.

A.II.1 Configuration 1:

Table 20. LSR in 3-planet ESIP 1200 Nm CCW (Conf. 1).

	Case 1	Case 2	Case 3	Case 4	Case 5	Case 6
Max LSR	0.3937	0.3396	0.3937	0.4018	0.4541	0.4665
Min LSR	0.3032	0.3302	0.3032	0.2991	0.273	0.2668

Table 21. LSR in 3-planet ESIP 1200 Nm CW (Conf. 1).

	Case 1	Case 2	Case 3	Case 4	Case 5	Case 6
Max LSR	0.3629	0.3397	0.3927	0.3605	0.3333	0.3461
Min LSR	0.2741	0.3301	0.3036	0.279	0.3333	0.3269

Table 22. LSR in 3-planet ESIP 3600 Nm CCW (Conf. 1).

	Case 1	Case 2	Case 3	Case 4	Case 5	Case 6
Max LSR	0.3557	0.3363	0.3557	0.3587	0.378	0.3838
Min LSR	0.3222	0.3318	0.3221	0.3207	0.311	0.3081

Table 23. LSR in 3-planet ESIP 3600 Nm CW (Conf. 1).

	Case 1	Case 2	Case 3	Case 4	Case 5	Case 6
Max LSR	0.3437	0.3358	0.3542	0.3433	0.3333	0.3396
Min LSR	0.3125	0.3321	0.3229	0.3134	0.3333	0.3302

Table 24. LSR in 3-planet ESSP 1200 Nm CCW (Conf. 1).

	Case 1	Case 2	Case 3	Case 4	Case 5	Case 6
Max LSR	0.4116	0.3616	0.4116	0.4166	0.4683	0.4782
Min LSR	0.2664	0.2899	0.2664	0.2641	0.2402	0.2361

Table 25. LSR in 3-planet ESSP 1200 Nm CW (Conf. 1).

	Case 1	Case 2	Case 3	Case 4	Case 5	Case 6
Max LSR	0.3865	0.362	0.413	0.3838	0.3571	0.367
Min LSR	0.2419	0.2899	0.2661	0.2466	0.292	0.2877

Table 26. LSR in 3-planet ESSP 3600 Nm CCW (Conf. 1).

	Case 1	Case 2	Case 3	Case 4	Case 5	Case 6
Max LSR	0.378	0.3596	0.378	0.3798	0.398	0.4016
Min LSR	0.2872	0.2966	0.2872	0.2862	0.277	0.2751

Table 27. LSR in 3-planet ESSP 3600 Nm CW (Conf. 1).

	Case 1	Case 2	Case 3	Case 4	Case 5	Case 6
Max LSR	0.3701	0.3615	0.3788	0.3692	0.3598	0.363
Min LSR	0.2746	0.291	0.2831	0.2762	0.2918	0.2903

Table 28. LSR in 5-planet ESIP 1200 Nm CCW (Conf. 1).

	Case 1	Case 2	Case 3	Case 4	Case 5	Case 6
Max LSR	0.2717	0.2086	0.2121	0.2777	0.2892	0.2957
Min LSR	0.1821	0.1978	0.197	0.1806	0.1777	0.1761

Table 29. LSR in 5-planet ESIP 1200 Nm CW (Conf. 1).

	Case 1	Case 2	Case 3	Case 4	Case 5	Case 6
Max LSR	0.2175	0.2071	0.2151	0.2159	0.2167	0.215
Min LSR	0.1298	0.1982	0.1962	0.1363	0.1332	0.1399

Table 30. LSR in 5-planet ESIP 3600 Nm CCW (Conf. 1).

	Case 1	Case 2	Case 3	Case 4	Case 5	Case 6
Max LSR	0.2247	0.2029	0.2041	0.2271	0.2293	0.232
Min LSR	0.1938	0.1993	0.199	0.1932	0.1927	0.192

Table 31. LSR in 5-planet ESIP 3600 Nm CW (Conf. 1).

	Case 1	Case 2	Case 3	Case 4	Case 5	Case 6
Max LSR	0.2061	0.2028	0.2051	0.2057	0.2054	0.2049
Min LSR	0.1755	0.1993	0.1987	0.1773	0.1783	0.1804

Table 32. LSR in 5-planet ESSP 1200 Nm CCW (Conf. 1).

	Case 1	Case 2	Case 3	Case 4	Case 5	Case 6
Max LSR	0.2299	0.2191	0.2203	0.2283	0.2305	0.2289
Min LSR	0.1159	0.172	0.1711	0.1211	0.1229	0.1284

Table 33. LSR in 5-planet ESSP 1200 Nm CW (Conf. 1).

	Case 1	Case 2	Case 3	Case 4	Case 5	Case 6
Max LSR	0.2802	0.2195	0.2211	0.2864	0.2934	0.3
Min LSR	0.1579	0.1711	0.1708	0.1566	0.1552	0.1538

Table 34. LSR in 5-planet ESSP 3600 Nm CCW (Conf. 1).

	Case 1	Case 2	Case 3	Case 4	Case 5	Case 6
Max LSR	0.2197	0.2157	0.2169	0.2191	0.2193	0.2187
Min LSR	0.1523	0.1715	0.1713	0.1541	0.1546	0.1569

Table 35. LSR in 5-planet ESSP 3600 Nm CW (Conf. 1).

	Case 1	Case 2	Case 3	Case 4	Case 5	Case 6
Max LSR	0.2357	0.2142	0.2154	0.2379	0.2398	0.242
Min LSR	0.1665	0.1712	0.1709	0.1662	0.1656	0.1653

A.II.2 Configuration 2:

Table 36. LSR in 3-planet ESIP 1200 Nm CCW (Conf. 2).

	Case 1	Case 2	Case 3	Case 4	Case 5	Case 6
Max LSR	0.3967	0.3592	0.4608	0.3851	0.3334	0.3592
Min LSR	0.2067	0.3204	0.2696	0.2299	0.3333	0.3204

Table 37. LSR in 3-planet ESIP 1200 Nm CW (Conf. 2).

	Case 1	Case 2	Case 3	Case 4	Case 5	Case 6
Max LSR	0.4605	0.3630	0.4605	0.4892	0.5882	0.6157
Min LSR	0.2697	0.3185	0.2697	0.2554	0.2059	0.1921

Table 38. LSR in 3-planet ESIP 3600 Nm CCW (Conf. 2).

	Case 1	Case 2	Case 3	Case 4	Case 5	Case 6
Max LSR	0.3553	0.3432	0.3774	0.3531	0.3334	0.3433
Min LSR	0.2894	0.3284	0.3113	0.2937	0.3333	0.3284

Table 39. LSR in 3-planet ESIP 3600 Nm CW (Conf. 2).

	Case 1	Case 2	Case 3	Case 4	Case 5	Case 6
Max LSR	0.3773	0.3478	0.3773	0.3922	0.4213	0.4348
Min LSR	0.3114	0.3261	0.3114	0.3044	0.2893	0.2826

Table 40. LSR in 3-planet ESSP 1200 Nm CCW (Conf. 2).

	Case 1	Case 2	Case 3	Case 4	Case 5	Case 6
Max LSR	0.4179	0.3813	0.4681	0.4066	0.3638	0.3814
Min LSR	0.1927	0.2712	0.2320	0.2097	0.2788	0.2711

Table 41. LSR in 3-planet ESSP 1200 Nm CW (Conf. 2).

	Case 1	Case 2	Case 3	Case 4	Case 5	Case 6
Max LSR	0.5144	0.4226	0.5144	0.5326	0.6244	0.6425
Min LSR	0.2128	0.2531	0.2128	0.2049	0.1646	0.1566

Table 42. LSR in 3-planet ESSP 3600 Nm CCW (Conf. 2).

	Case 1	Case 2	Case 3	Case 4	Case 5	Case 6
Max LSR	0.3908	0.3748	0.4096	0.3859	0.3679	0.3749
Min LSR	0.2872	0.2966	0.2872	0.2739	0.3036	0.3008

Table 43. LSR in 3-planet ESSP 3600 Nm CW (Conf. 2).

	Case 1	Case 2	Case 3	Case 4	Case 5	Case 6
Max LSR	0.4445	0.4098	0.4445	0.4507	0.4838	0.4901
Min LSR	0.2448	0.2636	0.2448	0.2418	0.2272	0.2245

Table 44. LSR in 5-planet ESIP 1200 Nm CCW (Conf. 2).

	Case 1	Case 2	Case 3	Case 4	Case 5	Case 6
Max LSR	0.2370	0.2295	0.2266	0.2303	0.2441	0.2363
Min LSR	0.0520	0.1926	0.1934	0.0788	0.0237	0.0549

Table 45. LSR in 5-planet ESIP 1200 Nm CW (Conf. 2).

	Case 1	Case 2	Case 3	Case 4	Case 5	Case 6
Max LSR	0.3507	0.2321	0.2268	0.3826	0.3876	0.4256
Min LSR	0.1623	0.1920	0.1933	0.1543	0.1531	0.1436

Table 46. LSR in 5-planet ESIP 3600 Nm CCW (Conf. 2).

	Case 1	Case 2	Case 3	Case 4	Case 5	Case 6
Max LSR	0.2129	0.2111	0.2076	0.2109	0.2136	0.2114
Min LSR	0.1483	0.1972	0.1981	0.1564	0.1456	0.1542

Table 47. LSR in 5-planet ESIP 3600 Nm CCW (Conf. 2).

	Case 1	Case 2	Case 3	Case 4	Case 5	Case 6
Max LSR	0.2519	0.2141	0.2078	0.2658	0.2563	0.2708
Min LSR	0.1870	0.1965	0.1980	0.1835	0.1859	0.1823

Table 48. LSR in 5-planet ESSP 1200 Nm CCW (Conf. 2).

	Case 1	Case 2	Case 3	Case 4	Case 5	Case 6
Max LSR	0.2423	0.2394	0.2439	0.2427	0.2666	0.2601
Min LSR	0.0688	0.1583	0.1391	0.0857	0.0249	0.0462

Table 49. LSR in 5-planet ESSP 1200 Nm CW (Conf. 2).

	Case 1	Case 2	Case 3	Case 4	Case 5	Case 6
Max LSR	0.3759	0.2619	0.2484	0.3991	0.4030	0.4331
Min LSR	0.1293	0.1535	0.1535	0.1245	0.1240	0.1174

Table 50. LSR in 5-planet ESSP 3600 Nm CW (Conf. 2).

	Case 1	Case 2	Case 3	Case 4	Case 5	Case 6
Max LSR	0.2379	0.2339	0.2287	0.2358	0.2416	0.2393
Min LSR	0.1255	0.1658	0.1642	0.1339	0.1200	0.1302

Table 51. LSR in 5-planet ESSP 3600 Nm CW (Conf. 2).

	Case 1	Case 2	Case 3	Case 4	Case 5	Case 6
Max LSR	0.2955	0.2550	0.2506	0.3035	0.2973	0.3059
Min LSR	0.1463	0.1547	0.1519	0.1446	0.1459	0.1441

A.III. Deltas

Numerical results of the ΔLSR generated by the errors studied in section 5.5.

Table 52. ΔLSR in 3 & 5-planet ESIP 1200 Nm (Conf. 1).

	3-planets				5-planets			
	CW		CCW		CW		CCW	
	MAX (%)	MIN (%)	MAX (%)	MIN (%)	MAX (%)	MIN (%)	MAX (%)	MIN (%)
Case 1	8.9	-17.8	18.1	-9	8.7	-35.1	35.8	-9
Case 2	1.9	-1	1.9	-1	3.5	-0.9	4.3	-1.1
Case 3	17.8	-8.9	18.1	-9	7.6	-1.9	6.1	-1.5
Case 4	8.2	-16.3	20.5	-10.3	7.9	-31.9	38.8	-9.7
Case 5	0	0	36.2	-18.1	8.3	-33.4	44.6	-11.2
Case 6	3.8	-1.9	40	-20	7.5	-30.1	47.9	-12

Table 53. ΔLSR in 3 & 5-planet ESIP 3600 Nm (Conf. 1).

	3-planets				5-planets			
	CW		CCW		CW		CCW	
	MAX (%)	MIN (%)	MAX (%)	MIN (%)	MAX (%)	MIN (%)	MAX (%)	MIN (%)
Case 1	3.1	-6.2	6.7	-9	3	-12.3	12.4	-3.1
Case 2	0.7	-0.4	0.7	-1	1.4	-0.4	1.4	-0.4
Case 3	6.3	-3.1	6.3	-9	2.5	-0.7	2	-0.5
Case 4	3	-6	3	-10.3	2.8	-11.3	13.5	-3.4
Case 5	0	0	0	-18.1	2.7	-10.9	14.6	-3.7
Case 6	1.9	-1	1.9	-20	2.4	-9.8	26	-12

Table 54. ΔLSR in 3 & 5-planet ESSP 1200 Nm (Conf. 1).

	3-planets				5-planets			
	CW		CCW		CW		CCW	
	MAX (%)	MIN (%)	MAX (%)	MIN (%)	MAX (%)	MIN (%)	MAX (%)	MIN (%)
Case 1	16	-27.4	23.5	-20.1	14.9	-42.1	40.1	-21.1
Case 2	8.6	-13	8.5	-13	9.5	-14	9.7	-14.5
Case 3	23.9	-20.2	23.5	-20.1	10.1	-14.5	10.5	-14.6
Case 4	15.1	-26	25	-20.8	14.1	-39.5	43.2	-21.7
Case 5	7.1	-12.4	40.5	-27.9	15.3	-38.6	46.7	-22.4
Case 6	10.1	-13.7	43.5	-29.2	14.4	-35.8	50	-23.1

Table 55. ΔLSR in 3 & 5-planet ESSP 3600 Nm (Conf. 1).

	3-planets				5-planets			
	CW		CCW		CW		CCW	
	MAX (%)	MIN (%)	MAX (%)	MIN (%)	MAX (%)	MIN (%)	MAX (%)	MIN (%)
Case 1	11	-17.6	13.4	-13.8	9.8	-23.9	17.8	-16.8
Case 2	8.5	-12.7	7.9	-11	7.8	-14.3	7.1	-14.4
Case 3	13.6	-15.1	13.4	-13.8	8.4	-14.4	7.7	-14.6
Case 4	10.8	-17.1	13.9	-14.1	9.5	-23	18.9	-16.9
Case 5	7.9	-12.5	19.4	-16.9	9.6	-22.7	19.9	-17.2
Case 6	8.9	-12.9	20.5	-17.5	9.3	-21.6	21	-17.4